Discovery Potential for Quantum Black Holes in the Di-Top Quark Final State at the Large Hadron Collider

by

Sina Safarabadi Farahani

A thesis submitted in partial fulfillment of the requirements for the degree of

Master of Science

in

Physics

Department of Physics

University of Alberta

Abstract

Models postulating large extra dimensions or a warped extra dimension allow the reduction of the Planck scale to the order of a few TeV. These energies may be accessible by the Large Hadron Collider particle accelerator. Quantum black holes are predicted to be produced from particle collisions with energies near the Planck scale. Quantum black holes decay into few-particle final states. This thesis looks into the simulation of such objects and their decay to the tt final state in the fully-hadronic and semi-hadronic topologies with a centre-of-mass energy of 13 TeV. Quantum chromodynamic processes dominate the background in both topologies. The ADD model (Arkani-Hamed, Dimopoulos, and Dvali) postulating $n = \{2, 4, 6\}$ large extra dimensions and the RS1 (Randall-Sundrum type I) model are studied. The discovery of quantum black holes with production mass threshold below $\{9.1, 8.9, 8.5\}$ TeV and $\{10.0, 9.8, 9.4\}$ TeV using 150 fb^{-1} and 3000 fb^{-1}, respectively, for the ADD model with $n = \{2, 4, 6\}$ could be possible. Quantum black holes in the RS1 model could be found with a production threshold mass below 6.2 TeV and 7.3 TeV, respectively. Also, using 37.4 fb^{-1} of ATLAS data, upper limits at the 95% confidence level on the quantum black hole production cross-section times branching ratio to the tt final state times acceptance times efficiency versus threshold production mass are calculated. The limits are found to be 5.9 fb at 4.0 TeV and 0.11 fb at 8.0 TeV. There are no data for masses above 8.3 TeV which sets the limit to 0.08 fb for higher masses. Using the above models, the result excludes the production of ADD quantum black holes with threshold mass less than $\{7.6, 7.2, 6.2\}$ TeV in the tt channel. Due to the lower cross-section of quantum black holes in the RS1 model, no exclusion limit could be set for quantum black holes decaying to tt in the RS1 model.

Dedication

I dedicate my work to my loving family, especially to my father whom I owe everything to and has been my biggest source of encouragement throughout the years. I hope I have made you proud, rest in peace.

Acknowledgements

I would like to thank my supervisor, Professor Douglas Gingrich, for taking me on as his graduate student and giving me the opportunity to study and work in one of the best universities in Canada under his great and everlasting supervision and helping me throughout my studies. I would also like to thank him for providing a safe and calm environment to do my research and making it possible for me to attend several conferences.

I would also like to thank Hulin Wang and Xiaohu Sun for all their help and guidance throughout my research.

I would like to thank all my great teachers during my undergraduate studies who equipped me the proper knowledge to continue my studies. I specially want to thank Prof. Hamid Reza Sepangi for all his great physics classes and life lessons, for all he taught me about life and how to be a better human being.

Last but not least, to my family who had my back in every single step of my life and helped me to get to the place I am today and always believed in me. To my beloved mother whom I had to leave and pursue my studies and dreams in a faraway country.

Contents

List of Tables

List of Figures

List of Abbreviations

A	Acceptance
ALFA	Absolute Luminosity For ATLAS
ALICE	A Large Ion Collider Experiment
ATLAS	A Toroidal LHC ApparatuS
BH	Black Hole
BR	Branching Ratio
BSM	Beyond the Standard Model
CDR	Conceptual Design Report
CL	Confidence Level
CMS	Compact Muon Solenoid
CSC	Cathode Strip Chamber
EFE	Einstein's Field Equations
EM	ElectroMagnetic
FCC	Future Circular Collider
FCal	Forward Calorimeter
GR	The General Theory of Relativity
GUT	Grand Unified Theory
HEC	Hadronic End-cap Calorimeter
HL-LHC	High-Luminosity LHC
HLT	High-Level Trigger
ID	Inner Detector
IP	Interaction Point
JER	Jet Energy Resolution
JES	Jet Energy Scale
KN	Kerr-Newman
LAr	Liquid Argon
LCW	Local Cluster Weighting
LEP	Large Electron-Positron
LHA	Les Houches accord
LHCb	Large Hadron Collider beauty
LHCf	LHC forward
LINAC	LINear ACcelerator
LS	Long Shutdown
LUCID	LUminosity measurement using Cerenkov Integrating Detector
MC	Monte Carlo
MDT	Monitored Drift Tube

MP	Myers-Perry
p	Proton
PDF	Parton Distribution Function
PDG	Particle Data Group
PS	Proton Synchrotron
PSB	Proton Synchrotron Booster
Pb	Lead
QBH	Quantum Black Hole
QCD	Quantum ChromoDynamics
QED	Quantum ElectroDynamics
RN	Reissner-Nordstrom
RPC	Resistive Plate Chamber
RoI	Region-of-Interest
SBH	Semiclassical Black Hole
SCT	Semi-Conductor Tracker
SM	The Standard Model
SPS	Super Proton Synchrotron
SSB	Spontaneous Symmetry Breaking
TGC	Thin Gap Chamber
TOTEM	TOTal Elastic and diffractive cross section Measurement
TRT	Transition Radiation Tracker

Chapter 1

Introduction

The Standard Model (SM) of particle physics is the best theory we have so far for explaining three of the four fundamental forces in nature: electromagnetic, weak, and strong forces. It has made many successful predictions, but some questions cannot be answered in this framework, including the hierarchy problem. The hierarchy problem is the huge difference between the strength of the weak force and the gravitational force. The model of large extra dimensions proposed by Arkani-Hamed, Dimopoulos, Dvali - often called the ADD model - is one of the possible ways of addressing the hierarchy problem [1]. Another famous model is the five-dimensional warped geometry model proposed by Randall and Sundrum [2, 3] (RS1 and RS2 models). The possible production of quantum black holes (QBHs) from particle collisions at the large hadron collider (LHC) is a consequence of such models.

In this study, we have two objectives. One of our objectives is to predict the discovery potential of QBH at the LHC in the tt channel. The studied models are the ADD model with $n = \{2, 4, 6\}$ large extra dimensions and the RS1 model. Our other task is to set an upper limit on the production cross-section times branching ratio times acceptance times efficiency and the production cross-section of QBHs in proton-proton (pp) collisions using the data and results from ATLAS dijet analysis [4]. Using a total integrated luminosity of 37.4 fb^{-1}, the ATLAS dijet analysis [4] has excluded QBH production with threshold mass below 8.9 TeV for the ADD model assuming $n = 6$. The ATLAS study was in the dijet channel and not just jets from the tt final state. We obtain a lower mass limit for the studied models in the tt decay channel.

Chapter 2 gives a brief review of theories and models relevant to this thesis including the SM of particles physics, the theory of General Relativity (GR), and the ADD and RS1 models.

Chapter 3 gives a more detailed review of the physics of black holes, from classical to quantum black holes. Higher dimensional black holes are also reviewed in this chapter.

Chapter 4 describes the LHC machine. The ATLAS detector and its constituents are described.

Chapter 5 reviews the object reconstructions in the ATLAS detector.

The procedure for studying the QBHs production and their decay to the tt final state at the LHC is described in chapter 6. This chapter describes in detail the search for resonances in the fully- and semi-hadronic topologies.

The results of the discovery potential at the LHC on QBHs mass is presented in chapter 7. The 95% confidence level (CL) upper limit on the quantum black hole production cross-section times branching ratio times acceptance times efficiency is also presented.

Finally, chapter 8 summarizes the study and its results.

Chapter 2

Review of Theory and Model

Electromagnetic, weak, and strong interactions are three of the four fundamental interactions described in a single framework known as the standard model (SM) of particle physics[1] which is based on quantum field theory. The fourth fundamental force, the gravitational force, is described by general relativity (GR). Unlike the SM, GR is a classical theory, and no consistent quantum theory has yet been found for gravitation. A typical problem of a quantum theory description of gravity is Nonrenormalizability of gravity (see Ref. [5] for more information).

The electroweak energy scale, $m_{\rm EW} \approx 0.2$ TeV [2] is given by the vacuum expectation value of the higgs field. The gravitational scale is known as the Planck scale $M_{Pl} = 10^{16}$ TeV. The huge difference between these two fundamental scales is known as the hierarchy problem. To explain all the four forces in a unified picture, the fundamental scales should be of the same order. The ADD model is one of the proposed models to tackle this problem using large extra dimensions. The RS1 model is another model which uses a single highly warped extra dimension to solve this problem.

This chapter reviews the theories and models used in this thesis, and serves as a motivation to our study. We first take a look at the SM of particle physics and GR, followed by the production of QBHs at the LHC.

2.1 Standard Model

The SM of particle physics is the most successful theory so far that describes the electromagnetic, weak, and strong interactions in a single framework. It has been capable of explaining most of the experimental observations and has made significant predictions among which were the existence of the W and Z bosons, gluons, top and charm quarks, and the Higgs boson found in 2012.

[1] We also have the standard model for cosmology, for example, known as ΛCDM.

[2] In this thesis we will use the natural units (unless stated otherwise) in which one takes $G = c = \hbar = \epsilon_0 = k_B = 1$.

In the SM, the elementary particles having half-integer spins are called fermions and obey Fermi-Dirac statistics. Particles carrying integer spins are called bosons obeying Bose-Einstein statistics. Fermions themselves are divided into two categories: leptons, along with their corresponding neutrinos, and the quarks. Both come in three generations. The electron (e), muon (μ), tau (τ) and their corresponding neutrinos (ν) are the three generations of the leptons. The first three (e, μ, τ) have an electric charge of $-1q_e$[1] and the neutrinos $(\nu_e, \nu_\mu, \nu_\tau)$ have no electric charge. The quarks are divided into up-type and down-type quarks each with three generations. Up-type quarks include up (u), charm (c), and top (t) quarks having an electric charge of $+\frac{2}{3}$. Down-type quarks include down (d), strange (s), and bottom (b) quarks with an electric charge of $-\frac{1}{3}$. Each of the leptons and quarks come with their corresponding anti-particle. Figure 2.1 shows the elementary particles of the SM.

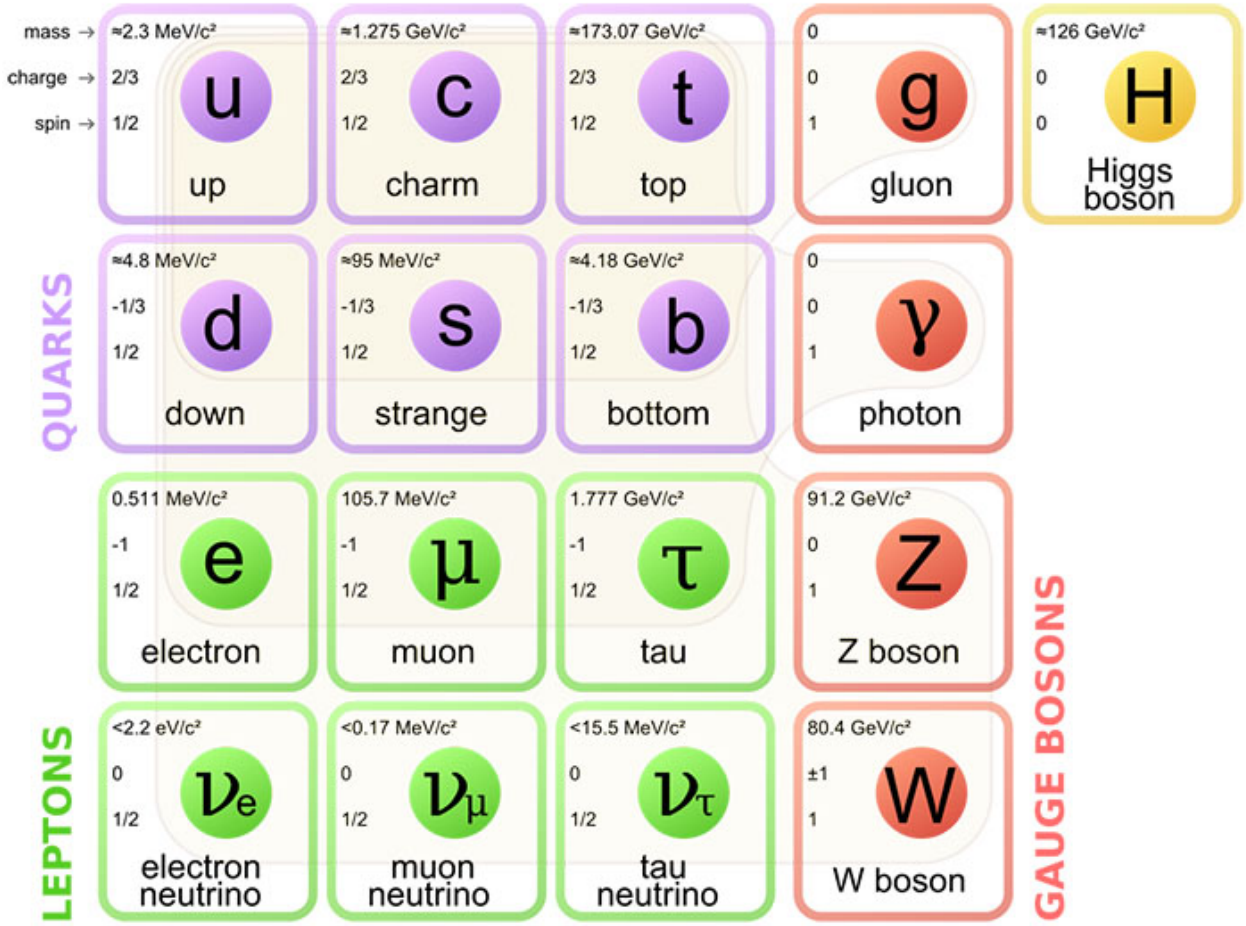

Figure 2.1: Elementary particles of the standard model.

In physics, symmetries can be categorized in two broad categories. Global symmetry

[1] $q_e \approx 1.60 \times 10^{-19}$ Coulombs (C) is the elementary charge carried by a single proton. It also is denoted by e which is not used here to avoid confusion with the electron particle. We use $q_e = 1$ here.

which does not depend on spacetime and local symmetry which is dependent on the spacetime. The SM is a gauge theory, meaning that its action is invariant under some local (internal) symmetries [1]. These symmetries correspond to gauge fields which in return give rise to gauge bosons. Gauge bosons are the force carriers. The symmetry groups of the SM are $SU(3)_C \otimes SU(2)_L \otimes U(1)_Y$, where the subscripts C, L, and Y are colour, left-handedness, and weak hypercharge, respectively. U and SU are unitary and special unitary groups, respectively.

The most straightforward piece of SM Lagrangian is quantum electrodynamics (QED). QED is a relativistic quantum field theory of the classical version of electrodynamics. It describes the interaction of electrically charged particles via gauge photons.

With the $SU(3)_C$ symmetry group, QCD describes the strong interactions. The mediators of QCD are the eight massless gluons. Gluons bind the quarks to form hadrons. Hadrons come in two categories, mesons and baryons. Based on the quark model, mesons are made of a quark and an anti-quark, and baryons are made of three quarks or anti-quarks. These quarks are called valence quarks. The proton contains two up quarks and a down quark, and is a baryon. Due to Pauli exclusion principle, two or more fermions are not allowed to exist the same exact quantum state. Yet, there are three quarks in hadrons. To overcome this problem another quantum number was suggested, colour charge. There are three colour charges: red, green, and blue for particles and anti-red, anti-green, and anti-blue for anti-particles. Quarks carry one of the colour charges and gluons have a combination of a color and an anti-color. The rest of the SM particles have no colour charge.

In high energy physics, instead of the quark model, the parton model is used. This model was proposed by Richard Feynman in 1969 [6]. In the parton model, the hadrons are not just made of the valence quarks but are made of partons. Gluons and quarks together are called partons. So, in a hadron, like a proton, all the partons are present but with different energies and probability. That's the reason in high energy collisions we use parton distribution functions (PDFs). The PDF $f_i\left(x, Q^2\right)$ determines the probability density of finding a parton with flavour i with a momentum fraction x of the hadron where Q is the energy scale of the hard interaction, also referred to as the resolution scale of the PDF [7].

The electromagnetic and weak interactions can be unified, and are collectively known as the electroweak interactions with a symmetry group of $SU(2)_L \otimes U(1)_Y$ and four massive gauge bosons, $W^{\pm}$ and Z for weak interactions and the photon (γ) for electromagnetic interactions. The existence of these four bosons can be explained by the spontaneous symmetry breaking (SSB) mechanism. In quantum mechanics, a set of states that result in the same energy are called degenerate states. Suppose the ground state, the state with the minimum

[1] It is also invariant under the global Poincare symmetry

energy, of a Lagrangian is degenerate. Also, the Lagrangian is invariant under a group of transformations which transform these ground states as a member of a multiplet [1]. The fact that only one of these states is chosen as the ground state of the system is called SSB. SSB has a general property of having massless degrees of freedom. In quantum field theory, the vacuum is the ground state. Suppose the electroweak Lagrangian is invariant under the continuous symmetry group G and the vacuum is invariant under H, where H is a subgroup of G ($H \subset G$). In such circumstance, the Goldstone theorem [8, 9, 10] states that there are n ($n \geq 1$) massless spin-0 Nambu-Goldstone bosons where n is the number of broken symmetries or generators. The symmetry group of $SU(2)_L \otimes U(1)_Y$ has four massless gauge fields before SSB happens. After SSB, three of the Goldstone bosons are absorbed by three gauge fields and acquire mass. These fields are the $W^{\pm}$ and Z bosons which now have a longitudinal polarization. These extra degrees of freedom come from the Goldstone bosons. One of the fields remains massless which is the photon. The leftover of the SSB is a massive field known as the Higgs field with its corresponding particle, the Higgs boson with a measured mass of 125 GeV. The Higgs boson is the last elementary boson discovered by both the ATLAS [11, 12] (a toroidal LHC apparatus) and the CMS [13] (compact muon solenoid) collaborations; completing the SM picture [14].

Although the SM has had many successes in predicting and explaining experimental observations, there are questions which have not yet been answered. Among the most important ones are: the nature of dark matter and dark energy, which together make up about 95% of the mass-energy content of the universe; matter/anti-matter asymmetry; strong CP violation; neutrino oscillations; and the hierarchy problem. These unanswered questions encourage physicists to look for theories beyond the standard model (BSM) such as those examined here.

2.2 General Theory of Relativity

Albert Einstein proposed his GR theory in 1915 [15], ten years after his special relativity theory, attempting to generalize special relativity and Newton's law of universal gravitation. Einstein's field equations (EFE) are a set of non-linear partial differential equations written as

$$R_{\mu\nu} - \frac{1}{2}Rg_{\mu\nu} + \Lambda g_{\mu\nu} = \frac{8\pi G}{c^4}T_{\mu\nu}. \tag{2.1}$$

They relate the gravitational force to the geometric property of spacetime which is curved by mass and energy. In Equation 2.1, $R_{\mu\nu}$ and R are the Ricci curvature tensor and the Ricci

[1] Multiplet is a terminology used in group theory usually referring to "an irreducible representation of a Lie group acting as linear operators on a real or complex vector space" https://en.wikipedia.org/wiki/Multiplet.

scalar (or scalar curvature), $g_{\mu\nu}$ is the metric tensor, $T_{\mu\nu}$ is the stress-energy tensor, G is Newton's gravitational constant, c is the speed of light, and Λ is the cosmological constant. The EFE are often written as

$$G_{\mu\nu} + \Lambda g_{\mu\nu} = \frac{8\pi G}{c^4} T_{\mu\nu}, \tag{2.2}$$

where $G_{\mu\nu} = R_{\mu\nu} - \frac{1}{2} R g_{\mu\nu}$ is called the Einstein tensor. The left-hand side of Equation 2.2 is a symmetric tensor which describes the curvature of the spacetime. The right-hand side describes the matter-energy content of the spacetime.

The Minkowski metric is the trivial solution to the EFE equation

$$g_{\mu\nu} = \text{diag}(-1, +1, +1, +1), \tag{2.3}$$

describing a flat spacetime with $T_{\mu\nu} = 0$. The Minkowski metric is often denoted as $\eta_{\mu\nu}$. There is a freedom in sign choice in the metric, also known as metric signature. Both $(+---)$ and $(-+++)$ give the same physical results but the sign of all spatial coordinates should be the same and opposite to the sign of the time coordinate. We use the former in our study.

The spacetime interval ds is a Lorentz invariant quantity defined from the metric as

$$ds^2 = g_{\mu\nu} dx^\mu dx^\nu, \tag{2.4}$$

where μ and ν are indices running from zero to three, and dx is an infinitesimal coordinate displacement.The components of the metric are the solutions of the EFE.

2.3 Hierarchy Problem

The hierarchy problem can be explained in different ways, each highlighting different aspects of the fact that there is a huge discrepancy between the strength of the weak and gravitational force. Regarding the strength of the force, the weak force is more than 10^{15} times stronger than the gravitational force. Since the strength of a force depends on the nature of the force and how far from the source one is performing measurements, it is not the best comparison. Another way to state this difference is their mass scales. The mass scale of the weak force is determined by the vacuum expectation value of the Higgs field given by

$$m_{\text{EW}} = \frac{1}{\sqrt{\sqrt{2} G_F^0}} = \frac{2 M_W}{g} \approx 0.25 \text{ TeV}, \tag{2.5}$$

where $G_F^0 = G_F/(\hbar c)^3$ is the reduced Fermi constant, g is the weak isospin coupling, and M_W is the mass of the W boson. The mass scale of gravity is the Planck mass defined as

$$M_{Pl} = \sqrt{\frac{\hbar G}{c}} \approx 10^{16} \text{ TeV}. \tag{2.6}$$

The ratio of the two mass scales is about 10^{16} which is bothersome for most physicists. The problem is in explaining that why the Higgs boson mass is so much lighter than the Planck scale. The huge quantum contributions to the Higgs mass-squared parameter should result in a huge Higgs boson mass unless there has been some incredible fine-tuning cancellation between the different quadratic radiative corrections and the bare mass of the Higgs to yield the observed Higgs mass. In theoretical physics, fine-tuning means that for a model to explain the observations, some parameters have to have very precise values and there is no known physical explanation or mechanism to give rise to such values.

2.4 ADD Models

Gunnar Nordström in 1914 was the first person to introduce the idea of adding extra spatial dimensions to the usual $3+1$ dimensions [16]. The most famous theories and models that make use of extra dimension(s) are the Kaluza-Klein (KK) theory, proposed by Theodore Kaluza and Oskar Klein in 1926, the ADD [1, 17] model, and RS model [2, 3]. In this study, we will be using the ADD and RS1 models, and we shall give a little bit more detail on them.

The ADD model tries to solve the hierarchy problem by adding large extra dimensions. This model is also known as the large extra dimensions (LED) model where the size of the extra dimensions are large compared to the Planck length $\ell_{Pl} \approx 10^{-35}$ m. In models with extra dimensions, the fundamental scale is the D-dimensional Planck scale and the four dimensional Planck scale is derived from it.

The universe is filled with baryons and since the Big Bang is believed to be a burst of just energy with no initial matter distribution, there has to be some baryon number violation during the Big Bang. If baryon number can be violated, the proton decay process won't be forbidden anymore. Considering that new physics is assumed to happen close to the grand unified theory (GUT) energy scale, 10^{16} GeV, or close to the Planck energy scale, 10^{19} GeV, the half-life of proton should at least be about 10^{34} years [18]. The ADD model allows the violation of baryon and lepton number but it also brings the scale of the new physics down to a few TeV which means the proton decay should happen a lot more frequent. In such cases, the proton decay should not be completely forbidden and only suppressed enough to explain the current observations. In models with extra dimensions, this issue can be solved in different ways. One way is to add a forth generation of matter [19] or introduce a "baryon

triality" which suppress the baryon number violation [20]. See Ref. [21] and [22] for more information on baryon and lepton number violation, respectively.

Let's add n extra compactified dimensions with the same radius R and consider a D-dimensional spacetime with $D = n + 4$. In such condition, using Gauss's law, the gravitational potential between the two masses m_1 and m_2 within $r \ll R$ is [1]

$$V(r) \sim \frac{m_1 m_2}{M_D^{n+2}} \frac{1}{r^{n+1}}, \quad (r \ll R), \tag{2.7}$$

where $M_D^{n+2} = M_{Pl(n+4)}^{n+2}$ is the fundamental Planck scale in D-dimensions. Although the gravitational flux lines at $r \ll R$ propagate into the extra dimensions and contribute to the potential, at $r \gg R$ the gravitational potential reduces to the usual $1/r$

$$V(r) \sim \frac{m_1 m_2}{M_D^{n+2} R^n} \frac{1}{r}, \quad (r \gg R), \tag{2.8}$$

where the effective four dimensional Planck scale becomes

$$M_{Pl}^2 \sim M_D^{n+2} R^n. \tag{2.9}$$

Although adding these extra dimensions weakens the force of the gravity in short distance, in this case the momentum of the matter fields that travel in these extra dimensions is quantized along the extra dimension, hence the fields' masses become quantized as well. This phenomenon is known as KK tower [23, 24] of masses which overcomes the weakening of the force of the gravity. Requiring the fundamental Planck scale to be close to the electroweak scale, $M_D \sim m_{\text{EW}}$, and choosing R such that the observed value of M_{Pl} is reproduced,

$$R \sim 10^{\frac{32}{n} - 19} \text{m} \times \left(\frac{1\text{TeV}}{m_{\text{EW}}} \right)^{1+\frac{2}{n}}. \tag{2.10}$$

The approximate values of R for different number of extra dimensions is given in Table 2.1.

n	1	2	3	4	5	6	7
$R\,(\text{m})$	10^{14}	10^{-2}	10^{-8}	10^{-11}	10^{-12}	10^{-13}	10^{-14}

Table 2.1: Approximate values for the size of the toroidal compactified extra dimensions for different number of extra dimensions in the ADD model.

The large value of R for $n = 1$ would cause deviation from the Newtonian gravity at scales of the solar system. Such deviations from Newtonian gravity have not been observed,

and $n = 1$ is observationally ruled out. A set of torsion-balance experiments [25] have set an upper limit on the size of extra dimensions of $R \leq 44$ μm which excludes $n = 2$ case as well. The treatment of the size of all the extra dimensions to be the same is just for simplification and not a necessity. Thus, $n = 2$ is still being studied and considered by ATLAS and CMS.

Although gravity has not been measured down to sizes of about a micrometre, the SM gauge forces have been probed in the weak scales, 10^{-18} m, and no evidence of extra dimensions have been found. As such, it was proposed that the SM particles are confined to a 4-dimensional submanifold and only $(n + 4)$-dimensional gravitons can propagate to these extra dimensions. This localization of SM fields is explained by embedding the ADD model in string theory [17]. In the string theory, the SM particles are described by open strings while the gravitational sector has closed strings capable of propagating into higher dimensions.

2.5 Randall–Sundrum Models

The RS models (RS1 [2] and RS2 [3]) also use extra dimensions. The RS1 model assumes two branes as the boundaries of a warped fifth dimension. In RS1, the two branes are located at the ends of the new dimension. In RS2, one of the branes is moved to the infinity and one is left with only one brane.

In RS1, the effect of the new dimension on the metric of spacetime does not enter in a factorizable way. This warped factor multiplies the usual four-dimensional metric [2]

$$ds^2 = e^{-2kr_c\phi}\eta_{\mu\nu}dx^\mu dx^\nu + r_c^2 d\phi^2, \tag{2.11}$$

where r_c is the compactification radius. The scale factor k is of the order of the fundamental Planck scale. Also, the coordinate of the new dimension, ϕ, is periodic ($0 < \phi < \pi$). The two branes located at $\phi = 0$ and $\phi = \pi$ are often called the Planck-brane and the TeV-brane, respectively. The TeV-brane is the brane in which gravity is strong and the Planck scale is of order of a few TeV and thus all the SM particles reside in the Planck-brane. In the RS1 model, a mass parameter m_0 corresponds to a physical mass m through

$$m \equiv e^{-kr_c\pi}m_0. \tag{2.12}$$

For example, to recover the Planck scale, 10^{16} TeV, from a 1 TeV physical mass scale, one only requires $kr_c \approx 12$.

As mentioned, the RS2 model has only one brane which is the Planck-brane. Since this model has no TeV-brane, it is not capable of reducing the Planck scale to orders of a few

TeV. Its geometry could be interesting for other studies but not for us.

The ADD model and RS1 model reduce the Planck scale using different approaches. In the ADD model, the Planck scale is determined by the volume of the extra dimensions and in the RS1 model the Planck scale is reduced by an exponential warped factor. Black holes in higher dimensional models will be discussed in section 3.2.

Chapter 3

Physics of Black Holes

In this chapter, we give a review of different types of classical four-dimensional black holes (BHs) with their properties, and then generalize them to higher dimensional BHs. We conclude this chapter by discussing the production and decay of the QBHs at the LHC.

3.1 Classical Four-Dimensional Black Holes

In GR, the curvature of spacetime is the force of gravity. The curvature is determined by how matter and energy are distributed and the trajectory of particles is dictated by the spacetime curvature. When a very massive star collapses at the end of its lifespan, it can create a BH; a region of spacetime with a gravitational force so strong that the escape velocity of any particle from it becomes greater than the speed of light. In this section, we will take a look at three different types of classical BHs in the usual 3+1 dimensions. Classical black holes are believed to be the product of massive stars collapsing under their own gravity when they reach the end of their lifespan. Solving Equation 2.2 is very complex and most of the times, instead of using the $T_{\mu\nu}$ directly for analytic solutions, other properties of the spacetime are exploit for the derivation of the metric which is out of the scope of this study.

3.1.1 Schwarzschild Black Hole

In 1915, Karl Schwarzschild found the first exact solution to the EFE describing the gravitational field of an electrically neutral non-rotating spherical object of mass M:

$$ds^2 = -\left(1 - \frac{2M}{r}\right) dt^2 + \left(\frac{1}{1 - \frac{2M}{r}}\right) dr^2 + r^2 d\Omega_2^2. \tag{3.1}$$

Equation 3.1 is known as the Schwarzschild metric where $d\Omega_2^2 = d\theta^2 + \sin^2\theta d\phi^2$ is the usual metric of a 2-sphere. The Schwarzschild coordinates has two singularities at $r = 0$ and at $r = 2M = r_s$. The singularity at $r = r_s$ is known as a coordinate singularity which appears only because of the choice of the coordinates, and can be removed. By a transformation to

Kruskal-Szekeres coordinates, the Schwarzschild solution is

$$ds^2 = \frac{32M^3}{r} \exp^{-r/2M} \left(-dT^2 + dX^2\right) + r^2 d\Omega_2^2, \tag{3.2}$$

where

$$\begin{aligned} T &= \left(\frac{r}{2M} - 1\right)^{1/2} \exp^{r/4M} \sinh\left(\frac{t}{4M}\right), \\ X &= \left(\frac{r}{2M} - 1\right)^{1/2} \exp^{r/4M} \cosh\left(\frac{t}{4M}\right), \end{aligned} \tag{3.3}$$

replaces the t and r in the Schwarzschild coordinates. But the singularity at $r = 0$ cannot be removed by any transformation and is known as the curvature singularity. Although $r = 2M$ is not a singularity, it has a specific feature. $r_s = 2M$ is called the Schwarzschild radius determining the location of the event horizon. The event horizon is defined as a boundary beyond which nothing can escape the gravitational pull of this object. At the event horizon, the sign of the metric components flip and the spatial coordinates of the metric become time coordinate and the time coordinate becomes spatial coordinate. Beyond r_s, the r coordinate becomes time coordinate and has to continue in the direction of increasing r. So, in the Schwarzschild metric the trajectory of every object within $r \leq 2M$ is doomed to hit the curvature singularity, even that of the light, hence the name black hole.

3.1.2 Reissner-Nordström Black Hole

A Reissner-Nordström (RN) BH is the solution to EFE with the assumption of a spherically symmetric electrically charged but still non-rotating object with mass M and electrical charge of Q. Although in the real world such objects should become electrically neutral via interaction with matters around the BH, the assumption here is that the charge is static, resulting in the RN metric

$$ds^2 = -\Delta dt^2 + \Delta^{-1} dr^2 + r^2 d\Omega_2^2, \tag{3.4}$$

with Δ defined as

$$\Delta(r) = 1 - \frac{2M}{r} + \frac{Q^2}{r^2}. \tag{3.5}$$

The RN metric can have a more general form by replacing $Q^2 \to Q^2 + P^2$, where P is the magnetic charge. Since no magnetic monopoles have been observed, we will set $P = 0$ but the above substitution can be done at every step. Note that setting $Q = 0$ yields the Schwarzschild metric. Usually the quantities $r_s = 2M$ and $r_Q = Q$ are defined, and Δ takes

the simple form of

$$\Delta(r) = 1 - \frac{r_s}{r} + \frac{r_Q^2}{r^2}. \tag{3.6}$$

This metric also has a curvature singularity at $r = 0$. The location of the event horizon can often be found from setting the g^{rr} component of the metric to zero which in our case translates to $\Delta(r) = 0$[1], resulting in

$$r_\pm = M \pm \sqrt{M^2 - Q^2}. \tag{3.7}$$

The three possible solutions of Equation 3.7 are:

- $M^2 < Q^2$: In this case, Δ can never be zero and there are no event horizons around the singularity. This type of singularity is known as a naked singularity. This is an unphysical solution because it implies that the mass of the collapsing object has to be negative since the total energy is less than the contribution of the electromagnetic field alone.

- $M^2 > Q^2$: This condition is the most probable result of a collapsing object. This case has two coordinate singularities at $r_\pm = M \pm \sqrt{M^2 - Q^2}$, where r_- and r_+ are called the inner and outer event horizon, respectively. The r_+ is like $r = 2M$ for the Schwarzschild BH. When an observer passes r_+, he has to continue in the direction of increasing r since r is a time coordinate now. Unlike the Schwarzschild metric, here exist another event horizon at r_-. This means another sign change of the coordinates and hence the observer is not doomed to hit $r = 0$ and can choose to escape the singularity. But once passed r_- again, she/he cannot return and has to cross r_+. This process can go on forever.

- $M^2 = Q^2$: This solution is also known as the extreme RN solution. In this case, there is only one event horizon at $r = M$ and since $\Delta = 0$, the r coordinate stays spacelike on both sides of the horizon and is null at $r = M$, meaning an observer can escape the singularity.

3.1.3 Kerr-Newman Black Hole

In 1963, Roy Kerr found the solution of the EFE for a rotating object [26]. Two years later, the solution was generalized to an electrically charged rotating object with an axial symmetry by Ezra Theodore Newman known as the Kerr-Newman (KN) [27, 28] metric.

[1]Note that the coefficients in ds^2 are $g_{\mu\nu}$. If the metric is diagonal, the components of the metric and the components of its inverse are related as $g_{\mu\mu} = 1/g^{\mu\mu}$

The Kerr solution in the Boyer-Lindquist coordinates takes the form

$$\begin{aligned} ds^2 = &-\left(1-\frac{r_s r}{\Sigma^2}\right)dt^2 + \frac{\Sigma^2}{\Delta_{\rm K}}dr^2 + \Sigma^2 d\theta^2 \\ &+\left(r^2+a^2+\frac{r_s r a^2}{\Sigma^2}\sin^2\theta\right)\sin^2\theta d\phi^2 - \frac{2r_s r a\sin^2\theta}{\Sigma^2}dtd\phi, \end{aligned} \tag{3.8}$$

with the length-scale parameters defined as

$$\Sigma^2(r,\theta) = r^2 + a^2\cos^2\theta, \tag{3.9}$$

$$\Delta_{\rm K}(r) = r^2 - r_s r + a^2, \tag{3.10}$$

$$a = \frac{J}{M}. \tag{3.11}$$

$r_s = 2M$ is the usual Schwarzschild radius, J is the angular momentum of the BH, and a is a constant. The Kerr-Newman metric can be written in the form

$$\begin{aligned} ds^2 = &-\Sigma^2\left(\frac{dr^2}{\Delta_{\rm KN}} + d\theta^2\right) + \frac{\Delta_{\rm KN}}{\Sigma^2}\left(dt - a\sin^2\theta d\phi\right)^2 \\ &-\frac{\sin^2\theta}{\Sigma^2}\left(\left(r^2+a^2\right)d\phi - adt\right)^2, \end{aligned} \tag{3.12}$$

where $\Delta_{\rm KN} = r^2 - r_s r + r_Q^2 + a^2$ and $r_Q = Q$. Note the similarity between $\Delta_{\rm K}$ and $\Delta_{\rm KN}$ used in Kerr and Kerr-Newman metrics, respectively. In other words, the KN metric can be obtained from Kerr metric by replacing $2GMr \to 2Mr - (Q^2+P^2)$. The event horizon of Kerr and Kerr-Newman metrics are given by $r_K^{\pm} = M \pm \sqrt{M^2 - a^2}$ and $r_{KN}^{\pm} = M \pm \sqrt{M^2 - a^2 - Q^2}$, respectively. The curvature singularities happen at $\Sigma = 0$. The outer event horizon is a rotating surface with an angular velocity of $\Omega_H = \frac{a}{r_+^2 + a^2}$. Note that similar to the RN BH, here we also have three possible solutions for the event horizon of Kerr and KN BHs. The two solutions that yield naked singularities and the extreme solution are not discussed.

The curvature singularity happens under the condition of $r^2 + a^2\cos^2\theta = 0$. Since both terms are strictly positive, it has a solution at

$$r = 0, \qquad \theta = \frac{\pi}{2}. \tag{3.13}$$

Instead of a point, the singularity is now a ring.

3.2 Black Holes in Higher Space Dimensions

Higher dimensional BHs are interesting but complex objects. The analytical solution of higher dimensional counterparts of the Schwarzschild and Kerr metrics have been found. Here we will give a brief review of them.

The Schwarzschild-Tangherlini [29] metric is a description of a spherically symmetric BH in $D = n + 4$ dimensions with no electrical charge and no rotation. The metric has the following form

$$ds^2 = -\rho dt^2 + \rho^{-1} dr^2 + r^2 d\Omega_{n+2}^2, \tag{3.14}$$

where $\rho = \left[1 - \left(\frac{r_H}{r}\right)^{n+1}\right]$ replaces the coefficient in the Schwarzschild metric, $\left(1 - \frac{r_s}{r}\right)$, r_H is the higher dimensional event horizon, and Ω_{n+2}^2 is the metric of a $(n+2)$-sphere. The area of a n-sphere of unit radius can be calculated as

$$S_n = \frac{2\pi^{\frac{n+1}{2}}}{\Gamma\left(\frac{n+1}{2}\right)}, \tag{3.15}$$

where Γ is the gamma function. The radius of the BH in the Tangherlini metric can be defined as

$$r_H^{n+1} = \frac{16\pi GM}{(n+2)\, S_{n+2}}. \tag{3.16}$$

The symbol $\mu = r_H^{n+1}$ is often defined.

The Myers-Perry (MP) metric [30] generalizes the Kerr metric to a $(n+4)$ dimensional electrically neutral rotating BH. In higher dimensions, the MP BH has a number of rotational axes given by $N = \frac{n+2}{2}$ for odd number of extra dimensions and $N = \frac{n+3}{2}$ for even numbers of n. This makes the metric a lot more complicated and different depending if n is even or odd. The metric of the simplest form, when the BH has only rotation along one axis, is

$$\begin{aligned} ds^2 = &-\left(1 - \frac{\mu}{\Sigma r^{n-1}}\right) dt^2 - \frac{2a\mu \sin^2\theta}{\Sigma r^{n-1}} dt d\phi + \frac{\Sigma}{\Delta_{\mathrm{MP}}} dr^2 + \Sigma d\theta^2 \\ &+ \left(r^2 + a^2 + \frac{a^2 \mu \sin^2\theta}{\Sigma r^{n-1}}\right) \sin^2\theta d\phi^2 + r^2 \cos^2\theta d\Omega_n^2, \end{aligned} \tag{3.17}$$

where as before $\Sigma = r^2 + a^2 \cos^2\theta$ and $\Delta_{\mathrm{MP}} = r^2 + a^2 - \frac{\mu}{r^{n-1}}$. The definition of mass stays the same as the one in Schwarzschild-Tangherlini metric. The angular momentum is defined as

$$J = \frac{2}{n+2} aM. \tag{3.18}$$

Combining the higher dimensional BHs and the ADD or RS1 model, we can study the possible production of QBHs at the LHC, discussed in the next section.

3.3 Quantum Black Holes at the Large Hadron Collider

QBHs in (3+1)-dimensions are predicted to be created from particle collisions with energies around the Planck scale which is of order 10^{19} GeV. This energy was only accessible during the big bang and surely cannot be reached by any current accelerator on the Earth. In low-scale gravity models [1, 17, 2, 3, 31, 32], the Planck scale can be reduced to a few TeV. The creation of QBHs at particle accelerators such as the LHC becomes a possibility under such models. From classical to quantum black holes, there is an intermediate mass regime with another type of BH known as semiclassical black holes (SBHs). It is believed that the decay process of SBHs would be a thermal decay at the Hawking temperature and thus can be described by BH thermodynamics. Unlike SBH, the back-reaction of a QBH decay on the spacetime is not negligible and as a consequence, it is not in thermal equilibrium with its radiation and will not decay thermally. In this case, the BH does not have a well-defined temperature or an entropy big enough to decay thermally. Considering BHs with a mass just above the Planck scale, it could be expected that decaying to few-particle final states becomes dominant [33]. Our study of QBHs is based on Douglas M. Gingrich's model for QBH production at the LHC [34, 33] which is built on Ref. [35, 36]. Ref.[34] defines a BH formed by particle collisions as "any matter or energy trapped behind the horizon formed by the available mass and energy of the particle collision."

In this section, we will first take a look at QBH states and their production at the LHC. The QBH cross-sections will also be discussed. Since we are interested in the decays of the QBHs to the ditop quark final state, whereby ditop we mean all three possible combinations of the top and anti-top quark final states ($tt, \bar{t}\bar{t}, t\bar{t}$), we will first give a review of the top quark and its decay modes followed by the decay modes of QBHs.

3.3.1 Quantum Black Holes Production and Cross-Section

Since QBHs can carry colour and electric charge, their state can be described by their $SU(3)_C$ and $U(1)_Y$ representations, respectively. Considering pp collisions at the LHC, the particles that can contribute to the QBH formation are quarks, anti-quarks, and gluons. Based on the electric charge, nine states can be produced: $\pm\frac{4}{3}, \pm1, \pm\frac{2}{3}, \pm\frac{1}{3}$, and 0. Since we are interested in the ditop final states, only charge $\pm\frac{4}{3}$ and 0 are considered. The $+\frac{4}{3}$ QBH state can only be created from uu, where u stands for up-type quarks and the $-\frac{4}{3}$ is from $\bar{u}\bar{u}$, where $\bar{u}$ is anti-up-type quark. The 0 state can be formed by either gg or $q\bar{q}$ where g is a gluon, and q can be either up-type or down-type quark, and the anti-quark is $\bar{q}$. See Ref.[33] for more information on other quantum numbers carried by the QBH such as colour and angular momentum.

Since we do not have a theory for quantum gravity, the production cross-section σ of QBHs is unknown. Since the gravitational radius is the only length scale, and considering classical arguments [34], the partonic cross-section is assumed to be geometrical:

$$\sigma \sim \pi r_g^2. \tag{3.19}$$

There are factors ignored in this assumption that can impact the cross-section, including:

- Gravitational radiation where all the energy of the colliding particles does not go into the creation of the QBHs. The numerical results of the trapped surface [37] approach can be found in Ref. [38, 39, 40].
- The effect of parton charge, spin, and finite size discussed in Ref. [41, 42, 43, 44, 45].

These effects can change the cross-section by more than two orders of magnitude [33].

A spinless QBH with a mass M will have a gravitational radius r_g of [46]

$$r_g = \left[G_D M \left(2^3 \pi^{(3-D)/2} \frac{\Gamma\left(\frac{D-1}{2}\right)}{D-2} \right) \right]^{\frac{1}{D-3}}. \tag{3.20}$$

To relate the D-dimensional Newton constant, G_D, to the fundamental Planck scale, one has to choose a convention. Using the PDG [47] definition, also know as Giudice-Rattazzi-Wells (GRW) convention [48],

$$M_D^{D-2} = \frac{(2\pi)^n}{8\pi G_D}. \tag{3.21}$$

The gravitational radius can be written as

$$r_g = k\left(D\right) \frac{1}{M_D} \left(\frac{M}{M_D} \right)^{\frac{1}{D-3}}, \tag{3.22}$$

where $k\left(D\right)$ is a numerical factor

$$k(D) = \left(2^{D-4} \sqrt{\pi}^{D-7} \frac{\Gamma\left(\frac{D-1}{2}\right)}{D-2} \right)^{\frac{1}{D-3}}. \tag{3.23}$$

$k\left(D\right)$ only depends on the total number of dimensions D and the definition of the fundamental Planck scale. Recall that based on Equation 3.15, $\Gamma\left(\frac{D-1}{2}\right)$ can be related to the area of a n-sphere with unit radius.

We should determine the mass range over which a BH could be considered a quantum BH. Recalling that in natural units, the units of mass becomes equivalent to inverse length,

the minimum mass is taken as the inverse of the gravitational radius while the maximum mass is taken to be the lower limit of the SBHs. A particle with a Planck mass has a Compton wavelength equal to its Schwarzschild radius. The Compton wavelength contains information about the location of a particle which becomes smaller than its Schwarzschild radius when the mass (energy) of the particle increases [49]. The condition translates to $M > \left(\frac{4\pi}{k(D)}\right)^{\frac{D-3}{D-2}} M_D$ which determines the lower mass of SBHs credibility. Setting this lower mass limit as our upper bound for QBH, the mass range of a QBH becomes

$$\left(\frac{1}{k\,(D)}\right)^{\frac{D-3}{D-2}} \lesssim \frac{M}{M_D} \lesssim \left(\frac{4\pi}{k\,(D)}\right)^{\frac{D-3}{D-2}} \tag{3.24}$$

with the corresponding values shown in Table 3.1. The minimum mass is less than the fundamental Planck scale which is just an artificial outcome of the choice of the M_D definition. The mass range is also dependent on the total number of dimensions. In our study, we choose a fixed mass range for all dimensions with $M_{\min} = M_D$ and $M_{\max} = 3M_D$ for $n = \{2, 4, 6\}$. Our choice of maximum mass is less than what is allowed by Equation 3.24 but very few events are removed by this requirement. This choice also prevents the QBH reaching the semiclassical region where thermal decays happens and the two-body decay picture would not be valid. On the other hand, the maximum allowed mass is also limited by the available production energy, hence the maximum mass can be written as $M_{\max} = \min\left(3M_D, \sqrt{s}\right)$, where $\sqrt{s} = 13$ TeV is the accessible centre-of-mass energy at the LHC so far.

D	6	7	8	9	10
$k\,(D)$	0.91	1.34	1.73	2.10	2.44
$\left(\frac{1}{k(D)}\right)^{\frac{D-3}{D-2}}$	1.07	0.79	0.63	0.53	0.46
$\left(\frac{4\pi}{k(D)}\right)^{\frac{D-3}{D-2}}$	7.17	6.00	5.21	4.63	4.19

Table 3.1: Values of $k\,(D)$, $\left(\frac{1}{k(D)}\right)^{\frac{D-3}{D-2}}$, and $\left(\frac{4\pi}{k(D)}\right)^{\frac{D-3}{D-2}}$ for different total number of dimensions from Equation 3.23. The last two rows correspond to the minimum and maximum allowed mass of a QBH relative to M_D, respectively.

In a pp hard scattering with a centre-of-mass energy of $\sqrt{s}$, only a fraction of the energy is available. Defining a and b as two parton types in the colliding protons, and x_a and x_b as

their corresponding fractional momentum, the particle-level cross-section will be [33]

$$\sigma\left(QBH^{q}_{p_1p_2}\right) = \sum_{a,b}\int_{M^2/s}^{1} dx_{\min}\int_{x_{\min}}^{1}\frac{dx}{x}f_a\left(\frac{x_{\min}}{x}\right)f_b\left(x\right)\pi r_g^2, \tag{3.25}$$

where $x_{\min} \equiv x_a x_b$ and $f_{a,b}$ are the PDFs of the partons in the protons. The PDFs fall quickly as the energy of the partons increase and so does σ, although r_g increases with increasing $\sqrt{s}$. The summation is over all parton pairs giving rise to the specific QBH state. Specifying the parton types, p_1 and p_2, would be sufficient for identifying a QBH state.

3.3.2 Top Quark

Makoto Kobayashi and Toshihide Maskawa first proposed a third generation of quarks in 1973 to explain the CP violation observed in kaon decay [50] and Haim Harari used the names top and bottom for them in 1975. The top quark was discovered 22 years later in 1995 by the CDF [51] and DØ [52] collaborations. It is the heaviest elementary particle in the standard model with a mass of 172.5 GeV [53]. Its anti-particle is called the anti-top quark.

The top quark is a fermion with spin $\frac{1}{2}$ and an electric charge of $+\frac{2}{3}$, and feels all the four fundamental forces. It interacts mainly via the strong force. Due to its enormous mass, it has a very short lifetime of about 5×10^{-25} s [47]. Since its lifetime is shorter than the characteristic time scale of the strong force ($< 10^{-22}$ s), the top quark decays before it can hadronize[1], giving the physicists an excellent opportunity to study a bare quark. The top quark can only decay through the weak force by decaying to a W and a down-type quark. Based on the CKM matrix[2], the dominant down-quark is the bottom quark, and strange and down quark come next where the latter is the rarest. Since the branching ratio of $t \to Wb$ is very close to 100%, the other two decays are neglected in most studies, including ours. With this assumption and the fact that the b-quark always forms hadrons, the decay mode of the W determines the decay mode of the top quark.

The W has two decay modes, hadronic and leptonic, with measured branching ratios

$$\begin{aligned} W &\to q\bar{q} \quad 68.32\% \\ W &\to e\bar{\nu}_e \quad 10.46\% \\ W &\to \mu\bar{\nu}_\mu \quad 10.50\% \\ W &\to \tau\bar{\nu}_\tau \quad 10.75\% \end{aligned} \quad \Longrightarrow \quad \begin{aligned} W &\to \text{Hadrons} \quad 68.3\%, \\ W &\to \text{Leptons} \quad 31.7\%. \end{aligned} \tag{3.26}$$

[1] The process of hadron formation from quarks and gluons.

[2] Cabibbo–Kobayashi–Maskawa matrix, is a unitary matrix characterizing the strength of the flavour mixing of the quarks. See Ref. [47] for the latest values and complete explanation of the CKM matrix.

The τ lepton from the W is not directly seen by a detector itself. It can decay either hadronically or leptonically. 64.79% of the time a τ decays hadronically, and the rest of the times (35.21%) decays leptonically. For simplification and later use, we will call the decay of the W leptonically only if it decays directly to e or μ, and hadronically only if it decays directly to hadrons. We also denote the hadronic decay of the τ as τ_q and its leptonic decay as τ_l.

The top quark is the only quark that has a coupling to the Higgs of order one and plays an essential role in the SM. In our study, we consider QBH decays to ditop final states because in most models that naturalness problem is studied, like the hierarchy problem, the new physics is thought to be connected with the top quark. See Ref. [47] under section *Searches for Physics Beyond the Standard Model* for more information on possible new physics associated with the top quark.

3.3.3 Quantum Black Hole Decay Modes

Our study is concentrated on QBHs decaying to ditop quark final states, and it is useful to know the decay modes of such states. The decay mode of the top-quark and the anti-top-quark are the same and only the electric charge of the decay products change. Below we only show decays of $QBH \to tt$.

Figure 3.1 shows the production and decay chain of the QBH. As mentioned, we have assumed that the top quark always decays to a W and a b quark. So, up until the decay of the Ws, the decay products are the same for all the events. Following the discussion

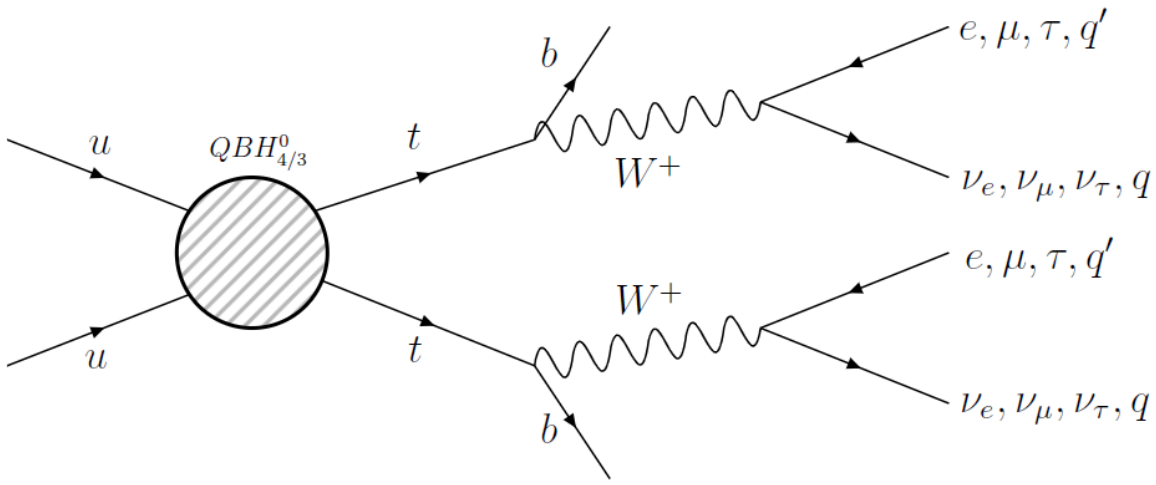

Figure 3.1: Production and decay chain of the $QBH \to tt$ decay. u stands for up-type quark, q also stands for an up-type quark but excluding the top quark due to the mass restriction ($M_{\text{top}} > M_W$) and q' is an anti-down-type quark. The reason for the two different notations is that u sets the state of the QBH while q is restricted by the W.

of the W decay modes in the previous section, the contribution of each decay mode of the QBH in fully-hadronic (or simply hadronic), semi-hadronic (or mixed), and fully-leptonic (or leptonic) topologies can be characterized as follows:

- Hadronic[1]:
  - Both Ws decay hadronically (81.4%, 45.9%) (also called type 1 hadronic)
  - Both Ws decay to τ_q (1.0%, 0.6%) (type 2 hadronic)
  - One W decays hadronically and the other to τ_q (17.6%, 9.9%) (type 2 hadronic)
- Mixed:
  - One W decays hadronically and the other decays leptonically (77.2%, 28.8%)
  - One W decays hadronically and the other decays to τ_l (14.1%, 5.2%)
  - One W decays to τ_q and the other decays leptonically (7.0%, 2.6%)
  - One W decays to τ_q and the other decays to τ_l (1.7%, 0.6%)
- Leptonic:
  - Both Ws decay leptonically (75.2%, 4.8%)
  - Both Ws decay to τ_l (2.6%, 0.2%)
  - One W decays leptonically and the other decays to τ_l (22.2%, 1.4%).

So the branching ratios of the $\text{QBH}_{4/3}$ state is

$$\begin{aligned} \text{QBH} \to \text{Hadronic} &= 56.4\% \\ \text{QBH} \to \text{Mixed} &= 37.2\% \\ \text{QBH} \to \text{Leptonic} &= 6.4\%. \end{aligned} \tag{3.27}$$

In this study, we consider these decays as categories. We study the hadronic and mixed decays separately and also the combination of the two. For reasons to be discussed later, the leptonic decays are not considered in our study. Also, in the mixed decays, we only consider decays where the lepton from the W or τ is a muon.

[1]The first number in the parenthesis represents the percentage within the category and the second is the percentage with respect to the whole sample.

Chapter 4

Large Hadron Collider and the ATLAS Detector

The large hadron collider (LHC) located at the CERN laboratory in Geneva, Switzerland is the largest accelerator and the state of art of particle physics colliders capable of colliding pp, p-Pb (proton-lead), and Pb-Pb beams. It has six different detectors [54] for different purposes. The ATLAS [55] and CMS [56] detectors are large general-purpose detectors. The LHCb (LHC beauty) [57] detector studies CP violation and also the rare decays of B hadrons. The LHCf (LHC forward) [58] detector is designed for understanding very high energy cosmic rays by measuring neutral particles with high energy in the very forward region. The purpose of the TOTEM (total elastic and diffractive cross section measurement) [59] detector is to measure the total, elastic, and inelastic cross-section of pp collisions and central diffraction analysis. The ALICE (a large ion collider experiment) [60] detector is devoted to the study of quark-gluon plasma which is formed from Pb-Pb nuclei collisions, and after BHs are the densest material. ALICE and LHCb are smaller detectors compared with ATLAS and CMS, and the rest are even smaller.

In this chapter, we will give a short review of the LHC machine with its injection chain followed by a more detailed description of the ATLAS detector and its constituents.

4.1 The Large Hadron Collider

Between 1984 and 1989, the LEP (large electron-positron) machine was built underground near Geneva in a tunnel with a circumference of 36.7 km. The depth of the underground tunnel varies from 45 to 170 m. LEP stopped its operation in 2000 and was removed in 2001 to be replaced by the LHC [54]. Reaching the energy of 209 GeV, LEP still is the most powerful electron-positron collider ever built.

Figure 4.1 shows the general layout of the LHC ring. It is built from eight arcs each with a length of 2987 m connected by eight straight sections each 528 m long. Out of the eight octants, four contain intersection points where the detectors are placed, and the rest are used by accelerator equipment. ATLAS and LHCf are located at point 1, CMS and TOTEM are placed at point 5 both of which are new sites. Points 2 and 8 originally built for LEP, host

ALICE and LHCb detectors, respectively.

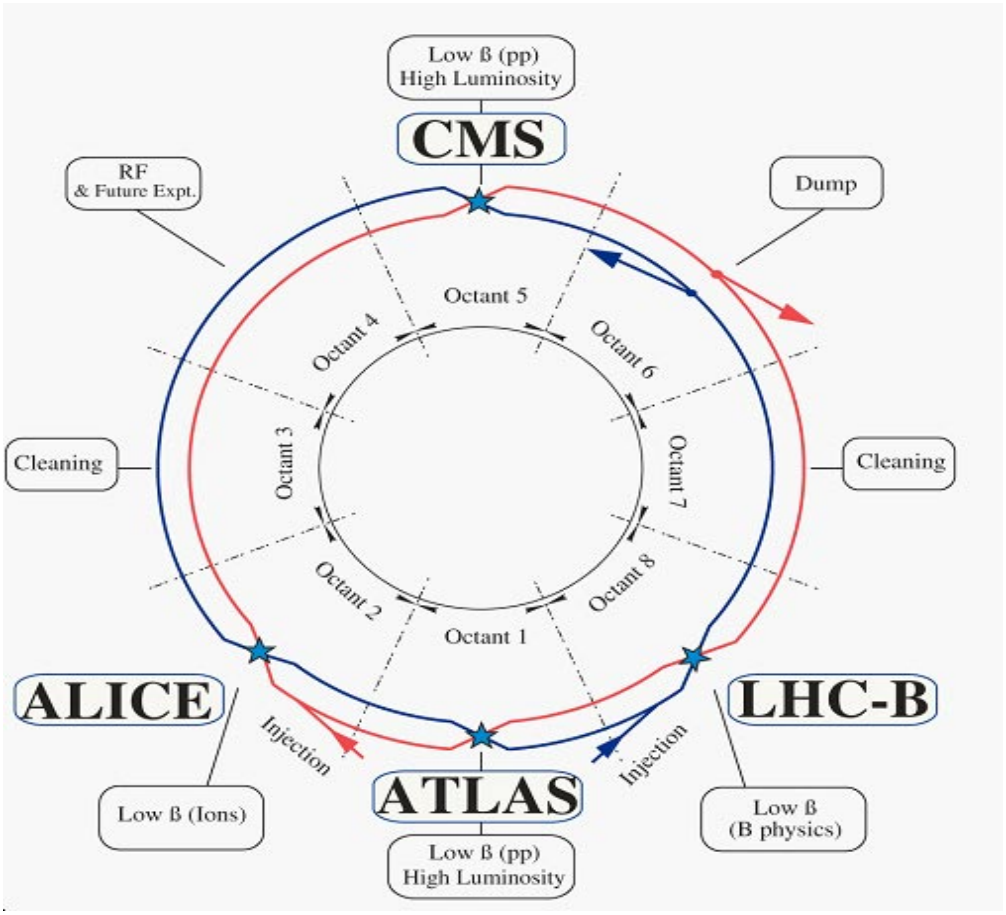

Figure 4.1: The overall layout of the LHC ring and the location of each detector [54].

CERN built the LHC in ten years from 1998-2008. The first period of data taking (Run1) was from 2009 to 2013 reaching total energies of 7 and 8 TeV, and an integrated luminosity of approximately 50 fb^{-1} and 23 fb^{-1}, respectively. The first long shutdown (LS1) was during 2013-2015 preparing the LHC to reach its designed centre-of-mass energy of 14 TeV and higher luminosity. After LS1, Run2 began from 2015 till the end of 2018 collecting an integrated luminosity of 150 fb^{-1} of which 94% is considered good for physics analysis[1] with the centre-of-mass energy of 13 TeV. LS2 is taking place in 2019 and 2020, and Run3 begins in 2021. The plan is to reach a 300 fb^{-1} luminosity at $\sqrt{s} = 14$ TeV by the end of 2022 [61]. At this point, most of the equipment reaches the end of its lifetime, due to radiation damage for example, and needs to be replaced. The LS3 is scheduled to happen during 2023-2025. The High-Luminosity LHC (HL-LHC) is planned to achieve a luminosity of 3000 fb^{-1} by 2035 and possibly 4000 fb^{-1} by 2037 [62].

[1] https://atlas.cern/updates/atlas-news/atlas-completes-data-taking-run-2

4.1.1 Injection Chain

The protons reach the desired value of the centre-of-mass energy by going through different sections of a complex. Figure 4.2 shows the LHC injector complex. The first part of the injector complex is LINAC2 (linear accelerator 2). At one end, there is a bottle of hydrogen gas. The electron of the hydrogen atom is removed using an electric field. The protons leave LINAC2 with an energy of 50 MeV and are injected into the second phase[1]. In the proton synchrotron booster (PSB), protons are accelerated to an energy of 1.4 GeV and later reach an energy of 25 GeV in the third stage at the proton synchrotron (PS) where the 25 ns bunch spacing is also achieved. Before being injected to the main ring, the protons are further accelerated to an energy of 450 GeV in the super proton synchrotron (SPS) where they are split into two beams travelling in the opposite direction in the main ring reaching the final energy of 6.5 TeV for each beam [54].

LINAC2 stopped its operation at the end of Run2 and will be replaced by LINAC4 for Run3. LINAC4 will accelerate protons to 160 MeV and is an essential part for the HL-LHC [63].

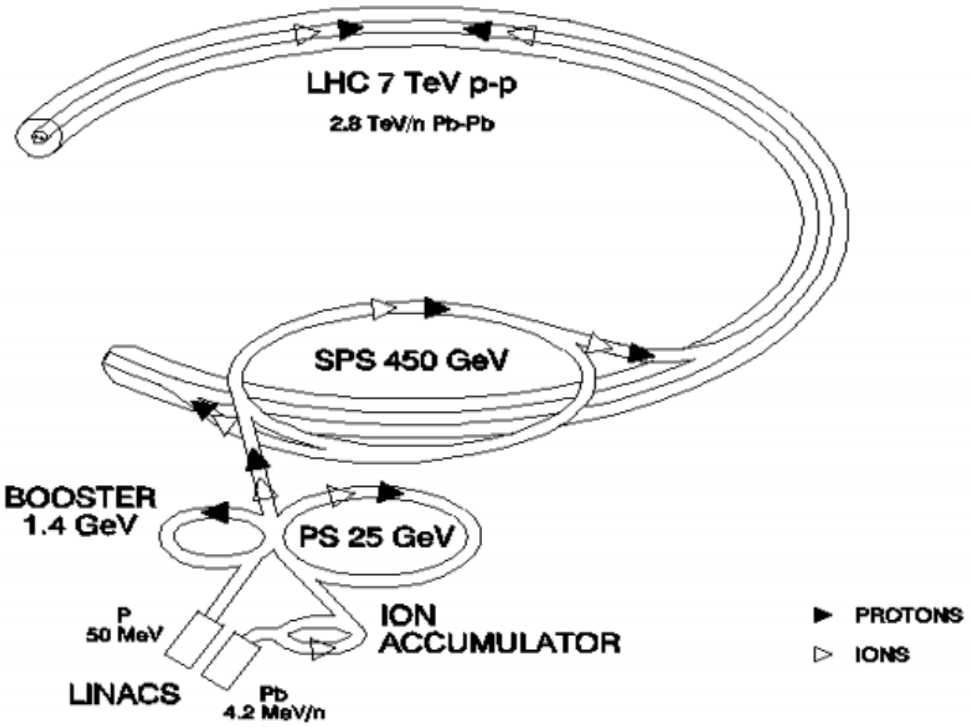

Figure 4.2: The LHC injector complex [54].

[1] https://home.cern/science/accelerators/linear-accelerator-2

4.2 The ATLAS Detector

A full detailed description of the ATLAS detector in the LHC can be found in Ref. [55] from which we will point out the most important aspects which are relevant to our study.

A right-handed coordinate system is used by the ATLAS detector where the nominal interaction point (IP) is the origin of the coordinate system with the z-direction set on the beam direction. The direction from the IP to the centre of the LHC ring defines the positive x-direction and the positive y-direction is then upward. In the transverse plane, x-y, cylindrical coordinates (r,ϕ) are used where the azimuthal angle ϕ is the angle around the z-axis measured from the x-axis and the polar angle θ is measured from the z-axis. The most important parameters in most of studies are the transverse momentum $p_T = \sqrt{p_x^2 + p_y^2}$ of an object (muons, electrons, jets), transverse energy $E_T = E \cdot \sin\theta$ of an object, pseudorapidity $\eta = -\ln(\tan\theta/2)$ and rapidity $y = \frac{1}{2}\ln\left(\frac{E+p_z}{E-p_z}\right)$ of an object, and missing transverse energy $\vec{E}_T^{\text{miss}} = \vec{E}_x^{\text{miss}} + \vec{E}_y^{\text{miss}}$ in an event,. Another important variable is the distance $\Delta R = \sqrt{\Delta\eta^2 + \Delta\phi^2}$ between two objects defined in the $\eta - \phi$ space. ΔR is a measure of how much two objects are separated. Note that except for $\vec{E}_T^{\text{miss}}$ which is an event variable, all others are object variables.

Figure 4.3 shows the overall view of the ATLAS detector. The detector has a dimension of 44 m in length by 25 m in diameter, weighing approximately 7000 tonnes. The most inner part, closest to the interaction point, is the inner detector (ID), followed by the calorimeters, the magnet system, and the muon spectrometer[1].

4.2.1 Inner Detector

The main purpose of the ID is to achieve a high track momentum resolution and vertex resolution which is very important since every 25 ns there are about 1000 particles produced from the collision within $|\eta| < 2.5$. Three independent subsystems achieve this. The pixel tracker has three barrel layers and three disks on each end. The silicon strip tracker or semi-conductor tracker (SCT) has eight layers of silicon microstrip detectors. The transition radiation tracker (TRT) covers $|\eta| < 2.0$ and uses many layers of gaseous straw tubes. Figure 4.4 shows the ID and its constituents. A cylindrical envelope contains the ID within a 2 T solenoidal magnetic field. The field bends the tracks of the charged particles to allow measuring their momentum by the ID.

[1] See also http://atlasexperiment.org/detector.html for a better view of the components of the detector.

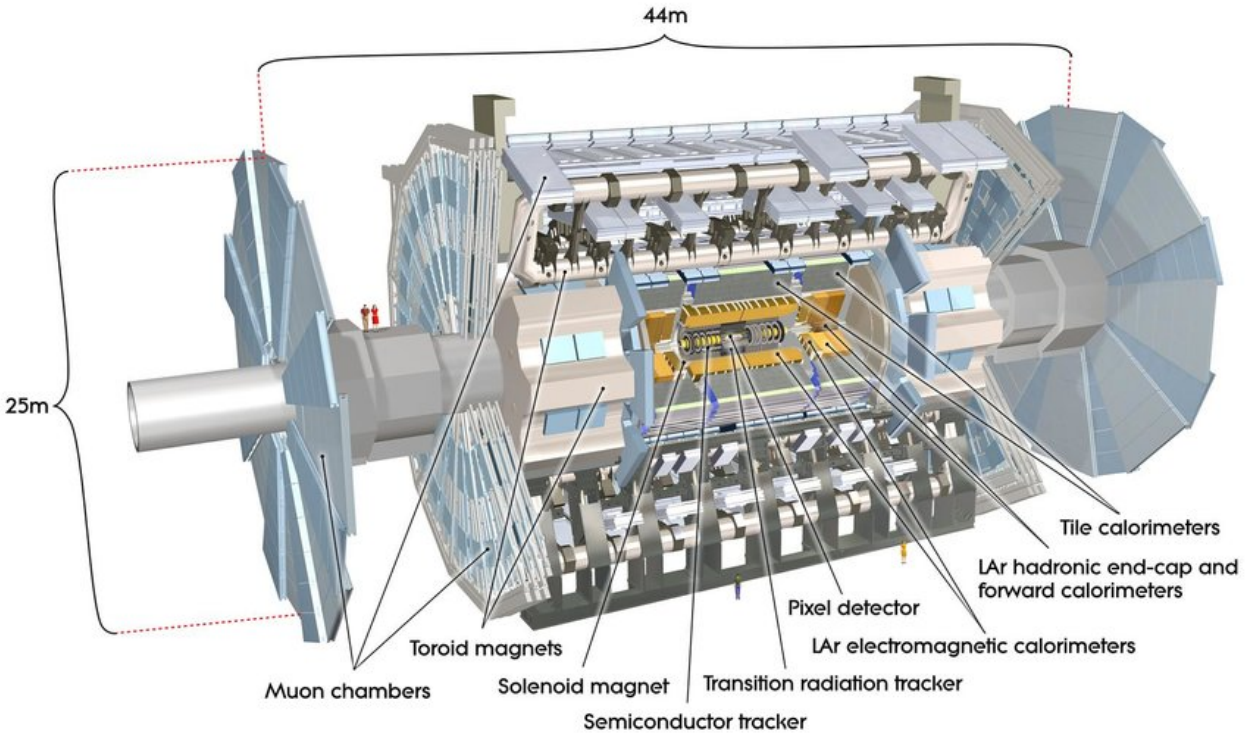

Figure 4.3: Cutaway diagram of the ATLAS detector [55].

4.2.2 Calorimetry

The next detector part on the outside of the ID is the calorimeter, shown in Figure 4.5. The calorimetry consists of two main parts that are the electromagnetic (EM) and the hadronic calorimeters which together cover a range of $|\eta| < 4.9$. Their purpose is to measure the energy of both the hadronic and EM showers, and also contain them as much as possible to reduce their punch-through to the muon system. The part of the EM calorimeter matching that of the ID in η has a fine granularity. This high granularity is necessary for precise measurements of electrons and photons. The remaining calorimeter does not have the same granularity but is sufficient for both the reconstruction of the jets and measurements of the E_T^{miss}. Another way to measure the thickness of the calorimeters is radiation and interaction lengths. High energy electrons and photons mainly loose their energy via Bremsstrahlung and e^+e^- pair production, respectively. The radiation length (X_0) is a property of a material which is related to both (a) the mean distance that the energy of an electron reduces to $1/e$ and (b) $\frac{7}{9}$ of the mean free path of the produced pair from photon [47]. The interaction length (λ) is the mean path of a shower of particles in a material that reduces the number of relativistic charged particles to $1/e$.

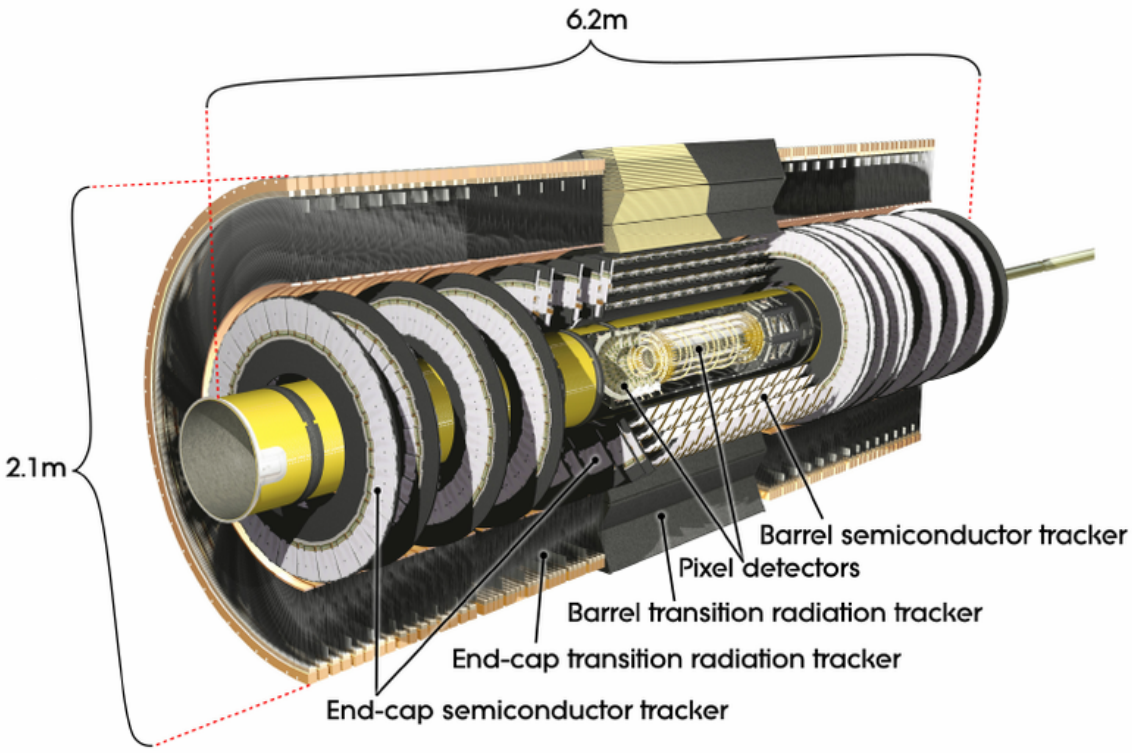

Figure 4.4: Cutaway diagram of the ATLAS inner detector [55].

Liquid Argon Electromagnetic Calorimeter

The EM calorimeter is a lead-LAr (liquid argon) detector. The LAr is used as the scintillating material and the lead as the absorber. It has a barrel part with a total thickness of greater than $22X_0$ which at $z = 0$ is halved into two identical half-barrels with a small gap of 4 mm and covers the region of $|\eta| < 1.475$. Using the same vacuum vessel as the central solenoid (from the magnet system) reduces the material in front of the calorimeter. Each of the two end-cap parts has a thickness of greater than $24X_0$ and are made into two coaxial wheels. The outer wheel covers $1.375 < |\eta| < 2.5$ and the inner wheel covers $2.5 < |\eta| < 3.2$. Each wheel has a separate cryostat for itself. The EM calorimeter was built with an accordion shape to achieve the full azimuthal symmetry and have no cracks in the ϕ direction.

Hadronic Calorimeter

The hadronic calorimeter consists of three different parts. The first part is the tile calorimeter which is right outside the LAr EM barrel and covers $|\eta| < 1.0$. It uses steel as the absorber and scintillating tiles as the active material. The tile calorimeter also has two extended barrels which cover $0.8 < |\eta| < 1.7$. The calorimeter has a diameter of about 2 m which extends from 2.28 m to 4.25 m from the centre. The barrel and extended calorimeter have

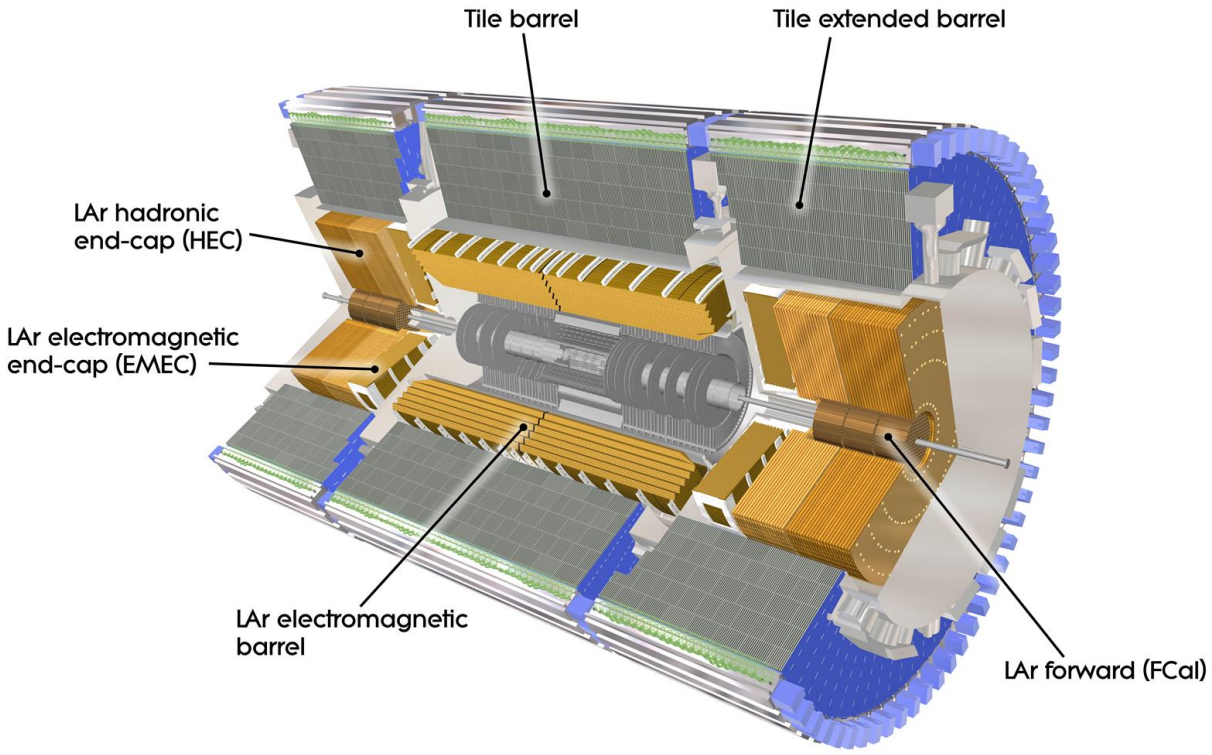

Figure 4.5: Cutaway diagram of the ATLAS calorimeter system [55].

three layers. The three layers in the barrel have thicknesses of about 1.5, 4.1, and 1.8 λ and those in the extended barrels have thicknesses of about 1.5, 2.6, and 3.3 λ.

The other two parts are the hadronic end-cap calorimeter (HEC) and the forward calorimeter (FCal). The HEC is placed right behind the EM end-cap and shares the same cryostats as the LAr EM calorimeter. Each end-cap has two independent wheels where each wheel is also divided into two parts (in depth) that makes four layers overall in each of the end-caps. The pseudorapidity coverage of the HEC is $1.5 < |\eta| < 3.2$. It overlaps with FCal near $|\eta| = 3.1$ and with the tile at around $|\eta| = 1.7$. The reason for the overlap is to reduce the decrease in the density of the material when transitioning from tile or the end-cap to the FCal. The FCal covers the region $3.1 < |\eta| < 4.9$ and uses the same cryostats as the end-cap. With a depth of about 10 λ, the FCal has three layers per end-cap. The first module is made of copper, and its job is electromagnetic measurements. The energy measurements of the hadronic interactions are obtained by the next two layers that are made of tungsten absorber. The FCal uses LAr as the active material [55].

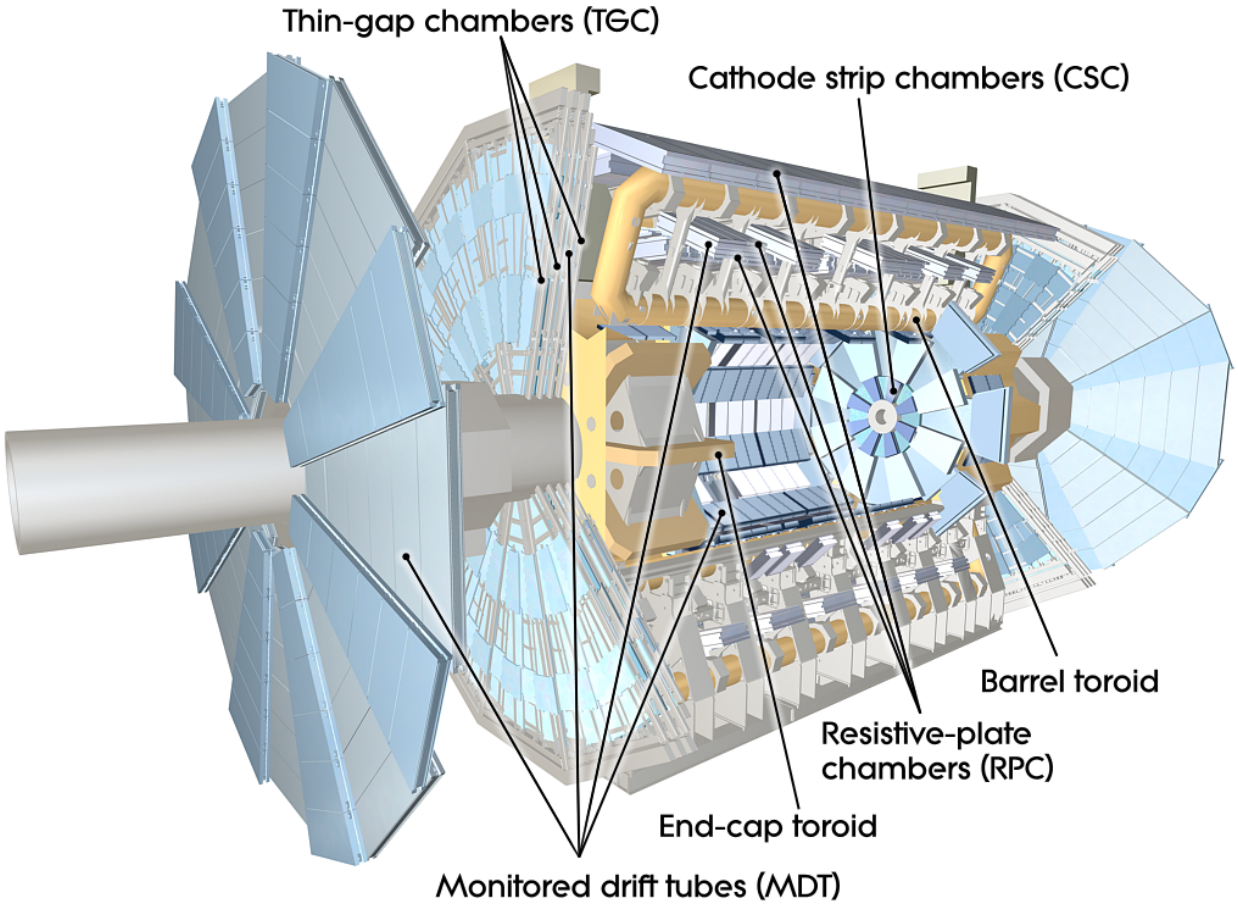

Figure 4.6: Cutaway diagram of the ATLAS muon system [55].

4.2.3 Muon System

The muon system, shown in Figure 4.6, is the largest subpart of the ATLAS detector placed at the outer part of the ATLAS detector. The muon system will detect the charged particles that were not absorbed in the calorimeter system. Their momentum will be measured in a range of $|\eta| < 2.7$ with a resolution of about 10% for a 1 TeV track. Its operation is built on the deflection of the muon tracks caused by the magnet system. This magnetic deflection is provided in different ways in different η regions. In the range $|\eta| < 1.4$ the large toroid does the bending with a power of 1.5 to 5.5 Tm. The two smaller end-cap magnets placed at both sides of the barrel, with a power of 1 to 7.5 Tm, do the deflection over $1.6 < |\eta| < 2.7$. For $1.4 < |\eta| < 1.6$ (transition region) both the barrel and end-caps are used to provide the bending of the tracks where the bending power is the lowest. Other than the toroids, the muon system has four other important components. The monitored drift tubes (MDTs) are used to measure the momentum of the charged tracks in the range $|\eta| < 2.7$ (only the

innermost layers for $|\eta| < 2.0$). For $2.0 < |\eta| < 2.7$, the cathode strip chambers (CSCs) are utilized. The identification of the muon tracks (or the trigger system) is done by the other two components, resistive plate chambers (RPC) in the range $|\eta| < 1.05$ and thin gap chambers (TGCs) over $1.05 < |\eta| < 2.4$ (TGC covers up to $|\eta| = 2.7$ but triggering is only covered up to $\eta = 2.4$) [55].

4.2.4 Luminosity Detectors

There are two small detector systems in the forward region of the ATLAS detector to measure the luminosity. LUCID (luminosity measurement using cerenkov integrating detector) is a relative luminosity detector, and its main goal is to monitor the luminosity online. It is located at a distance of ± 17 m from the IP and detects the inelastic scattering of pp collisions. Placed at ± 240 m is the ALFA (absolute luminosity for ATLAS) detector. Using the optical theorem, in the forward region, the elastic-scattering amplitudes can be related to the total cross-section which further can be used to measure luminosity. Using these scatterings is a well-known method for measuring the absolute luminosity at a hadron collider [64].

4.2.5 Trigger System

When the LHC is operating, there is a proton bunch pair collision every 25 ns in ATLAS and CMS; a rate of 40 MHz. It is impossible to store data at such a frequency, due to limitation of storage space. On top of that, most collisions are low energy scatterings and thus not of interest. For this reason, there is an event selection procedure to reduce the amount of stored data and also choose the collisions that could be most interesting. This trigger system consists of three levels which are Level-1 (L1), Level-2 (L2), and the event filter. The last two triggers combined comprise the high-level trigger (HLT). The most important difference between these two triggers is that L1 uses custom-made electronics, while the HLT is mostly based on computers and network hardware.

In the first trigger step, the L1 looks for signatures of objects with high transverse momentum, events with large E_T^{miss}, or events with large total E_T. For high-p_T muons, the L1 trigger uses the information from the RPC and TGC while for all the other cases information is obtained from calorimeter subsystems. In both cases, only reduced-granularity information is utilized. At this stage, the trigger acceptance rate cannot exceed 75 kHz. The L1 trigger also defines one or more regions-of-interest (RoI) which is determined in the $\eta - \phi$ coordinates. These are the regions where the L1 has found features of interest. The RoI also contains the information on what this feature is and the criteria (a threshold on quantities like p_T, for example) that was passed. This information is subsequently used in the next level. The processing time of the L1 trigger should be less than 2.5 μs after the corresponding

bunch-crossing.

The L2 trigger uses all the available information of the detectors, this time with full granularity and precision, in the RoI found by the L1 trigger. On average, the processing time at L2 is about 40 ms, and the rate is reduced to less than 3.5 kHz. In the last step, using an offline analysis and a processing time of about 4 s, the event filter reduces the event frequency to about 200 Hz which is manageable by the event data recording. Events passing these three trigger levels are stored in permanent storage with an average size of 1.3 MB per event which accounts for more than 250 MB/s worth of data [55].

Chapter 5

Object Identification and Reconstruction in ATLAS

In each collision, many different particles are produced, and the ATLAS detector is designed to identify object type and reconstruct their kinematics using the information it gathers from its different subsystems. In this section, we will cover the identification and reconstruction of muons, electrons, jets, and missing transverse momentum. In this study, we will not be using any information from photons, τ or b-jets, and will not describe them here (See Ref. [55]).

5.1 Charged Leptons

Charged leptons, e and μ, are very important to most studies and their energy, momentum and charge should be measured by the ATLAS detector. For both leptons, the information from the ID is necessary. For the case of electrons, the ID information is combined with the information of the LAr calorimeter while for muons it is combined with the information gathered from the muon system.

5.1.1 Electron

Reconstruction of electrons and photons, is one of the most challenging tasks at the LHC for two main reasons. Firstly, they can be misidentified easily with a hadronic jet. Secondly, in front of the electromagnetic calorimeters, there is a large amount of material which makes the identification of these objects, and measuring their energy and direction difficult [55].

For reconstructing electrons, first "a seed cluster is taken from the electromagnetic calorimeter"[55], and then if the object matches a reconstructed track in the ID, it will be identified as an electron. However, these electrons could be classified as photons if consistency is found between the matched track to tracks coming from a photon conversion or a conversion vertex [65]. More identification cuts are applied to these objects to reduce fakes which based on their fake rejection ability are called loose, medium, and tight electrons [66].

5.1.2 Muon

The muon system is the outermost part of the ATLAS detector, and since most of the particles that interact hadronically or electromagnetically are absorbed by the calorimetry system, any charged particle that makes it to the muon system are muon candidates. Based on the reconstruction algorithm, there are four types of muons. Stand-alone muons are those that only muon detector information is available for reconstruction, but at least two layers of the muon chambers must be crossed by the candidates. To measure the momentum of the muon at the IP, the momentum measured in the muon system is corrected to take into account the energy loss in the calorimeter system. Combined muons utilize the momentum of the stand-alone muons and combines it with the measurements of the ID. Segment tagged muons are those where a trajectory in the ID is extrapolated to the muon system, and then nearby hits in the muon system are searched for. Calorimeter tagged muons are also defined as a trajectory in the ID but with the condition that a minimum ionization signal is found in the calorimeter system.

Stand-alone muons can be found over the full range of the muon system, $|\eta| < 2.7$ with gaps at $|\eta| \sim 0$ and 1.2 which are covered by the calorimeter tagged muons. Low-p_T muons, $p_T \lesssim 5$ GeV, bend too much to cross at least two layers in the muon spectrometer and must be found by the stand-alone algorithm. The segment tagged algorithm works best for low p_T muons but the coverage is limited by the ID η coverage which only covers $|\eta| < 2.5$. This η coverage is the same as that of the combined muons. See Ref. [67, 68] for more details.

5.2 Jets

Jets are one of the most important objects in any hadron collider and are of crucial importance to many different studies. ATLAS uses the anti-k_t algorithm [69] for jet reconstruction. The inputs to the jet reconstruction are topological clusters [70] which are reconstructed from the energy deposits of hadrons in the calorimeter cells.

One of the most critical points in the jet reconstruction algorithm is infrared and collinear safety. The former means that if a soft particle is added or subtracted from the jet, the number of jets found by the algorithm should not change. In other words, if two particles initially made a jet, the soft particle should not change that and they should still form a jet. Collinear safety means if a specific amount of transverse momentum is given to one particle or that particle decays (splits) into two collinear particles, the p_T of the final jet should not be affected [67].

The two important variables in the jet reconstruction algorithms are

$$d_{ij} = \min\left(p_{Ti}^{2p}, p_{Tj}^{2p}\right) \frac{\Delta y_{ij}^2 + \Delta\phi_{ij}^2}{R^2} = \min\left(p_{Ti}^{2p}, p_{Tj}^{2p}\right) \frac{\Delta_{ij}^2}{R^2}, \qquad d_{iB} = p_{Ti}^{2p}, \tag{5.1}$$

where $\Delta_{ij}^2 = \Delta y_{ij}^2 + \Delta\phi_{ij}^2$, and p_{Ti}, y_i, and ϕ_i are transverse momentum, rapidity, and the azimuthal angle of calorimeter energy cluster i, respectively. R is a free parameter and the values of 0.4 and 1.0 are the most common choices in ATLAS. Three possible choices of p define three different algorithms. For $p = 0$, the Cambridge-Aachen [71] algorithm is recovered, and $p = 1$ corresponds to the k_T algorithm [72] where the distance d_{iB} becomes important. ATLAS uses the anti-k_t algorithm [69] which means a choice of $p = -1$, and has the advantage of being infrared and collinear safe.

This choice of p has interesting features due to the definition of $d_{ij} = \min\left(p_{Ti}^{-2}, p_{Tj}^{-2}\right) \Delta_{ij}^2/R^2$ which now is proportional to the inverse of the transverse momentum. Suppose we have two well-separated high energy calorimeter clusters called 1 and 2, and some low energy calorimeter clusters j. The d_{1j} is mostly dependent on p_T of the high energy calorimeter cluster and the distance Δ_{1j} while the distance between low energy calorimeter cluster, d_{ij}, becomes huge due to low p_T. This way, high energy calorimeter clusters, cluster with low energy calorimeter cluster close to them and low energy calorimeter cluster do not get the chance to cluster with themselves. Moreover, if the distance between two high energy calorimeter cluster is greater than $2R$, then a jet with a conical shape is formed from the high energy calorimeter cluster and all the low energy calorimeter cluster around it within a circle of radius R.

If two high energy calorimeter cluster have a distance $R < \Delta_{12} < 2R$, two jets will still be reconstructed, but since there is an overlap between them, both cannot have a conical shape. There are three possible conditions based on the p_T of the particles. If $p_{T1} \gg p_{T2}$, jet 1 is conical and jet 2 misses the overlap and is just partially conical. If $p_{T1} = p_{T2}$, the overlap is equally divided between them by a straight line and neither are conical. This non-conical shape also happens for $p_{T1} \sim p_{T2}$, but this time the boundary, b, is defines by $\Delta_{1b}/p_{T1} = \Delta_{2b}/p_{T2}$.

The only case where one jet is formed is when $\Delta_{12} < R$. For $p_{T1} \gg p_{T2}$, the jet has a conical shape around p_{T1}. If $p_{T1} \sim p_{T2}$, around each calorimeter cluster there will be a cone of radius less than R and the overall shape is a cone with radius R around the final jet.

5.3 Missing Transverse Energy

Neutrinos are the only SM stable particles that do not interact with any parts of the detector and therefore cannot be detected directly. Since the incoming protons have no transverse momentum before the collision and energy-momentum conservation should be obeyed, the vector sum of the transverse momentum of the produced particles should add up to zero. The fact that the vector sum of the transverse momentum of the reconstructed particles is not zero can be associated with the production of neutrinos[1], and the negative of this value is assigned as the $\vec{p}_T$ of the neutrino. Like all the other objects, the missing transverse energy variable (missing E_T or MET) plays a vital role in many different studies like searches for new physics, such as supersymmetry and extra dimensions, or measuring the mass of the top quark from $t\bar{t}$ production [67]. In this section, we follow the description of the reconstruction algorithm of MET given in Ref. [73].

The missing transverse momentum vector is defined as

$$\vec{E}_T^{\text{miss}} = \vec{E}_x^{\text{miss}} + \vec{E}_y^{\text{miss}}, \tag{5.2}$$

with a magnitude and azimuthal angle defined as

$$E_T^{\text{miss}} = \sqrt{\left(E_x^{\text{miss}}\right)^2 + \left(E_y^{\text{miss}}\right)^2} \quad \text{and} \quad \phi^{\text{miss}} = \arctan\left(E_y^{\text{miss}}/E_x^{\text{miss}}\right). \tag{5.3}$$

The missing transverse momentum has two main terms: calorimeter and muon terms

$$E_{x(y)}^{\text{miss}} = E_{x(y)}^{\text{miss,calo}} + E_{x(y)}^{\text{miss},\mu}. \tag{5.4}$$

Calorimeter Term

The calorimeter term in MET is defined as

$$E_x^{\text{miss,calo}} = -\sum_{i=1}^{N_{\text{cell}}} E_i \sin\theta_i \cos\phi_i \quad \textit{and} \quad E_y^{\text{miss,calo}} = -\sum_{i=1}^{N_{\text{cell}}} E_i \sin\theta_i \sin\phi_i, \tag{5.5}$$

where N_{cell} is the number of all the cells of the calorimeter in the range $|\eta| < 4.5$, E_i is the energy, and the polar and azimuthal angles are θ_i and ϕ_i, respectively. For a better calibration, this term is decomposed to different terms based on the association of each energy cluster to a well reconstructed high p_T parent object in order of: electrons, photons, τ-leptons

[1] This is the case if we only consider SM particles. This missing energy can also be associated with BSM particles that do not interact with the detector, such as gravitons.

decaying hadronically, hadronic jets, and muons. In this way, each term is calibrated based on the identified object. So

$$E_{x(y)}^{\text{miss,calo}} = E_{x(y)}^{\text{miss},e} + E_{x(y)}^{\text{miss},\gamma} + E_{x(y)}^{\text{miss},\tau} + E_{x(y)}^{\text{miss,jets}} + E_{x(y)}^{\text{miss,softjets}} + E_{x(y)}^{\text{miss,calo},\mu} + E_{x(y)}^{\text{miss,CellOut}}, \quad (5.6)$$

where the following conditions have been used for reconstruction of each term:

- $E_T^{\text{miss},e}$: from *medium* electrons with $p_T > 10$ GeV using the electron calibration [65].
- $E_T^{\text{miss},\gamma}$: from *tight* photons with $p_T > 10$ GeV using EM scale [65].
- $E_T^{\text{miss},\tau}$: from *tight* taus with $p_T > 10$ GeV [74] calibrated with local cluster weighting (local hadronic calibration or LCW) scheme.
- $E_T^{\text{miss,jets}}$: high p_T jets ($p_T > 20$ GeV) using LCW calibration with applied jet energy scale (JES) factor.
- $E_T^{\text{miss,sofjets}}$: low p_T jets ($7 < p_T < 20$ GeV) using LCW calibration scheme.
- $E_T^{\text{miss,calo},\mu}$: the energy loss of muons passing through the calorimeter system.
- $E_T^{\text{miss, CellOut}}$: the energy cluster of cells not associated with any of the above objects and uses the LCW calibration scheme.

Note that each term is the sum of all the objects falling into a specific category. Also, each term is the negative of the cell energies which is the reason for plus signs in Equation 5.6 rather than a minus.

Muon Term

The muon term is defined as

$$E_{x(y)}^{\text{miss},\mu} = -\sum_{\text{selected muons}} p_{x(y)}^{\mu}, \quad (5.7)$$

which includes all the muons in the fully covered region ($|\eta| < 2.7$) of the muon system. In the range of $|\eta| < 2.5$ these muons are matched with a track in the ID which reduces the contribution from fake muons significantly. If the muon is isolated[1] with $|\eta| < 2.5$, its momentum is reconstructed using the muon spectrometer and ID measurements, and its energy loss will not be included in the $E_T^{\text{miss,calo},\mu}$ term to prevent double counting. For the

[1] An isolated muon is defined as a muon with $\Delta R_{\mu,jet} > 0.3$ from its closest jet.

non-isolated muons, the energy loss is not separable from that of the jet and the cluster energies are already included in a jet term.

Chapter 6

Analysis

This chapter is dedicated to describing the analysis used in our study for searching for QBHs. Our study is based on Monte Carlo (MC) simulated kinematics of particle four-vectors with no detector simulation. Some of the information available in this simulation may not be available in the data or full detector simulation. Only information that would be available in the ATLAS reconstructed data is used. We determine the discovery potential of the QBHs threshold mass assuming an integrated luminosity of 150 fb^{-1} and 3000 fb^{-1}. Possible sources of background include QCD multijet process, $t\bar{t}$ production, and W/Z plus jets processes. Using the results of ATLAS dijet analysis corresponding to 37.4 fb^{-1} of data, we set a 95% CL upper limit on the production cross-section times branching ratio (BR) times acceptance (A) times efficiency (ϵ), and production cross-section.

6.1 MC Simulated and Data Samples

As mentioned previously, in our study we are pursuing two goals. Firstly, we determine the discovery potential on the QBH threshold mass. We also set an upper limit at 95% CL on the QBH production cross-section times BR times A times ϵ, production cross-section, and set a lower limit on the production mass threshold using the results of ATLAS dijet analysis [4]. The type of analysis used for the discovery potential and limit setting is completely different. The discovery potential uses MC samples of simulated QBH signals and MC samples of different possible contributing backgrounds without detector simulation or reconstruction.

The QBH signal is simulated using the QBH generator[1] [75]. QCD multijet background is simulated using PYTHIA8 [76] and HERWIG [77]. Additional potential backgrounds like $t\bar{t}$ production and W/Z + jets are simulated using the POWHEG [78] generator. Appendix A lists the set of ATLAS official MC simulated samples that are used in our study. Each will be discussed in the subsequent sections.

[1]The name of the generator, QBH, should not be mistaken with the acronym QBH for quantum black holes.

6.2 QBH Signal Samples

For the QBH signal, both the ADD model assuming $n = \{2, 4, 6\}$ extra dimensions and the RS1 model will be considered. Note that in the RS1 model $n = 1$. Recall that in the ADD model, the case of $n = 1$ is excluded. Also, ATLAS usually considers up to six extra dimensions. So, choosing $n = \{2, 4, 6\}$ allows the interpolation for odd number of extra dimension. In other words, there is nothing special about even number of extra dimensions.

To avoid repetition, we will represent the different ADD models as ADDn2, ADDn4, and ADDn6, respectively. For the Planck scale, we use eight values ranging from 4-10 TeV in 1 TeV steps, and 9.5 TeV. As discussed earlier, the minimum or threshold mass of the QBH is set to be the same as the Planck scale. The maximum QBH mass is 13 TeV, except for the $M_D = 4$ TeV sample in which the maximum QBH mass is 12 TeV, i.e only one sample is different. In the QBH generator, we use CTEQ6L1 [79] as our PDF set. Appendix B shows the set of parameters we have used in the QBH generator for our study.

Note that model refers to the ADD model with the different choices of n and the RS1 model. The choice of different QBH parameters is referred to as samples.

6.2.1 QBH States and Signal Validation

We are interested in QBH states decaying to ditop quark pairs. There are four different states shown in Table 6.1. Each state is distinguished by two codes, Q-state and I-state, $\mathrm{QBH}^{\mathrm{Istate}}_{\mathrm{Qstate}}$. Q-state is the electric charge, and I-state is the initial state with three possible choices, 0 for q-q (quark-quark), 1 for q-g (quark-gluon), and 2 for g-g (gluon-gluon) production [75]. The branching ratio of a given state depends on particle degrees of freedom that conserve quantum numbers and symmetries. Table 6.1 shows the different ditop BRs.

QBH Production	QBH Decay	Branching Ratio to Ditop
$uu \to QBH^0_{4/3}$	$QBH^0_{4/3} \to tt$	0.074
$\bar{u}\bar{u} \to QBH^0_{-4/3}$	$QBH^0_{-4/3} \to \bar{t}\bar{t}$	0.074
$q\bar{q} \to QBH^0_0$	$QBH^0_0 \to t\bar{t}$	0.039
$gg \to QBH^2_0$	$QBH^2_0 \to t\bar{t}$	0.030

Table 6.1: Possible QBH production states decaying to ditop quark pairs and their branching ratio. u stands for up-type quark, q for up- or down-type quark and g for gluon.

Figure 6.1 shows the pp cross-section times branching ratio of the different QBH states

decaying to ditop final states for RS1 QBH and ADD QBH with $n = \{2, 4, 6\}$ as a function of threshold mass (M_{th}). The uncertainty of the cross-section comes from the QBH generator which is a statistical uncertainty based on the number of events used to integrate the cross-section. As can be seen from these two plots, the only significant QBH state giving ditop final states is the $\text{QBH}^0_{4/3}$. From now on, our study only includes the $\text{QBH}^0_{4/3}$ state that decays to tt and that is what we shall mean by ditop hereafter. This choice underestimates the cross-section by about 7% for the 4 TeV samples and less than 1% for samples with with M_{th} greater than 7 TeV.

Figure 6.2 shows the pp cross-section of the $\text{QBH}^0_{4/3}$ state for different models as a function of M_{th}. In the ADD model, this cross-section increase with increasing number of extra dimensions. Although the RS1 model corresponds to the choice of $D = 5$, the definition of the fundamental Planck scale is different. In the RS1 model, the fundamental Planck scale is defined as

$$M_D^{D-2} = \frac{1}{4\,(2\pi)^{1/3}\,G_D}, \tag{6.1}$$

where $D = 5$. The signal shape of the QBH can differ between the models because both the partonic-level cross-section, Equation 3.25, and the resolution scale of the PDF $Q = 1/r_g$ depends on r_g. The dependence of the gravitational radius on the number of extra dimensions and the Planck scale definition affects both.

For the bulk of our study we use the ADDn6 model and only represent the final and important intermediate results for all four models. Hereafter, all the results are for the ADDn6 model unless stated otherwise. For each mass threshold sample in each model, we have simulated 1 million $\text{QBH}_{4/3}$ events decaying to tt final state.

Figure 6.3 shows the simulated mass distributions of the events for the eight different M_{th} samples. In Appendix C we show the kinematics of the QBH and each of the top quarks of the QBH decay for the 4 TeV and 9 TeV M_{th} samples for the ADDn6 model to validate the simulated events.

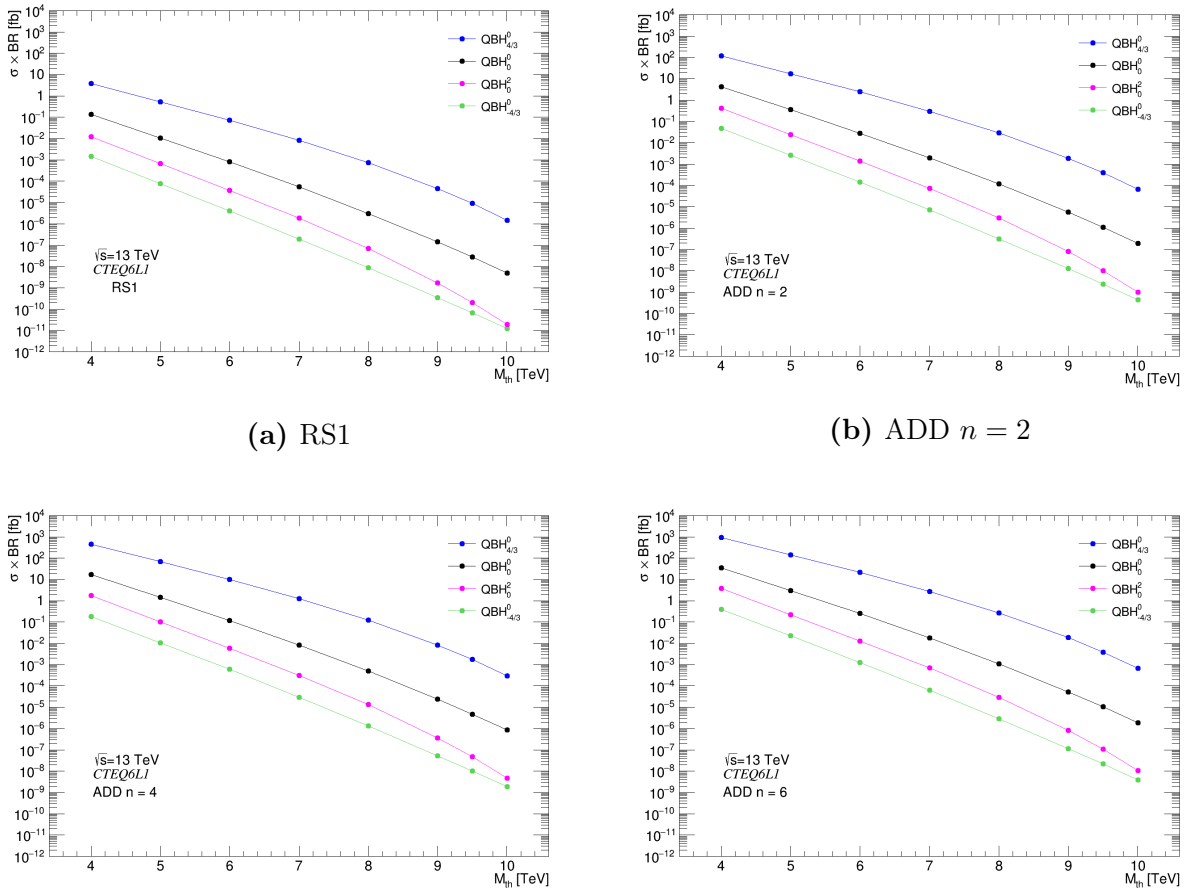

(a) RS1

(b) ADD $n = 2$

(c) ADD $n = 4$

(d) ADD $n = 6$

Figure 6.1: Proton-proton cross-section times the branching ratio of different QBH states decaying to tt, $\bar{t}\bar{t}$ and $t\bar{t}$ for **(a)** RS1 QBH and ADD QBH with **(b)** $n = 2$, **(c)** $n = 4$, and **(d)** $n = 6$ as a function of threshold mass M_{th}.

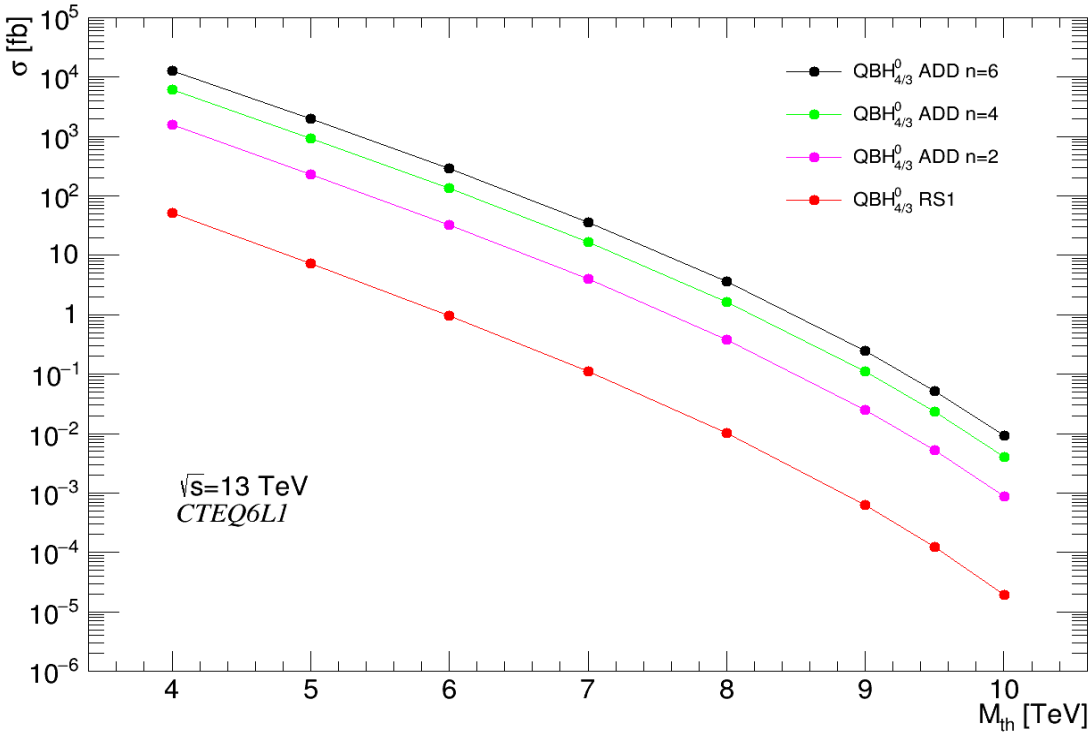

Figure 6.2: Proton-proton cross-section of the $\mathrm{QBH}^0_{4/3}$ state for the RS1 QBH and the ADD QBHs with $n = \{2, 4, 6\}$.

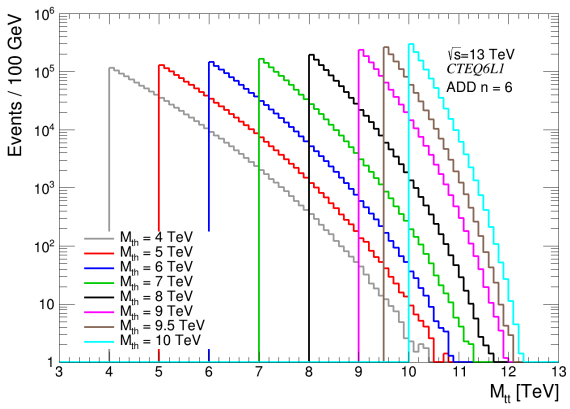

(a) Log scale

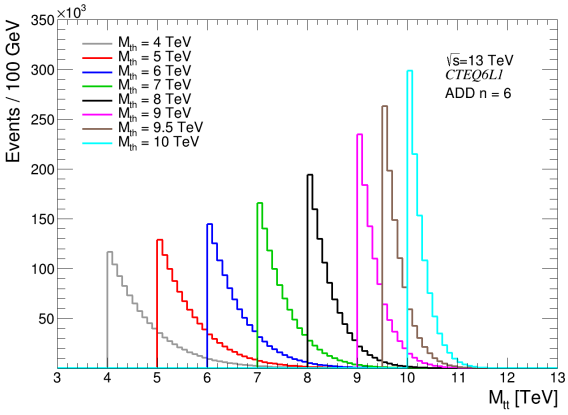

(b) Linear scale

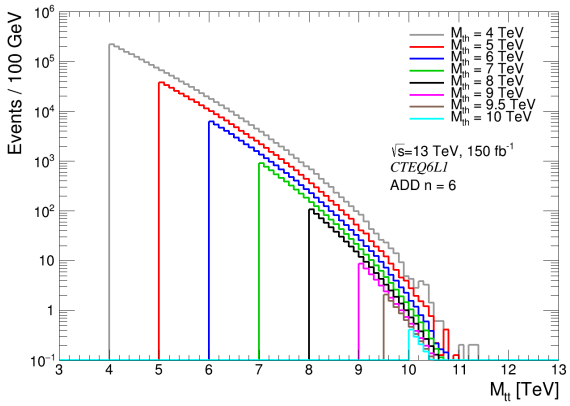

(c) Normalized log scale

Figure 6.3: Ditop mass distribution for ADDn6 QBH samples with **(a)** log scale and **(b)** linear scale normalized to 1 million events in each sample, and **(c)** log scale normalized to 150 fb^{-1}.

6.3 Object Definition and Algorithm

Both QBH simulated signal events and simulated background events, discussed in section 6.8, are produced using MC event generators. Pythia [76] simulates the final states of high-energy collisions down to stable particles by showering, fragmentation, hadronizing, and decaying [80]. After these processes, we run a jet reconstruction algorithm using the particle four-momentum as inputs. After this stage we have four main truth containers:

- TruthParticles: Using the PDG IDs [47], one can find the particles involved in an event and its four-momentum. The decay chain can be followed using *Parent* and *Child* information which is useful to determine the top decay mode which will be used later in this study. The other important use of this container is for identifying electrons and muons.

- AntiKt4TruthDressedWZJets: A jet container with anti-k_t algorithm jets with a distance parameter of $R = 0.4$ [69]. *DressedWZ* means that electrons and muons produced from $W/Z/\tau$ decays are not included in the jet. We will refer to these jets as small-cone jets. These jets have mass.

- AntiKt10TruthTrimmedPtFrac5SmallR20Jets: Another jet container with anti-k$_t$ jets with distance parameter of $R = 1.0$ and also $p_T > 100$ GeV. TruthTrimmedPtFrac5 means that if $\frac{Pt_{\text{subjet}}}{Pt_{\text{jet}}} < 0.05$, the subjet is removed from the jet. SmallR20Jets means that the subjets use $R = 0.2$. These jets also have mass.

- MET_Truth: This container contains information about the missing transverse momentum in an event.

The reason the containers are called truth is that they are based on MC simulated four-vectors. Unlike what happens in data, the input of the jet reconstruction algorithm are particle four-vectors rather than the energy deposits in the calorimeter. These jets are also often referred to as truth jets. The first three containers have the four-momentum of the objects, and the MET_Truth container has the components p_x and p_y of the missing transverse momentum of an event. The truth algorithms have the ideal information of the objects.

The jets reconstructed with the anti-k$_t$ algorithm with $R = 0.4$ ($R = 1.0$) are often referred to as small-R (large-R) jets. The large-R jets were developed mostly to use the substructure information of jets, for example for b-tagging [81] and t-tagging [82]. These information are mostly used to reject background to make the signal observable. In our case, as we will see, the simulated signals are well above the background and although these tags

could reduce the background, they would also reduce the signal as well. Also, the subjet working points are tuned for jets with p_T less than 2 TeV while our higher QBH threshold mass samples produce jets with p_T greater than 4 TeV that have no counterpart in data. In our study we will only be using the small-R jets and simply refer to them as jets. We also will not use any tagging, or τ reconstruction.

6.4 Detector Effects

All the truth algorithms mentioned above are for the MC event simulations (event generators) which differ from the reconstruction algorithms for data and ATLAS detector simulated events and reconstruction. Although this study is only based on the particle generator level and no detector simulation or object reconstruction is used, we can try to incorporate some of the effects of the ATLAS detector without any simulation. Some of the detector effects include:

- object misidentification
- geometrical (pseudo-rapidity) acceptance
- trigger efficiency
- object efficiency
- muon energy resolution
- jet energy resolution (JER) and its uncertainty
- jet energy scale (JES) and its uncertainty
- pileup effects.

In this section we will discuss these effects and apply some of them to our simulated events.

One of the most important differences between MC simulation and data is the misidentification of objects. The most important one being misidentification of electrons and jets. This misidentification of electrons and jets has two consequences. Firstly, as was mentioned, in our jet container, the electrons and muons that are produced from $W/Z/\tau$ decays are not included in jets. The case of muon is not problematic but if an electron is within the cone size of a jet, the ATLAS detector will not be able to separate the electron and it will be included as a part of the jet. To make our simulation more like data, if the electrons produced from W or τ are within a distance less than the jet cone size, $\Delta R_{ej} < R = 0.4$,

the four-momentum of the electron will be added to the jet. The information of the separated electrons would not be reliable and realistic, and this is the reason it was previously mentioned that we only consider the mixed decays where the lepton is a muon. The other consequence of this misidentification, is the ability of the ATLAS detector to distinguish an electron from a jet since they leave similar traces in the EM calorimeter. So, the same energy deposits in the EM calorimeter can be reconstructed as a jet and also as an electron. In every ATLAS study, we have an overlap removal algorithm to take care of this double counting of objects. Since our study is based on MC simulated events and truth information, there is no double counting, and we do not need this overlap removal. We will assume that in data, the overlap removal will pick the right object with 100% efficiency and neglect this effect. So, the only objects that we use in this study will be muons and jets. If one does not need electrons, all tracks can simply be considered to be jets.

Another effect is the geometrical acceptance of the ATLAS detector for different objects, shown in Table 6.2 [67]. In Appendix D we show the η distribution of the jets and muons.

Object	$\lvert\eta\rvert$
Jet	< 4.9
Muon	< 2.7

Table 6.2: Detector pseudo-rapidity acceptance for jets and muons in the ATLAS detector [67].

Trigger efficiency is an effect of the ATLAS data taking. The trigger system is responsible for deciding whether to keep an event or not. In our study, we used a jet p_T trigger that requires at least one jet with p_T greater than 420 GeV [83]. The efficiency of $M_{\text{th}} = 4$ TeV and $M_{\text{th}} = 9$ TeV QBH samples are 96.9% and 98.8%, respectively. Since these events would have not been recorded by the ATLAS detector, the events that do not pass this trigger threshold are excluded from the study.

Another effect is the object efficiency, which is the probability that an object will be detected. Figure 6.4 shows the efficiency of the muons with $p_T > 10$ GeV as a function η. To include this effect, first we find the η of the muon and generate a linearly distributed random number between zero and one. If the random number is less than the value of the efficiency for the given η, we keep the muon, otherwise it will be discarded. There is no efficiency for jets and missing transverse momentum; in another word, it is always 100%.

Another effect we can include is the p_T resolution of the objects and MET. The p_T resolution is a measure of the ability of the detector to accurately determine the p_T of the objects. Since the angles (the direction that the particle hits the detector) are found with

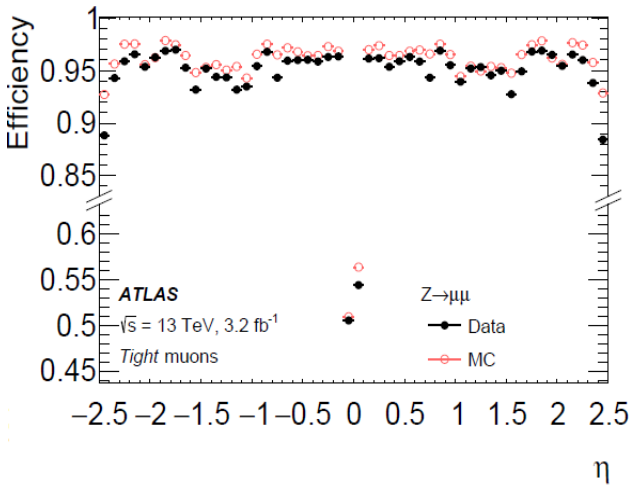

Figure 6.4: The efficiency of muons with $p_T > 10$ GeV as a function of pseudo-rapidity [84].

great accuracy, the p_T resolution will be introduced to p_x and p_y components such that the azimuthal angle doesn't change. Figure 6.5 shows the p_T resolution of muons as a function of η. Similar to the muon efficiency, we first find its η so that we can find the corresponding resolution. We then create a Gaussian distribution with mean of the truth p_T and a standard deviation of $p_T \times \sigma_{p_T}$ where σ_{p_T} is the relative p_T resolution. The p_T of the muon is then picked from this distribution.

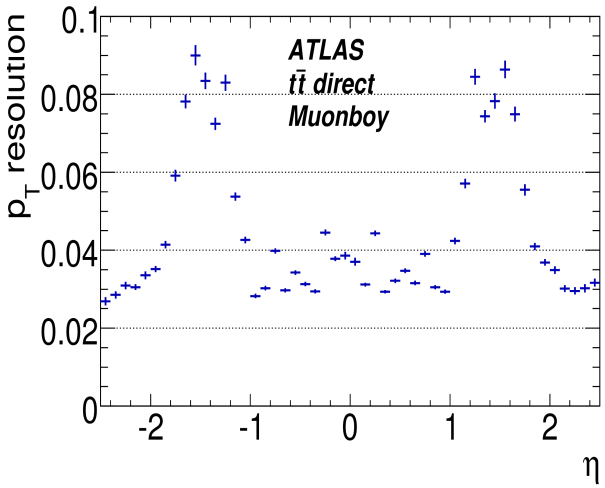

Figure 6.5: p_T resolution of muons as a function of η [85].

For jets, the mass and angular resolutions are often neglected and jet energy resolution

is considered the same as jet p_T resolution

$$\frac{\sigma_E}{E} \approx \frac{\sigma_{p_T}}{p_T}. \tag{6.2}$$

For sampling calorimeters, the JER can be parameterized as [86]:

$$\frac{\sigma_{p_T}}{p_T} = \frac{N}{p_T} \oplus \frac{S}{\sqrt{p_T}} \oplus C, \tag{6.3}$$

where the terms correspond to noise, stochastic, and a constant uncertainty, respectively. N is mostly due to pileup and electric noise which is significant in the low p_T region ($\sim$30 GeV). S comes from the statistical Poisson fluctuations which is the sampling nature of the calorimeter and is the dominant term in the intermediate p_T region ($30 < p_T < 500$ GeV). C is a constant term that can, for example, be due to signal lost in passive materials and is the dominant term for high p_T jets (above 400 GeV). JER is found as a function of p_T for different η regions [87]. The resolution is about 10% for jets with $p_T = 0.1$ TeV and reduces to about 3% for jets with $p_T = 1.0$ TeV. The absolute JER uncertainty is about 3% (0.5%) for jets with $p_T = 20$ GeV ($p_T = 1$ TeV). Figure 6.6 shows the p_T resolution of anti-k$_t$ $R = 0.4$ jets in the region of $0.0 < \eta < 0.2$ [87]. The official ATLAS results are for internal use only and cannot be shown in this study. The five η regions used in this study are: $0.0 < \eta < 0.2$, $0.2 < \eta < 0.7$, $0.7 < \eta < 1.3$, $1.3 < \eta < 1.8$, and $1.8 < \eta < 2.5$. The smearing process is similar to the p_T resolution of μ. First, we find the η of the jet to determine the η region. Using the truth p_T of the jet, we find its resolution. We then create a Gaussian distribution with mean of the truth p_T and a standard deviation of $p_T \times \sigma_{p_T}$ where σ_{p_T} is the p_T resolution. The p_T of the jet is then picked from this distribution. To consider the JER uncertainty, a similar Gaussian distribution is created, this time with a standard deviation of $p_T \times (\sigma_{p_T} \pm$ JER uncertainty) where JER uncertainty is a linearly distributed random number from zero to the difference of the nominal value of JER and its highest (lowest) value.

In the case of jets, in addition to jet energy resolution, we also have jet energy scale (or response). The jet energy response defined as

$$\mathcal{R} = \frac{E^{\text{reco}}}{E^{\text{truth}}} \tag{6.4}$$

corrects the MC simulation of events to the response in data, shown in Figure 6.7 [88]. Since we are using truth level jets, we do not need to apply this factor. But the uncertainty of JES should be and will be considered. For including JES uncertainty, a linearly distributed

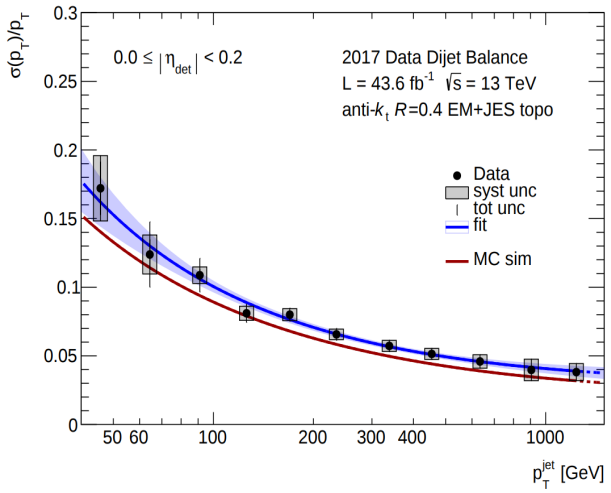

Figure 6.6: p_T resolution of anti-k$_t$ $R = 0.4$ jets in the region of $0.0 < \eta < 0.2$ [87].

random number from zero to the difference of the nominal value of JES and its highest (lowest) value is generated and the p_T of the jet is scaled with $1\pm$ the random number.

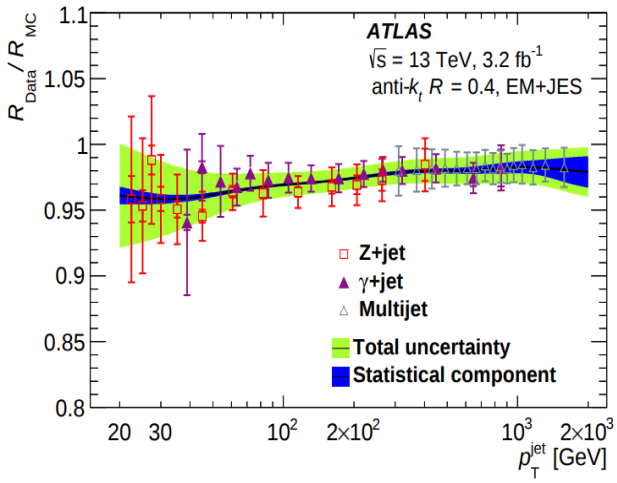

Figure 6.7: Jet energy response of jets and its uncertainty as a function of p_T [88].

Since MET is the vector sum of the p_T of all the contributing objects, its resolution is also based on the resolution of the objects. We take the MET resolution to be the p_T difference of the objects (muons and jets) before and after considering their resolution. Note that in the case of μ, only those that pass the efficiency requirement are included. In Appendix E we show the p_T ratio of jets, muons, and MET before and after adding the resolution.

There are still other effects that are ignored in our study, such as pileup effects. The cross-section of pp collisions is the sum of elastic and inelastic events, i.e $\sigma_{\text{tot}} = \sigma_{\text{el}} + \sigma_{\text{inel}}$. Elastic events are not of interest since none of the beam particles break apart, and go down

the beam pipe. On the other hand, the inelastic events are the events we are interested in. The dominant inelastic events are soft interactions and hard scattering does not happen very often. Soft and hard scatterings refer to events with low and high momentum transfer, respectively. In each bunch crossing that happens every 25 ns, there are about 50 pp collisions [89]. Whenever a hard pp collision happens, the additional particles produced from other soft pp collisions in the same bunch crossing, make it harder to reconstruct the hard scattering. This effect is known as pileup [89].

The definition of minimum-bias events depends on the triggers used in an experiment. In general, it refers to inelastic events that are accepted with a minimum set of requirements [90]. The minimum-biased pileup events are those soft interactions that have passed the minimum-biased trigger and produce some soft particles along with those created by the hard scattering.

The readouts of the detector often span over the time range of a few bunch crossings and creates out-of-time pileup [89].

Previous studies by ATLAS shows that the pileup effects can be dealt with and their effect can be completely ignored for jets with p_T greater than 50 GeV [91]. For jets with $p_T > 50$ GeV, jet multiplicity as a function of the number of primary vertices becomes flat, i.e no extra jet is reconstructed from pileup events. For the HL-LHC, the number of pp collisions per bunch crossing will be about 132 [92] and can become an issue. In this study we will assume that even at these high pileup condition, we will have algorithms to take care of it and the effects remain negligible.

From now on, the study includes the geometrical acceptance of the detector for the objects, the efficiency of muons, and the p_T resolution of the muons, jets, and MET unless explicitly stated otherwise. As previously mentioned, we are interested in higher QBH threshold masses. On top of choosing the ADDn6 model, we take the 9 TeV mass threshold sample for our study. Some of results will also be shown for the 4 TeV mass threshold sample to show the difference. The final and important results will be shown for all threshold mass samples and models.

6.5 Object Preselection

We have two different selection criteria, object selection and event selection. The event selection will be discussed in the next section. The object selection criteria are shown in Table 6.3. The η cut is just a geometrical acceptance requirement to make sure that the object goes into the well-instrumented detector and not down the beam pipe. For muons, the p_T cut removes low energy muons that are produced later in the decay chain and are not direct products of the W or τ. The p_T cut on jets removes the low energy jets created from low p_T hadrons failing to cluster around the hard jet and created a low p_T jet themselves.

Object	p_T (GeV) >	$\|\eta\|$ <
Jet	100	2.5
Muon	25	2.5

Table 6.3: Object selection cuts applied to jets and muons.

6.6 Event Selection and Cut Flow

Our goal is to reconstruct the four-momentum of the QBH that was produced by the QBH generator. To this end, we first have to identify the QBH decay mode so that we can use the proper algorithm for the reconstruction. At the same time, we should keep an eye on the background rejection. A looser cut might pick more signal events but at the cost of more background. Note that since the W bosons are W^+, the decay product is an anti-lepton but for simplicity we will call it a lepton.

In our study, we found that identifying leptonic decays and separating them from the other two decay modes is very difficult; low efficiency and high contamination. Leptonic decays are only 6.4% of all the events and ignoring them is not going to affect our study by much. Although in the leptonic case the background is significantly lower, the background is not the issue. In QBH production, in the high mass region especially, the cross-section is a lot larger than the SM cross-section. This means that if the hypothesized process exists, it won't be hard to distinguish it from the background. So, it is more important to get more signal events than to reduce the background. For the same reason, since the hadronic decays have the highest probability, we concentrate on finding hadronic events with high efficiency. The exception to this argument is the RS1 model which has a significantly lower cross-section compared to the ADD model and the background becomes important.

For identifying events using the objects previously selected, we choose the two highest p_T jets. The leading p_T jet will be called jet1 and the second leading p_T jet will be jet2. As for muons, there are two different cases. For leptonic decays, we need two muons while for mixed decays we only need one. The muon in mixed decays will be called the match muon, the muon coming directly from the W boson. For the leptonic case, at least two muons must have been found. We first take the highest p_T muon as our first muon, called muon1, since it is most likely to be a decay product of one of the Ws. Then, we take the other muons and check if it is well-separated from the first muon, $\Delta R > 2.5$[1]. If there is more than one muon, we take the highest p_T one among them as our second muon which will be called

[1]In some studies a $\Delta\phi > \pi/2$ is used to require the objects to be back-to-back in the transverse plane which in our study was also studied and yielded very similar results.

muon2. Another way of choosing these two muons would be by taking the two highest p_T muons that are close, $\Delta R < 2.5$, to the two highest p_T jets, which also ended up with very similar results. On the other hand, for mixed decays, we only need one muon. In case there is already only one muon found, we choose it as our match muon. If there are more than one, we first pick all the muons that are close to the jet2, $\Delta R < 2.5$ and if there are more than one muon satisfying this condition, we take the highest p_T muon as our match.

Now that we have our objects selected, we try to identify the QBH decay mode by putting cuts on the kinematics of these objects based on the kinematic properties of each decay mode. First, we will try to reduce the contamination of leptonic decays and then search for hadronic and mixed decays. If we find two well-separated muons where each have a $p_T > 50$ GeV, that event is discarded since it is a candidate for leptonic topology.

Next, we would like to find mixed decays. For mixed events, we concentrate on finding events where the lepton produced from the W is a muon. This is due to the fact that, for example for the case of $M_{\text{th}} = 9$ TeV QBH sample, 87% of the times the electron is close to the jet and cannot be separated in real data. Using the information of electrons in these cases would not be useful. In the mixed decays, one W has decayed hadronically and the other one has decayed leptonically. This means that jet1 should have a higher p_T compared to jet2. So, the jet1 and jet2 are required to be well-separated and have a p_T ratio $\frac{p_{T_{\text{jet1}}}}{p_{T_{\text{jet2}}}} > 1.25$. The highest p_T jet is required to have $p_{T_{\text{jet1}}} > 1.2$ TeV and $m_{\text{jet1}} > 120$ GeV. The match muon should have $p_{T_{\text{match}}} > 75$ GeV, and the event should have MET > 200 GeV.

In the hadronic case, both Ws have decayed to hadrons which form jets. We require each jet to have $p_T > 1$ TeV. As we will see later, in hadronic decays, the two highest p_T jets are top quark candidates. As such, we also require $m_j > 100$ GeV for these two jets. After all these requirements, there are still about 18% of the tt signal events that have not passed any of the selections. Table 6.4 shows the event selection criteria for each category in the order they are applied.

Event type	Selection criteria
Leptonic	$\Delta R_{\mu\mu} > 2.5$, $p_{T_{\mu_{1,2}}} > 50$ GeV
Mixed	$\Delta R_{jj} > 2.5$, $\frac{p_{T_{\text{jet1}}}}{p_{T_{\text{jet2}}}} > 1.25$, $p_{T_{\text{jet1}}} > 1.2$ TeV, $p_{T_{\text{match}}} > 75$ GeV, $M_{\text{jet1}} > 120$ GeV, MET > 200 GeV
Hadronic	$\Delta R_{jj} > 2.5$, $p_{T_{\text{jet1,2}}} > 1$ TeV, $M_{\text{jet}_{1,2}} > 100$ GeV

Table 6.4: Summary of selection criteria for identifying each event topology.

To better understand the selection criteria used, the cut-flow of the hadronic decay se-

lection is shown in Table 6.5. Table 6.6 shows the cut-flow of the mixed decays selection. Note that in these tables, contamination from other decay modes have been removed using the cuts shown in Table 6.4. By misidentified events we mean the events that belong to a category have passed the cuts of another category and are misidentified. The distribution of the variables used in the selection criteria for the three decay modes of the QBH signal and also the QCD dijet background (from PYTHIA), discussed in Sec. 6.8.1, are shown in Figure F.1-F.9 in Appendix F.

Selection criteria	Mixed(%)	Misidentified (%)
$\Delta R_{jj} > 2.5$	58.3	43.7
$\frac{p_{T_{\text{jet1}}}}{p_{T_{\text{jet2}}}} > 1.25$	49.0	7.9
$p_{T_{jet1}} > 1.2$ TeV	47.5	7.7
$m_{jet1} > 120$ GeV	44.0	7.5
MET > 150 GeV	40.6	6.5
$p_{T_{\text{match}}} > 75$ GeV	35.6	4.3

Table 6.5: The impact of each selection criteria on the mixed decay of the QBH $M_{\text{th}} = 9$ TeV sample. Percents are with respect to the mixed decays, i.e mixed $= \frac{\text{number of observed mixed events}}{\text{number of real mixed events}}$ and misidentified $= \frac{\text{number of observed misidentified events}}{\text{number of real mixed events}}$. The contamination of leptonic events is removed first.

Selection criteria	Mixed(%)	Misidentified (%)
$\Delta R_{jj} > 2.5$	96.4	67.7
$p_T > 1.0$ TeV	92.4	54.0
$m_j > 100$ GeV	85.8	33.0

Table 6.6: The impact of each selection criteria on the hadronic decay of the QBH $M_{\text{th}} = 9$ TeV sample. The p_T and mass cuts are applied to both of the two highest p_T jets. Percents are with respect to the hadronic sample, i.e hadronic $= \frac{\text{number of observed hadronic events}}{\text{number of real hadronic events}}$ and misidentified $= \frac{\text{number of observed misidentified events}}{\text{number of real hadronic events}}$. The contamination of leptonic and mixed events are removed first.

To summarize the result of the event selection cuts we define an efficiency matrix as:

$$\begin{pmatrix} N_H \\ N_M \\ N_L \\ N_l \end{pmatrix} = \begin{pmatrix} \eta_{HH} & \eta_{HM} & \eta_{HL} & \eta_{Hl} \\ \eta_{MH} & \eta_{MM} & \eta_{ML} & \eta_{Hl} \\ \eta_{LH} & \eta_{LM} & \eta_{LL} & \eta_{Hl} \\ \eta_{lH} & \eta_{lM} & \eta_{lL} & \eta_{ll} \end{pmatrix} \begin{pmatrix} n_H \\ n_M \\ n_L \\ n_l \end{pmatrix}, \tag{6.5}$$

where N_X is the number of observed events in each category ($H \equiv$ hadronic, $M \equiv$ mixed, $L \equiv$ leptonic, $l \equiv$ lost) and n_X is the number of real events in that category. n is found using truth information which is exact and N is found using the selection criteria and contains the misidentified events as well. The diagonal elements shows that the event's topology is found correctly and off-diagonal elements mean that the event is placed in a wrong topology. We refer to off-diagonal elements as misidentified events. So, the goal is to get the diagonal elements close to one and off-diagonal elements to zero. Choosing the set of cuts discussed for the QBH $M_{\text{th}} = 9$ TeV sample with 50,000 events we get

$$\begin{pmatrix} 30423 \\ 7468 \\ 2716 \\ 9393 \end{pmatrix} = \begin{pmatrix} 0.84 & 0.33 & 0.17 & 0 \\ 0.03 & 0.33 & 0.17 & 0 \\ 0.02 & 0.07 & 0.24 & 0 \\ 0.11 & 0.27 & 0.42 & 0 \end{pmatrix} \begin{pmatrix} 28155 \\ 18651 \\ 3194 \\ 0 \end{pmatrix}. \tag{6.6}$$

Since the misidentified events are significant, it's important to see what kind of events they are. 33% of mixed decays have pass the cuts designed for choosing hadronic decays. Recall that one of the criterion for picking hadronic and mixed decays was the p_T ratio of the two leading jets. About 89% of these misidentified mixed events are those that one of the Ws have decayed to an electron. For this reason, the second highest p_T jet is only missing a neutrino and becomes very similar to a hadronic event. The leptonic misidentified events are negligible, 2% of N_H, and about 55% of them are those leptonic decays that both Ws have decayed to electron. It's harder to track how 3% of hadronic events have passed mixed decays. In the decay chain of hadronic events, a muon has been produced that is close to jet2 and has a high enough p_T to pass the p_T threshold. About 84% of the leptonic decays that have been categorized as mixed decays are those that one W has decayed to muon and the other one has decayed to an electron.

It is useful to see how these cuts affect the lower mass threshold samples. Using our

lowest threshold mass sample, i.e $M_{\text{th}} = 4$ TeV, we have the following efficiency matrix:

$$\begin{pmatrix} 23531 \\ 5003 \\ 1861 \\ 19605 \end{pmatrix} = \begin{pmatrix} 0.69 & 0.20 & 0.07 & 0 \\ 0.02 & 0.23 & 0.07 & 0 \\ 0.01 & 0.05 & 0.19 & 0 \\ 0.28 & 0.52 & 0.67 & 0 \end{pmatrix} \begin{pmatrix} 28255 \\ 18575 \\ 3170 \\ 0 \end{pmatrix}. \tag{6.7}$$

Since our cuts were optimized for higher threshold masses, our efficiencies for hadronic and mixed decays are down to 69% and 23%, respectively, compared to 84% and 33%.

Note that the matrix elements are the acceptance with respect to the given topology, not the whole sample. Finding the decay mode correctly is important for applying the proper event reconstruction algorithm. Since we want events with a reconstructed mass above a given threshold mass, the misidentified events are not necessarily a bad thing. We will not have the proper reconstruction but as long as the reconstructed mass is below the threshold mass of the sample, it will not contaminate our sample.

6.7 Event Reconstruction Algorithm

Having chosen the essential objects and classified the decay mode, we will reconstruct the kinematics of the events, or in other words, the four-momentum of the QBH. As was seen in the previous section, we are only able to pick hadronic and mixed decays with reasonable efficiencies. The reconstruction algorithm is different for each of them. First, we will consider the hadronic case since it is the easier of the two, and then will move on to mixed decays. Since the misidentified events in both categories are significant, we show the results for both real and misidentified events. The reconstruction algorithm study uses 100,000 events for each M_{th} sample.

6.7.1 Hadronic Decays

Top quark reconstruction for the hadronic decays is straightforward. Both top quarks have high energies, and the decay products are highly boosted, and they fit in a small cone-jet. In this case, the four-momentum of the two highest p_T jets are our top quark candidates. To reconstruct the QBH state we just need to add the four-momentum of the two jets together. Figure 6.8 and Figure 6.9 show the mass distribution of each jet and the dijet mass for the QBH $M_{\text{th}} = 9$ TeV and $M_{\text{th}} = 4$ TeV samples, respectively. Figure 6.10 compares the reconstructed QBH mass versus its truth mass for QBH $M_{\text{th}} = 9$ TeV and $M_{\text{th}} = 4$ TeV samples. In this figure, the case of hadronic, misidentified mixed, and misidentified leptonic events are shown separately. As could be expected, the case of misidentified mixed and

misidentified leptonic events have a lower reconstructed mass due to the missing neutrino(s). We denote the QBH reconstructed mass from the hadronic decay mode as m_{jj}.

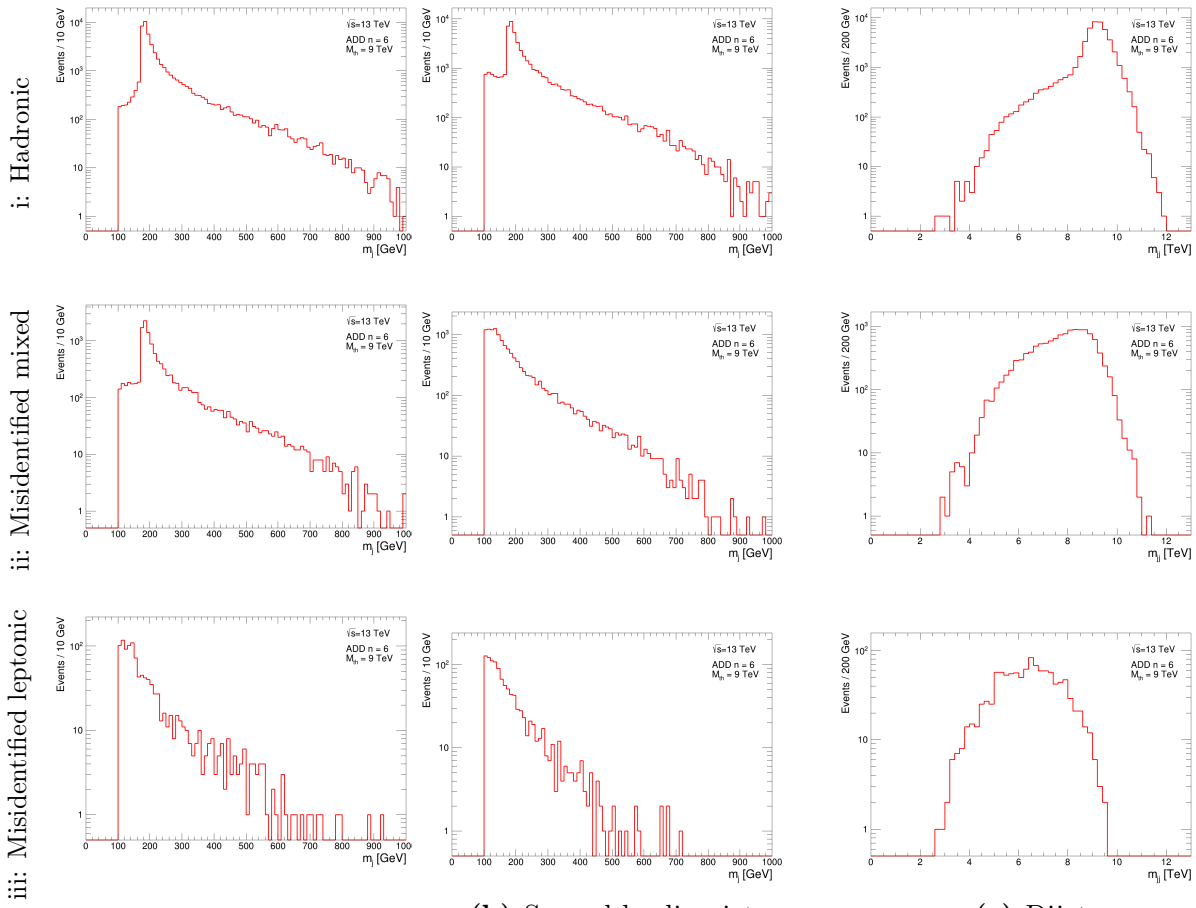

(a) First leading jet **(b)** Second leading jet **(c)** Dijet

Figure 6.8: Mass distribution of first and second leading p_T jets and the dijet mass distribution. The three columns from left to right show the mass distribution of **(a)** the first p_T leading jet, **(b)** the second p_T leading jet, and **(c)** dijet. The three rows show the **(i)** hadronic, **(ii)** misidentified mixed, and **(iii)** misidentified leptonic events. The results are for the QBH $M_{\text{th}} = 9$ TeV sample.

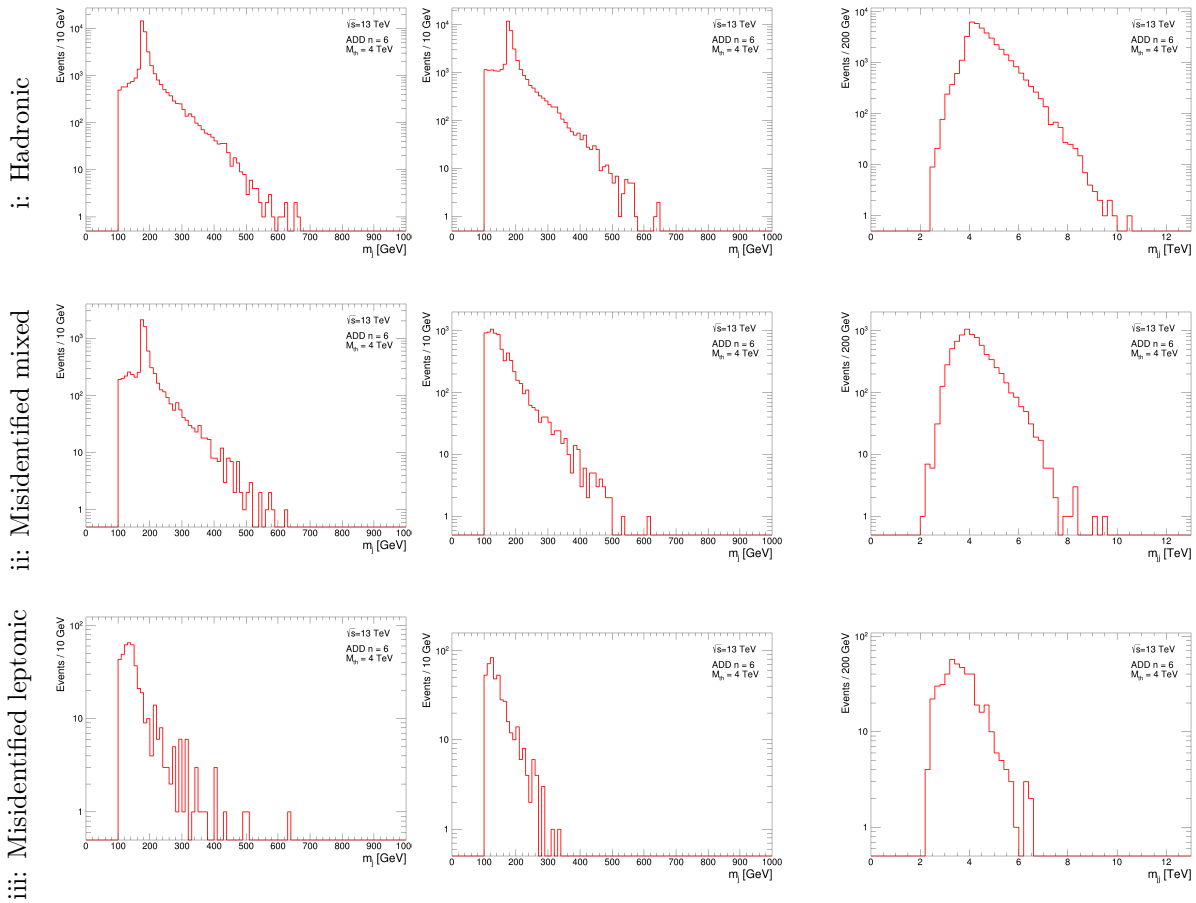

(a) First leading jet **(b)** Second leading jet **(c)** Dijet

Figure 6.9: Mass distribution of first and second leading p_T jets and the dijet mass distribution. The three columns from left to right show the mass distribution of **(a)** the first p_T leading jet, **(b)** the second p_T leading jet, and **(c)** dijet. The three rows show the **(i)** hadronic, **(ii)** misidentified mixed, and **(iii)** misidentified leptonic events. The results are for the QBH $M_{\text{th}} = 4$ TeV sample.

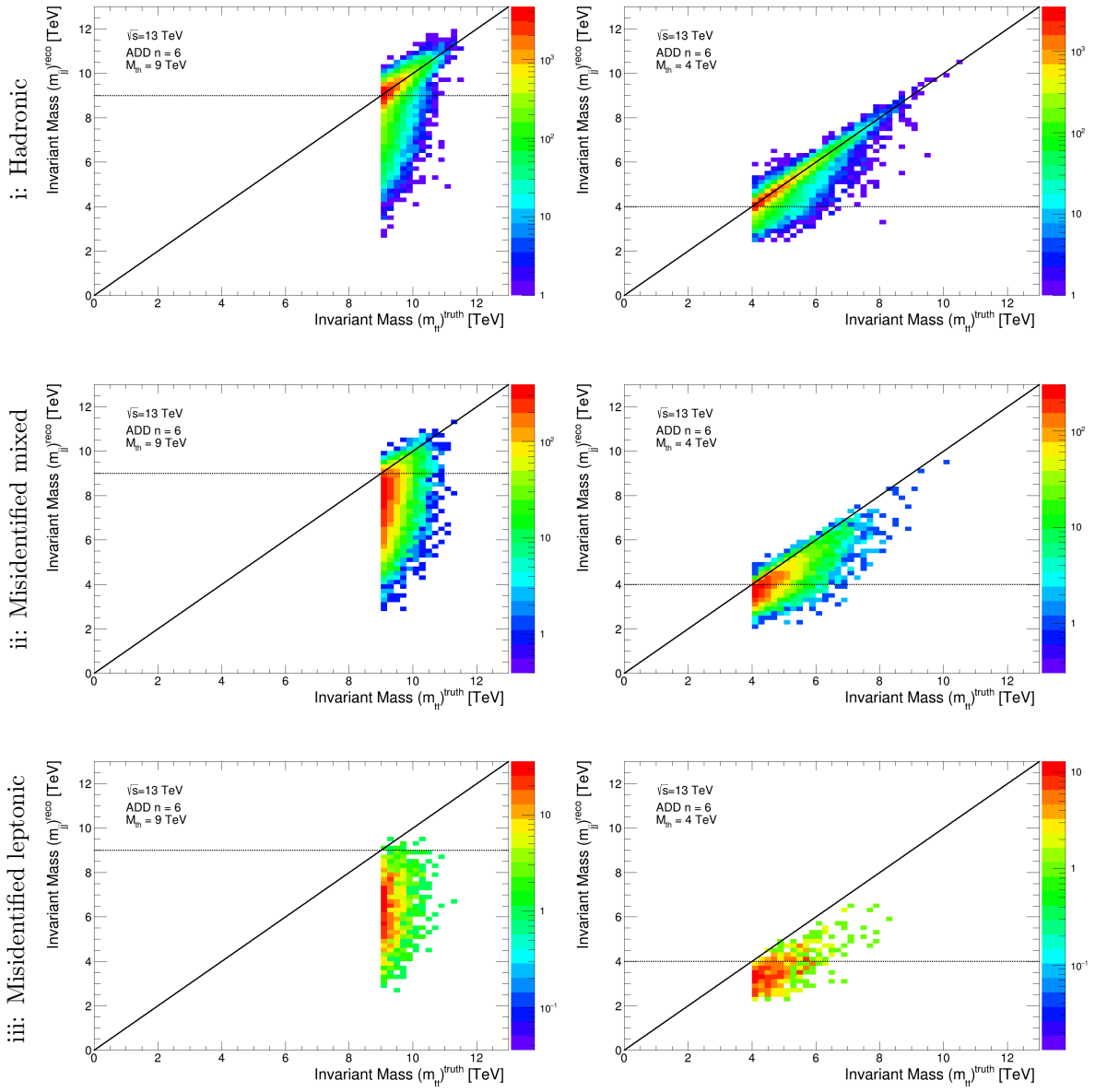

(a) $M_{\text{th}} = 9$ TeV **(b)** $M_{\text{th}} = 4$ TeV

Figure 6.10: Comparison of the QBH reconstructed mass and the QBH truth mass. The two columns from left to right show the QBH **(a)** $M_{\text{th}} = 9$ TeV sample, and **(b)** $M_{\text{th}} = 4$ TeV sample. The three rows show the **(i)** hadronic, **(ii)** misidentified mixed, and **(iii)** misidentified leptonic events. The horizontal line indicates the threshold mass of the sample.

6.7.2 Mixed Decays

To reconstruct the mixed events, the highest p_T jet is considered as one of the top quark candidates. To reconstruct the second top, we should first reconstruct the W and add it to the b-jet which is our second highest p_T jet. The b-jet is jet2 because since the W has decayed to μ, the produced hadrons are the decay product of the b-quarks. The QBH four-momentum would be the four-momentum of the two highest p_T jets plus the four-momentum of the reconstructed W.

The W decays to a muon and the corresponding neutrino. For reconstructing the W, we need the four-momentum of its products. We have already chosen our muon in the object selection, where we called it the match muon. The neutrino appears as the missing transverse momentum. First, let us see how good we are doing at picking the right muon coming from the W or τ_l, both in the case of mixed decays. Using the PDG ID and the Barcode information, about 95% of the times we pick the exact muon that comes from W or τ_l. Having found the muon, we follow the method in Ref. [93] to reconstruct the four-momentum of the W. In our case, the W is a real particle, not a force mediator, and so it is on its mass shell. Using its mass as a constraint, we can get a quadratic equation for the z-component of the four-momentum of the neutrino. The mass of the W is set to 80.4 GeV [53]. To avoid too many subscripts let us first set some notations. We use normal variables for muon and primed ones for neutrino, boldface for three-vectors and normal font for four-vectors. So

$$p_\mu = p = (E, p_x, p_y, p_z)\,, \qquad p_\nu = p' = \left(|\mathbf{p}'|, p'_x, p'_y, p'_z\right), \tag{6.8}$$

where we have supposed that the neutrino is massless and so $E' = |\mathbf{p}'|$. Since $W \to \mu\nu$, then $p_W = p + p'$ and using the mass constraint

$$\begin{aligned} m_W^2 = p_W^2 &= (p + p')^2 = (E + E')^2 - (\mathbf{p} + \mathbf{p}')^2 \\ &= (E + |\mathbf{p}'|)^2 - (\mathbf{p} + \mathbf{p}')^2 \\ &= E^2 - |\mathbf{p}|^2 + |\mathbf{p}'|^2 - |\mathbf{p}'|^2 + 2E|\mathbf{p}'| - 2\mathbf{p}\cdot\mathbf{p}', \end{aligned} \tag{6.9}$$

where $E^2 - |\mathbf{p}|^2 = m_l^2$. We can ignore the mass of the μ compared to the mass of the W. Rearranging Equation 6.9, we get

$$E|\mathbf{p}'| = \frac{m_W^2}{2} + \mathbf{p}\cdot\mathbf{p}'. \tag{6.10}$$

Squaring Equation 6.10 and using $|\mathbf{p}'|^2 = p_T'^2 + p_z'^2$

$$\begin{aligned} E^2\left(p_T'^2 + p'^2\right) &= \frac{m_W^4}{4} + (p_T \cdot p_T')^2 + p_z^2 p_z'^2 + m_W^2(p_T \cdot p_T' + p_z p_z') + 2p_T \cdot p_T' p_z p_z', \\ p_z'^2(E^2 - p_z^2) &= -E^2 p_T'^2 + p_z'(m_W^2 p_z + 2p_T' \cdot p_T p_z) + \frac{m_W^4}{4} + (p_T \cdot p_T')^2 + m_W^2 p_T \cdot p_T'. \end{aligned} \tag{6.11}$$

Defining $\mu = \frac{m_W^2}{2} + p_T \cdot p_T'$ where $p_T \cdot p_T' = |p_T||p_T'| \cos\phi$ and ϕ is the azimuthal angle between the muon and the missing transverse momentum vector. So,

$$p_z'^2 - 2\frac{\mu p_z}{E^2 - p_z^2} p_z' + \frac{E^2 p_T'^2 - \mu^2}{E^2 - p_z^2} = 0, \tag{6.12}$$

which in general has two possible solutions

$$p_z' = \frac{\mu p_z}{p_T^2} \pm \sqrt{\frac{\mu^2 p_z^2}{p_T^4} - \frac{E^2 p_T'^2 - \mu^2}{p_T^2}}. \tag{6.13}$$

In our study, 77% of the time the discriminant is positive, and between the two solutions people usually take the one with smaller $|p_z'|$. This is because when a heavy particle like W decays, its products tend to have a high p_T and thus a small $|p_z|$ [93]. In our studies, it was shown that there is not much of a difference between the two solutions and we also took the smaller $|p_z'|$. In case of imaginary solutions, we only choose the real part but now the combined four-momentum of the muon and the neutrino does not yield the mass of the W. So, we modify the energy of the neutrino such that we still get $m_W = 80.4$ GeV.

Figure 6.11 shows the comparison of the top quark and QBH reconstructed mass with and without reconstructing the p_z of the neutrino and the QBH reconstructed mass using both values of p_z' of Equation 6.13 in cases of positive discriminant. The impact of using the p_z' is significant for reconstructing the top quark but it does not affect the QBH mass very much. Also, the two different values of p_z' in Equation 6.13 do not have a notable effect on the QBH reconstructed mass.

Figure 6.12 and Figure 6.13 show the mass distribution of the first p_T leading jet, reconstructed jet mass, and reconstructed QBH mass for the QBH $M_{\text{th}} = 9$ TeV and $M_{\text{th}} = 4$ TeV samples. Figure 6.14 shows the reconstructed QBH mass versus its truth mass for QBH $M_{\text{th}} = 9$ TeV and $M_{\text{th}} = 4$ TeV samples. In this figure, the case of misidentified hadronic, mixed, and misidentified leptonic events are shown separately. We denote the QBH reconstructed mass from the mixed decay mode as $m_{j,j\mu\nu}$.

In Appendix G, we show the QBH reconstructed mass versus its truth mass for inclusive hadronic and mixed decays for all the eight QBH samples in ADDn6 model. By inclusive

we mean they contain the matched and misidentified events altogether.

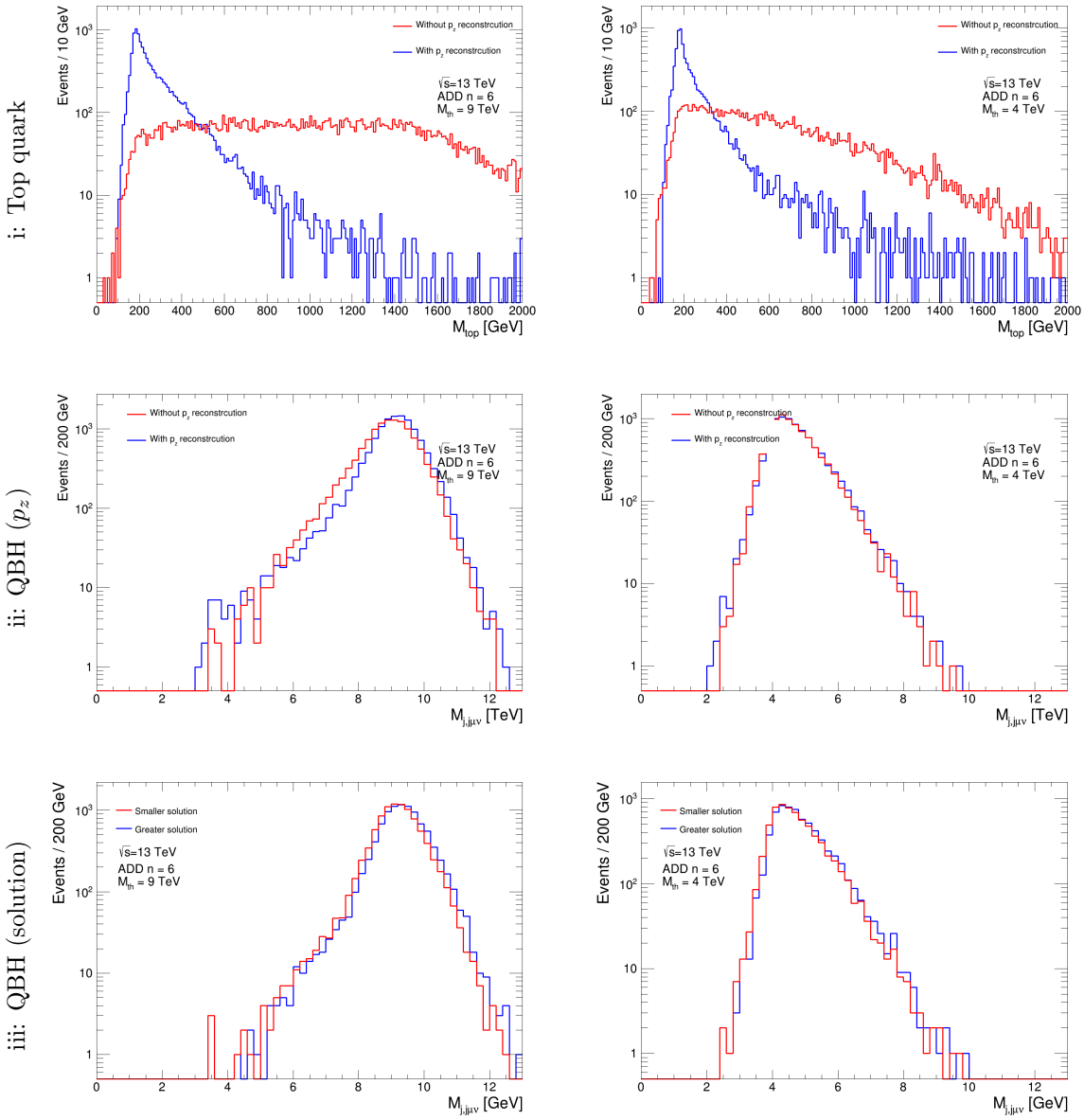

(a) $M_{\text{th}} = 9$ TeV **(b)** $M_{\text{th}} = 4$ TeV

Figure 6.11: Comparison of the top quark and QBH reconstructed mass with and without reconstructing the p_z of the neutrino and the QBH mass using both possible solutions of Equation 6.13. The two columns from left to right show the QBH **(a)** $M_{\text{th}} = 9$ TeV, and **(b)** $M_{\text{th}} = 4$ TeV samples. Row **(i)** shows top quark mass distribution. Row **(ii)** shows the QBH mass distribution with and without reconstructing the p_z of the neutrino where the smaller value of Equation 6.13 is chosen as the value of p'_z. Row **(iii)** shows the QBH mass using both values of p'_z. Misidentified events are excluded from these plots.

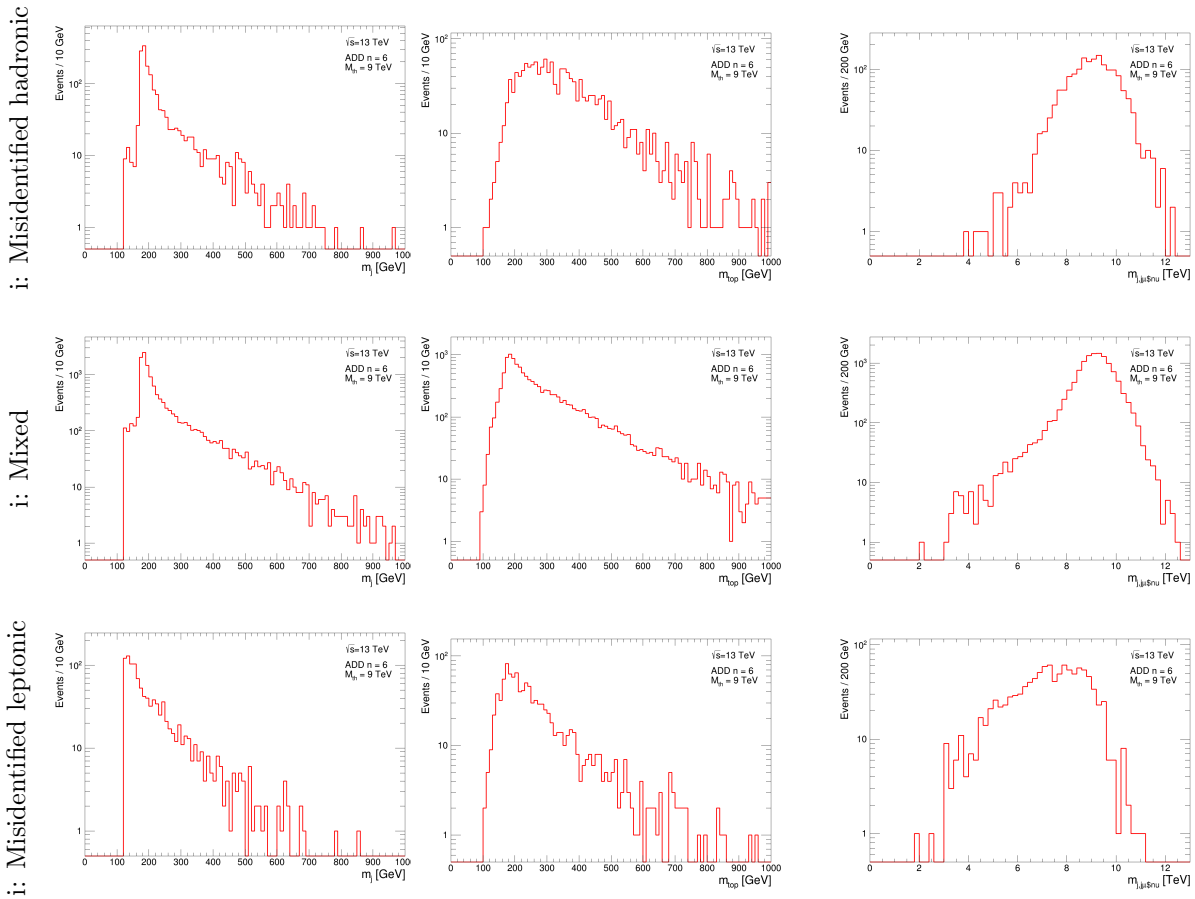

(a) First leading jet **(b)** Top quark **(c)** QBH

Figure 6.12: Mass distribution of first and second p_T leading jets and the dijet invariant mass. The three columns from left to right show the mass distribution of **(a)** the first leading p_T jet, **(b)** the second leading p_T jet, and **(c)** dijet. The three rows show the **(i)** misidentified hadronic, **(ii)** mixed, and **(iii)** Misidentified leptonic events. The results are for the QBH $M_{\text{th}} = 9$ TeV sample.

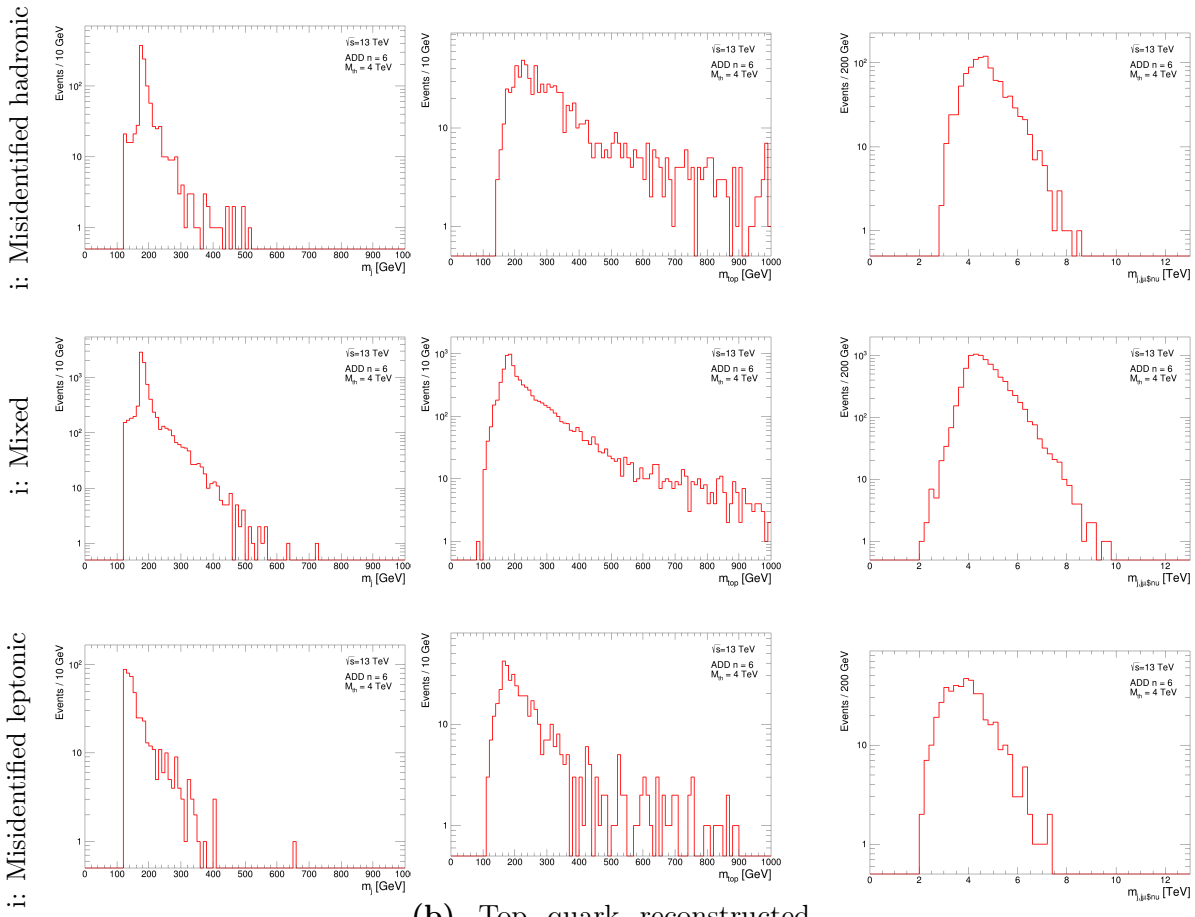

(a) First leading jet mass

(b) Top quark reconstructed mass

(c) QBH reconstructed mass

Figure 6.13: Mass distribution of first and second p_T leading jets and the dijet invariant mass. The three columns from left to right show the mass distribution of **(a)** the first leading p_T jet, **(b)** the second leading p_T jet, and **(c)** dijet. The three rows show the **(i)** misidentified hadronic, **(ii)** mixed, and **(iii)** misidentified leptonic events. The results are for the QBH $M_{\text{th}} = 4$ TeV sample.

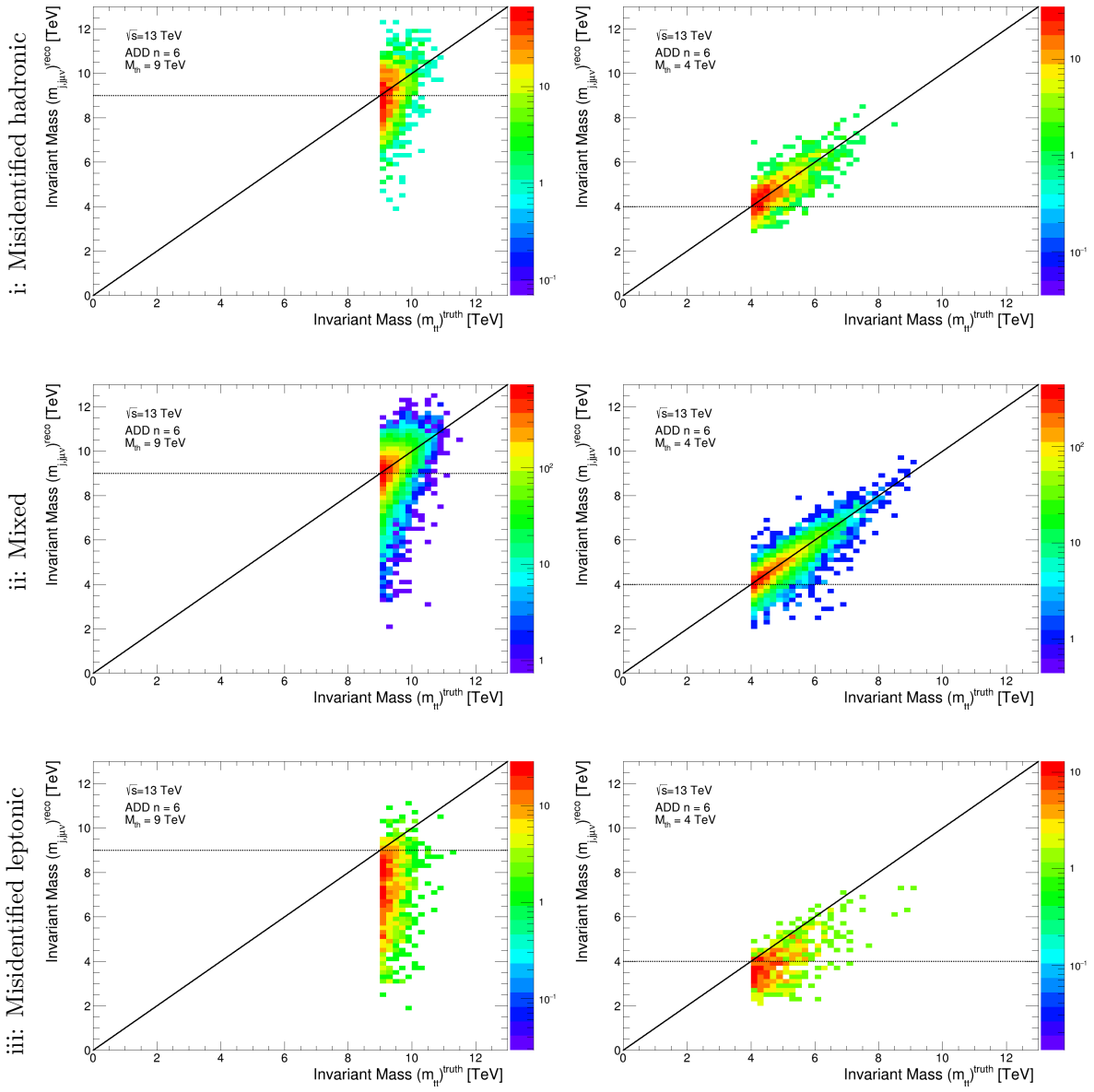

(a) $M_{\text{th}} = 9$ TeV **(b)** $M_{\text{th}} = 4$ TeV

Figure 6.14: Comparison of the QBH reconstructed mass and the QBH truth mass. The two columns from left to right show the QBH **(a)** $M_{\text{th}} = 9$ TeV sample, and **(b)** $M_{\text{th}} = 4$ TeV sample. The three rows show the **(i)** misidentified hadronic, **(ii)** mixed, and **(iii)** misidentified leptonic events. The horizontal line indicates the threshold mass of the sample.

6.7.3 Mass Distribution

We have found a satisfying event selection algorithm to identify the decay modes and applied an appropriate mass reconstruction for each decay mode. Figure 6.15 shows the reconstructed QBH invariant mass for all the samples of the ADDn6 model in each topology. Appendix H shows the comparison of the mass distribution of the different models for QBH sample with $M_{\text{th}} = \{4, 6, 8, 10\}$ TeV.

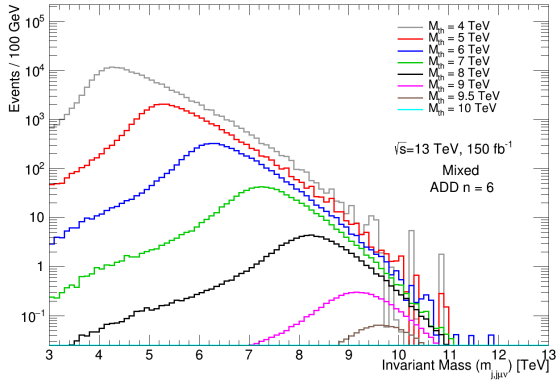

(a) Mixed

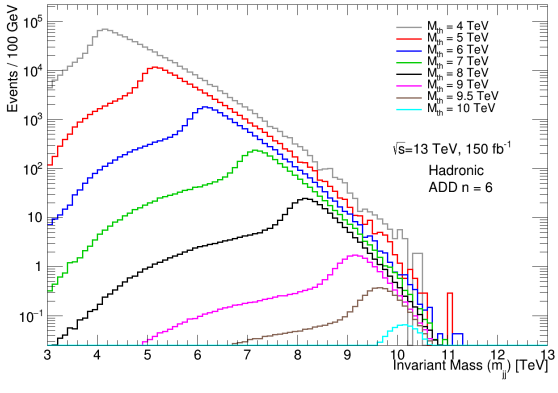

(b) Hadronic

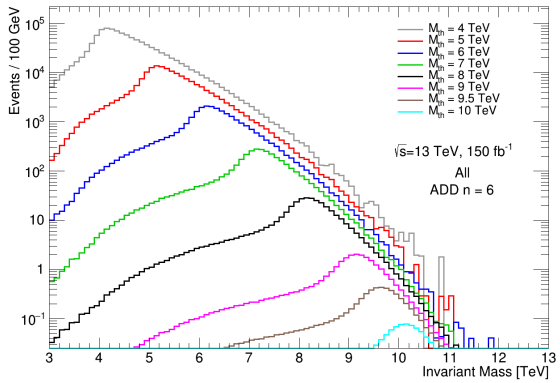

(c) All

Figure 6.15: The reconstructed QBH invariant mass distribution for **(a)** mixed decays, **(b)** hadronic decays, and **(c)** all the decay modes normalized to 150 fb^{-1}. The distributions are for ADDn6 model.

6.8 Background Sources

Having an algorithm for signal reconstruction, we need to consider the different possible contributions to the background of a QBH $\rightarrow tt$ signal. The most important contribution to

the background comes from the QCD multijet events and, possibly, the $t\bar{t}$ production and W/Z plus jet processes, each to be discussed in the next sections.

6.8.1 QCD Dijet

As we will see, the most important contribution to the background comes from the QCD multijet processes which are modeled as a $2 \to 2$ scattering process followed by showering and hadronization. We use both Pythia and Herwig to simulate these events and compare their results.

PYTHIA

To simulate the QCD multijet process the Pythia generator is used with LO NNPDF2.3 [94] as the PDF set. The ATLAS A14 [95] set of tuned parameters is used for the parton shower and hadronization.

In this process, there are two incoming and two outgoing partons. The MC simulation of such processes is sliced in 13 regions of the leading jet p_T and are called JZ{0-12}W. The W at the end means that each event has a weight [96]. The properties of each region are shown in Table 6.7. In each region, there are two p_T requirements. One on the incoming partons, shown as $\hat{p}_T$ in the centre-of-mass frame. The other p_T requirement is on the leading jet, in the lab frame, using the anti-k_t jet algorithm with $R = 0.6$, shown as p_T. The most significant difference between these two parameters is that $\hat{p}_T$ is at the generator level and does not have any physical meaning. On the other hand, p_T is for the jets which are observable objects, created after parton showering, hadronization, fragmentation, and jet reconstruction.

There are two reasons for the $\hat{p}_T$ cut. The first is that in calculating the differential cross-section of QCD scattering, two types of divergences happens. The infrared divergence happens in theories with massless particles and appears from the contribution of particles with energies close to zero. These types of divergences vanish by including one-loop vertex corrections which are not included in Pythia dijet. Also, in high energy collisions where one can assume the quarks to be massless, like in our case, the mass divergence happens when the incident quark emits a collinear gluon. The latter is also not physical and can be dealt with, but one can simply ignore it by setting a minimum on $\hat{p}_T$ and ignoring the details as $\hat{p}_T \to 0$ (See Ref. [97] for more details). This cut can be applied using the Pythia member function called *PhaseSpace:pTHatMin* [98] which has a default value of 0. As can be seen from Table 6.7, the first two JZW slices have no $\hat{p}_T$ cut but the divergence is avoided by another member function: *PhaseSpace:pTHatMinDiverge* [98] has a default value of 1 GeV and a minimum of 0.5 GeV. Pythia uses the larger of *pTHatMin* and *pTHatMinDiverge* when necessary to avoid divergences in processes where $\hat{p}_T \to 0$.

The second reason is computational-wise. If one wants to generate events inclusively, it takes a huge amount of time and power to produce enough number of events in the higher p_T region. To deal with this problem, a cut is placed on p_T. To produce these events, a looser cut on $\hat{p}_T$ is applied at the generator level to increase the efficiency of generating these events. If we only consider the $\hat{p}_T$ requirement, the distribution would look like Figure 6.16a. An event is stored only if the p_T criteria on the outgoing jets are also satisfied which in return changes the distribution of $\hat{p}_T$ to Figure 6.16b. Note that Figure 6.16 is just a schematic plot of JZ3W and except for the cut values, it is not the actual distribution and is just shown for explanation. The ratio of the two distributions defines the filter efficiency of a given slice. See Ref. [99] for more information on JZW slices.

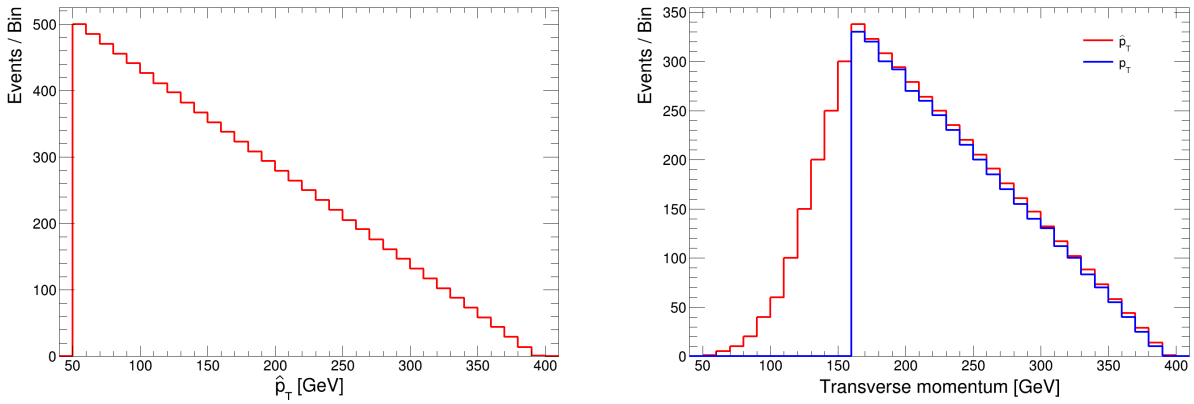

(a) **(b)**

Figure 6.16: A schematic plot of $\hat{p}_T$ and p_T using JZ3W cuts for illustration.

It was shown in our study that the first five dijet p_T slices do not contribute to masses above 4 TeV, but we only neglected the first four slices in case some events pass the cuts due to emulated detector effects.

Sample	Total number of events	Minimum $\hat{p}_T$ (GeV)	Minimum p_T (GeV)	Maximum p_T (GeV)	σ (pb)	Filter efficiency
JZ0W	1999400	0 (N/A)	0	20	7.8420e+10	9.76e-01
JZ1W	1999000	0 (N/A)	20	60	7.8420e+10	6.71e-04
JZ2W	1994600	15	60	160	2.4332e+09	3.34e-04
JZ3W	7884500	50	160	400	2.6454e+07	3.20e-04
JZ4W	1997000	150	400	800	2.5463e+05	5.31e-04
JZ5W	1999500	350	800	1300	4.5535e+03	9.24e-04
JZ6W	1997000	600	1300	1800	2.5753e+02	9.42e-04
JZ7W	1996500	950	1800	2500	1.6215e+01	3.93e-04
JZ8W	2000000	1500	2500	3200	6.2503e-01	1.02e-02
JZ9W	2000000	2200	3200	3900	1.9639e-02	1.21e-02
JZ10W	2000000	2800	3900	4600	1.1962e-03	5.91e-03
JZ11W	1999000	3500	4600	5300	4.2300e-05	2.68e-03
JZ12W	1997500	4200	5300	∞	1.0000e-06	4.26e-04

Table 6.7: Basic information of each JZW slice for the Pythia QCD dijet background. p_T cut in the lab frame is used for the jets and $\hat{p}_T$ cut in the centre-of-mass is used for hadrons. The four samples above the drawn line are not used.

Normalizing MC Dijet to the Data. The simulation of the QCD multijet processes usually do not exactly agree with data. In our case, there are two main reasons for this discrepancy between MC simulation and data. The first is detector effects which we have tried to consider by including the p_T resolution of the jet's momentum. The second reason is that although the dijet mass shape produced by simulation is similar, its total cross-section prediction is not. This is because the data includes all QCD processes while MC simulation is just the QCD $2 \rightarrow 2$ scattering process with showering used to estimate higher order effects.

For comparing the MC simulated background and data, we need to reconstruct the dijet invariant mass in the simulated background with a set of criteria that are identical to those for data since we are using preselected data [100]. Using the same requirements as Ref.[4], we require the leading (sub-leading) jets to have $p_T > 440$ (60) GeV, and $|y^*| < 0.6$ where $y^* = \frac{y_1 - y_2}{2}$ and y is the rapidity of the jet. Figure 6.17 shows the simulated events and ATLAS data.

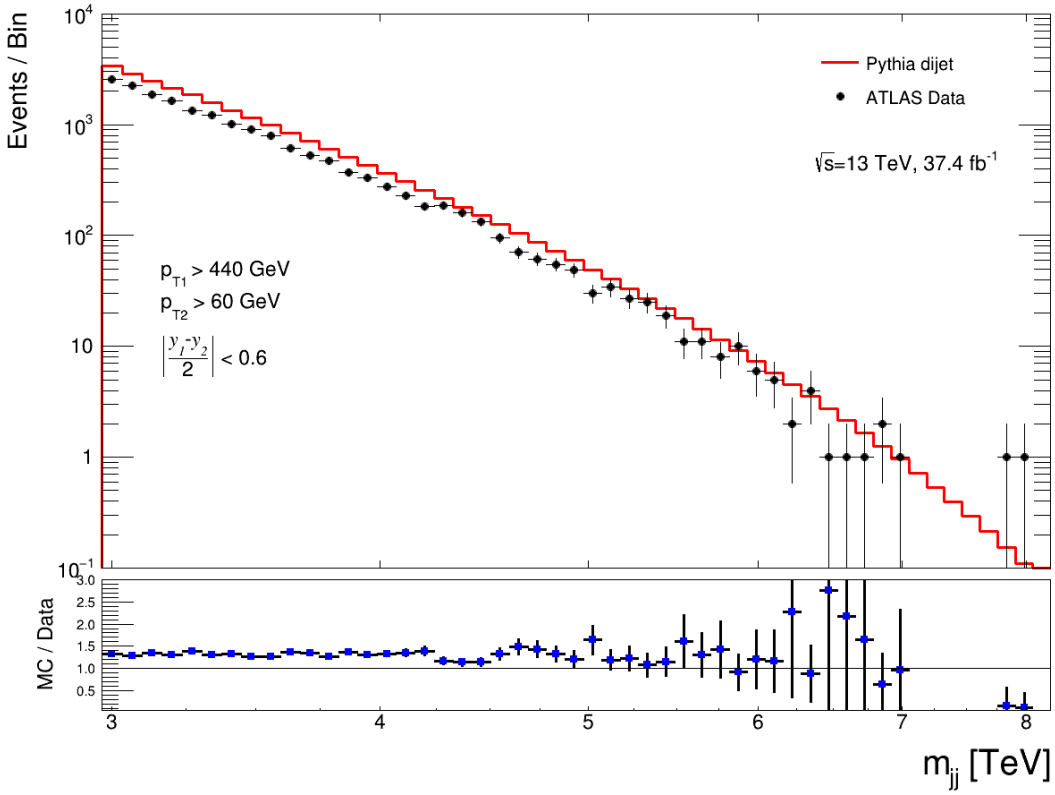

Figure 6.17: The reconstructed dijet mass distribution from PYTHIA simulation of QCD processes for small-cone jets, $R = 0.4$, using events with $p_T > 440$ GeV for the leading and $p_T > 60$ GeV for the sub-leading jet satisfying $|y^*| < 0.6$. The data is taken from [100].

Using the event-by-event generator weights, cross-sections, filter efficiencies, and luminosity, the MC simulation does not reproduce the total cross-section. As can be seen from Figure 6.17, the shapes are similar but the area is not. The ratio of the integrals of these two distributions is 0.76 which is used to normalize MC simulation to data. Figure 6.18 shows the distribution after normalizing the MC simulation to data.

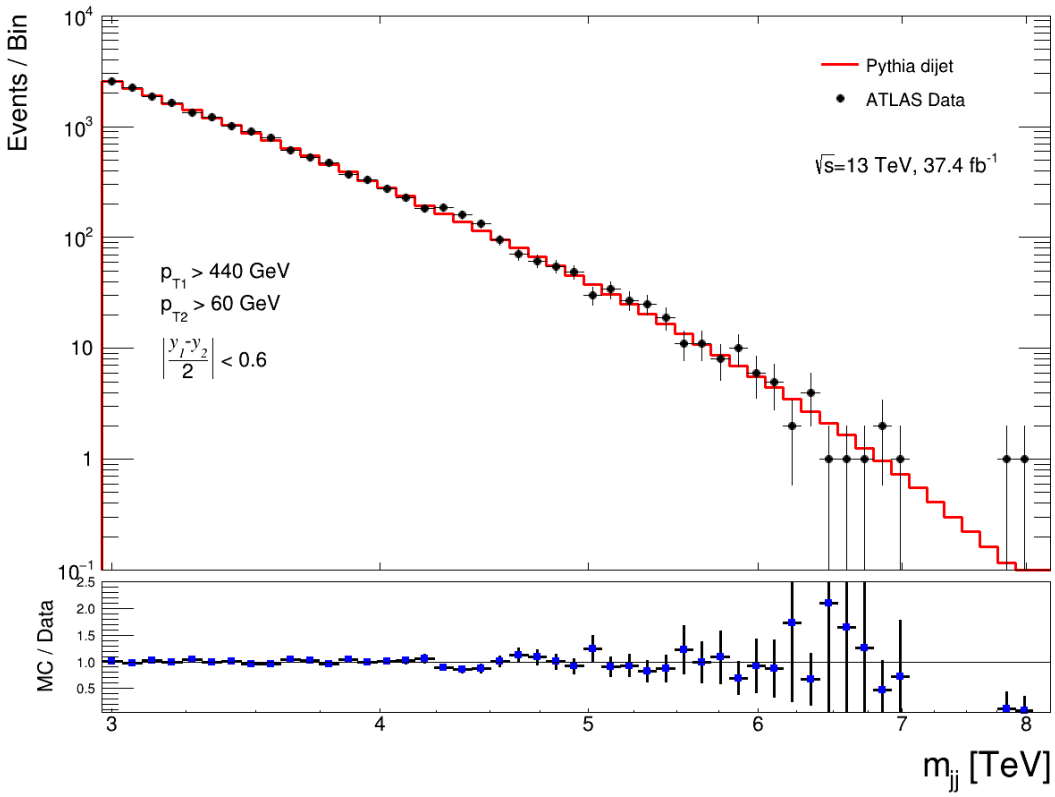

Figure 6.18: The reconstructed dijet mass distribution from Pythia simulation after normalizing the Pythia simulation to the data. The data is taken from [100].

Background Cut Flow. Table 6.8 and Table 6.9 shows the cut-flow of the QCD dijet background using the event selection used for the QBH signals, see Table 6.4. Note that in these tables, the individual weights of the events, and also the weights of the JZW slices are included.

HERWIG

Another well-known event generator for simulating multijet process is Herwig [77] in which ATLAS uses the UEEE5 [101] tune and the CTEQ6L1 PDF set. As in Pythia, properties of

$\Delta R_{jj} >$	$\frac{p_{T_{\text{jet1}}}}{p_{T_{\text{jet2}}}} >$	$p_{T_{jet1}} >$ (TeV)	$m_{jet1} >$ (GeV)	MET > (GeV)	$p_{T_{\text{match}}} >$	Acceptance (%)
2.5	———	———	———	———	———	1.4
2.5	1.25	———	———	———	———	0.7
2.5	1.25	1.2	———	———	———	1×10^{-3}
2.5	1.25	1.2	120	———	———	1×10^{-4}
2.5	1.25	1.2	120	150	———	1×10^{-5}
2.5	1.25	1.2	120	150	75	1×10^{-5}

Table 6.8: The impact of each selection criteria, made for picking mixed decays of the QBH signals, on the acceptance of the QCD dijet background.

$\Delta R_{jj} >$	$p_T >$ (TeV)	$m_j >$ (GeV)	Acceptance (%)
2.5	———	———	95.21
2.5	1.0	———	0.18
2.5	1.0	100	0.01

Table 6.9: The impact of each selection criteria, made for picking hadronic decays of the QBH signals, on the acceptance of the QCD dijet background.

the bottom and charm hadron decays are described using the EvtGen program [102]. ATLAS Herwig has a very similar slicing to ATLAS Pythia, but it uses JZ slices instead of JZW. Meaning that the events themselves have equal weight of one. Following the same procedure as used in the case of Pythia, we normalize the Herwig distribution to data. Figure 6.20 shows the dijet invariant mass distribution of events with the leading (sub-leading) jet having a $p_T > 440$ (60) GeV with a rapidity difference of $|y^*| < 0.6$. The mass distribution of the Herwig simulation of the QCD multijet events also follows the same shape as the data as can be seen in the lower panel of Figure 6.19. The ratio of the integrals of these two distributions is 1.61. Figure 6.20 compares the simulated mass distribution to data after normalizing the MC events.

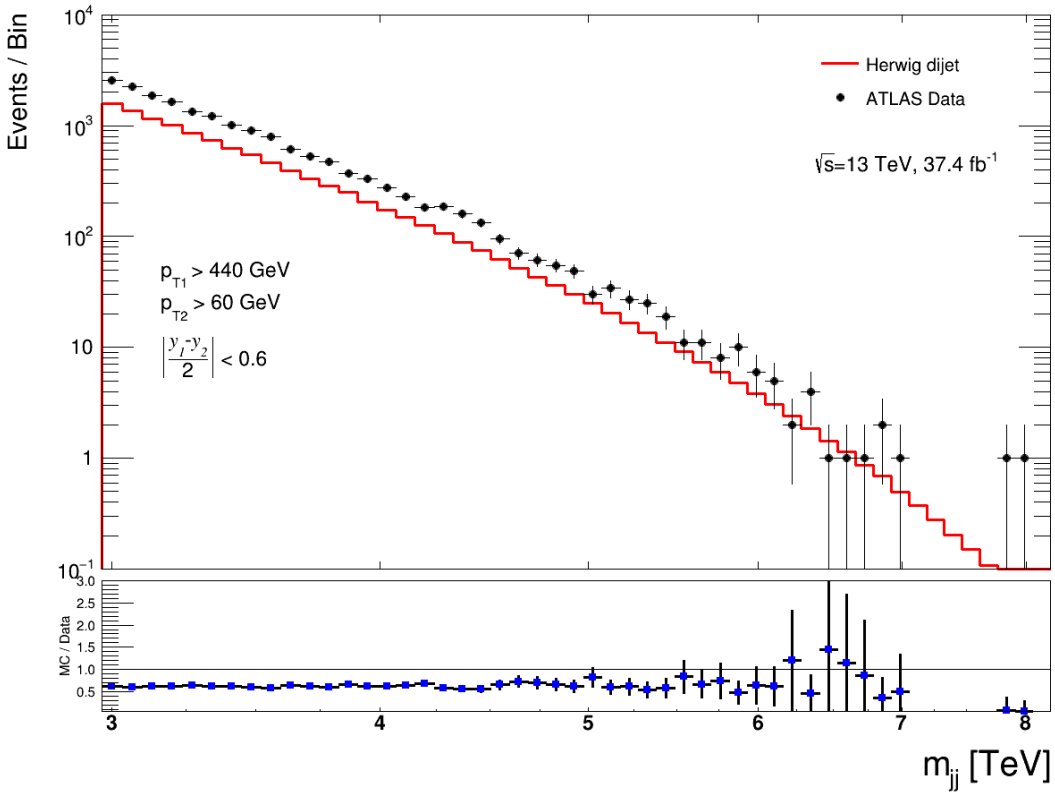

Figure 6.19: The reconstructed dijet mass distribution from HERWIG simulation of QCD processes for small-cone jets, $R = 0.4$, using events with $p_T > 440$ GeV for the leading and $p_T > 60$ GeV for the sub-leading jet satisfying $|y^*| < 0.6$. The data is taken from [100].

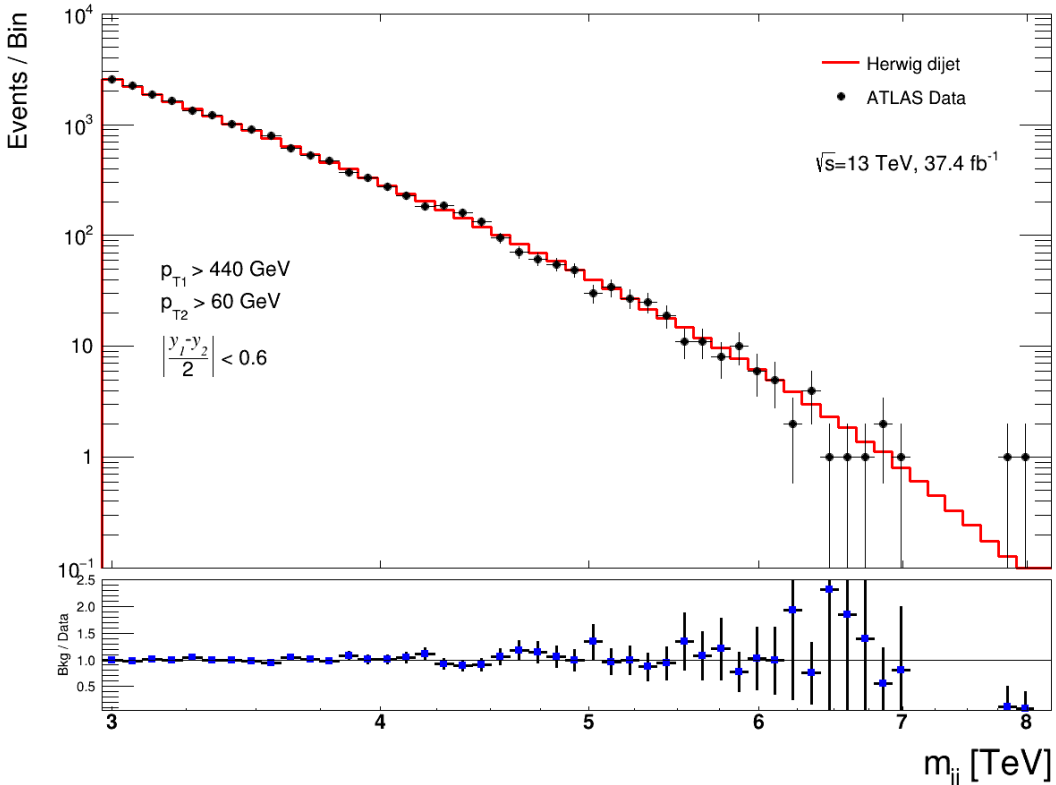

Figure 6.20: The reconstructed dijet mass distribution from HERWIG simulation after normalizing the HERWIG simulation to the data. The data is taken from [100].

PYTHIA and HERWIG Comparison

As was seen in the previous sections, both PYTHIA and HERWIG reproduce the shape of the data invariant mass distribution for the QCD multijet events. To normalize to data, PYTHIA is multiplied by 0.76 and HERWIG is multiplied by 1.61. Figure 6.21 shows the dijet mass distribution from both generators along with the data before normalization.

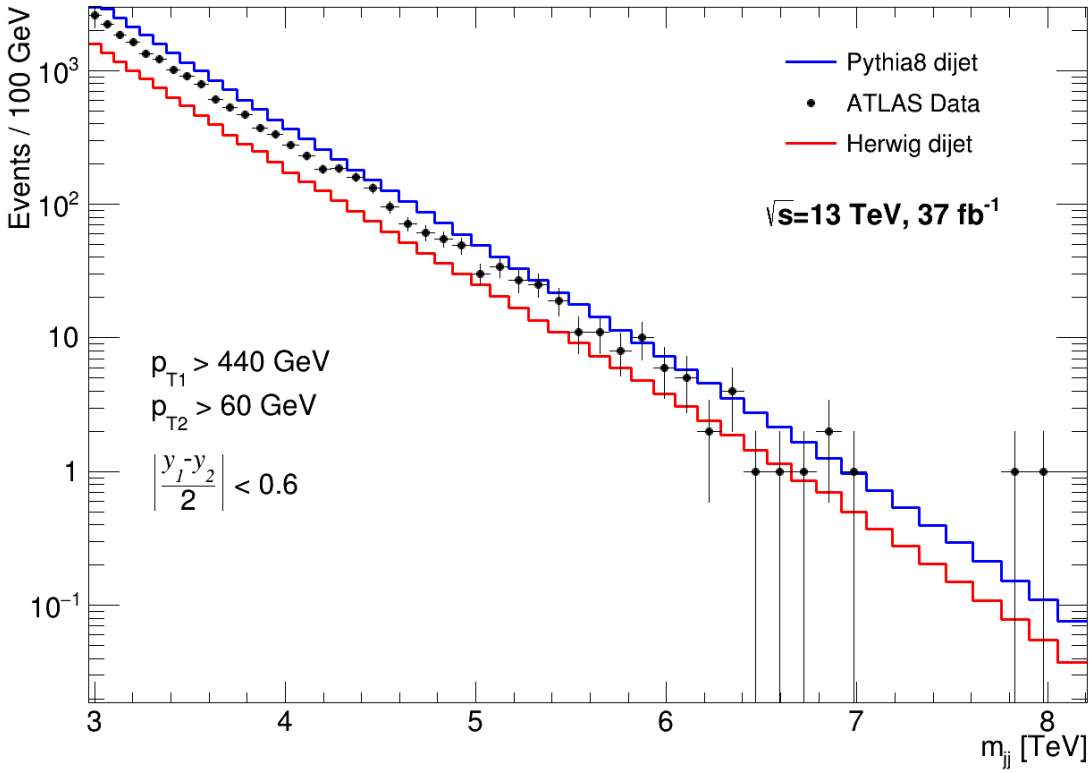

Figure 6.21: The reconstructed dijet mass distribution of HERWIG and PYTHIA simulation of the QCD dijet background along with the ATLAS data. The data is taken from [100].

A clearer comparison between the two simulations is shown in Figure 6.22, where the ratio of the number of events N_{PYTHIA} / N_{HERWIG} is plotted after normalizing each to the data.

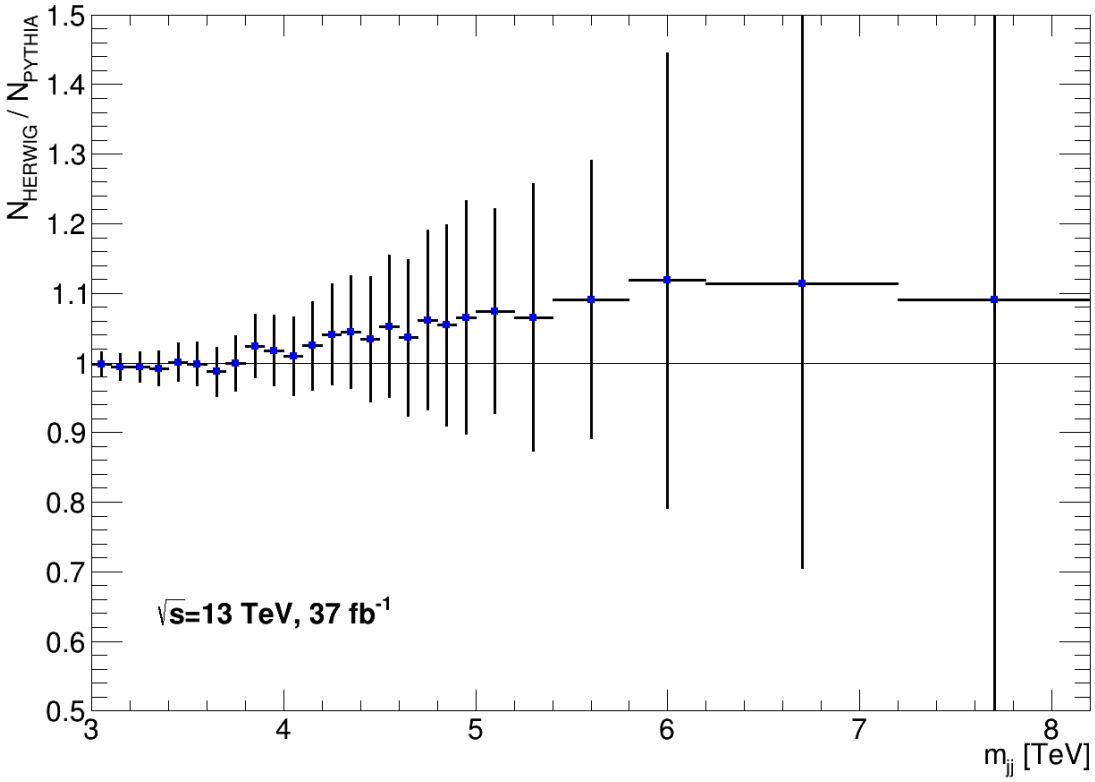

Figure 6.22: The ratio of Herwig to Pythia events after normalizing each distribution to the ATLAS data.

For Pythia, we have more entries compared to Herwig. To have less statistical uncertainty, we pick Pythia as our main generator and take the difference with Herwig as an estimate of systematic uncertainty due to the choice of generator, discussed in section 6.10.

6.8.2 Other Background Sources

We also considered three other backgrounds that might contribute to our signals, $t\bar{t}$ production, W + jets, Z + jets.

$t\bar{t}$ production is also simulated using the ATLAS A14 set of tune parameters using POWHEG, PYTHIA, and EvtGen (PhPy8EG) with a hdamp parameter of 258.75 (hdamp258p75) and all hadronic decays of $t\bar{t}$ (allhad). hdamp is a user parameter in Powheg which is a resummation scale (See Ref.[103] for more details). Like the QCD dijet background, the $t\bar{t}$ background is also sliced but in invariant mass of the top quarks at the parton level instead of p_T. The slices we have used in this study are 1.7 TeV - 2.0 TeV, and 2.0 TeV - 14.0 TeV. These slices do not have official names and we will simply refer to them as Slice1 and Slice2. Table 6.10 shows the basic information of these two slices.

Slice	Total number of events	Minimum mass (GeV)	Maximum mass (GeV)	σ (pb)	Filter efficiency	Acceptance (%)
Slice1	345830	1700	2000	7.2975e+02	4.2639E-04	0.005
Slice2	194150	2000	14000	7.2976E+02	2.4874E-04	0.7

Table 6.10: Basic information of the two slice for the $t\bar{t}$ production background.

About 0.7% of $t\bar{t}$ production events passed the hadronic event cuts and non passed the mixed event cuts. Figure 6.23 shows the dijet mass distribution of $t\bar{t}$ production. Neglecting the $t\bar{t}$ background means less than 1% background events compared to dijet in the 4.0-4.1 TeV mass bin and there are no events for masses above 5 TeV. In Figure 6.23, the small extra number of events in the range 4.2 - 4.4 TeV is not an indication of any new physics and is only due to small number of events.

The two background mentioned so far, QCD multijet and $t\bar{t}$ production, were expected to dominate in the hadronic decay mode. For mixed decays, W + jets and Z + jets were considered. Previous studies have recorded lepton+jet masses below 3 TeV [104]. More recent studies (ATLAS internal results at this point) using $\sqrt{s} = 13$ TeV and 140.4 fb^{-1} show no events above 4 TeV for Z + jets and only about two events in the range of 4.0-5.0 TeV for W + jets.

Hereafter, the only background source we will consider in our study is the QCD multijet.

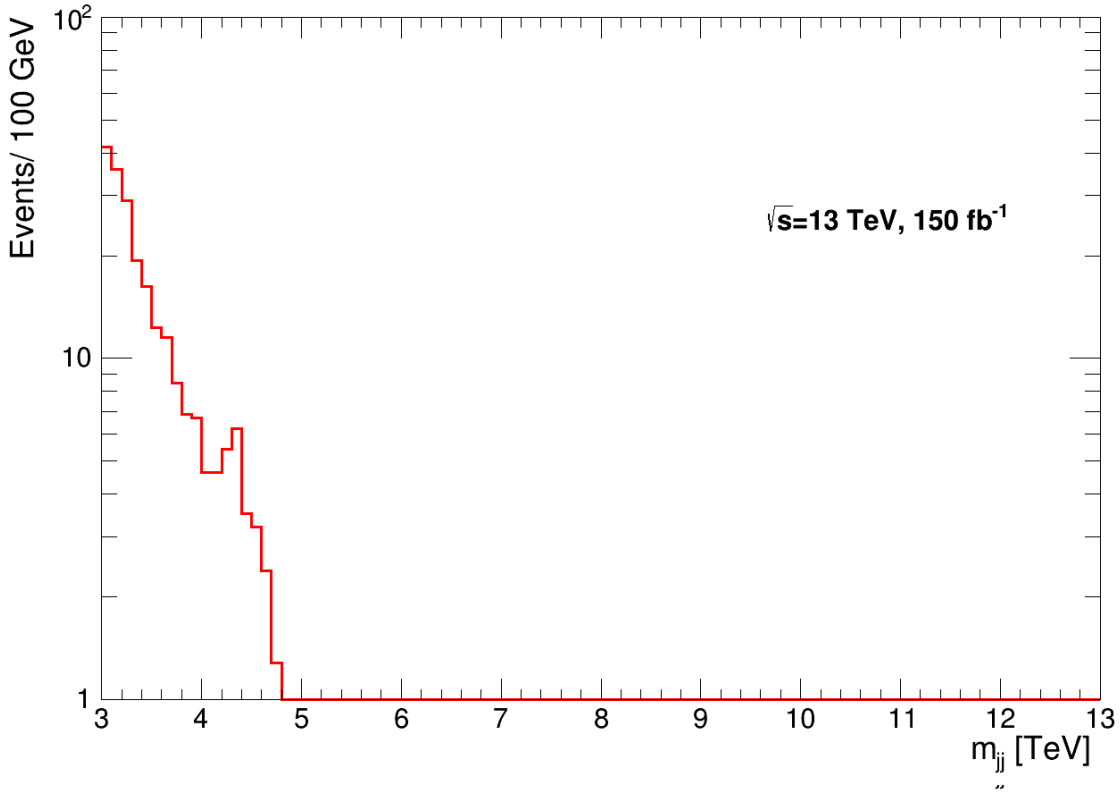

Figure 6.23: The reconstructed dijet mass distribution from $t\bar{t}$ production normalized to 150 fb^{-1} of data.

6.9 Event Selection Summary

In this section we summarize the effect of the object and event selection criteria on both signal and background. Table 6.11 shows the basic information of each slice of the background, for both Pythia and Herwig. Table 6.12 shows the basic information of different signal samples for all the models. These two tables also show the effect of the cuts discussed in Sec. 6.6 on each of the dijet p_T slices and signal samples. Since the background is multijet, very few events are passing the cuts designed to pick mixed decays of the QBH signal. Note that in Table 6.11 the individual weights of events are not considered for calculating the fraction, it's just the raw number of events passing the cuts.

	Sample	Total number of events	Weight (pb)	Fraction (%)	
				Hadronic	Mixed
PYTHIA	JZ4W	1.9970e+06	6.773e-05	0.0	0.0
	JZ5W	1.9995e+06	2.104e-06	1.9	0.00
	JZ6W	1.9970e+06	1.215e-07	10.4	0.02
	JZ7W	1.9965e+06	3.192e-09	22.1	0.04
	JZ8W	2.0000e+06	3.188e-09	27.7	0.05
	JZ9W	2.0000e+06	1.188e-10	36.1	0.05
	JZ10W	2.0000e+06	3.535e-12	43.2	0.05
	JZ11W	1.9990e+06	5.671e-14	49.0	0.04
	JZ12W	1.9975e+06	2.133e-16	53.1	0.03
HERWIG	JZ4	0.9800e+06	1.726e-03	0.0	0.0
	JZ5	0.9800e+06	3.286e-05	0.3	0.00
	JZ6	0.9840e+06	1.220e-06	7.8	0.01
	JZ7	0.9840e+06	9.388e-08	17.9	0.02
	JZ8	0.4920e+06	7.138e-09	29.6	0.04
	JZ9	0.4920e+06	2.747e-10	39.4	0.05
	JZ10	0.4890e+06	8.047e-12	47.4	0.06
	JZ11	0.4890e+06	1.186e-13	54.1	0.06
	JZ12	0.4902e+06	4.141e-16	58.5	0.06

Table 6.11: Basic information and the effect of the event selection cuts on each of the background slice, for both Pythia and Herwig. The weights of the p_T slices are defined as $W = \frac{\text{cross-section} \times \text{filter\_efficiency}}{\text{number of events}}$. The fractions are with respect to the whole sample, and not the two subsample created by the different topology cuts.

	Sample	Total number of events	Weight (pb)	Acceptance (%)	
				Hadronic	Mixed
ADD $n = 6$	4 TeV	1.0e+06	1.468e-07	47.7	9.8
	5 TeV	1.0e+06	2.282e-08	53.3	11.4
	6 TeV	1.0e+06	3.342e-09	56.6	12.6
	7 TeV	1.0e+06	4.240e-10	56.5	13.5
	8 TeV	1.0e+06	4.240e-11	60.5	14.2
	9 TeV	1.0e+06	2.904e-12	61.7	14.8
	9.5 TeV	1.0e+06	6.152e-13	62.2	15.0
	10 TeV	1.0e+06	1.065e-13	62.6	15.2
ADD $n = 4$	4 TeV	1.0e+06	3.488e-07	47.8	9.8
	5 TeV	1.0e+06	5.425e-08	53.3	11.2
	6 TeV	1.0e+06	7.942e-09	56.6	12.4
	7 TeV	1.0e+06	1.008e-09	59.0	13.2
	8 TeV	1.0e+06	1.008e-10	60.7	14.0
	9 TeV	1.0e+06	6.902e-12	61.8	14.6
	9.5 TeV	1.0e+06	1.462e-12	62.4	14.8
	10 TeV	1.0e+06	2.532e-13	62.7	15.1
ADD $n = 2$	4 TeV	1.0e+06	1.685e-07	47.9	9.8
	5 TeV	1.0e+06	2.582e-08	53.1	11.4
	6 TeV	1.0e+06	3.730e-09	56.5	12.6
	7 TeV	1.0e+06	4.673e-10	58.8	13.5
	8 TeV	1.0e+06	4.613e-11	60.4	14.2
	9 TeV	1.0e+06	3.117e-12	61.6	14.7
	9.5 TeV	1.0e+06	6.550e-13	62.2	15.0
	10 TeV	1.0e+06	1.125e-13	62.6	15.2
RS1	4 TeV	1.0e+06	1.435e-09	47.5	9.8
	5 TeV	1.0e+06	2.017e-10	53.0	11.3
	6 TeV	1.0e+06	2.688e-11	56.4	12.6
	7 TeV	1.0e+06	3.112e-12	58.8	13.4
	8 TeV	1.0e+06	2.822e-13	60.4	14.1
	9 TeV	1.0e+06	1.723e-14	61.6	14.7
	9.5 TeV	1.0e+06	3.398e-15	62.1	15.0
	10 TeV	1.0e+06	5.377e-16	62.6	15.2

Table 6.12: Basic information and the effect of the event selection cuts on each of the QBH signal samples for all the models. The weight is defined as $W = \frac{\text{cross-section}}{\text{number of events}}$. The acceptances are with respect to the whole sample, and not the two subsample created by the different topology cuts.

6.10 Background Uncertainties

As was discussed, the most dominant background comes from the QCD multijet. Now that we have an estimate of the background, we should try to find the uncertainty of the background. There are two sources of uncertainty:

- Statistical uncertainty of MC samples.
- Systematic uncertainty, which in our case, includes the theory modelling (generator difference), the emulated detector effects. We include the PDF difference in the theory modelling.

The subsequent sections describe these uncertainties.

6.10.1 Statistical Uncertainty

Because of the way that the QCD multijet process is sliced, the statistical uncertainty calculation needs explanation. For calculating the statistical uncertainty for the PYTHIA background, one should realize the two different weights used for the simulation of the background. First of all, each slice has its own weight which is $W_i = \frac{(\text{cross-section})_i \times (\text{filter efficiency})_i}{(\text{number of events})_i}$. No uncertainty on luminosity, cross-section, or filter efficiency is included. In addition to W_i, each event also has its own weight. To find the statistical uncertainty one should use the unweighted events first, and then scale the uncertainty with the same weight as the content itself. We denote the number of events excluding the individual weights as N, and N_w denotes the weighted events.

Instead of simply taking $\sqrt{N}$ as the uncertainty for a given N, we use the Feldman-Cousins method with CL = 68.27% which gives an asymmetric uncertainty, lower and upper limits. This method is accessible in the ROOT language [105] through the TFeldmanCousins() class. This class only works for $N < 36$, and so we switch back to $\sqrt{N}$ for $N \geq 36$ which has a 6% difference between the two methods at $N = 35$.

The calculation method for the upper and lower uncertainties are the same, and the only difference comes from the asymmetric value coming from the Feldman-Cousins method. For a given slice s in a given bin b [1] the unweighted (u) uncertainty $\sigma_{u_{sb}}$ is

$$\sigma_{u_{sb}} = \begin{cases} \sqrt{N_{sb}} & \text{if} \quad N_{sb} > 35 \\ \text{TFeldmanCousins}(N_{sb}) & \text{if} \quad N_{sb} < 35 \end{cases}. \tag{6.14}$$

[1] Not to be mistaken with s and b in the next chapter used for number of signal and background events.

Now that the uncertainty of the slice in the bin is found, it should be properly weighted. The first weight is the W mentioned above. The second one comes from the weights of the events contributing in that bin. Instead of following the weight of each event, we introduce an overall weight for the bin b which is

$$\alpha_{sb} = \frac{N_{w_{sb}}}{N_{sb}}. \tag{6.16}$$

This overall factor replaces all the individual weights. The weighted (w) uncertainty for bin b from slice s becomes

$$\sigma_{w_{sb}} = \sigma_{u_{sb}} \times W_s \times \alpha_{sb}. \tag{6.17}$$

The next step is to combine all the slices for the given bin yielding the final uncertainty

$$\sigma_{w_b} = \sqrt{\sum_s (\sigma_{w_{sb}})^2}. \tag{6.18}$$

6.10.2 Systematic Uncertainty

One of the systematic uncertainties is the choice of a generator. Pythia and Herwig produce similar results and since we have better statistics for Pythia, it will be chosen as our main generator. We use the difference between Pythia and Herwig as an uncertainty. We apply the same cuts as used for the QBH signal to the background simulated by both Pythia and Herwig. Because we want to find the difference coming directly from the generators, we exclude the detector effects. Then we take the ratio of the two and fit a second order polynomial to them. The difference from unity is introduced as a relative uncertainty. Figure 6.24 shows the comparison of the two generators for each decay mode and their ratio with the curve of best fit. This uncertainty ranges from about 1% for the 4 TeV sample to about 16% for the 10 TeV sample.

Another contribution to the systematic uncertainty comes from the emulated detector effects, i.e JER and JES uncertainty. First, for including JER and its uncertainty, we run the same event selection and event reconstruction algorithm thousands of times (pseudo-experiments). The reason for this is that for a given truth level jet, the jet p_T has a Gaussian distribution and running the algorithm just once only samples the distribution once. This effect is reduced by the number of events since similar events are simulated. Since we will be using counting experiments for the potential discovery, we count the number of background events above the threshold masses for a given QBH signal. The number of background events is the average value of the pseudo-experiments, and its 1 σ deviation is included as an uncertainty on the background due to JER and its uncertainty. Appendix I shows the

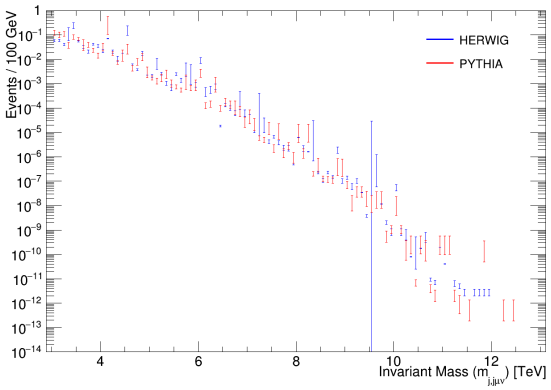

(a) Mixed background

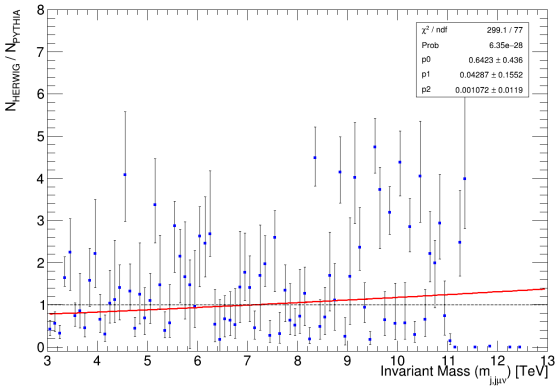

(b) Mixed fit

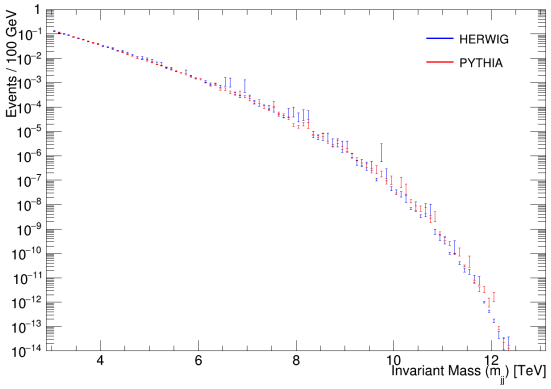

(c) Hadronic background

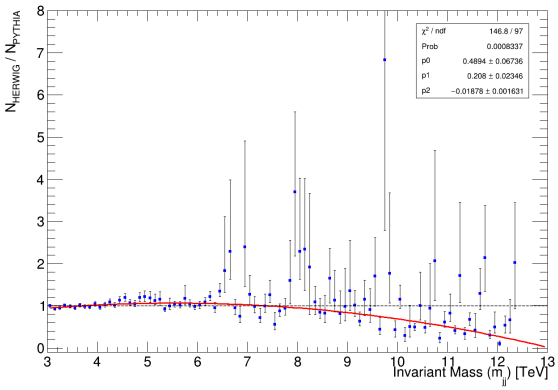

(d) Hadronic fit

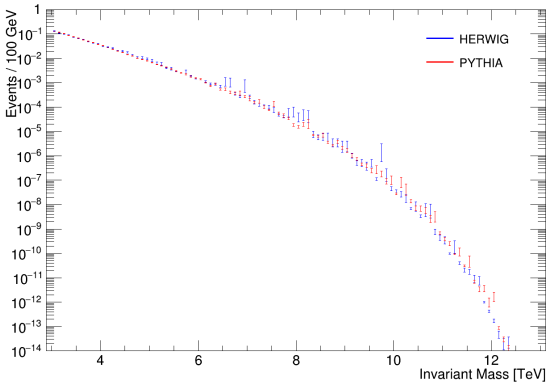

(e) All background

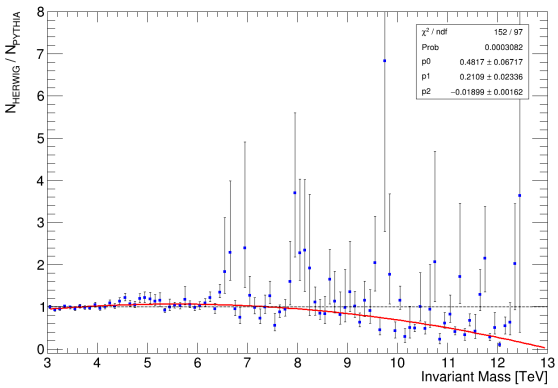

(f) All fit

Figure 6.24: The comparison of Pythia and Herwig for each decay mode and a second order polynomial fit to their ratio.

distribution of the number of events for each decay mode and threshold mass of the QBH

sample and also the background. This uncertainty in negligible (less than 1%) for the entire range, except in the case of mixed decays.

Similar to JER uncertainty, we use pseudo-experiments for JES uncertainty. We scale the p_T of the jet, both up and down, based on the JES uncertainty. The difference between the number of events between the two cases, the average number of events with including the JES uncertainty and not including JES uncertainty, is another systematic uncertainty of the background. This uncertainty ranges from about 7% for the 4 TeV sample to about 59% for the 10 TeV sample.

Figure 6.25 shows the background contribution for each decay mode with the statistical and systematic uncertainty. Note that only the systematic uncertainty of the theory modelling is done bin-by-bin and the JER and JES uncertainty are calculated for the number of events above a threshold mass. Appendix L shows the contribution of the different background uncertainties for each decay mode and threshold mass.

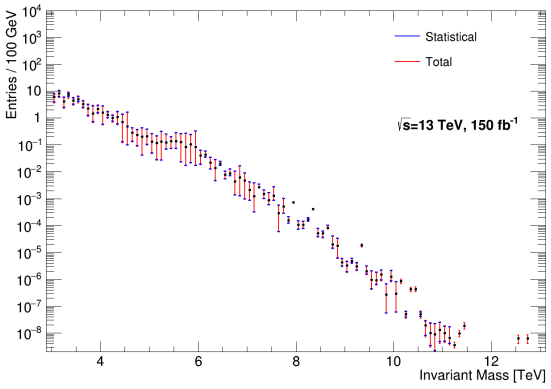

(a) Mixed

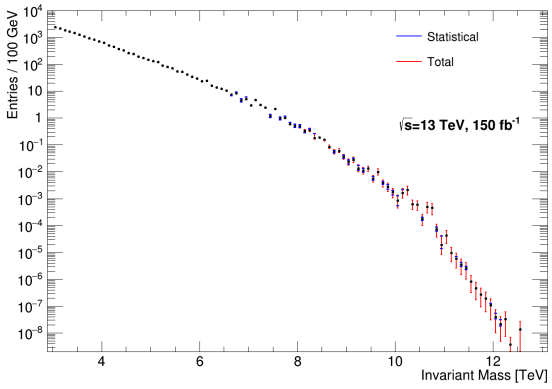

(b) Hadronic

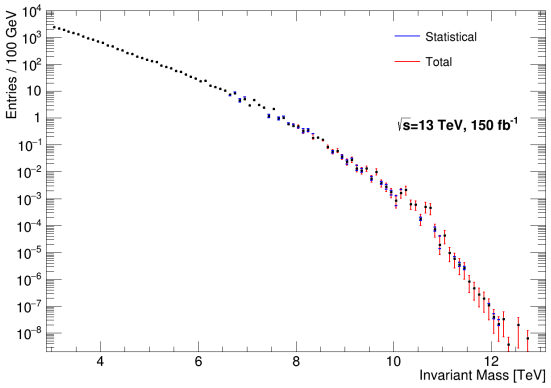

(c) All

Figure 6.25: Background contribution to each decay mode with statistical and total uncertainty.

Chapter 7

Results

In this chapter we present the results of the discovery potential on QBH threshold mass at the LHC and the 95% CL upper limit on the quantum black hole production cross-section times BR times A times ϵ, and production cross-section.

7.1 Discovery Potential

Figure 7.1 shows the mass distribution of each ADDn6 signal sample including detector effects, for all the topologies along with the background. The distributions are normalized to a luminosity of 150 fb^{-1}. The normalization factors make it possible for the number of events to be non-integer which is not physical. As an example, Figure 7.1d shows the same distribution as Figure 7.1c with rounding the number of events in each bin to the nearest integer number. Appendix J shows the mass distribution of the QBH signal samples and the background in different topologies for all the models.

For calculating the discovery significance of signal above background, different statistical methods can be used, such as Gaussian approximation, Poisson model, Poisson-Poisson and Poisson-Gaussian model with asymptotic formulae. All these have been studied and compared [106]. The results are shown in Ref. [106] where it is suggested to use the Poisson-Poisson model. In a counting experiment, the likelihood function then takes the form [107]

$$\mathcal{L}(s,b) = \text{Pois}(n|s+b)\,\text{Pois}(m|\tau b)\,, \tag{7.1}$$

where n, s, and b are the number of observed events, number of expected signal events, and number of expected background events. We take s to be known and take b as a nuisance parameter. Since we are not using data, we use $n = s+b$. $s = 0$ is referred to as background-only or null hypothesis. The second Poisson distribution is another set of measurements, called control measurement. It is used to constraint the nuisance parameter(s) which is often taken to be the background uncertainty. $\tau = \frac{b}{\sigma^2}$ where σ is the absolute background

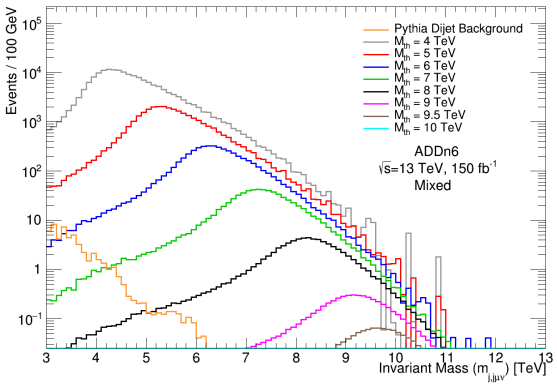

(a) Mixed $(j, j\mu\nu)$

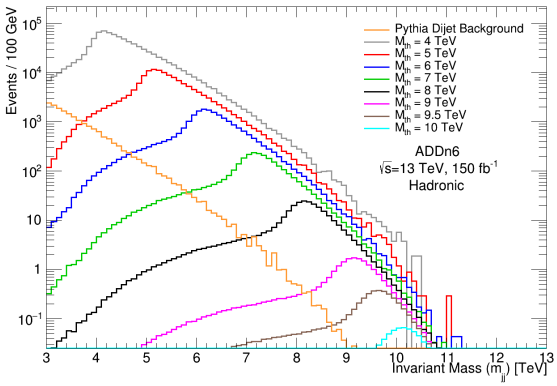

(b) Hadronic (jj)

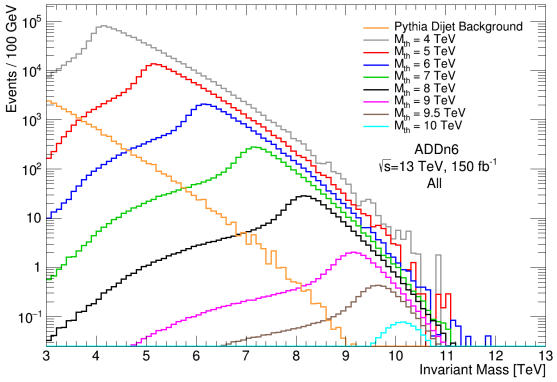

(c) All

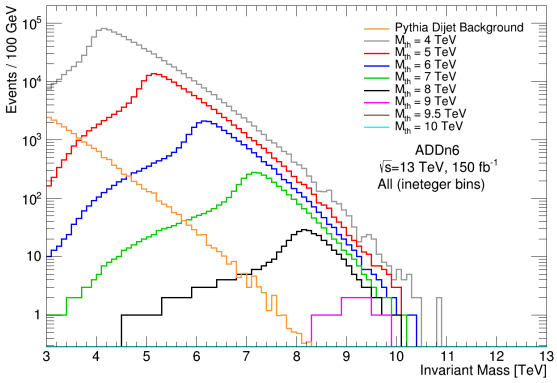

(d) All (integer bins)

Figure 7.1: The reconstructed mass distribution of the QBH signal and PYTHIA QCD dijet background using **(a)** mixed, **(b)** hadronic, and **(c)** all the decays. **(d)** shows the same distribution as **(c)** with rounding the bin content of the signal in each bin to the nearest integer value. The results are for the ADDn6 model.

uncertainty. The profile likelihood ratio

$$\lambda(s) = \frac{\mathcal{L}\left(s, \hat{\hat{b}}\right)}{\mathcal{L}\left(\hat{s}, \hat{b}\right)}, \tag{7.2}$$

is often used to test a hypothesized value of s [107]. $\hat{\hat{b}}$ is the value of b which maximizes $\mathcal{L}$ for a given value of s (conditional). $\hat{s}$ and $\hat{b}$ maximize the $\mathcal{L}$ for the general case (unconditional). They are often referred to as maximum likelihood estimators (ML estimators). For

a discovery potential, the test statistic

$$q_0 = -2 \ln \lambda (0) , \tag{7.3}$$

is used (given $\hat{s} = n - b > 0$). It is to check the theory against the background-only (or null) hypothesis. The p-value is then found from

$$p_0 = \int_{q_{0,\text{obs}}}^{\infty} f (q_0|0) \, dq_0, \tag{7.4}$$

where $f (q_0|0)$ is the probability distribution function (p.d.f) of q_0 under the null hypothesis and $q_{0,\text{obs}}$ is the observed value of q_0 from data. The p-value is usually converted to a significance level using

$$Z = \Phi^{-1} (1 - p) , \tag{7.5}$$

where Φ^{-1} is the quantile of the standard Gaussian distribution. The significance can also be directly found from q_0 via [106, 107]:

$$Z = \sqrt{q_0} = \sqrt{2 \left((s + b) \ln \left[\frac{(s + b) (b + \sigma_b^2)}{b^2 + (s + b) \sigma_b^2} \right] - \frac{b^2}{\sigma_b^2} \ln \left[1 + \frac{\sigma_b^2 s}{b (b + \sigma_b^2)} \right] \right)}. \tag{7.6}$$

Note that σ_b is the total uncertainty. the statistical and systematic uncertainties for each mass bin are added in quadrature. The different systematic uncertainties are due to orthogonal sources and have been added in quadrature. Recall that we are using counting experiments and s, b, and σ_b are the sum of the events and uncertainties above the threshold mass. When summing the uncertainties in each mass bin, we add them linearly since the cumulative mass bins are highly correlated with the same events. Also, since Z takes the absolute uncertainty, we cannot use asymmetric uncertainties. So, we take the larger of the two as σ_b. Appendix K shows a detailed derivation of Equation 7.6.

The usual value for Z for considering a discovery is $Z \geq 5\sigma$ (p-value $< 2.9 \times 10^{-7}$). The statistical significance is a way of quantifying that the observed events are due to a new phenomenon and not background fluctuations. $Z \geq 5\sigma$ means that the probability that the observed events are due to background fluctuation is the same or smaller than the probability of observing a value of a Gaussian statistic five standard deviation away from its mean. This is a probability of 5.7×10^{-7} or 2.9×10^{-7} depending on if one uses a deviation from the mean or a one-sided fluctuation [108]. In simpler words, it declares a new phenomenon with 99.99994% confidence. $Z \geq 5\sigma$ can also happen if the background and signal both are small. Usually, another condition is imposed on the number of observed events, $s \geq 10$. So, for a

potential discovery, we should have

$$\begin{aligned} s &\geq 10 \text{ and,} \\ Z &\geq 5. \end{aligned} \tag{7.7}$$

With the condition on the significance, we make sure that the signal can be detected above the background and then with the condition on s we make sure that there are enough signal events so that it can be seen in the experiment.

Figure 7.2 shows the number of signal and background events, the relative and absolute background uncertainty and the significance of each decay mode of the signal samples using a Poisson-Poisson model and also the minimum required luminosity so that the signal sample would satisfy Equation 7.7. Over the entire mass range, the minimum required luminosity is determined by satisfying the condition on the number of signal events which is expected since, in all decay modes of all the samples, the signal is significantly above the background.

Table 7.1 shows the number of signal and background events, background uncertainty and the significance for each signal sample. It also shows the minimum required luminosity for each decay mode of each signal sample to satisfy Equation 7.7.

Although the lower mass threshold samples have high significance and signal events, these regions have been well probed, and no QBH signal has been observed [4, 104]. The ATLAS dijet analysis [4] has excluded QBH production decaying to all quark final states with threshold mass below 8.9 TeV for the ADDn6 model.

With the total integrated luminosity of 150 fb^{-1} of the LHC run 2, 9.14 TeV is the highest mass threshold we can hope to be able to find a QBH signal decaying to tt using fully- and semi-hadronic topologies. With the coming HL-LHC, 9.98 TeV threshold mass would be detectable. Table 7.2 shows the highest detectable mass using an integrated luminosity of 150 fb^{-1} and 3000 fb^{-1} for each decay mode and each model.

QBHs in the ADD model with different number of extra dimensions, behave very similar. Since the cross-sections of the QBH signals are big and the signals are well above the background, the highest detectable threshold mass is only set by the condition $s \geq 10$. For this reason, the combined topology is more favourable because it provides more signal events. This is different for the RS1 model. Since the cross-section is smaller than those in the ADD model, the number of signal events are close to the number of background events ($s \approx b$). As such, the criterion $Z \geq 5$ also becomes important. Since the hadronic topology has the biggest background, the hadronic topology is not favourable in this model, and the semi-hadronic topology is the more favourable topology.

Appendix L shows the number of background events and different contributions to the

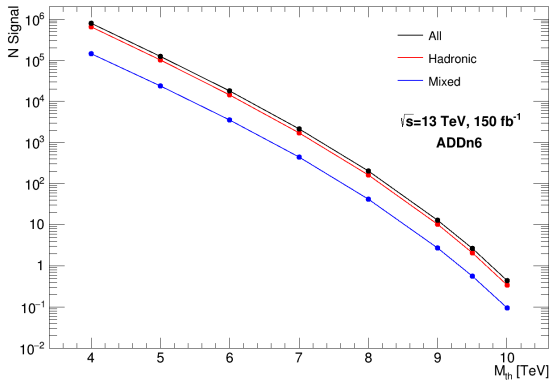

(a) Number of signal events

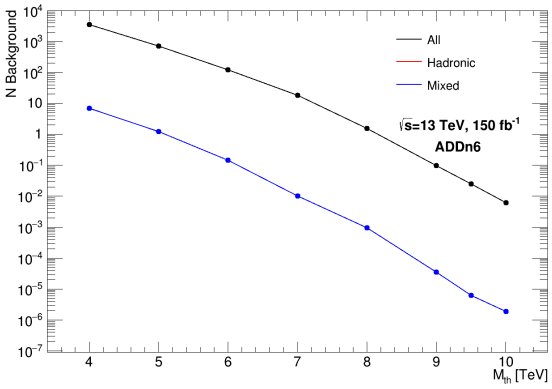

(b) Number of background events

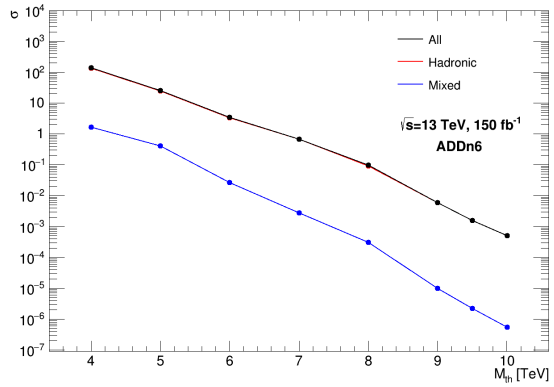

(c) Absolute background uncertainty

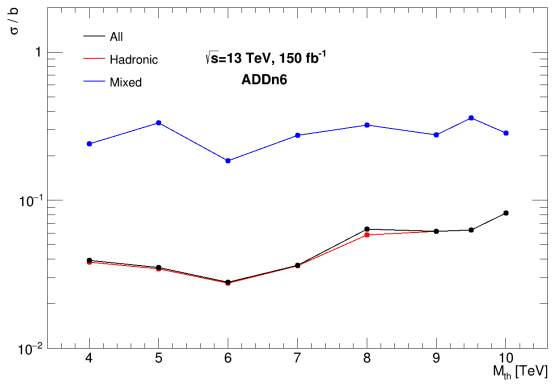

(d) Relative background uncertainty

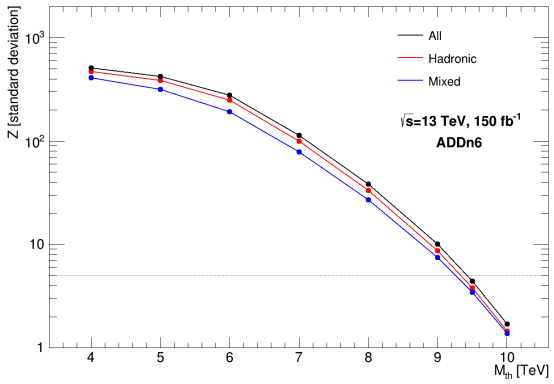

(e) Significance

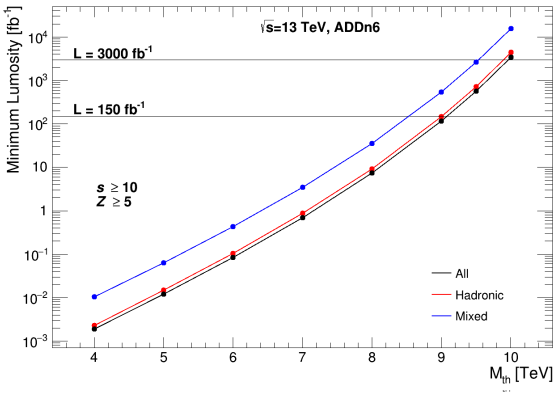

(f) Minimum required luminosity

Figure 7.2: Number of **(a)** signal and **(b)** background events, **(c)** absolute and **(d)** relative background uncertainty, **(e)** significance, and **(f)** the minimum required luminosity to satisfy potential discovery criteria, for each decay mode of each QBH sample. In **(b)**, the red curve is under the black curve. Results are for the ADDn6 model.

background uncertainty for each decay mode. Appendix M shows the number of signal events, and statistical and systematic uncertainties of the QBH signals for the different threshold mass and models.

M_{th} [TeV]	Decay Mode	s	b	σ_b	Z	L_{min} [fb^{-1}]
4.0	Mixed	1.4360e+05	6.9734e+00	1.68e+00	3.0235e+02	1.0446e-02
	Hadronic	6.4863e+05	3.5055e+03	1.34e+02	2.5746e+02	2.3126e-03
	All	7.9223e+05	3.5238e+03	1.38e+02	2.7050e+02	1.8934e-03
5.0	Mixed	2.3574e+04	1.2377e+00	4.13e-01	2.1445e+02	6.3629e-02
	Hadronic	1.0052e+05	7.2235e+02	2.48e+01	1.3786e+02	1.4923e-02
	All	1.2409e+05	7.2496e+02	2.56e+01	1.5021e+02	1.2088e-02
6.0	Mixed	3.5129e+03	1.4491e-01	2.68e-02	1.2822e+02	4.2700e-01
	Hadronic	1.4277e+04	1.2305e+02	3.39e+00	1.0115e+02	1.0507e-01
	All	1.7790e+04	1.2332e+02	3.44e+00	1.1205e+02	8.4319e-02
7.0	Mixed	4.3703e+02	1.0239e-02	2.80e-03	6.7508e+01	3.4323e+00
	Hadronic	1.7260e+03	1.8540e+01	6.68e-01	4.5639e+01	8.6906e-01
	All	2.1630e+03	1.8550e+01	6.74e-01	5.1318e+01	6.9347e-01
8.0	Mixed	4.2297e+01	9.4671e-04	3.04e-04	2.4734e+01	3.5463e+01
	Hadronic	1.6188e+02	1.5598e+00	9.08e-02	2.5122e+01	9.2659e+00
	All	2.0418e+02	1.5607e+00	9.95e-02	2.8429e+01	7.3464e+00
9.0	Mixed	2.7632e+00	3.5230e-05	9.80e-06	7.2740e+00	5.4285e+02
	Hadronic	1.0235e+01	9.6312e-02	5.95e-03	8.3480e+00	1.4655e+02
	All	1.2999e+01	9.6347e-02	5.95e-03	9.6279e+00	1.1540e+02
9.5	Mixed	5.6853e-01	6.1629e-06	2.20e-06	3.4184e+00	2.6384e+03
	Hadronic	2.0719e+00	2.5348e-02	1.60e-03	3.6918e+00	7.2399e+02
	All	2.6404e+00	2.5354e-02	1.60e-03	4.2847e+00	5.6810e+02
10.0	Mixed	9.5751e-02	1.9039e-06	5.00e-07	1.3688e+00	1.5666e+04
	Hadronic	3.4066e-01	6.1901e-03	5.09e-04	1.4387e+00	4.4033e+03
	All	4.3641e-01	6.1920e-03	5.09e-04	1.6849e+00	3.4372e+03

Table 7.1: Number of signal (s) and background (b) events, absolute background uncertainty (σ_b), significance (Z), and the minimum required luminosity (L_{min}) for each decay mode of each signal sample to satisfy Equation 7.7. The minimum required luminosity is determined by the number of signal events for all decay modes over all mass ranges. The results are for the ADDn6 model.

Model	Decay mode	M_{th} [TeV]	
		$L = 150$ fb^{-1}	$L = 3000$ fb^{-1}
ADD $n = 6$	Mixed	8.81	9.57
	Hadronic	9.01	9.95
	All	9.14	9.98
ADD $n = 4$	Mixed	8.50	9.37
	Hadronic	8.92	9.77
	All	8.95	9.84
ADD $n = 2$	Mixed	7.87	8.94
	Hadronic	8.33	9.32
	All	8.48	9.38
RS1	Mixed	6.18	7.69
	Hadronic	4.73	7.03
	All	4.88	7.30

Table 7.2: Maximum detectable QBH mass threshold using 150 fb^{-1} and 3000 fb^{-1} for each decay mode and model.

7.2 Limit Study

In this section, we will put limits on the $\sigma \times \epsilon \times A \times BR$, and σ of the QBH$_{4/3}$ decaying to tt as a function of threshold mass and QBH$_{4/3}$ in general. The considered models are ADD models with $n = \{2, 4, 6\}$ and RS1 model. This study uses the results of ATLAS dijet analysis [4].

As mentioned previously, in Ref. [4], the m_{jj} distribution is reconstructed from events where the p_T of the leading (sub-leading) jet is $p_T > 440(60)$ GeV. The rapidity difference of the two leading jets should also satisfy $|y^*| = |(y_1 - y_2)/2| < 0.6$. Since we are using a cut-and-count method, we also require $M_{jj} > M_{th}$ for different values of M_{th} which reduces A.

Figure 7.3 shows the distribution of data points and the fit function taken from [4].

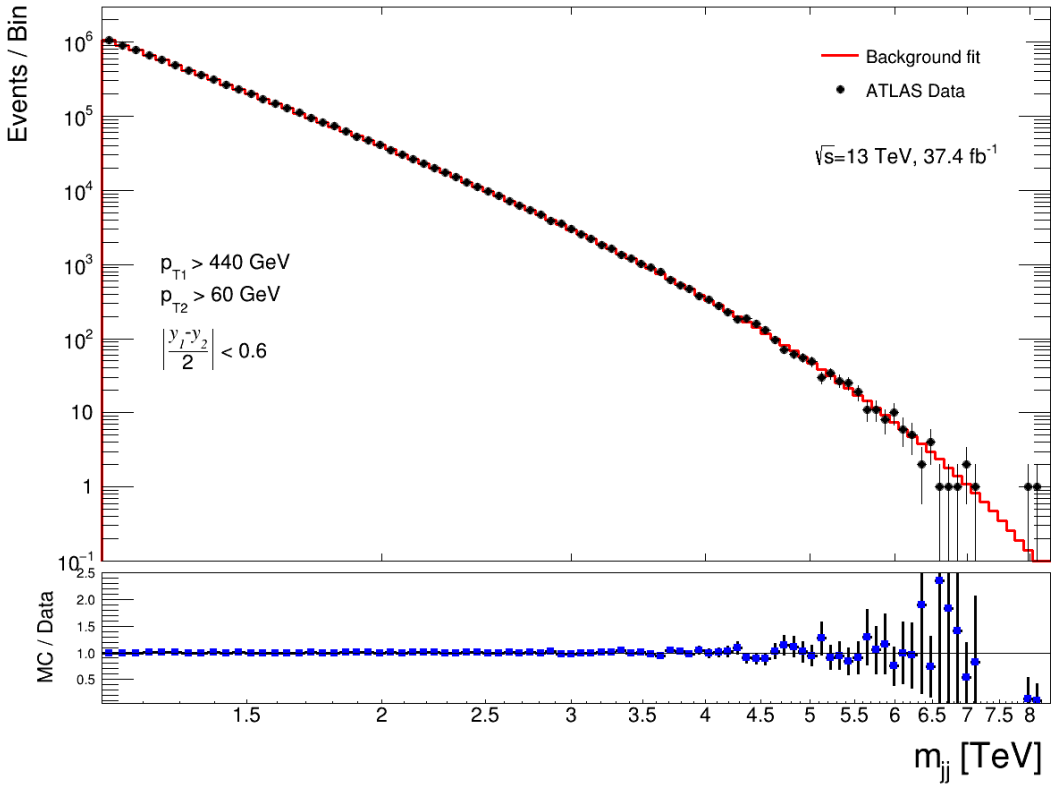

Figure 7.3: The dijet mass distribution of events with $p_T > 440$ GeV for the leading and $p_T > 60$ GeV for the sub-leading jet satisfying $|y^*| < 0.6$. Both the data and background fit are taken from [100].

For setting a 95% CL upper limit of the quantities mentioned above, we use the Frequentist CL_s method. For this study, the same profile likelihood ratio as Equation 7.2 is used with the condition $\hat{s} \leq s$. But in this case, another form of p-value and threshold is used. The p-value used for the limit setting is defined as

$$CL_s = \frac{CL_{s+b}}{CL_b} = \frac{p_{s+b}}{1 - p_b}, \tag{7.8}$$

where CL_{s+b} is the p-value of the signal+background hypothesis and CL_b is one minus the p-value of the background-only hypothesis. The p-values are found in the same way as

Equation 7.4, meaning

$$p_{s+b} = \int_0^{q_{\text{obs}}} f\,(q|s+b)\,dq, \tag{7.9}$$

$$1 - p_b = \int_0^{q_{\text{obs}}} f\,(q|b)\,dq. \tag{7.10}$$

The p-value threshold used in most studies is $\alpha \leq 0.05$ where α is also called the size of the test. The confidence level is $CL = 1 - \alpha$. A 95% CL limit corresponds to the biggest value of s (often referred to as s_{up}) for which $CL_s \leq 0.05$. So, any model predicting $s > s_{up}$ will be excluded. In the case of no data

$$CL_s = \frac{e^{-(s+b)}}{e^{-b}} = e^{-s} \qquad \Rightarrow \qquad s = -\ln CL_s, \tag{7.11}$$

which for the 95% CL limit

$$s_{\text{up}} = -\ln 0.05 \approx 3. \tag{7.12}$$

The CL_s method cannot set a lower limit on s_{up} than $s_{up} < 3$ when there is no data.

The number of data (signal+background) and background events are modeled with Poisson distributions and the systematic uncertainties (nuisance parameters) of signal or background are modeled with the convolution of Gaussian p.d.fs (no correlation matrix is used). The systematic uncertainties of the background are taken from the ATLAS dijet analysis [4] which correspond to the choice of the fit function and the uncertainty of the fit parameters. There is a 2% uncertainty for the luminosity recorded by ATLAS detector [109]. Note that in Hepdata [100], the absolute uncertainties are given for each bin. Since we are using cut-and-count method, we sum the uncertainties in each mass bin linearly since the cumulative mass bins are highly correlated with the same events.

The uncertainties of the signal are those related to A and ϵ. Figure 7.4 shows the A and ϵ of the considered models as a function of threshold mass. The ϵ increases with M_{th} since the leading jet p_T increase with M_{th}. A decreases with M_{th} because of the mass cut. The peak of the distribution is at M_{th} and can only extend to 13 TeV. With increasing mass, the area above the M_{th} decreases and so does A.

The uncertainty of ϵ due to the JER and JES uncertainties is negligible ($< 1\%$). The statistical uncertainty on the determination of ϵ is also negligible and ignored. The significant uncertainty related to the signal is the uncertainty of A from the uncertainties of JER and JES.

First, we will consider the uncertainty of A due to the JER uncertainty. In Appendix N, Figure N.1 shows the mass distribution of QBH samples with and without applying the

nominal JER. Figure N.2 shows the mass distribution of QBH samples with applying the nominal JER and JER uncertainties. Figure 7.5a shows the acceptance of QBH samples with applying nominal JER value and JER ± JER uncertainty. Figure 7.5b shows the uncertainty of A due to JER uncertainty.

Although we are using truth jets and should not apply any JES, the JES uncertainty should be considered. Figure N.3 in Appendix N shows the mass distribution of QBH samples with applying JES uncertainty. Note that nominal JER is considered to already be applied to the jets in this case. Figure 7.6a shows the acceptance of QBH samples with applying nominal JER value and JES uncertainty. Figure 7.6b shows the uncertainty of A due to JES uncertainty. These uncertainties are calculated from using the ADDn6 model. Since the different models have very similar mass distributions, Appendix H, we use the same results for all the models.

The BR is the same for all the models and all the QBH mass threshold samples. Based on the QBH generator, BR can have two values. In the QBH generator, the global symmetries, like baryon and lepton number, can be violated (V) or kept conserved (C). If the global symmetries can be violated, $QBH_{4/3}$ can decay both to an anti-lepton and an anti-down-type quark, and two up-type quarks with a probability of 1/3 and 2/3, respectively. So, the BR of $QBH_{4/3} \to tt$ can be either $\frac{1}{9}$ for conserved or $\frac{2}{3} \times \frac{1}{9}$ for violated. The factor of $\frac{1}{9}$ comes from the fact that tt is one combination out of nine possible combinations for the two outgoing up-type quarks. If global symmetries can be violated, $\frac{1}{3}$ of the times the QBH decays to an anti-lepton and anti-down-type quark while the rest of the time it decays to up-type quark, hence the extra factor of $\frac{2}{3}$.

Recall that because we are using a cut-and-count method, limits for each cumulative mass bin are highly correlated. The dataset for each cumulative mass bin is not unique and includes the events of each mass bin above the given mass bin.

Figure 7.7 shows the 95% CL upper limit of $\sigma \times A \times BR \times \epsilon$ for $\mathrm{QBH}_{4/3} \to tt$ in the ADD model with $n = \{2, 4, 6\}$ and the RS1 model, and Figure 7.8 shows the 95% CL upper limit on σ. The expected values quantify the sensitivity of the experiment and the $\pm N\sigma$ bands are the error bands obtained by varying $\hat{s}$ (see Equation 7.2) by $\pm N\sigma$ around $\hat{s}$ [107]. The numerical values are collected in Table 7.4. Note that in the CL_s method, if there is no uncertainty, when number of data events is greater than the number of background events, the observed limit is higher than the expected and vise versa. If the number of events are equal, so are the observed and expected limits. In the presence uncertainties, this rule may not hold. Our observed exclusion limits are biased and give slightly lower limits than expected for all the mass bins, except the last one.

M_{th}	Data	Background	Absolute (relative %) fit function uncertainty	Absolute (relative %) fit parameter uncertainty	Absolute (relative %) JER uncertainty	Absolute (relative %) JES uncertainty
4.03	2027.0	2020.9	± 0.94 (0.05)	± 36.1 (1.8)	$^{+8.7(0.4)}_{-5.5(0.3)}$	$^{+81.6(4.0)}_{-92.4(4.6)}$
4.55	663.0	670.0	± 0.87 (0.13)	± 19.6 (2.9)	$^{+3.6(0.5)}_{-2.8(0.4)}$	$^{+31.1(4.6)}_{-35.7(5.3)}$
5.02	249.0	249.7	± 0.79 (0.32)	± 11.1 (4.4)	$^{+1.6(0.6)}_{-1.4(0.5)}$	$^{+13.0(5.2)}_{-15.0(6.0)}$
5.54	84.0	87.3	± 0.65 (0.74)	± 5.7 (6.5)	$^{+0.6(0.7)}_{-0.6(0.6)}$	$^{+5.1(5.8)}_{-6.0(6.9)}$
5.99	35.0	34.7	± 0.58 (1.67)	± 3.0 (8.6)	$^{+0.3(0.8)}_{-0.3(0.7)}$	$^{+2.2(6.4)}_{-2.6(7.6)}$
6.59	8.0	9.7	± 0.36 (3.70)	± 1.1 (11.8)	$^{+0.1(1.0)}_{-0.1(0.8)}$	$^{+0.7(7.2)}_{-0.8(8.6)}$
6.98	5.0	4.1	± 0.23 (5.64)	± 0.6 (13.9)	$^{+0.05(1.1)}_{-0.03(0.8)}$	$^{+0.3(7.8)}_{-0.4(9.3)}$
7.54	2.0	1.11	± 0.10 (9.45)	± 0.2 (17.0)	$^{+0.015(1.4)}_{-0.01(0.8)}$	$^{+0.10(8.9)}_{-0.12(10.7)}$
7.98	2.0	0.31	± 0.04 (13.38)	± 0.06 (19.2)	$^{+0.005(1.6)}_{-0.003(0.9)}$	$^{+0.03(9.7)}_{-0.04(11.8)}$

Table 7.3: The cumulative number of data and background events and the systematic uncertainties with $m_{jj} \geq M_{\text{th}}$ using results of Ref .[4] given in Hepdata [100]. The systematic uncertainties of fit function and fit parameter are symmetric while JER and JES uncertainties or not. The luminosity uncertainty is 2% and the same for all mass points.

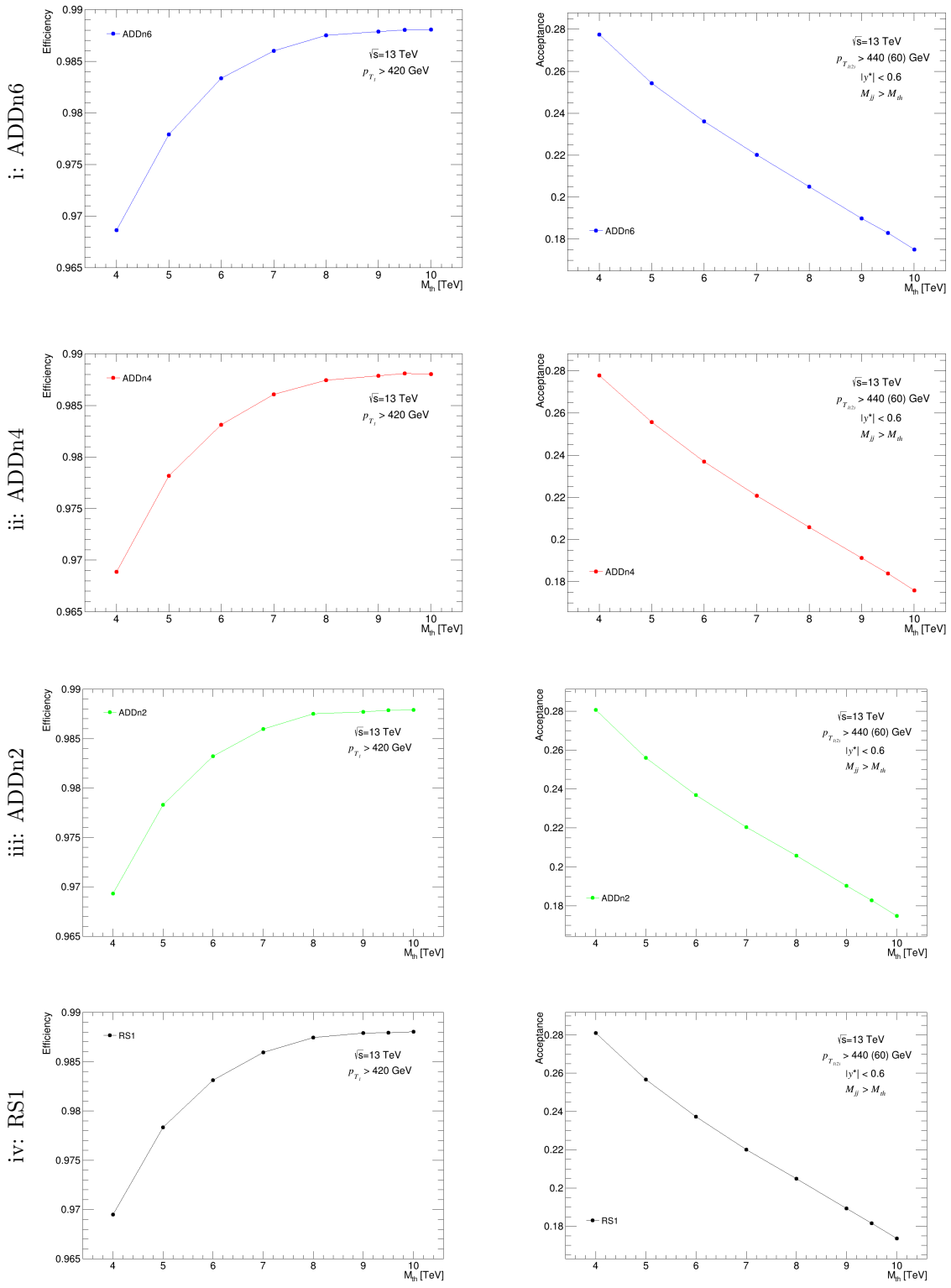

(a) Trigger efficiency **(b)** Acceptance

Figure 7.4: Trigger efficiency and acceptance of QBH samples in ADD models with $n = \{2, 4, 6\}$ and RS1 model. The two columns from left to right show **(a)** the trigger efficiency, and **(b)** the acceptance. The four rows are the **(i)** ADDn6, **(ii)** ADDn4, **(iii)** ADDn2, and **(iv)** RS1 models.

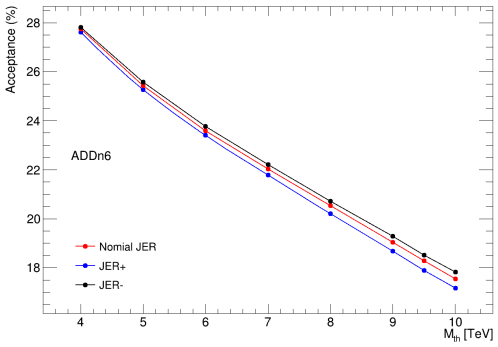

(a) Acceptance

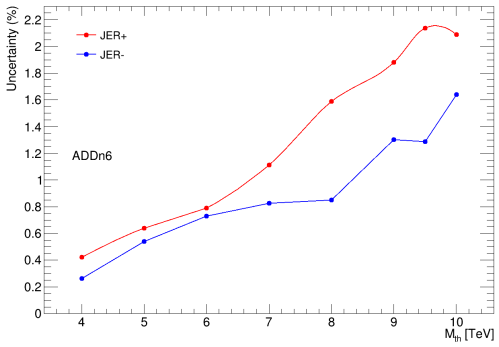

(b) Acceptance uncertainty

Figure 7.5: **(a)** Acceptance, and **(b)** acceptance uncertainty of QBH samples due to JER uncertainty. Results are for the ADDn6 model.

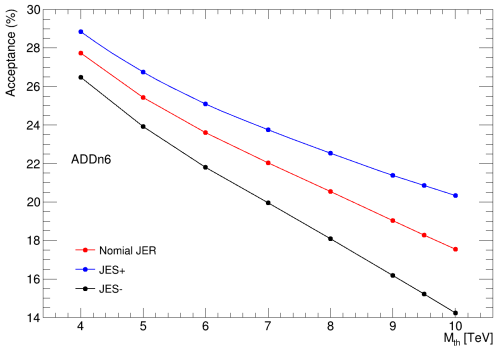

(a) Acceptance

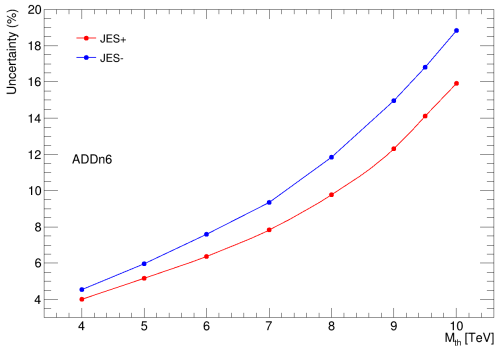

(b) Acceptance uncertainty

Figure 7.6: **(a)** Acceptance, and **(b)** acceptance uncertainty of QBH samples due to JES uncertainty. Results are for the ADDn6 model.

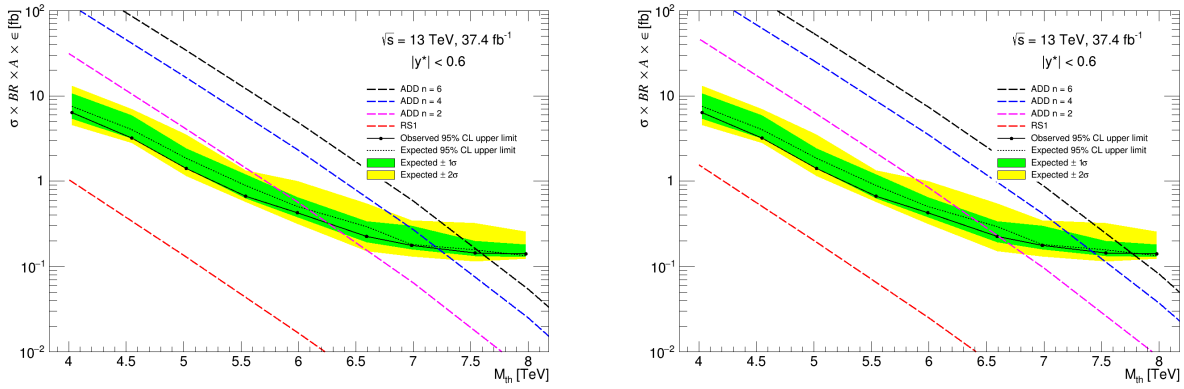

(a) Global symmetries can be violated **(b)** Global symmetries conserved

Figure 7.7: The 95% CL upper limit on QBH production cross-section times branching ratio times acceptance times efficiency for $\mathrm{QBH}_{4/3} \to tt$ in the ADD model with $n = \{2, 4, 6\}$ and the RS1 model, using the results of ATLAS dijet analysis corresponding to 37.4 fb^{-1} of data [4], with global symmetries **(a)** violated and **(b)** conserved.

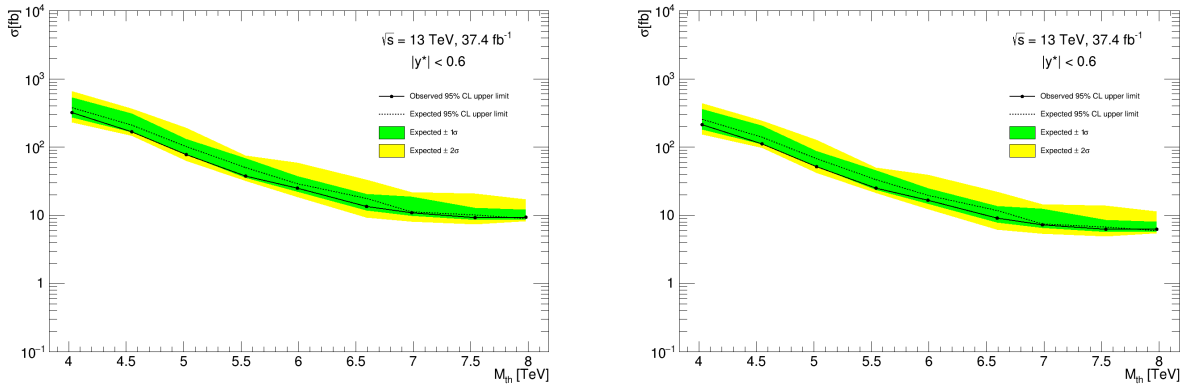

(a) Global symmetries can be violated **(b)** Global symmetries conserved

Figure 7.8: The 95% CL upper limit on σ of $\mathrm{QBH}_{4/3} \to tt$ using the results of ATLAS dijet analysis corresponding to 37.4 fb^{-1} of data [4] with global symmetries **(a)** violated and **(b)** conserved.

Model	95% CL exclusion limit [TeV]			
	Global symmetries conserved		Global symmetries can be violated	
	Observed	Expected	Observed	Expected
ADDn6	7.8	7.8	7.6	7.6
ADDn4	7.4	7.4	7.2	7.2
ADDn2	6.5	6.3	6.2	6.0
RS1	———	———	———	———

Table 7.4: The 95% CL upper limits on $\sigma \times BR \times A \times \epsilon$ of the $\mathrm{QBH}_{4/3} \to tt$ mass threshold for ADD model with $n = \{2, 4, 6\}$ and RS1 model.

As a conclusion to this study, we compare our results to those in the ATLAS dijet analysis [4]. As mentioned previously, we used a cut-and-count and the Frequentist CL_s method while a Bayesian method [110] and the signal shape had been used in the ATLAS analysis. Since they have been using the signal shape, the definition of A is not due to the mass cut. For the same reason, the limits are not just limited to the observed data and extends to 10 TeV. Since our acceptance also includes a mass threshold requirement, $M_{jj} > M_{th}$, our lower mass limit is lower than that of the ATLAS. Also, the samples in the ATLAS analysis are inclusive QBH samples and there is no BR factor. Figure 7.10 shows the 95% CL upper limit of $\sigma \times A \times \epsilon$.

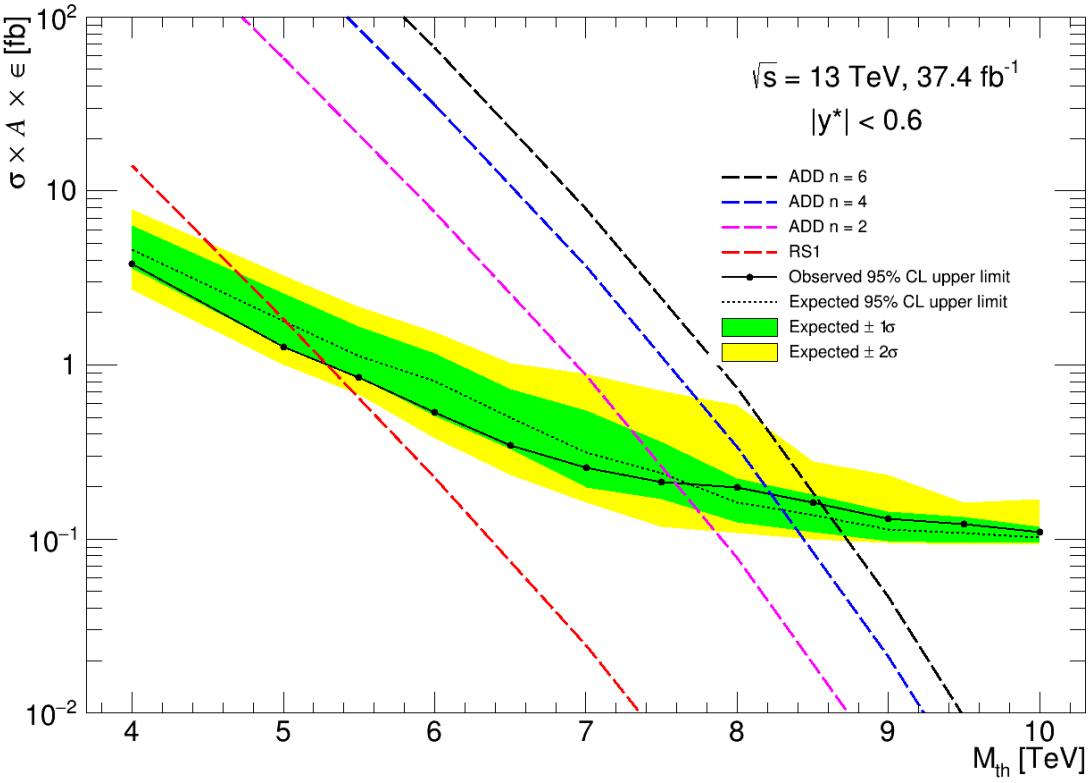

Figure 7.9: With mass cut

Figure 7.10: The 95% CL upper limit on QBH production cross-section times A times ϵ for $\mathrm{QBH}_{4/3}$ in ADD model with $n = \{2, 4, 6\}$ and RS1 model. The limits are taken directly from the ATLAS dijet analysis [4].

Chapter 8

Summary

Low-scale gravity models like the ADD model introduce a fundamental Planck scale which can be as low as a few TeV and the usual four-dimensional Planck scale can be derived from it. In this model, the production of quantum black holes from particle collisions at energies accessible at the LHC becomes an interesting possibility. We studied the creation of QBHs and their decay to the tt final state at the centre-of-mass energy of $\sqrt{s} = 13$ TeV using MC simulated events. Our study achieved two outcomes: finding the discovery potential limit on the QBH mass threshold and setting a 95% CL upper limit on the cross-section times branching ratio times acceptance times efficiency of QBHs using a cut-and-count approach and the Frequentist CL_s method. For the latter we used the results of ATLAS dijet analysis with an integrated luminosity of 37.4 fb^{-1} [4].

We reconstructed the four-momentum of the QBH in the fully- and semi-hadronic topologies of the tt state which have a branching ratio of about 56% and 37%, respectively.

We studied different possible background processes. The most important and the only significant contribution to the background of the QBH $\rightarrow tt$ signal for both of the decay topologies came from the QCD multijet processes.

For declaring a potential discovery, we imposed two criteria: observing at least ten signal events above the background ($s \geq 10$) and a significance level of $Z \geq 5$ standard deviations. Assuming an integrated luminosity of 150 fb^{-1}, we set the mass threshold limit for potential discovery in the ADDn6 model at $M_{\text{th}} = 9.1$ TeV. Using $L = 3000$ fb^{-1}, which will be reached using the HL-LHC, this limit increases to $M_{\text{th}} = 10.0$ TeV. We also set the potential discovery limit on the quantum black hole production mass for the {ADDn4, ADDn2, RS1} models using $L = (150, 3000)$ fb^{-1} at $\{(8.9, 9.8), (8.5, 9.4), (6.2, 7.3)\}$ TeV.

Using the results of ATLAS dijet analysis corresponding to 37.4 fb^{-1} of data, our limit setting calculation excluded QBHs decaying to tt final state with $M_D = M_{\text{th}} < \{7.6, 7.2, 6.2\}$ TeV for the {ADDn6, ADDn4, ADDn2} models. We also set a 95% CL on $\sigma \times BR \times A \times \epsilon$ in the range of 4 TeV to 10 TeV. The limit reduces from 5.9 fb at 4 TeV to 0.11 fb at 8.0 TeV. There were no data for masses above 8.3 TeV which sets the limit to 0.08 fb for higher masses.

References

[1] N. Arkani-Hamed, S. Dimopoulos, and G. R. Dvali, "The Hierarchy problem and new dimensions at a millimeter," *Phys. Lett.*, vol. B429, pp. 263–272, 1998. DOI: 10.1016/S0370-2693(98)00466-3. arXiv: hep-ph/9803315 [hep-ph] (cit. on pp. 1, 8, 9, 17).

[2] L. Randall and R. Sundrum, "A Large mass hierarchy from a small extra dimension," *Phys. Rev. Lett.*, vol. 83, pp. 3370–3373, 1999. DOI: 10.1103/PhysRevLett.83.3370. arXiv: hep-ph/9905221 [hep-ph] (cit. on pp. 1, 8, 10, 17).

[3] L. Randall and R. Sundrum, "An Alternative to compactification," *Phys. Rev. Lett.*, vol. 83, pp. 4690–4693, 1999. DOI: 10.1103/PhysRevLett.83.4690. arXiv: hep-th/9906064 [hep-th] (cit. on pp. 1, 8, 10, 17).

[4] ATLAS Collaboration, "Search for new phenomena in dijet events using 37 fb^{-1} of pp collision data collected at $\sqrt{s}$ =13 TeV with the ATLAS detector," *Phys. Rev.*, vol. D96, no. 5, p. 052 004, 2017. DOI: 10.1103/PhysRevD.96.052004. arXiv: 1703.09127 [hep-ex] (cit. on pp. 1, 40, 71, 89, 93–95, 97, 100–103).

[5] A. Shomer, "A Pedagogical explanation for the non-renormalizability of gravity," 2007. arXiv: 0709.3555 [hep-th] (cit. on p. 3).

[6] R. P. Feynman, "The behavior of hadron collisions at extreme energies," *Conf. Proc.*, vol. C690905, pp. 237–258, 1969 (cit. on p. 5).

[7] R. Placakyte, "Parton Distribution Functions," in *Proceedings, 31st International Conference on Physics in collisions (PIC 2011): Vancouver, Canada, August 28-September 1, 2011*, 2011. arXiv: 1111.5452 [hep-ph] (cit. on p. 5).

[8] Y. Nambu, "Quasi-Particles and Gauge Invariance in the Theory of Superconductivity," *Phys. Rev.*, vol. 117, pp. 648–663, 3 1960. DOI: 10.1103/PhysRev.117.648. [Online]. Available: https://link.aps.org/doi/10.1103/PhysRev.117.648 (cit. on p. 6).

[9] J. Goldstone, "Field theories with « Superconductor » solutions," *Il Nuovo Cimento (1955-1965)*, vol. 19, no. 1, pp. 154–164, 1961, ISSN: 1827-6121. DOI: 10.1007/BF02812722. [Online]. Available: https://doi.org/10.1007/BF02812722 (cit. on p. 6).

[10] J. Goldstone, A. Salam, and S. Weinberg, "Broken Symmetries," *Phys. Rev.*, vol. 127, pp. 965–970, 3 1962. DOI: 10.1103/PhysRev.127.965. [Online]. Available: https://link.aps.org/doi/10.1103/PhysRev.127.965 (cit. on p. 6).

[11] ATLAS Collaboration, "Observation of a new particle in the search for the Standard Model Higgs boson with the ATLAS detector at the LHC," *Physics Letters B*, vol. 716, no. 1, pp. 1 –29, 2012, ISSN: 0370-2693. DOI: https://doi.org/10.1016/j.physletb.2012.08.020. [Online]. Available: http://www.sciencedirect.com/science/article/pii/S037026931200857X (cit. on p. 6).

[12] ATLAS Collaboration, "Evidence for the spin-0 nature of the Higgs boson using ATLAS data," *Physics Letters B*, vol. 726, no. 1, pp. 120 –144, 2013, ISSN: 0370-2693. DOI: https://doi.org/10.1016/j.physletb.2013.08.026. [Online]. Available: http://www.sciencedirect.com/science/article/pii/S0370269313006527 (cit. on p. 6).

[13] CMS Collaboration, "Observation of a new boson at a mass of 125 GeV with the CMS experiment at the LHC," *Physics Letters B*, vol. 716, no. 1, pp. 30 –61, 2012, ISSN: 0370-2693. DOI: https://doi.org/10.1016/j.physletb.2012.08.021. [Online]. Available: http://www.sciencedirect.com/science/article/pii/S0370269312008581 (cit. on p. 6).

[14] A. I. Butt, "Search for Microscopic Black Holes in Multi-Jet Final-States using Multiple Single-Jet Triggers with ATLAS Detector with 8 TeV Proton-Proton Collisions at the Large Hadron Collider," PhD thesis, TRIUMF, 2016-09-19 (cit. on p. 6).

[15] A. Einstein, "The Foundation of the General Theory of Relativity," *Annalen Phys.*, vol. 49, no. 7, pp. 769–822, 1916, [Annalen Phys.354,no.7,769(1916)]. DOI: 10.1002/andp.200590044,10.1002/andp.19163540702 (cit. on p. 6).

[16] G. Nordstrom, "On the possibility of unifying the electromagnetic and the gravitational fields," *Phys. Z.*, vol. 15, pp. 504–506, 1914. arXiv: physics/0702221 [physics.gen-ph] (cit. on p. 8).

[17] I. Antoniadis, N. Arkani-Hamed, S. Dimopoulos, *et al.*, "New dimensions at a millimeter to a Fermi and superstrings at a TeV," *Phys. Lett.*, vol. B436, pp. 257–263, 1998. DOI: 10.1016/S0370-2693(98)00860-0. arXiv: hep-ph/9804398 [hep-ph] (cit. on pp. 8, 10, 17).

[18] B. Bajc, J. Hisano, T. Kuwahara, *et al.*, "Threshold corrections to dimension-six proton decay operators in non-minimal SUSY SU (5) GUTs," *Nucl. Phys.*, vol. B910, pp. 1–22, 2016. DOI: 10.1016/j.nuclphysb.2016.06.017. arXiv: 1603.03568 [hep-ph] (cit. on p. 8).

[19] C. D. Carone, L. J. Hall, and H. Murayama, "A Supersymmetric theory of flavor and R-parity," *Phys. Rev.*, vol. D54, pp. 2328–2339, 1996. DOI: 10.1103/PhysRevD.54.2328. arXiv: hep-ph/9602364 [hep-ph] (cit. on p. 8).

[20] L. E. Ibanez and G. G. Ross, "Discrete gauge symmetries and the origin of baryon and lepton number conservation in supersymmetric versions of the standard model," *Nucl. Phys.*, vol. B368, pp. 3–37, 1992. DOI: 10.1016/0550-3213(92)90195-H (cit. on p. 9).

[21] K. S. Babu *et al.*, "Working Group Report: Baryon Number Violation," in *Proceedings, 2013 Community Summer Study on the Future of U.S. Particle Physics: Snowmass on the Mississippi (CSS2013): Minneapolis, MN, USA, July 29-August 6, 2013*, 2013. arXiv: 1311.5285 [hep-ph]. [Online]. Available: http://www.slac.stanford.edu/econf/C1307292/docs/IntensityFrontier/BaryonNo-13.pdf (cit. on p. 9).

[22] C. Dib, V. Gribanov, S. Kovalenko, *et al.*, "Lepton number violating processes and Majorana neutrinos," *Part. Nucl. Lett.*, vol. 106, pp. 42–55, 2001. arXiv: hep-ph/0011213 [hep-ph] (cit. on p. 9).

[23] S. Leizerovitch and B. Reznik, "Kaluza-Klein tower of masses in compactified Bose-Einstein condensates," 2017. arXiv: 1711.00078 [quant-ph] (cit. on p. 9).

[24] D. Bailin and A. Love, "KALUZA-KLEIN THEORIES," *Rept. Prog. Phys.*, vol. 50, pp. 1087–1170, 1987. DOI: 10.1088/0034-4885/50/9/001 (cit. on p. 9).

[25] D. J. Kapner, T. S. Cook, E. G. Adelberger, *et al.*, "Tests of the gravitational inverse-square law below the dark-energy length scale," *Phys. Rev. Lett.*, vol. 98, p. 021 101, 2007. DOI: 10.1103/PhysRevLett.98.021101. arXiv: hep-ph/0611184 [hep-ph] (cit. on p. 10).

[26] R. P. Kerr, "Gravitational Field of a Spinning Mass as an Example of Algebraically Special Metrics," *Phys. Rev. Lett.*, vol. 11, pp. 237–238, 5 1963. DOI: 10.1103/PhysRevLett.11.237. [Online]. Available: https://link.aps.org/doi/10.1103/PhysRevLett.11.237 (cit. on p. 14).

[27] E. T. Newman and A. I. Janis, "Note on the Kerr Spinning-Particle Metric," *Journal of Mathematical Physics*, vol. 6, no. 6, pp. 915–917, 1965. DOI: 10.1063/1.1704350. eprint: https://doi.org/10.1063/1.1704350. [Online]. Available: https://doi.org/10.1063/1.1704350 (cit. on p. 14).

[28] E. T. Newman, E. Couch, K. Chinnapared, *et al.*, "Metric of a Rotating, Charged Mass," *Journal of Mathematical Physics*, vol. 6, no. 6, pp. 918–919, 1965. DOI: 10.1063/1.1704351. eprint: https://doi.org/10.1063/1.1704351. [Online]. Available: https://doi.org/10.1063/1.1704351 (cit. on p. 14).

[29] F. R. Tangherlini, "Schwarzschild field in n dimensions and the dimensionality of space problem," *Il Nuovo Cimento (1955-1965)*, vol. 27, no. 3, pp. 636–651, 1963, ISSN: 1827-6121. DOI: 10.1007/BF02784569. [Online]. Available: https://doi.org/10.1007/BF02784569 (cit. on p. 16).

[30] R. Myers and M. Perry, "Black holes in higher dimensional space-times," *Annals of Physics*, vol. 172, no. 2, pp. 304 –347, 1986, ISSN: 0003-4916. DOI: https://doi.org/10.1016/0003-4916(86)90186-7. [Online]. Available: http://www.sciencedirect.com/science/article/pii/0003491686901867 (cit. on p. 16).

[31] G. Dvali, "Black Holes and Large N Species Solution to the Hierarchy Problem," *Fortsch. Phys.*, vol. 58, pp. 528–536, 2010. DOI: 10.1002/prop.201000009. arXiv: 0706.2050 [hep-th] (cit. on p. 17).

[32] G. Dvali and M. Redi, "Black Hole Bound on the Number of Species and Quantum Gravity at LHC," *Phys. Rev.*, vol. D77, p. 045 027, 2008. DOI: 10.1103/PhysRevD.77.045027. arXiv: 0710.4344 [hep-th] (cit. on p. 17).

[33] D. M. Gingrich, "Quantum black holes with charge, colour, and spin at the LHC," *J. Phys.*, vol. G37, p. 105 008, 2010. DOI: 10.1088/0954-3899/37/10/105008. arXiv: 0912.0826 [hep-ph] (cit. on pp. 17, 18, 20).

[34] D. M. Gingrich, "Black hole cross-section at the large hadron collider," *Int. J. Mod. Phys.*, vol. A21, pp. 6653–6676, 2006. DOI: 10.1142/S0217751X06035087. arXiv: hep-ph/0609055 [hep-ph] (cit. on pp. 17, 18).

[35] P. Meade and L. Randall, "Black Holes and Quantum Gravity at the LHC," *JHEP*, vol. 05, p. 003, 2008. DOI: 10.1088/1126-6708/2008/05/003. arXiv: 0708.3017 [hep-ph] (cit. on p. 17).

[36] X. Calmet, W. Gong, and S. D. H. Hsu, "Colorful quantum black holes at the LHC," *Phys. Lett.*, vol. B668, pp. 20–23, 2008. DOI: 10.1016/j.physletb.2008.08.011. arXiv: 0806.4605 [hep-ph] (cit. on p. 17).

[37] R. Penrose, "Gravitational collapse and space-time singularities," *Phys. Rev. Lett.*, vol. 14, pp. 57–59, 3 1965. DOI: 10.1103/PhysRevLett.14.57. [Online]. Available: https://link.aps.org/doi/10.1103/PhysRevLett.14.57 (cit. on p. 18).

[38] D. M. Eardley and S. B. Giddings, "Classical black hole production in high-energy collisions," *Phys. Rev.*, vol. D66, p. 044 011, 2002. DOI: 10.1103/PhysRevD.66.044011. arXiv: gr-qc/0201034 [gr-qc] (cit. on p. 18).

[39] H. Yoshino and Y. Nambu, "Black hole formation in the grazing collision of high-energy particles," *Phys. Rev.*, vol. D67, p. 024 009, 2003. DOI: 10.1103/PhysRevD.67.024009. arXiv: gr-qc/0209003 [gr-qc] (cit. on p. 18).

[40] H. Yoshino and V. S. Rychkov, "Improved analysis of black hole formation in high-energy particle collisions," *Phys. Rev.*, vol. D71, p. 104 028, 2005, [Erratum: Phys. Rev.D77,089905(2008)]. DOI: 10.1103/PhysRevD.71.104028,10.1103/PhysRevD.77.089905. arXiv: hep-th/0503171 [hep-th] (cit. on pp. 18, 118).

[41] H. Yoshino and R. B. Mann, "Black hole formation in the head-on collision of ultra-relativistic charges," *Phys. Rev.*, vol. D74, p. 044 003, 2006. DOI: 10.1103/PhysRevD.74.044003. arXiv: gr-qc/0605131 [gr-qc] (cit. on p. 18).

[42] D. M. Gingrich, "Effect of charged partons on black hole production at the Large Hadron Collider," *Journal of High Energy Physics*, vol. 2007, no. 02, p. 098, 2007. [Online]. Available: http://stacks.iop.org/1126-6708/2007/i=02/a=098 (cit. on p. 18).

[43] H. Yoshino, A. Zelnikov, and V. P. Frolov, "Apparent horizon formation in the head-on collision of gyratons," *Phys. Rev.*, vol. D75, p. 124 005, 2007. DOI: 10.1103/PhysRevD.75.124005. arXiv: gr-qc/0703127 [gr-qc] (cit. on p. 18).

[44] E. Kohlprath and G. Veneziano, "Black holes from high-energy beam–beam collisions," *Journal of High Energy Physics*, vol. 2002, no. 06, p. 057, 2002. [Online]. Available: http://stacks.iop.org/1126-6708/2002/i=06/a=057 (cit. on p. 18).

[45] D. Ida, K.-y. Oda, and S. C. Park, "Rotating black holes at future colliders: Greybody factors for brane fields," *Phys. Rev.*, vol. D67, p. 064 025, 2003, [Erratum: Phys. Rev.D69,049901(2004)]. DOI: 10.1103/PhysRevD.67.064025,10.1103/PhysRevD.69.049901. arXiv: hep-th/0212108 [hep-th] (cit. on p. 18).

[46] R. C. Myers and M. J. Perry, "Black Holes in Higher Dimensional Space-Times," *Annals Phys.*, vol. 172, p. 304, 1986. DOI: 10.1016/0003-4916(86)90186-7 (cit. on p. 18).

[47] M. Tanabashi, K. Hagiwara, K. Hikasa, *et al.*, "Review of Particle Physics," *Phys. Rev. D*, vol. 98, p. 030 001, 3 2018. DOI: 10.1103/PhysRevD.98.030001. [Online]. Available: https://link.aps.org/doi/10.1103/PhysRevD.98.030001 (cit. on pp. 18, 20, 21, 28, 46).

[48] Giudice, Gian F. and Rattazzi, Riccardo and Wells, JamesD., "Transplanckian collisions at the LHC and beyond," *Nucl. Phys.*, vol. B630, pp. 293–325, 2002. DOI: 10.1016/S0550-3213(02)00142-6. arXiv: hep-ph/0112161 [hep-ph] (cit. on p. 18).

[49] E. Spallucci and A. Smailagic, "Regular black holes from semi-classical down to Planckian size," *Int. J. Mod. Phys.*, vol. D26, no. 07, p. 1 730 013, 2017. DOI: 10.1142/S0218271817300130. arXiv: 1701.04592 [hep-th] (cit. on p. 19).

[50] M. Kobayashi and T. Maskawa, ""cp-violation in the renormalizable theory of weak interaction"," *Progress of Theoretical Physics*, vol. 49, no. 2, pp. 652–657, 1973. DOI: 10.1143/PTP.49.652. eprint: /oup/backfile/content_public/journal/ptp/49/2/10.1143/ptp.49.652/2/49-2-652.pdf. [Online]. Available: http://dx.doi.org/10.1143/PTP.49.652 (cit. on p. 20).

[51] F. Abe *et al.*, "Observation of top quark production in $\bar{p}p$ collisions," *Phys. Rev. Lett.*, vol. 74, pp. 2626–2631, 1995. DOI: 10.1103/PhysRevLett.74.2626. arXiv: hep-ex/9503002 [hep-ex] (cit. on p. 20).

[52] S. Abachi *et al.*, "Search for high mass top quark production in $p\bar{p}$ collisions at $\sqrt{s} = 1.8$ TeV," *Phys. Rev. Lett.*, vol. 74, pp. 2422–2426, 1995. DOI: 10.1103/PhysRevLett.74.2422. arXiv: hep-ex/9411001 [hep-ex] (cit. on p. 20).

[53] [Online]. Available: https://twiki.cern.ch/twiki/bin/viewauth/AtlasProtected/McProductionCommonParametersMC15 (cit. on pp. 20, 61).

[54] L. Evans and P. Bryant, "LHC Machine," *Journal of Instrumentation*, vol. 3, no. 08, S08001, 2008. [Online]. Available: http://stacks.iop.org/1748-0221/3/i=08/a=S08001 (cit. on pp. 24–26).

[55] ATLAS Collaboration, "The ATLAS Experiment at the CERN Large Hadron Collider," *Journal of Instrumentation*, vol. 3, no. 08, S08003, 2008. [Online]. Available: http://stacks.iop.org/1748-0221/3/i=08/a=S08003 (cit. on pp. 24, 27–34).

[56] CMS Collaboration, "The CMS experiment at the CERN LHC," *Journal of Instrumentation*, vol. 3, no. 08, S08004, 2008. [Online]. Available: http://stacks.iop.org/1748-0221/3/i=08/a=S08004 (cit. on p. 24).

[57] LHCb Collaboration, "The LHCb Detector at the LHC," *Journal of Instrumentation*, vol. 3, no. 08, S08005, 2008. [Online]. Available: http://stacks.iop.org/1748-0221/3/i=08/a=S08005 (cit. on p. 24).

[58] LHCf Collaboration, "The LHCf experiment," *AIP Conference Proceedings*, vol. 1492, no. 1, pp. 182–188, 2012. DOI: 10.1063/1.4763514. eprint: https://aip.scitation.org/doi/pdf/10.1063/1.4763514. [Online]. Available: https://aip.scitation.org/doi/abs/10.1063/1.4763514 (cit. on p. 24).

[59] TOTEM Collaboration, "The TOTEM experiment at the LHC and its physics results," *Nuclear Physics B - Proceedings Supplements*, vol. 245, pp. 275 –282, 2013, The Proceedings of the 7th Joint International Hadron Structure'13 Conference, ISSN: 0920-5632. DOI: https://doi.org/10.1016/j.nuclphysbps.2013.10.054. [Online]. Available: http://www.sciencedirect.com/science/article/pii/S0920563213006439 (cit. on p. 24).

[60] ALICE Collaboration, "The ALICE detector at LHC," in *11th International Conference on Elastic and Diffractive Scattering: Towards High Energy Frontiers: The 20th Anniversary of the Blois Workshops, 17th Rencontre de Blois (EDS 05) Chateau de Blois, Blois, France, May 15-20, 2005*, 2005. arXiv: hep-ph/0509259 [hep-ph] (cit. on p. 24).

[61] S. Akatsuka, "The Phase-1 Upgrade of the ATLAS Level-1 Endcap Muon Trigger," *Springer Proc. Phys.*, vol. 212, pp. 341–345, 2018. DOI: 10.1007/978-981-13-1313-4_65. arXiv: 1806.09234 [physics.ins-det] (cit. on p. 25).

[62] G. Apollinari, O. Brüning, T. Nakamoto, *et al.*, "High Luminosity Large Hadron Collider HL-LHC," *CERN Yellow Report*, no. 5, pp. 1–19, 2015. DOI: 10.5170/CERN-2015-005.1. arXiv: 1705.08830 [physics.acc-ph] (cit. on p. 25).

[63] A. Lombardi, "Linac4: From Initial Design to Final Commissioning," in *Proceedings, 8th International Particle Accelerator Conference (IPAC 2017): Copenhagen, Denmark, May 14-19, 2017*, 2017, TUYA1. DOI: 10.18429/JACoW-IPAC2017-TUYA1 (cit. on p. 26).

[64] H Stenzel, "Luminosity calibration from elastic scattering," CERN, Geneva, Tech. Rep. ATL-LUM-PUB-2007-001. ATL-COM-LUM-2006-010. CERN-ATL-LUM-PUB-2007-001, 2006. [Online]. Available: http://cds.cern.ch/record/1007180 (cit. on p. 32).

[65] ATLAS Collaboration, "Electron and photon energy calibration with the ATLAS detector using LHC Run 1 data," *Eur. Phys. J.*, vol. C74, no. 10, p. 3071, 2014. DOI: 10.1140/epjc/s10052-014-3071-4. arXiv: 1407.5063 [hep-ex] (cit. on pp. 34, 38).

[66] ATLAS Collaboration, "Electron efficiency measurements with the ATLAS detector using 2012 LHC proton–proton collision data," *Eur. Phys. J.*, vol. C77, no. 3, p. 195, 2017. DOI: 10.1140/epjc/s10052-017-4756-2. arXiv: 1612.01456 [hep-ex] (cit. on p. 34).

[67] ATLAS Collaboration, "Expected Performance of the ATLAS Experiment - Detector, Trigger and Physics," 2009. arXiv: 0901.0512 [hep-ex] (cit. on pp. 35, 37, 48).

[68] ATLAS Collaboration, *Muon Performance in Minimum Bias pp Collision Data at* $\sqrt{s} = 7$ *TeV with ATLAS*. [Online]. Available: https://cds.cern.ch/record/1277675/files/ATLAS-CONF-2010-036.pdf (cit. on p. 35).

[69] M. Cacciari, G. P. Salam, and G. Soyez, "The anti-k_t jet clustering algorithm," *JHEP*, vol. 04, p. 063, 2008. DOI: 10.1088/1126-6708/2008/04/063. arXiv: 0802.1189 [hep-ph] (cit. on pp. 35, 36, 46).

[70] W Lampl, S Laplace, D Lelas, *et al.*, "Calorimeter Clustering Algorithms: Description and Performance," CERN, Geneva, Tech. Rep. ATL-LARG-PUB-2008-002. ATL-COM-LARG-2008-003, 2008. [Online]. Available: https://cds.cern.ch/record/1099735 (cit. on p. 35).

[71] Y. L. Dokshitzer, G. D. Leder, S. Moretti, *et al.*, "Better jet clustering algorithms," *JHEP*, vol. 08, p. 001, 1997. DOI: 10.1088/1126-6708/1997/08/001. arXiv: hep-ph/9707323 [hep-ph] (cit. on p. 36).

[72] S. Catani, Y. Dokshitzer, and B. Webber, "The $k_\perp$-clustering algorithm for jets in deep inelastic scattering and hadron collisions," *Physics Letters B*, vol. 285, no. 3, pp. 291 –299, 1992, ISSN: 0370-2693. DOI: https://doi.org/10.1016/0370-2693(92)91467-N. [Online]. Available: http://www.sciencedirect.com/science/article/pii/037026939291467N (cit. on p. 36).

[73] ATLAS Collaboration, "Performance of Missing Transverse Momentum Reconstruction in Proton-Proton Collisions at 7 TeV with ATLAS," *Eur. Phys. J.*, vol. C72, p. 1844, 2012. DOI: 10.1140/epjc/s10052-011-1844-6. arXiv: 1108.5602 [hep-ex] (cit. on p. 37).

[74] "Tau Reconstruction and Identfication Performance in ATLAS," CERN, Geneva, Tech. Rep. ATLAS-CONF-2010-086, 2010. [Online]. Available: http://cds.cern.ch/record/1298857 (cit. on p. 38).

[75] D. M. Gingrich, "Monte Carlo event generator for black hole production and decay in proton-proton collisions," *Comput. Phys. Commun.*, vol. 181, pp. 1917–1924, 2010. DOI: 10.1016/j.cpc.2010.07.027. arXiv: 0911.5370 [hep-ph] (cit. on pp. 40, 41, 118).

[76] Sjostrand, Torbjorn and Mrenna, Stephen and Skands, Peter Z., "A Brief Introduction to PYTHIA 8.1," *Comput. Phys. Commun.*, vol. 178, pp. 852–867, 2008. DOI: 10.1016/j.cpc.2008.01.036. arXiv: 0710.3820 [hep-ph] (cit. on pp. 40, 46).

[77] Bahr, M. and others, "Herwig++ Physics and Manual," *Eur. Phys. J.*, vol. C58, pp. 639–707, 2008. DOI: 10.1140/epjc/s10052-008-0798-9. arXiv: 0803.0883 [hep-ph] (cit. on pp. 40, 72).

[78] Alioli, Simone and Nason, Paolo and Oleari, Carlo and Re, Emanuele, "A general framework for implementing NLO calculations in shower Monte Carlo programs: the POWHEG BOX," *JHEP*, vol. 06, p. 043, 2010. DOI: 10.1007/JHEP06(2010)043. arXiv: 1002.2581 [hep-ph] (cit. on p. 40).

[79] J. Pumplin, D. R. Stump, J. Huston, *et al.*, "New generation of parton distributions with uncertainties from global QCD analysis," *JHEP*, vol. 07, p. 012, 2002. DOI: 10.1088/1126-6708/2002/07/012. arXiv: hep-ph/0201195 [hep-ph] (cit. on pp. 41, 118).

[80] S. Höche, "Introduction to parton-shower event generators," in *Proceedings, Theoretical Advanced Study Institute in Elementary Particle Physics: Journeys Through the Precision Frontier: Amplitudes for Colliders (TASI 2014): Boulder, Colorado, June 2-27, 2014*, 2015, pp. 235–295. DOI: 10.1142/9789814678766_0005. arXiv: 1411.4085 [hep-ph] (cit. on p. 46).

[81] "Search for new phenomena with large jet multiplicities and missing transverse momentum using large-radius jets and flavour-tagging at ATLAS in 13 TeV pp collisions," CERN, Geneva, Tech. Rep. ATLAS-CONF-2017-033, 2017. [Online]. Available: http://cds.cern.ch/record/2265802 (cit. on p. 46).

[82] M. Aaboud *et al.*, "Performance of top-quark and W-boson tagging with ATLAS in Run 2 of the LHC," 2018. arXiv: 1808.07858 [hep-ex] (cit. on p. 46).

[83] "Search for new phenomena in dijet events using 139 fb^{-1} of pp collision at $\sqrt{s}$ =13 TeV collected with the ATLAS detector," CERN, Geneva, Tech. Rep. ATLAS-CONF-2019-007, 2019. [Online]. Available: https://cds.cern.ch/record/2668385 (cit. on p. 48).

[84] G. Aad *et al.*, "Muon reconstruction performance of the ATLAS detector in proton–proton collision data at $\sqrt{s}$ =13 TeV," *Eur. Phys. J.*, vol. C76, no. 5, p. 292, 2016. DOI: 10.1140/epjc/s10052-016-4120-y. arXiv: 1603.05598 [hep-ex] (cit. on p. 49).

[85] [Online]. Available: https://twiki.cern.ch/twiki/bin/view/AtlasPublic/MuonPerformancePublicPlotsSimulation (cit. on p. 49).

[86] G. Aad *et al.*, "Jet energy resolution in proton-proton collisions at $\sqrt{s}$ = 7 TeV recorded in 2010 with the ATLAS detector," *Eur. Phys. J.*, vol. C73, no. 3, p. 2306, 2013. DOI: 10.1140/epjc/s10052-013-2306-0. arXiv: 1210.6210 [hep-ex] (cit. on p. 50).

[87] T. H. Park and D. Gillberg, "Jet energy resolution measurement of the ATLAS detector using momentum balance," Presented 31 Aug 2018, 2018. [Online]. Available: http://cds.cern.ch/record/2642494 (cit. on pp. 50, 51).

[88] M. Aaboud *et al.*, "Jet energy scale measurements and their systematic uncertainties in proton-proton collisions at $\sqrt{s}$ = 13 TeV with the ATLAS detector," *Phys. Rev.*, vol. D96, no. 7, p. 072 002, 2017. DOI: 10.1103/PhysRevD.96.072002. arXiv: 1703.09665 [hep-ex] (cit. on pp. 50, 51).

[89] G. Soyez, "Pileup mitigation at the LHC: a theorist's view," habilitation, IPhT, Saclay, 2018. arXiv: 1801.09721 [hep-ph] (cit. on p. 52).

[90] R. Field, "Min-Bias and the Underlying Event at the LHC," *Acta Phys. Polon.*, vol. B42, pp. 2631–2656, 2011. DOI: 10.5506/APhysPolB.42.2631. arXiv: 1110.5530 [hep-ph] (cit. on p. 52).

[91] ATLAS Collaboration, "Search for New Phenomena in Dijet Events with the ATLAS Detector at $\sqrt{s}$ =13 TeV with 2016 data," CERN, Geneva, Tech. Rep. ATL-COM-PHYS-2016-471, 2016. [Online]. Available: https://cds.cern.ch/record/2151829 (cit. on p. 52).

[92] L. Medina Medrano, G. Arduini, and R. Tomás, "Studies on Luminous Region, Pile-up and Performance for HL-LHC Scenarios," no. CERN-ACC-2017-135, TUPIK089. 4 p, 2017. DOI: 10.18429/JACoW-IPAC2017-TUPIK089. [Online]. Available: https://cds.cern.ch/record/2289694 (cit. on p. 52).

[93] T. Chwalek, "Measurement of the W boson helicity in top-antitop quark events with the CDF II experiment," PhD thesis, Karlsruhe U., EKP, 2006. DOI: 10.2172/911839. [Online]. Available: http://lss.fnal.gov/archive/thesis/2000/fermilab-thesis-2006-100.pdf (cit. on pp. 61, 62).

[94] R. D. Ball *et al.*, "Parton distributions with LHC data," *Nucl. Phys.*, vol. B867, pp. 244–289, 2013. DOI: 10.1016/j.nuclphysb.2012.10.003. arXiv: 1207.1303 [hep-ph] (cit. on p. 68).

[95] ATLAS Collaboration, "ATLAS Run 1 Pythia8 tunes," CERN, Geneva, Tech. Rep. ATL-PHYS-PUB-2014-021, 2014. [Online]. Available: http://cds.cern.ch/record/1966419 (cit. on p. 68).

[96] Z Marshall, "Re-defining the Standard QCD Di-Jet Samples," CERN, Geneva, Tech. Rep. ATL-COM-PHYS-2011-992, 2011. [Online]. Available: https://cds.cern.ch/record/1370089 (cit. on p. 68).

[97] Barger, V.D. and Phillips, R.J.N., *Collider Physics*, ser. Frontiers in Physics. Avalon Publishing, 1996, ISBN: 9780201149456. [Online]. Available: https://books.google.ca/books?id=UFcutAEACAAJ (cit. on p. 68).

[98] [Online]. Available: http://home.thep.lu.se/Pythia/pythia82html/PhaseSpaceCuts.html (cit. on p. 68).

[99] ATLAS Collaboration, *Re-re-defining the Standard QCD Di-Jet Samples: Beginning to like event weights*, 2015 (cit. on p. 69).

[100] [Online]. Available: https://www.hepdata.net/record/77265 (cit. on pp. 71, 72, 74, 75, 94, 95, 97).

[101] S. Gieseke, C. Rohr, and A. Siodmok, "Colour reconnections in Herwig++," *Eur. Phys. J.*, vol. C72, p. 2225, 2012. DOI: 10.1140/epjc/s10052-012-2225-5. arXiv: 1206.0041 [hep-ph] (cit. on p. 72).

[102] D. J. Lange, "The EvtGen particle decay simulation package," *Nuclear Instruments and Methods in Physics Research Section A: Accelerators, Spectrometers, Detectors and Associated Equipment*, vol. 462, no. 1, pp. 152 –155, 2001, BEAUTY2000, Proceedings of the 7th Int. Conf. on B-Physics at Hadron Machines, ISSN: 0168-9002. DOI: https://doi.org/10.1016/S0168-9002(01)00089-4. [Online]. Available: http://www.sciencedirect.com/science/article/pii/S0168900201000894 (cit. on p. 73).

[103] T. Jezo, J. M. Lindert, N. Moretti, *et al.*, "New NLOPS predictions for $\boldsymbol{t\bar{t}+b}$-jet production at the LHC," *Eur. Phys. J.*, vol. C78, no. 6, p. 502, 2018. DOI: 10.1140/epjc/s10052-018-5956-0. arXiv: 1802.00426 [hep-ph] (cit. on p. 77).

[104] G. Aad *et al.*, "Search for Quantum Black Hole Production in High-Invariant-Mass Lepton+Jet Final States Using *pp* Collisions at $\sqrt{s} = 8$ TeV and the ATLAS Detector," *Phys. Rev. Lett.*, vol. 112, no. 9, p. 091 804, 2014. DOI: 10.1103/PhysRevLett.112.091804. arXiv: 1311.2006 [hep-ex] (cit. on pp. 77, 89).

[105] Brun, R. and Rademakers, F., "ROOT: An object oriented data analysis framework," *Nucl. Instrum. Meth.*, vol. A389, pp. 81–86, 1997. DOI: 10.1016/S0168-9002(97)00048-X (cit. on p. 81).

[106] W. Buttinger, M. Lefebvre, *Formulae for calculating significance in a counting experiment*. [Online]. Available: https://cernbox.cern.ch/index.php/s/Qxngvi0Rt2NbASi (cit. on pp. 86, 88).

[107] G. Cowan, K. Cranmer, E. Gross, *et al.*, "Asymptotic formulae for likelihood-based tests of new physics," *Eur. Phys. J.*, vol. C71, p. 1554, 2011, [Erratum: Eur. Phys. J.C73,2501(2013)]. DOI: 10.1140/epjc/s10052-011-1554-0, 10.1140/epjc/s10052-013-2501-z. arXiv: 1007.1727 [physics.data-an] (cit. on pp. 86–88, 96).

[108] P. K. Sinervo, "Signal significance in particle physics," in *Advanced Statistical Techniques in Particle Physics. Proceedings, Conference, Durham, UK, March 18-22, 2002*, 2002, pp. 64–76. arXiv: hep-ex/0208005 [hep-ex]. [Online]. Available: http://www.ippp.dur.ac.uk/Workshops/02/statistics/proceedings//sinervo.pdf (cit. on p. 88).

[109] [Online]. Available: https://cernbox.cern.ch/index.php/s/Qxngvi0Rt2NbASi (cit. on p. 95).

[110] ATLAS Collaboration, "Search for New Physics in Dijet Mass and Angular Distributions in pp Collisions at $\sqrt{s} = 7$ TeV Measured with the ATLAS Detector," *New J. Phys.*, vol. 13, p. 053 044, 2011. DOI: 10.1088/1367-2630/13/5/053044. arXiv: 1103.3864 [hep-ex] (cit. on p. 101).

Appendix A

List of MC Simulated Samples used in the Analysis

List of MC samples used in this study.

Sample	Name
$t\bar{t}$	mc15_13TeV.410287.PhPy8EG_A14_ttbar_hdamp258p75_allhad_mtt_1700_2000.evgen.EVNT.e6686
	mc15_13TeV.410288.PhPy8EG_A14_ttbar_hdamp258p75_allhad_mtt_2000_14000.evgen.EVNT.e6686
PYTHIA	mc16_13TeV.361024.Pythia8EvtGen_A14NNPDF23LO_jetjet_JZ4W_evgen.EVNT.e3668
	mc16_13TeV.361025.Pythia8EvtGen_A14NNPDF23LO_jetjet_JZ5W_evgen.EVNT.e3668
	mc16_13TeV.361026.Pythia8EvtGen_A14NNPDF23LO_jetjet_JZ6W_evgen.EVNT.e3668
	mc16_13TeV.361027.Pythia8EvtGen_A14NNPDF23LO_jetjet_JZ7W_evgen.EVNT.e3668
	mc16_13TeV.361028.Pythia8EvtGen_A14NNPDF23LO_jetjet_JZ8W_evgen.EVNT.e3668
	mc16_13TeV.361029.Pythia8EvtGen_A14NNPDF23LO_jetjet_JZ9W_evgen.EVNT.e3668
	mc16_13TeV.361030.Pythia8EvtGen_A14NNPDF23LO_jetjet_JZ10W_evgen.EVNT.e3668
	mc16_13TeV.361031.Pythia8EvtGen_A14NNPDF23LO_jetjet_JZ11W_evgen.EVNT.e3668
	mc16_13TeV.361032.Pythia8EvtGen_A14NNPDF23LO_jetjet_JZ12W_evgen.EVNT.e3668

Table A.1: List of POWHEG $t\bar{t}$ and PYTHIA QCD background MCs.

Sample	Name
HERWIG	mc15_13TeV.364434.HerwigppEvtGen_UEEE5_CTEQ6L1_jetjet_JZ4.evgen.EVNT.e5899
	mc15_13TeV.364435.HerwigppEvtGen_UEEE5_CTEQ6L1_jetjet_JZ5.evgen.EVNT.e5899
	mc15_13TeV.364436.HerwigppEvtGen_UEEE5_CTEQ6L1_jetjet_JZ6.evgen.EVNT.e5899
	mc15_13TeV.364437.HerwigppEvtGen_UEEE5_CTEQ6L1_jetjet_JZ7.evgen.EVNT.e5899
	mc15_13TeV.364438.HerwigppEvtGen_UEEE5_CTEQ6L1_jetjet_JZ8.evgen.EVNT.e5899
	mc15_13TeV.364439.HerwigppEvtGen_UEEE5_CTEQ6L1_jetjet_JZ9.evgen.EVNT.e5899
	mc15_13TeV.364440.HerwigppEvtGen_UEEE5_CTEQ6L1_jetjet_JZ10.evgen.EVNT.e5899
	mc15_13TeV.364441.HerwigppEvtGen_UEEE5_CTEQ6L1_jetjet_JZ11.evgen.EVNT.e5899
	mc15_13TeV.364442.HerwigppEvtGen_UEEE5_CTEQ6L1_jetjet_JZ12.evgen.EVNT.e5899

Table A.2: List of Herwig QCD background MCs.

Appendix B

Parameters of the QBH Generator

The set of parameters used in the QBH generator for this study. A set of Planck scales ranging from 4-10 TeV in 1 TeV steps plus 9.5 TeV is used. The maximum QBH mass is 13 TeV, except for the $M_D = 4$ TeV which the maximum QBH mass is 12 TeV. RS1 model correspond to a total number of dimensions of five using Randal-Sundrum definition of Planck scale. ADD model is considered with three different choices of number of extra dimensions, $n = \{2, 4, 6\}$, with the PDG definition of Planck scale. In the QBH generator, the global symmetries, like baryon number and lepton number, can be violated which affects the branching ratios and both were considered in our study.

Parameter name	Parameter description	Parameter value
mplanck	Planck scale (TeV)	$\{4.0, 5.0, 6.0, 7.0, 8.0, 9.0, 9.5, 10.0\}$
minmass	Minimum black hole mass	= Planck scale
maxmass	Maximum black hole mass (TeV)	$\{12.0, 13.0\}$
qstate	Black hole charge state	$\{\pm 4/3, 0\}$
istate	Black hole initial state	$\{0, 2\}$
ecm	Proton-proton centre-of-mass energy (TeV)	13.0
RS1	ADD or RS1 model	Both
totdim	Total number of extra dimensions	$\{5, 6, 8, 10\}$
planckdef	Planck scale definition	Randall-Sundrum and PDG
lhaglue	Parton distribution function	CTEQ6L1 [79]
qscale	QCD scale definition	Inverse gravitational radius
trap	Yoshino-Rychkov trapped surface [40]	0
yrform	Yoshino-Rychkov factors [40]	0
poisson	Two-particle decay probability	0
sm	Global gauge symmetries conserved	$\{\pm 0, 1\}$
higgs	Include standard model higgs as particle	1
graviton	Include graviton as particle	1
chiral	Neutrions left- and right-handed	left-handed neutrinos only
majorana	Majorana neutrinos	Dirac neutrinos

Table B.1: Basic parameters of the QBH generator used in this study. 0 stands for false and 1 for true; i.e using or not using a specific property. See Ref. [75] for more information on each parameter definition and also other possible choices available in the QBH generator.

Appendix C

Particle Kinematics

For validating the QBH generator, we will plot some of the kinematics of the top quarks, Figure C.1-C.2, and the QBH, Figure C.3, for the 4 TeV sample and also for 9 TeV sample in Figure C.4-C.6, respectively.

Each particle at the parton showering level can be identified with its PDG ID but each particle has a unique *BarCode*. In each event, the top quark with $BarCode = 5$ is called top1 and the top quark with $BarCode = 6$ is called top2. The QBH is simply the addition of the two top quarks.

C.1 4 TeV mass threshold

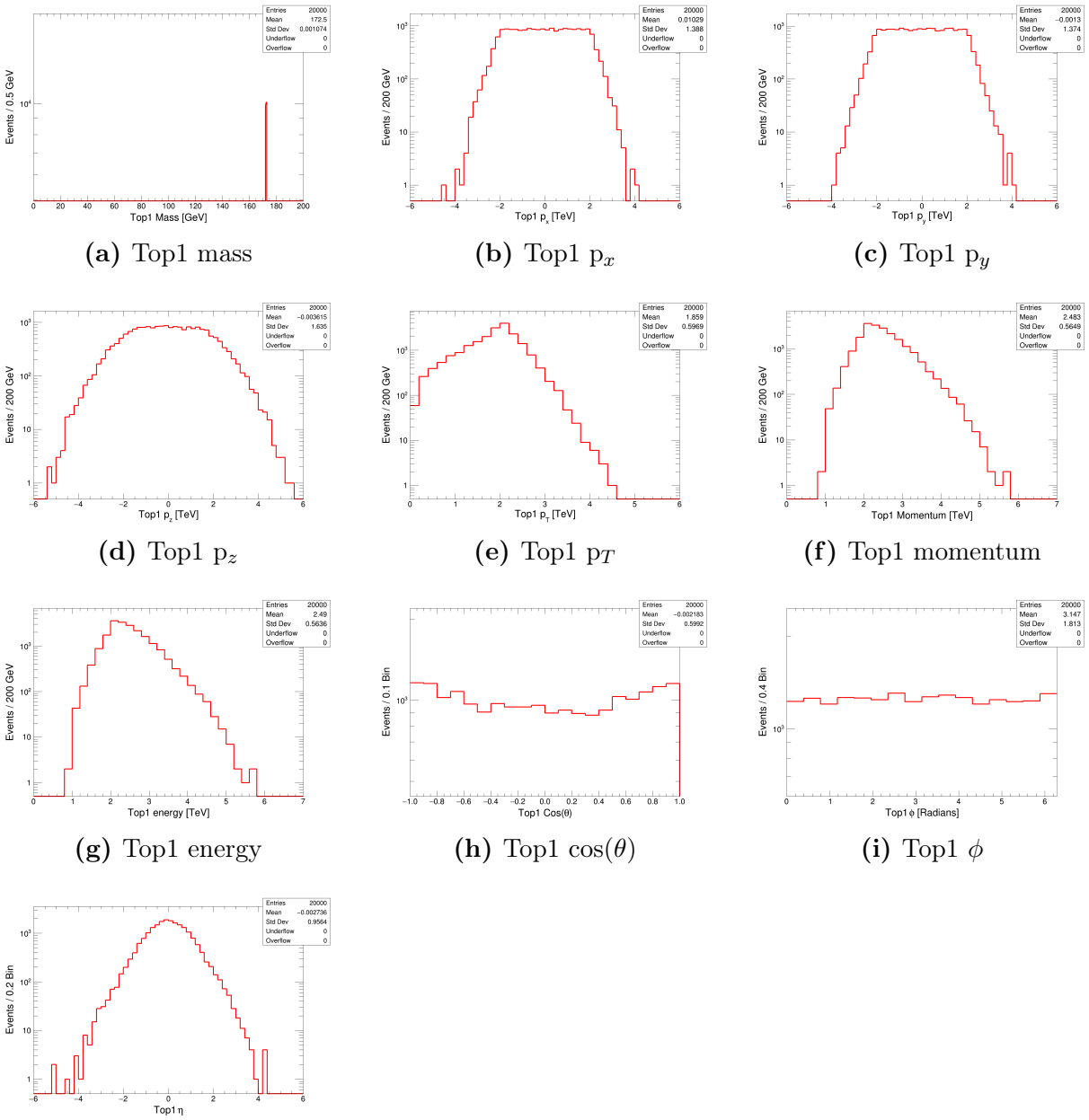

(a) Top1 mass **(b)** Top1 p_x **(c)** Top1 p_y

(d) Top1 p_z **(e)** Top1 p_T **(f)** Top1 momentum

(g) Top1 energy **(h)** Top1 $\cos(\theta)$ **(i)** Top1 ϕ

(j) Top1 η

Figure C.1: Top1 kinematics for $M_{th} = 4$ TeV mass threshold sample.

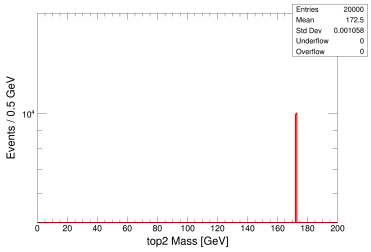

(a) Top2 mass

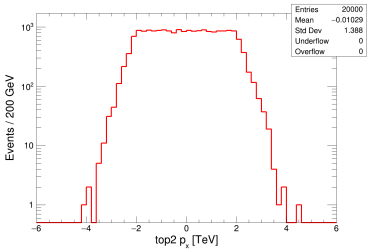

(b) Top2 p_x

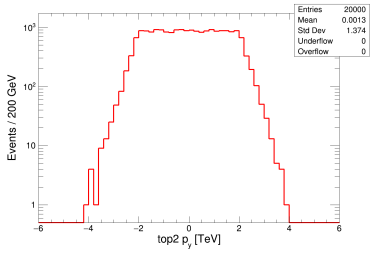

(c) Top2 p_y

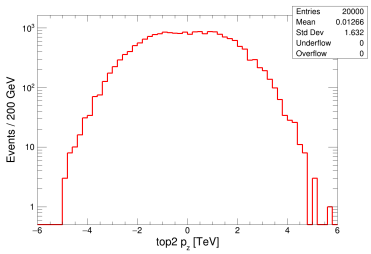

(d) Top2 p_z

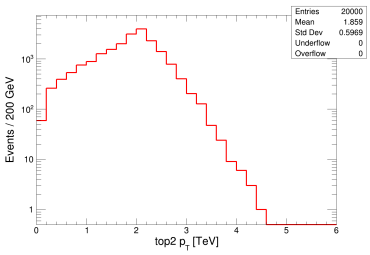

(e) Top2 p_T

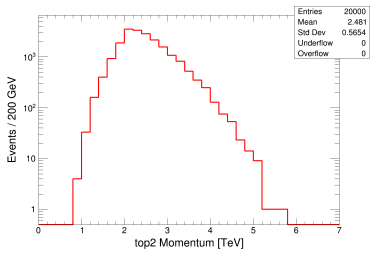

(f) Top2 momentum

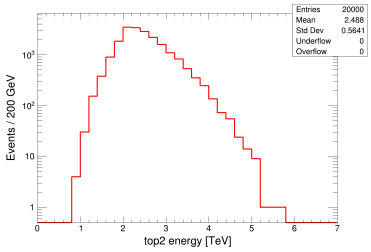

(g) Top2 energy

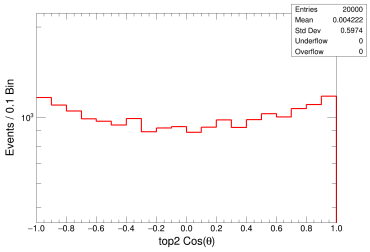

(h) Top2 $\cos(\theta)$

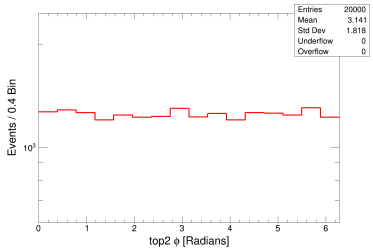

(i) Top2 ϕ

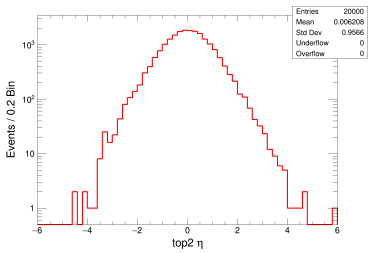

(j) Top2 η

Figure C.2: Top2 kinematics for $M_{th} = 4$ TeV mass threshold sample.

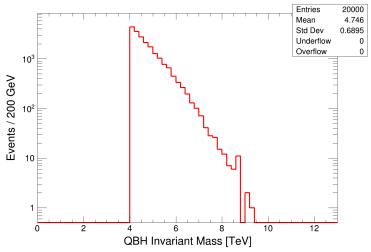

(a) QBH invariant mass

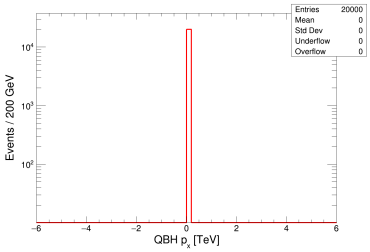

(b) QBH p_x

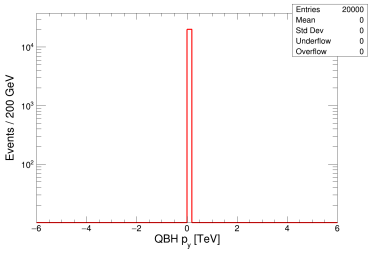

(c) QBH p_y

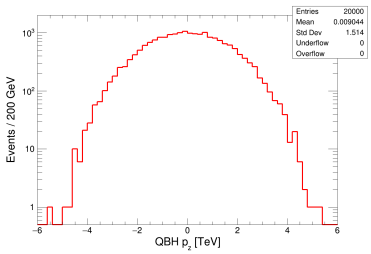

(d) QBH p_z

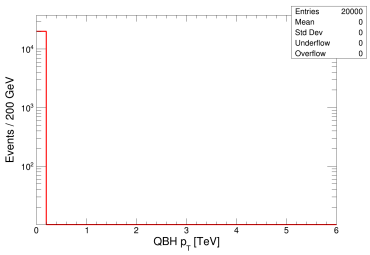

(e) QBH p_T

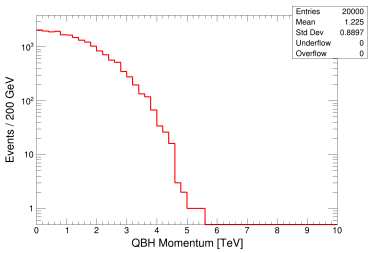

(f) QBH momentum

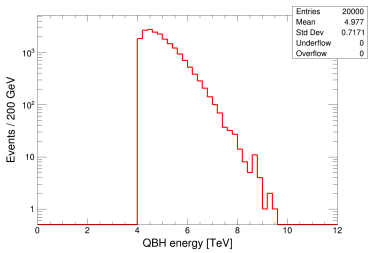

(g) QBH energy

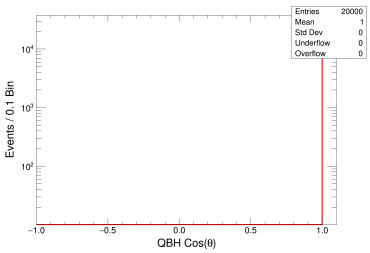

(h) QBH $\cos(\theta)$

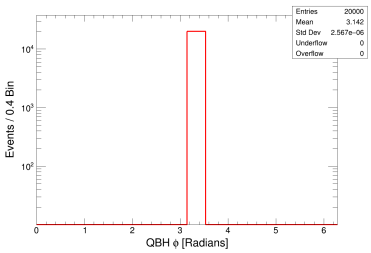

(i) QBH ϕ

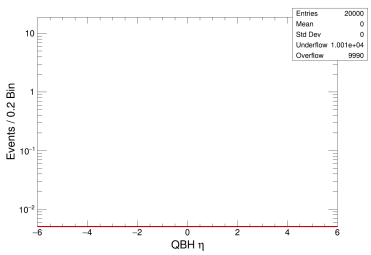

(j) QBH η

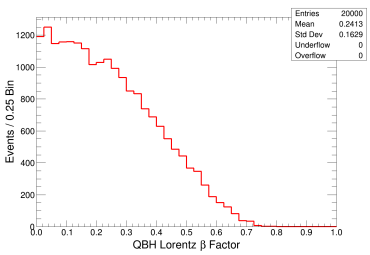

(k) QBH lorentz β factor

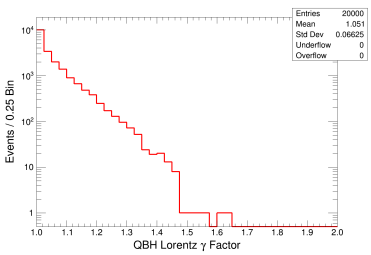

(l) QBH lorentz γ factor

Figure C.3: QBH kinematics for $M_{th} = 4$ TeV mass threshold sample.

C.2 9 TeV mass threshold

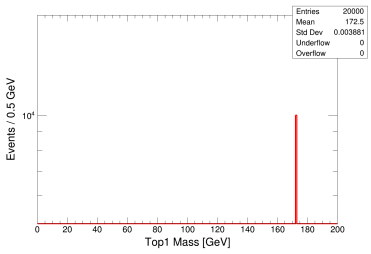

(a) Top1 mass

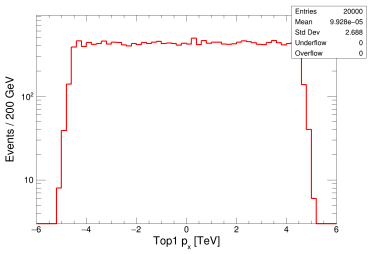

(b) Top1 p_x

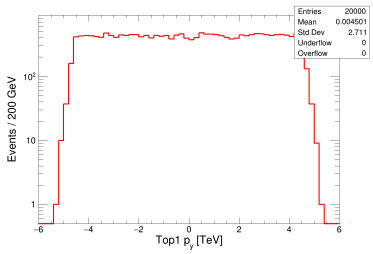

(c) Top1 p_y

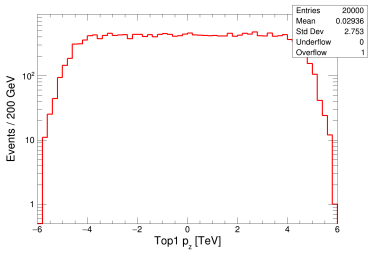

(d) Top1 p_z

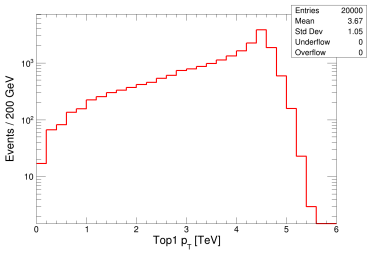

(e) Top1 p_T

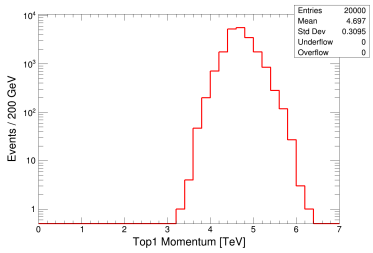

(f) Top1 momentum

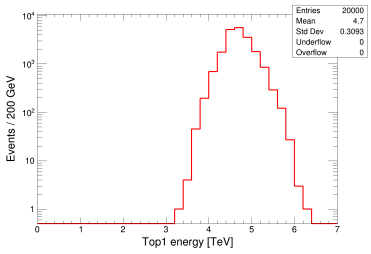

(g) Top1 energy

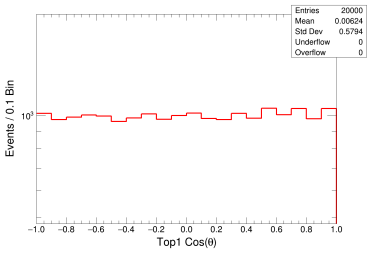

(h) Top1 $\cos(\theta)$

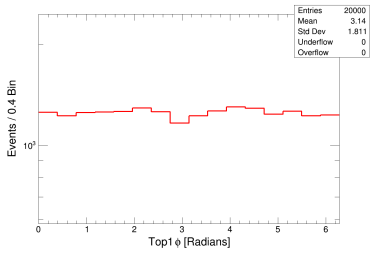

(i) Top1 ϕ

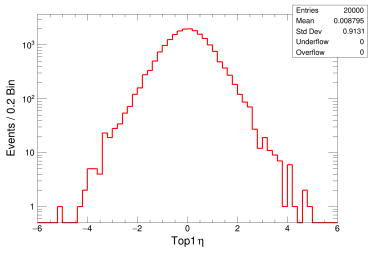

(j) Top1 η

Figure C.4: Top1 kinematics for $M_{th} = 9$ TeV mass threshold sample.

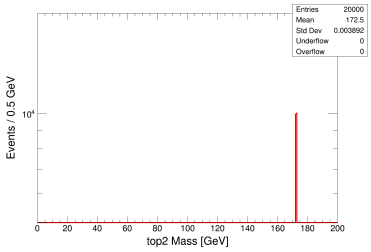

(a) Top2 mass

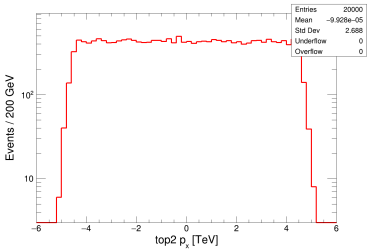

(b) Top2 p_x

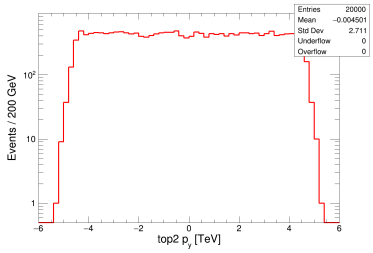

(c) Top2 p_y

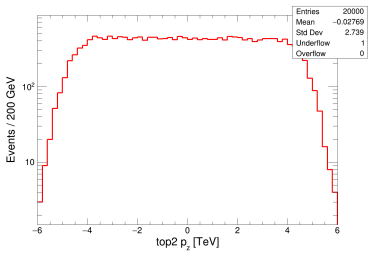

(d) Top2 p_z

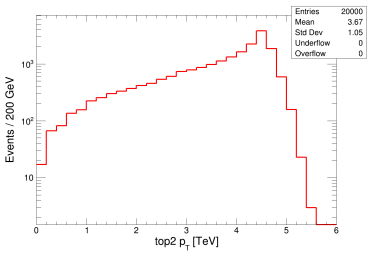

(e) Top2 p_T

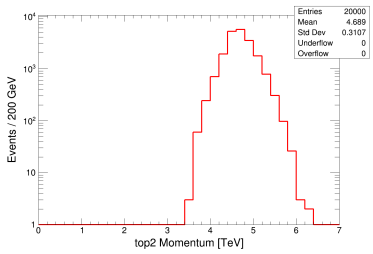

(f) Top2 momentum

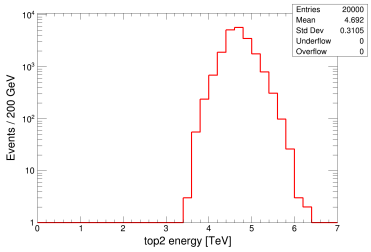

(g) Top2 energy

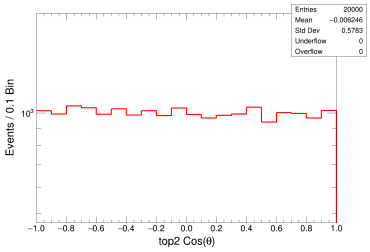

(h) Top2 $\cos(\theta)$

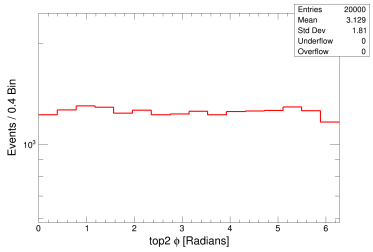

(i) Top2 ϕ

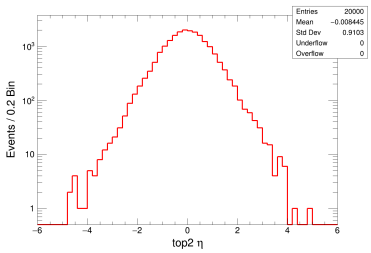

(j) Top2 η

Figure C.5: Top2 kinematics for $M_{th} = 9$ TeV mass threshold sample.

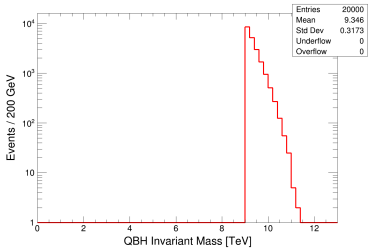

(a) QBH invariant mass

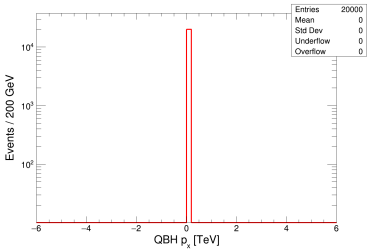

(b) QBH p_x

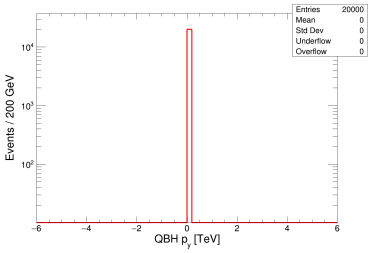

(c) QBH p_y

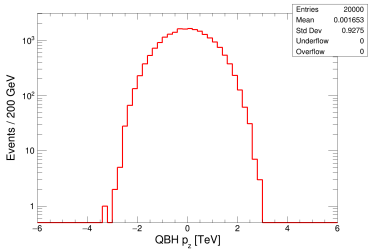

(d) QBH p_z

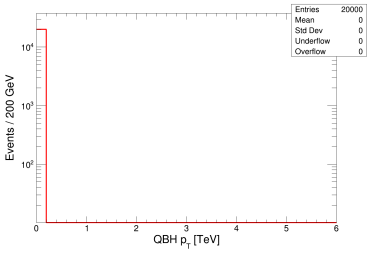

(e) QBH p_T

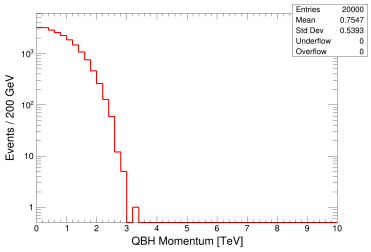

(f) QBH momentum

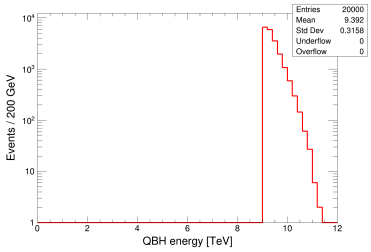

(g) QBH energy

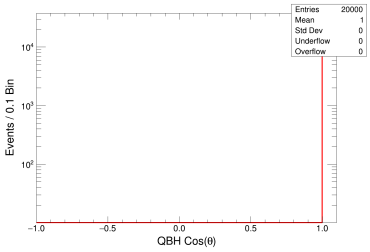

(h) QBH $\cos(\theta)$

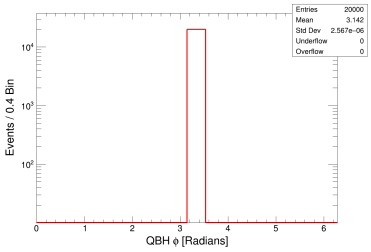

(i) QBH ϕ

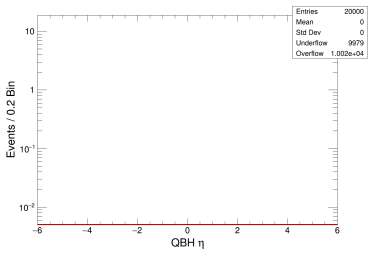

(j) QBH η

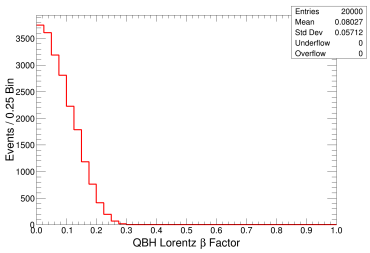

(k) QBH lorentz β factor

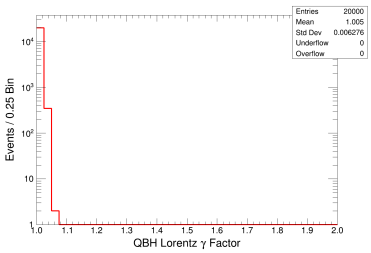

(l) QBH lorentz γ factor

Figure C.6: QBH kinematics for $M_{th} = 9$ TeV mass threshold sample.

Appendix D

η Distribution

η distribution of the two highest p_T jets for hadronic and mixed decays of the QBH and the Pythia QCD. Also the η distribution of the highest p_T lepton of the mixed decay and the two highest p_T leptons of the leptonic decays of the QBH signal.

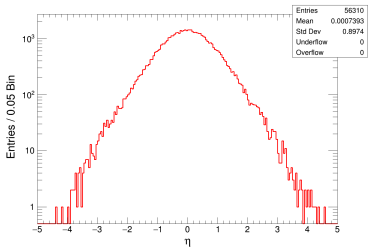

(a) Hadronic jets

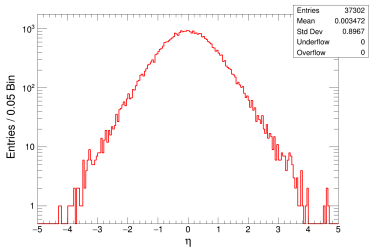

(b) Mixed jets

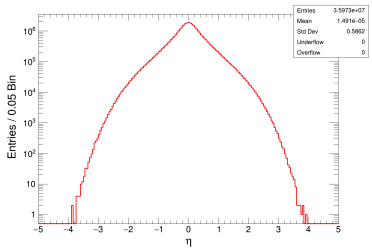

(c) Pythia jets

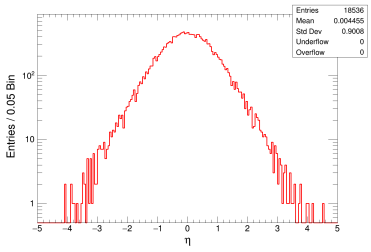

(d) Mixed lepton

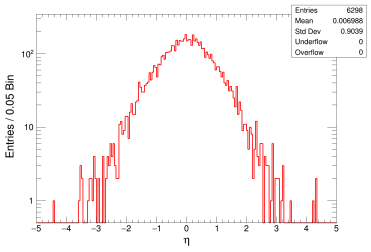

(e) Leptonic leptons

Figure D.1: η distribution of jets for **(a)** hadronic, and **(b)** mixed decays of the $M_{th} = 9$ TeV of ADDn6 QBH sample, and jets from **(c)** Pythia. **(d)** η distribution of the highest p_T lepton for mixed decays of the QBH and **(e)** the two highest p_T leptons for leptonic decays.

Appendix E

p_T Resolution

The p_T ratio of muons, jets and MET before and after including the p_T resolution. These ratios for the QBH signal and PYTHIA QCD dijet are shown in Figure E.1 and Figure E.2, respectively. The η acceptance of all the objects are included.

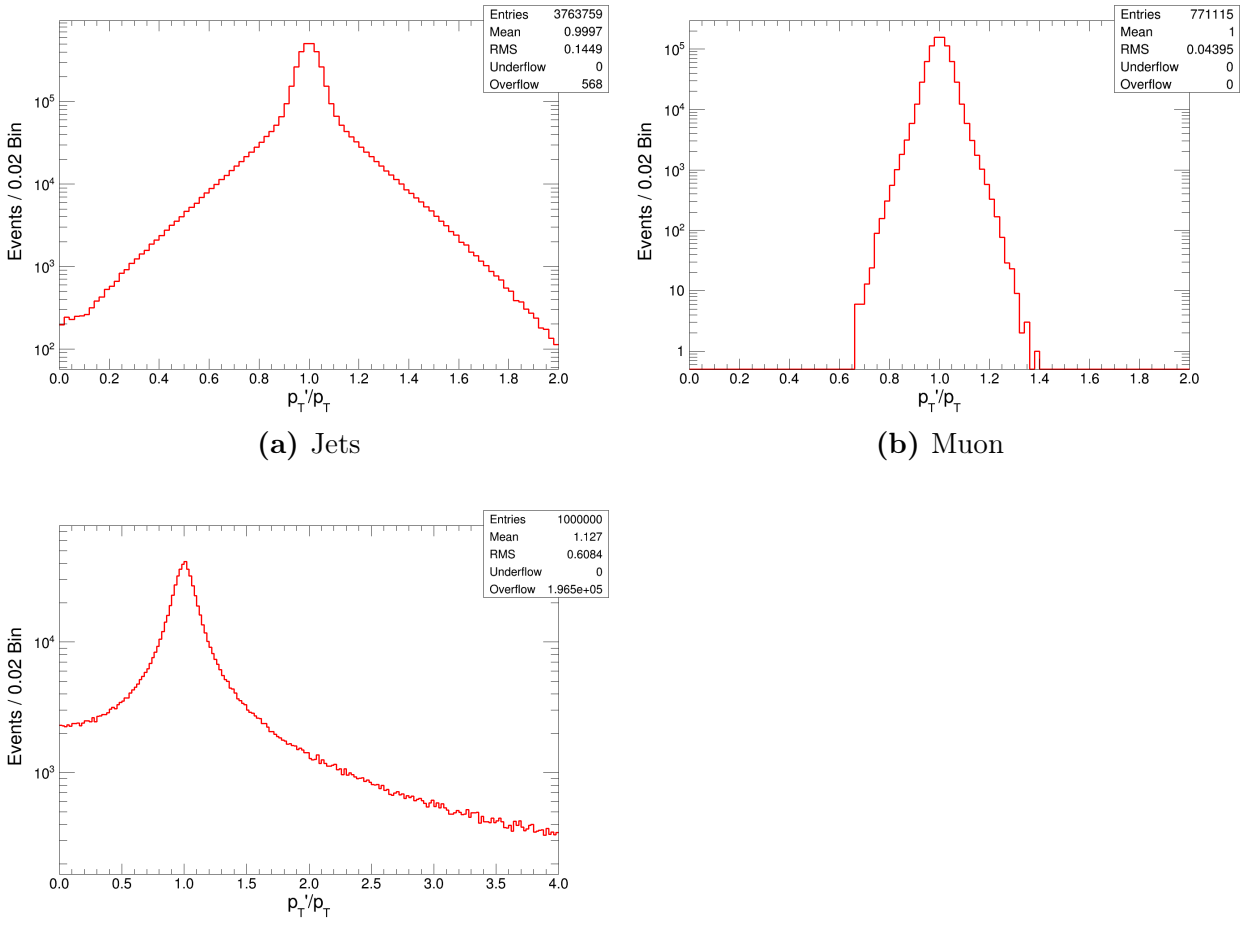

(a) Jets

(b) Muon

(c) MET

Figure E.1: The p_T ratio of **(a)** jets ,**(b)** muons, and **(c)** MET before and after the resolution for the $M_{th} = 9$ TeV QBH signal.

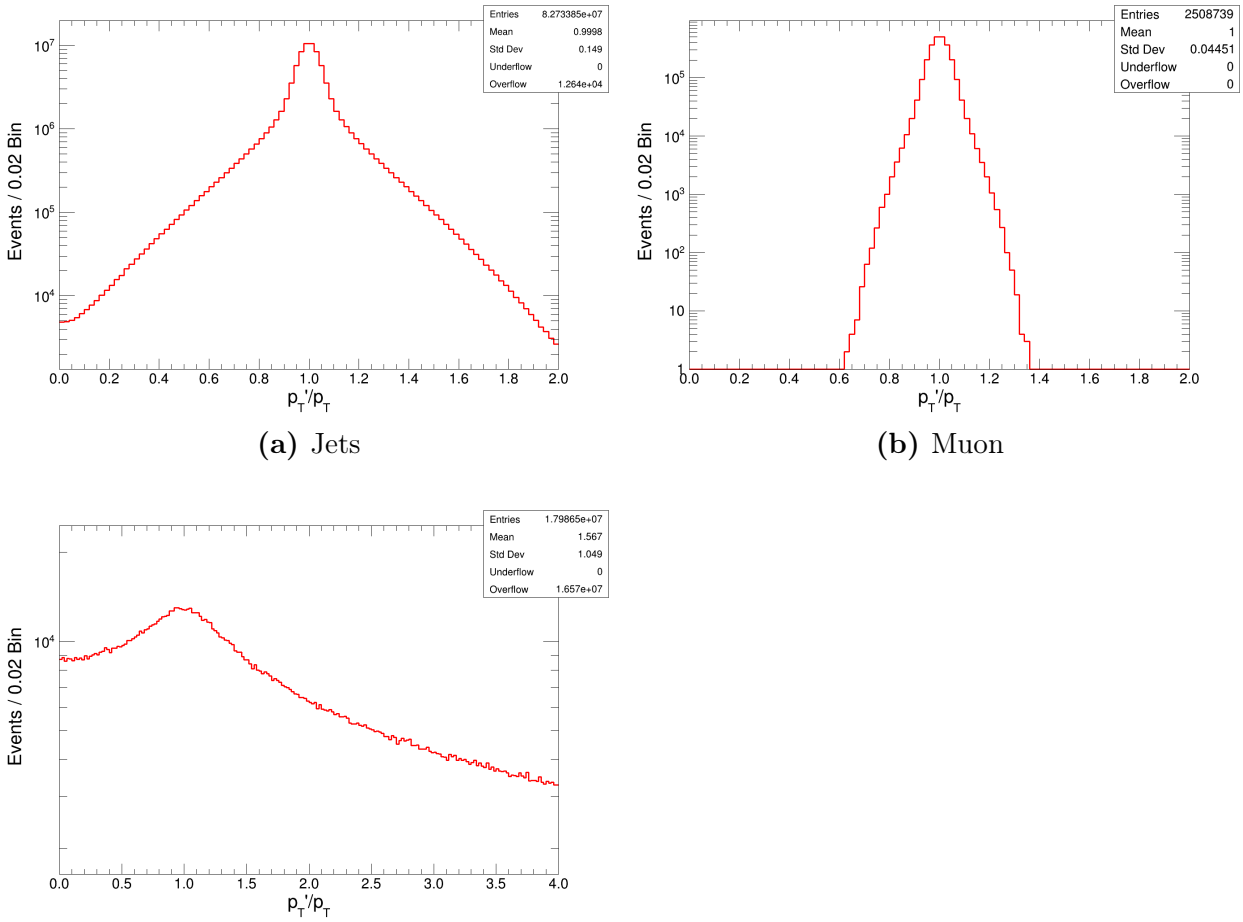

(a) Jets

(b) Muon

(c) MET

Figure E.2: The p_T ratio of **(a)** jets ,**(b)** muons, and **(c)** MET before and after the resolution for the PYTHIA QCD dijet background.

Appendix F

Distribution of the Event Selection Variables

The distribution of the variables used for event selection for the three decay modes of the $M_{th} = 9$ TeV ADDn6 QBH sample and the QCD background.

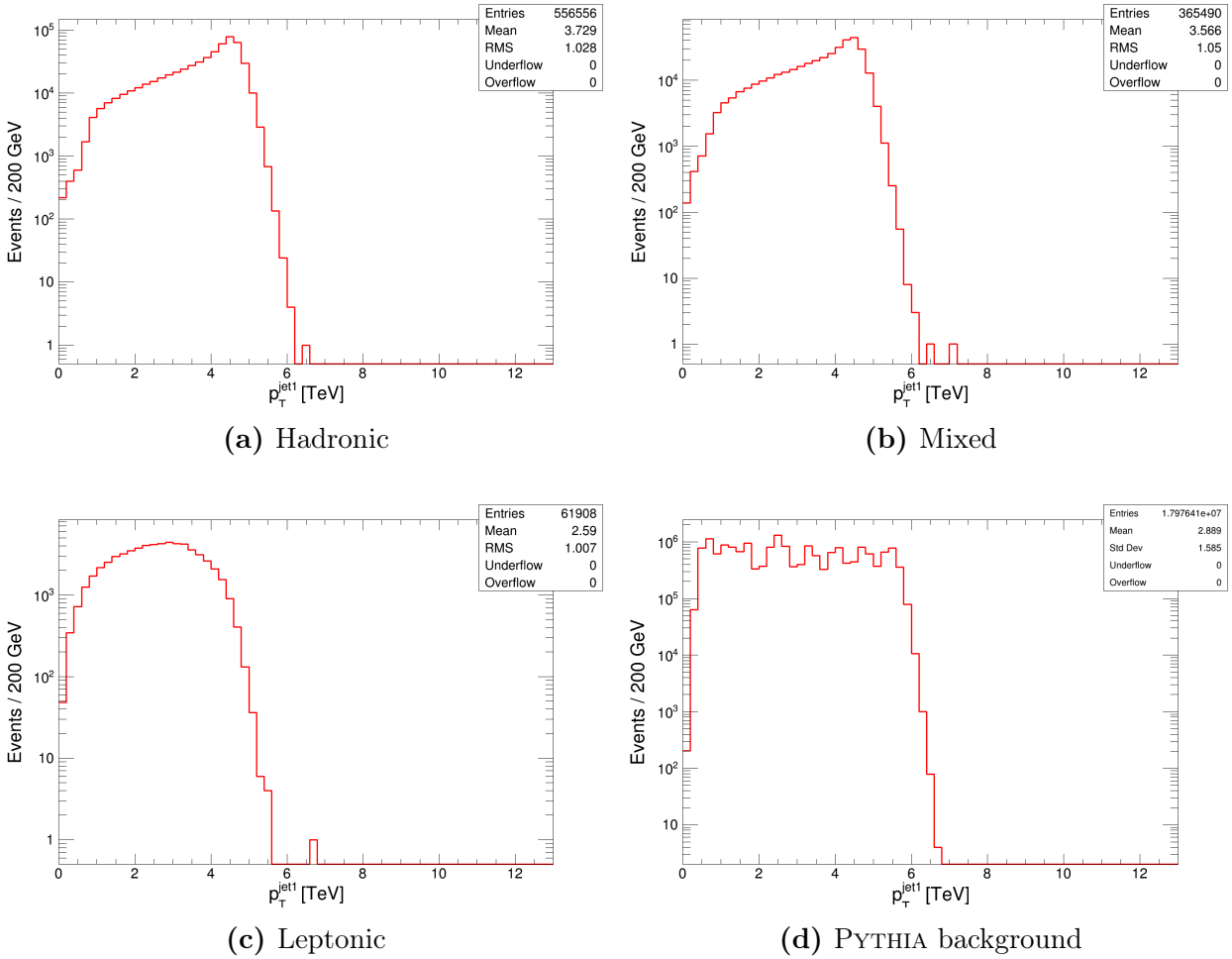

(a) Hadronic **(b)** Mixed

(c) Leptonic **(d)** Pythia background

Figure F.1: First leading jet p_T for **(a)** hadronic, **(b)** mixed, and **(c)** leptonic decays for $M_{th} = 9$ TeV signal and **(d)** the QCD dijet background.

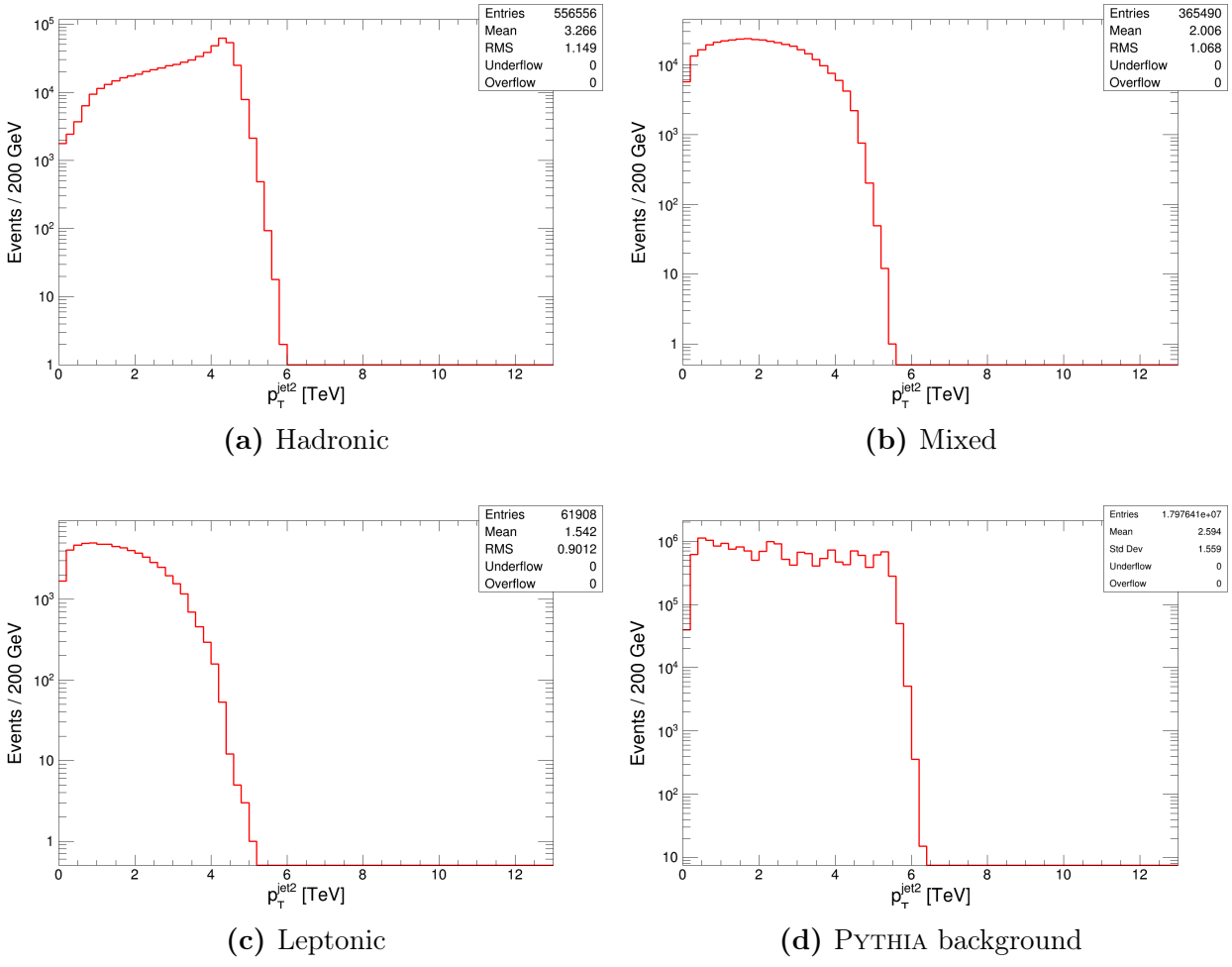

(a) Hadronic **(b)** Mixed

(c) Leptonic **(d)** Pythia background

Figure F.2: Second leading jet p_T for **(a)** hadronic, **(b)** mixed, and **(c)** leptonic decays for $M_{th} = 9$ TeV signal and **(d)** the QCD dijet background.

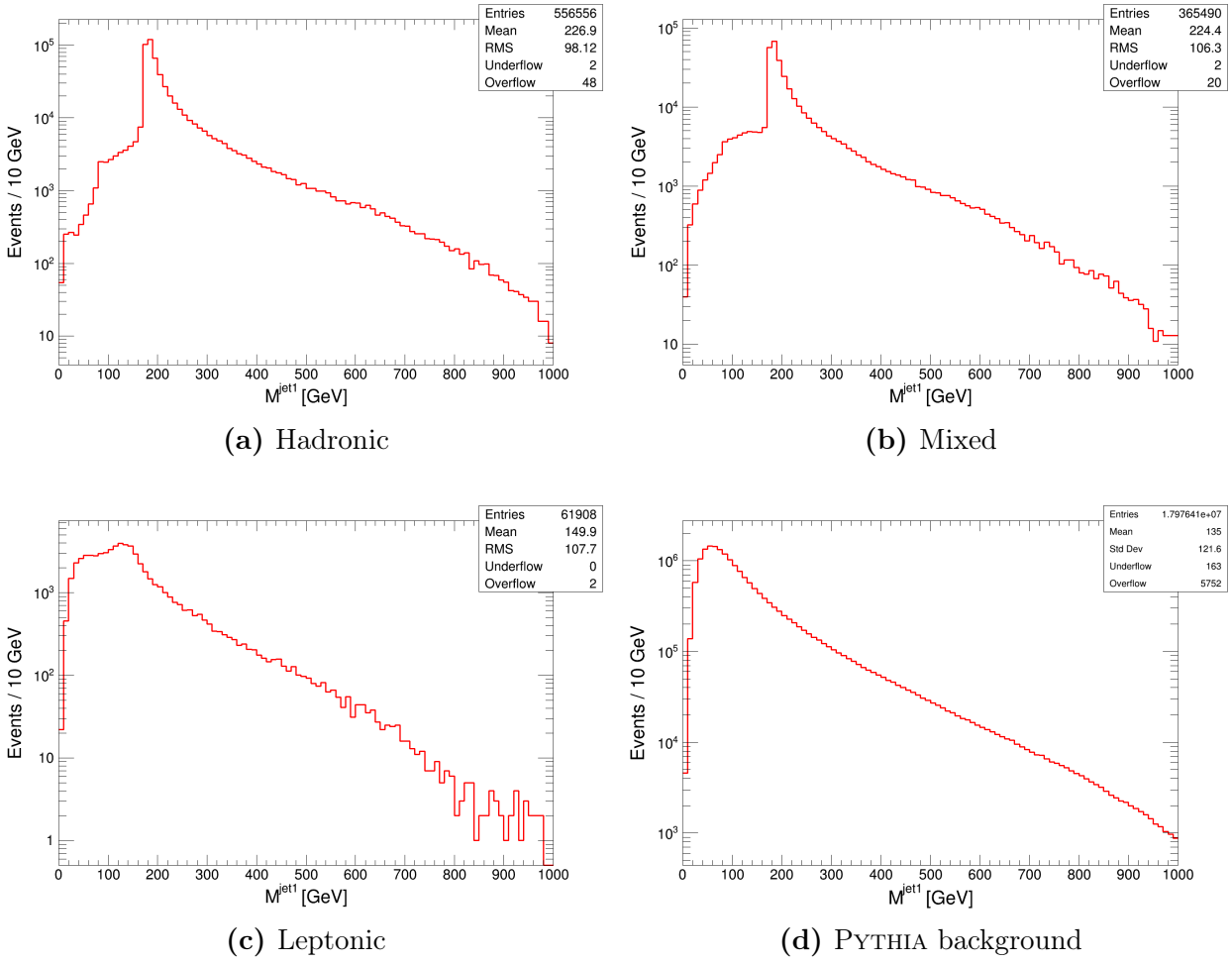

(a) Hadronic **(b)** Mixed

(c) Leptonic **(d)** Pythia background

Figure F.3: Mass distribution of the first leading jet for **(a)** hadronic, **(b)** mixed, and **(c)** leptonic decays for $M_{th} = 9$ TeV signal and **(d)** the QCD dijet background.

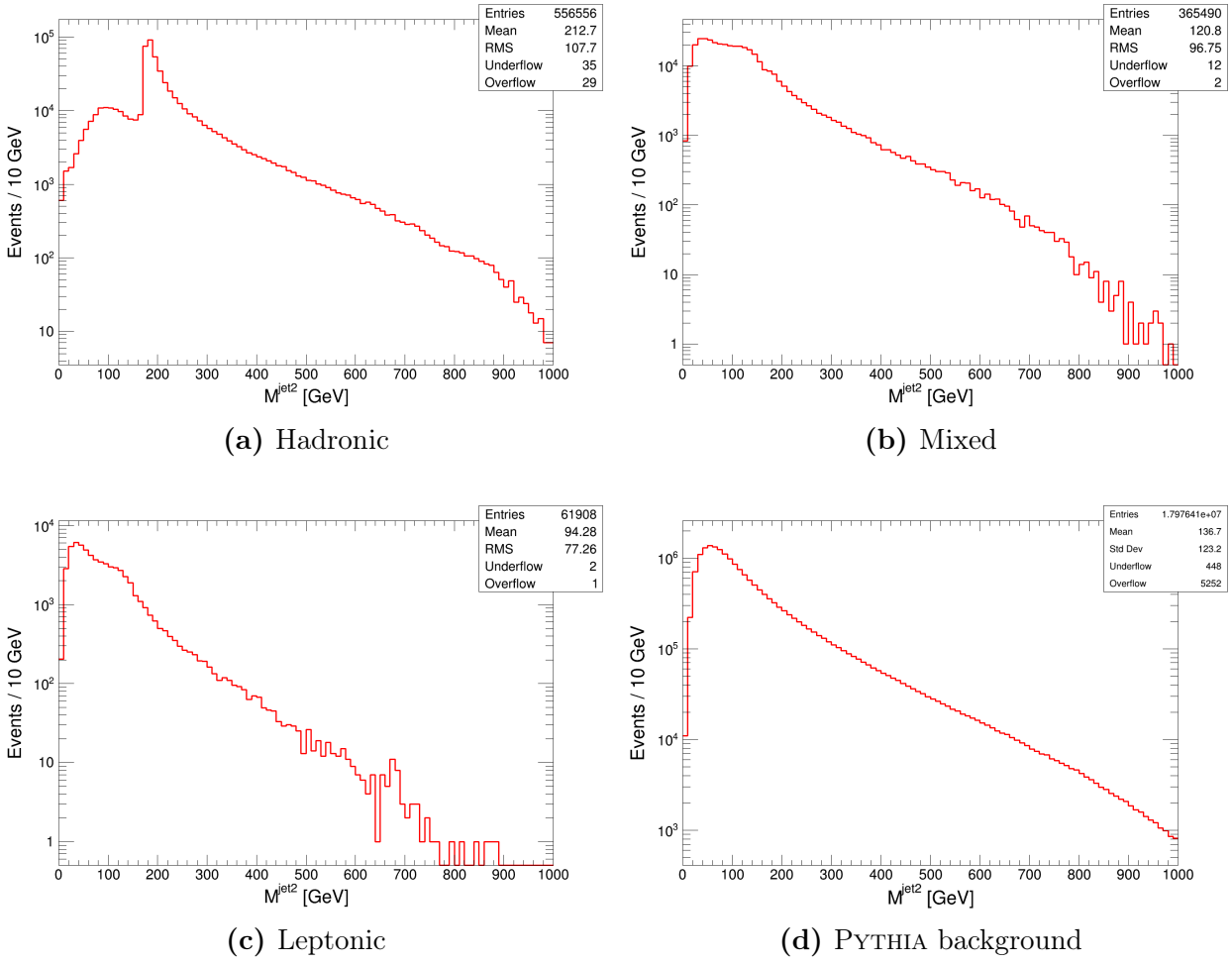

(a) Hadronic **(b)** Mixed

(c) Leptonic **(d)** Pythia background

Figure F.4: Mass distribution of the second leading jet for **(a)** hadronic, **(b)** mixed, and **(c)** leptonic decays for $M_{th} = 9$ TeV signal and **(d)** the QCD dijet background.

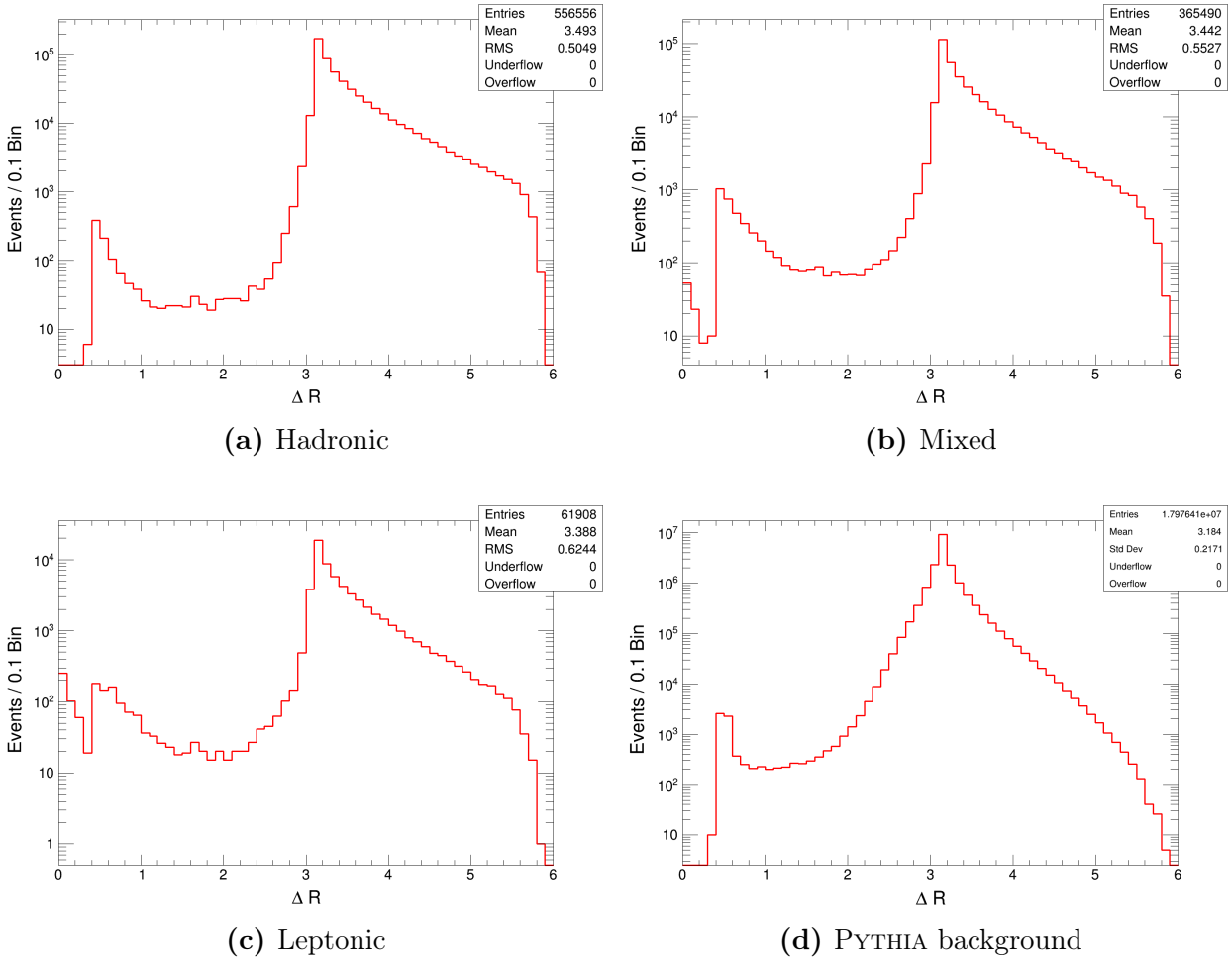

(a) Hadronic **(b)** Mixed

(c) Leptonic **(d)** Pythia background

Figure F.5: ΔR of the two highest p_T jets for **(a)** hadronic, **(b)** mixed, and **(c)** leptonic decays for the $M_{th} = 9$ TeV signal and **(d)** the QCD dijet background.

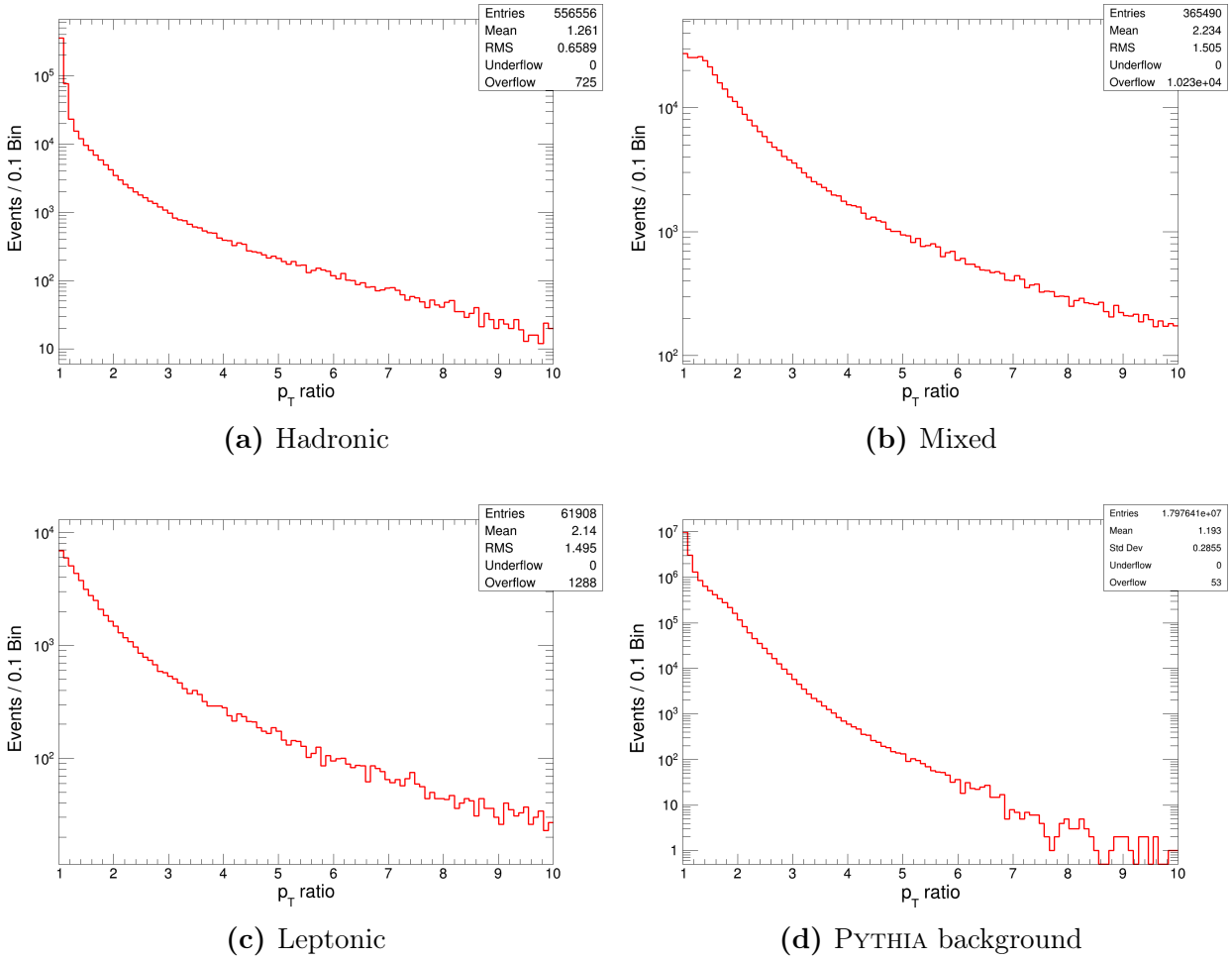

(a) Hadronic **(b)** Mixed

(c) Leptonic **(d)** Pythia background

Figure F.6: p_T ratio of the two highest p_T jets, $\frac{p_{T\text{jet1}}}{p_{T\text{jet2}}}$, for **(a)** hadronic, **(b)** mixed, and **(c)** leptonic decays for $M_{th} = 9$ TeV signal and **(d)** the QCD dijet background.

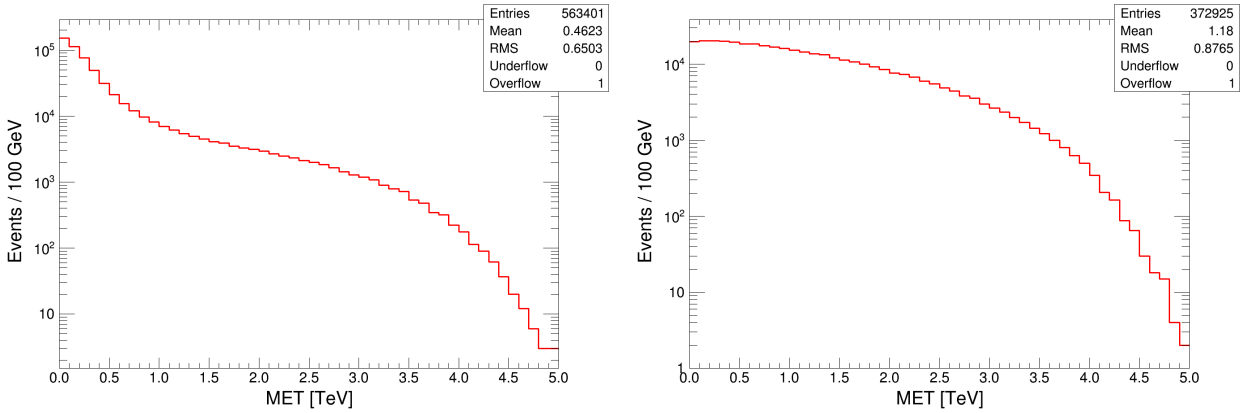

(a) Hadronic **(b)** Mixed

(c) Leptonic **(d)** PYTHIA background

Figure F.7: MET distribution for **(a)** hadronic, **(b)** mixed, and **(c)** leptonic decays for $M_{th} = 9$ TeV signal and **(d)** the QCD dijet background.

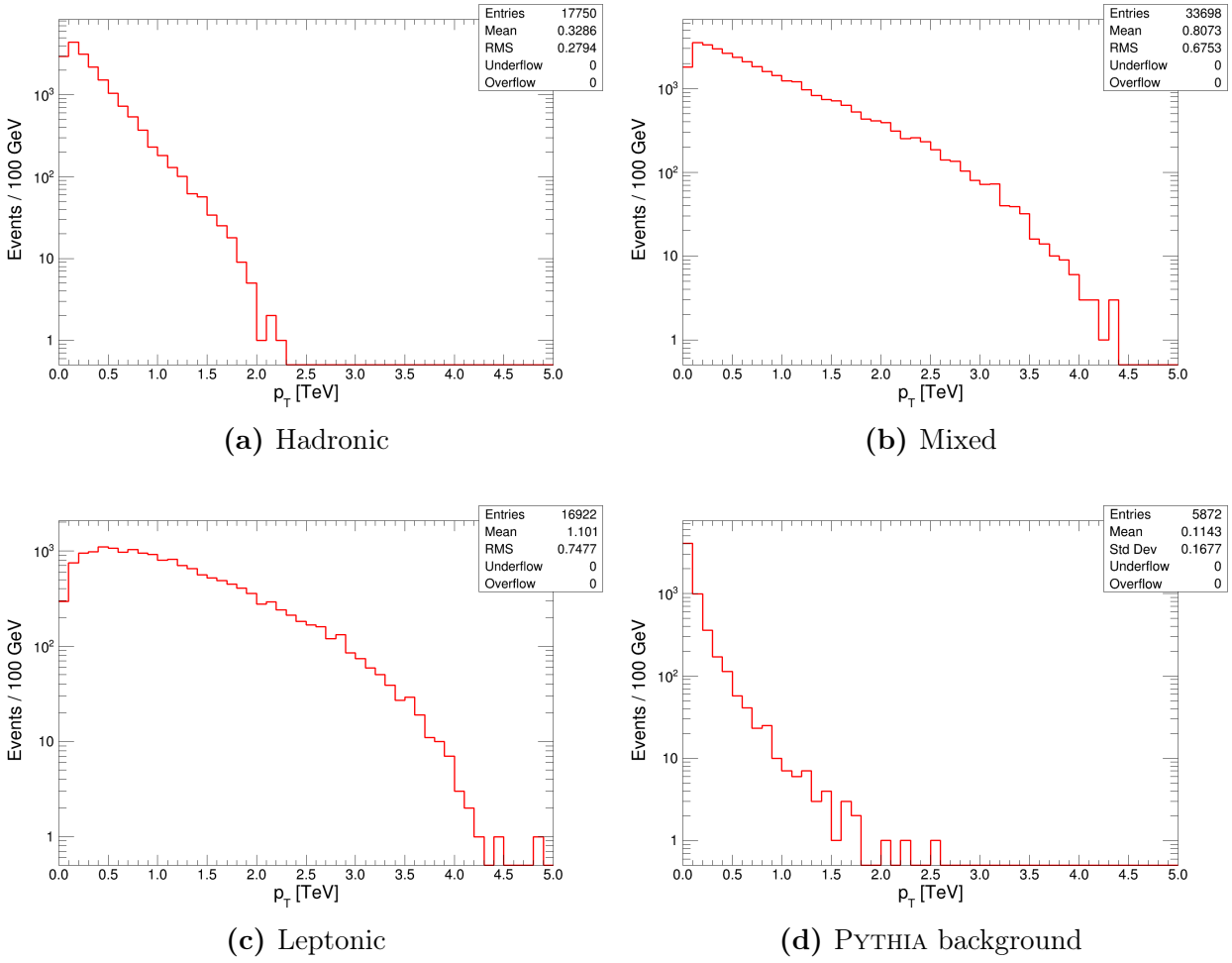

(a) Hadronic **(b)** Mixed

(c) Leptonic **(d)** PYTHIA background

Figure F.8: p_T of the highest p_T lepton for **(a)** hadronic, **(b)** mixed, and **(c)** leptonic decays for the $M_{th} = 9$ TeV signal and **(d)** the QCD dijet background.

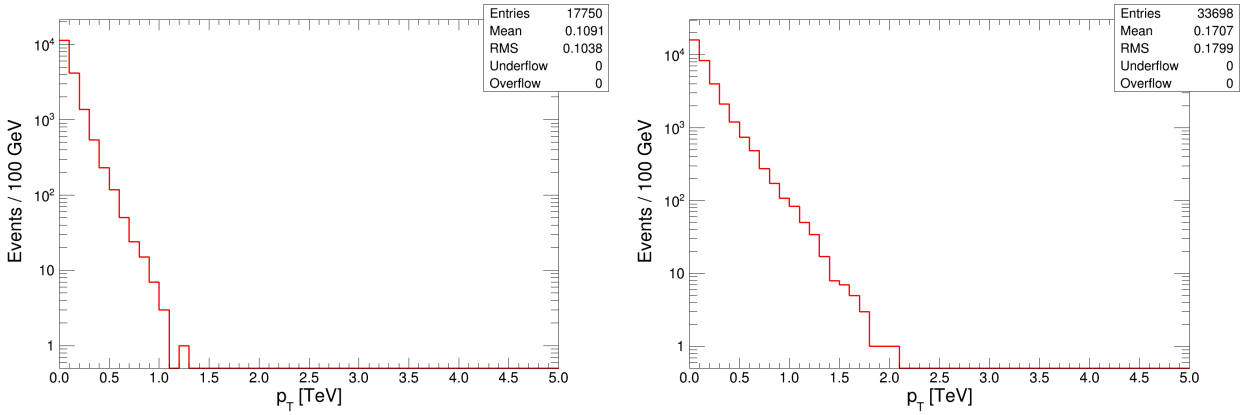

(a) Hadronic

(b) Mixed

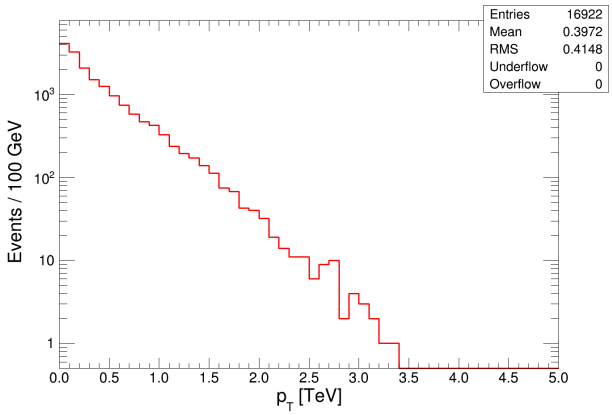

(c) Leptonic

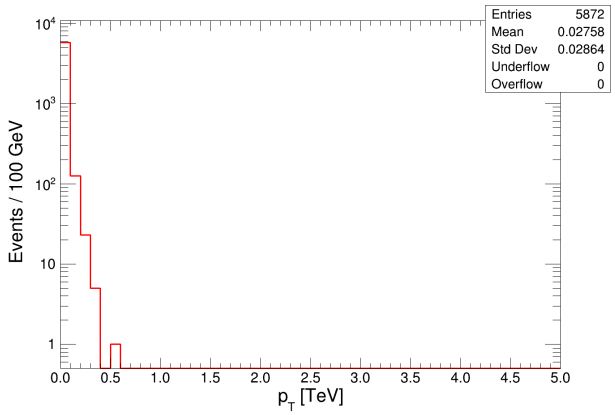

(d) Pythia background

Figure F.9: p_T of the second highest p_T lepton for **(a)** hadronic, **(b)** mixed, and **(c)** leptonic decays for the $M_{th} = 9$ TeV signal and **(d)** the QCD dijet background.

Appendix G

Truth versus Reconstructed Mass Distribution

The comparison of the reconstructed mass distribution versus the truth mass for all the decay modes and all the QBH signal samples in the ADDn6 model.

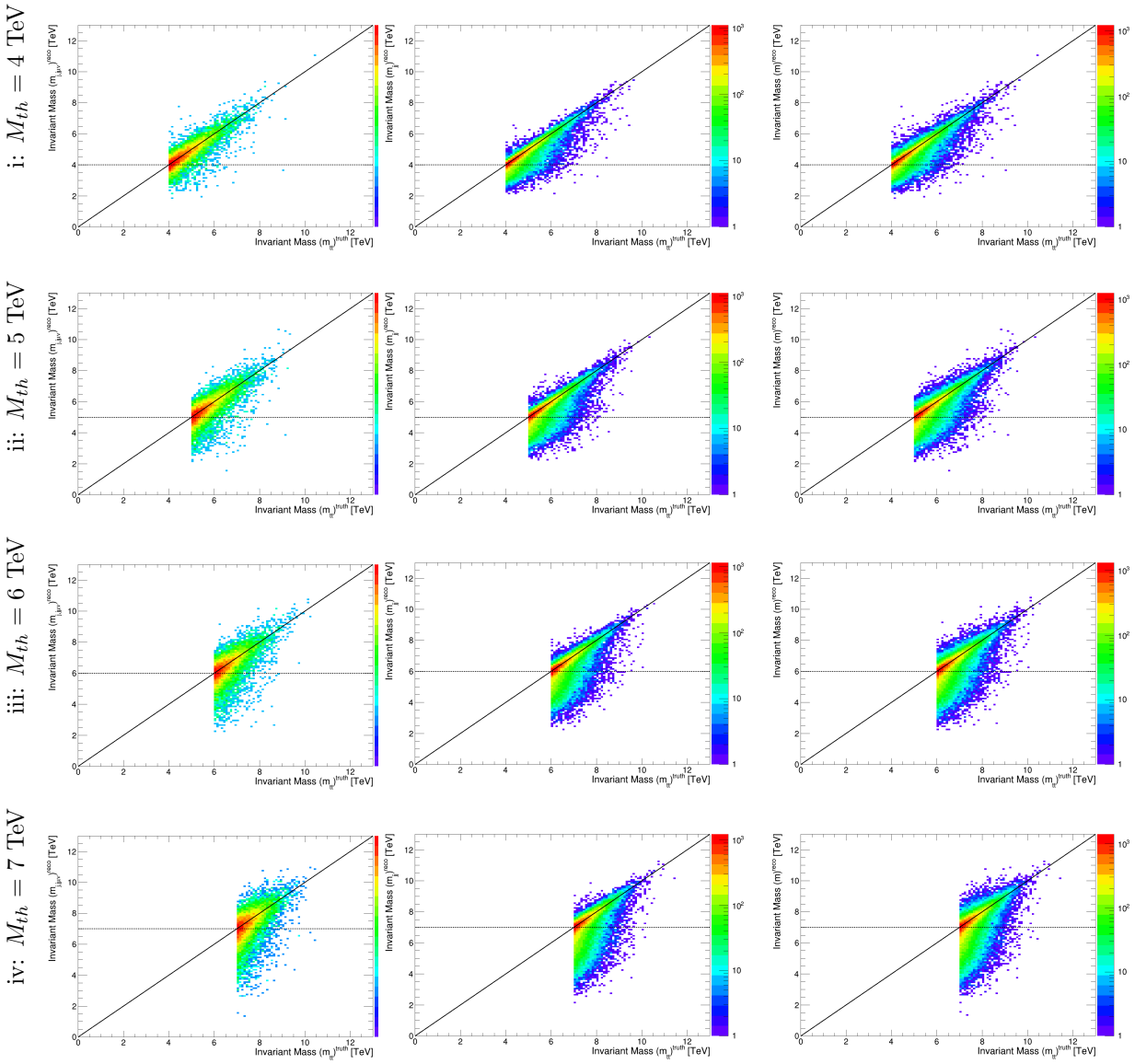

(a) Mixed **(b)** Hadronic **(c)** All

Figure G.1: Comparison of the QBH reconstructed mass and the QBH truth mass. The three columns from left to right show the **(a)** mixed, **(b)** hadronic, and **(c)** all decay modes. The four rows show the QBH **(i)** $M_{th} = 4$ TeV, **(ii)** $M_{th} = 5$ TeV, **(iii)** $M_{th} = 6$ TeV, and **(iv)** $M_{th} = 7$ TeV samples. The results are for the ADDn6 model

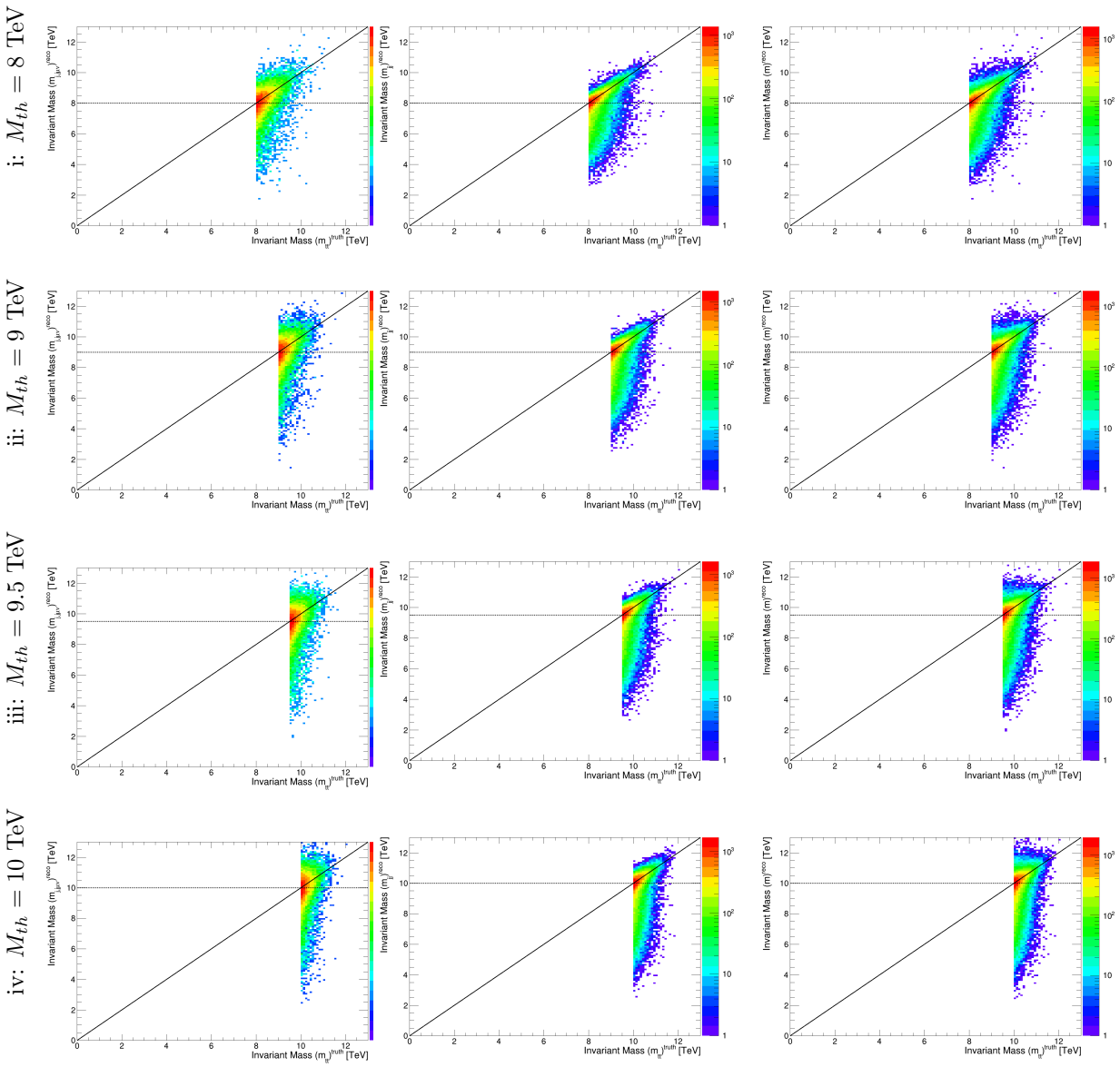

(a) Mixed **(b)** Hadronic **(c)** All

Figure G.2: Comparison of the QBH reconstructed mass and the QBH truth mass. The three columns from left to right show the **(a)** mixed, **(b)** hadronic, and **(c)** all decay modes. The four rows show the QBH **(i)** $M_{th} = 8$ TeV, **(ii)** $M_{th} = 9$ TeV, **(iii)** $M_{th} = 9.5$ TeV, and **(iv)** $M_{th} = 10$ TeV samples. The results are for the ADDn6 model

Appendix H

Comparison of the Mass Distribution of the Different Models

Comparison of the reconstructed mass distribution of the QBH signal samples for all the considered models. The distributions include the detector effects and hence the bin contents are the average value of the generated pseudo-experiments. The comparison is done for the mixed, hadronic and all decays using even QBH threshold mass samples, i.e 4, 6, 8, and 10 TeV samples. Only in this section, for the labels we have used n6, n4, n2, and n1 to represent the ADDn6, ADDn4, ADDn2, and the RS1 model, respectively.

H.1 4 TeV mass threshold

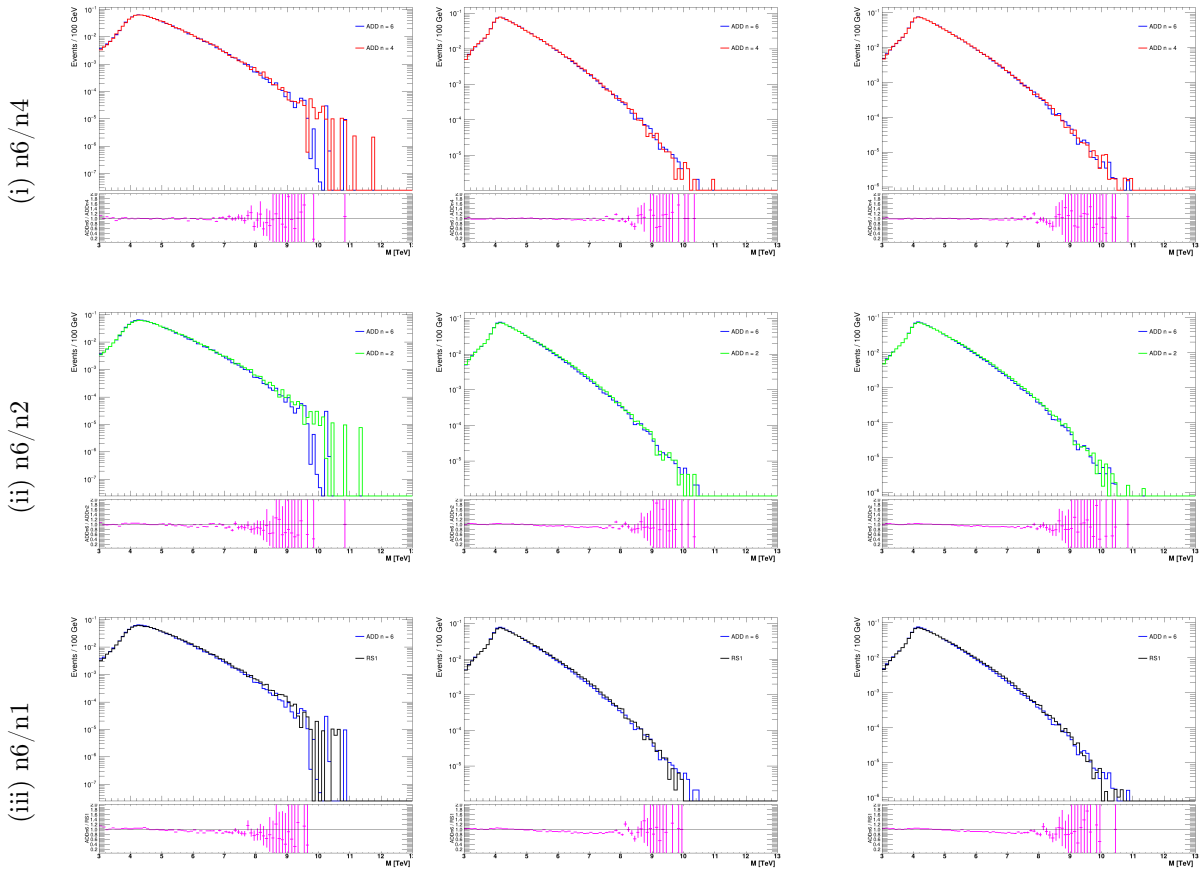

(a) Mixed **(b)** Hadronic **(c)** All

Figure H.1: Mass distribution comparison of the $M_{th} = 4$ TeV QBH sample for different models. The three columns from left to right represent the **(a)** mixed, **(b)** hadronic and **(c)** all decay modes. The three rows show the ratio of the ADDn6 model to **(i)** ADDn4, **(ii)** ADDn2 and **(iii)** RS1 models.

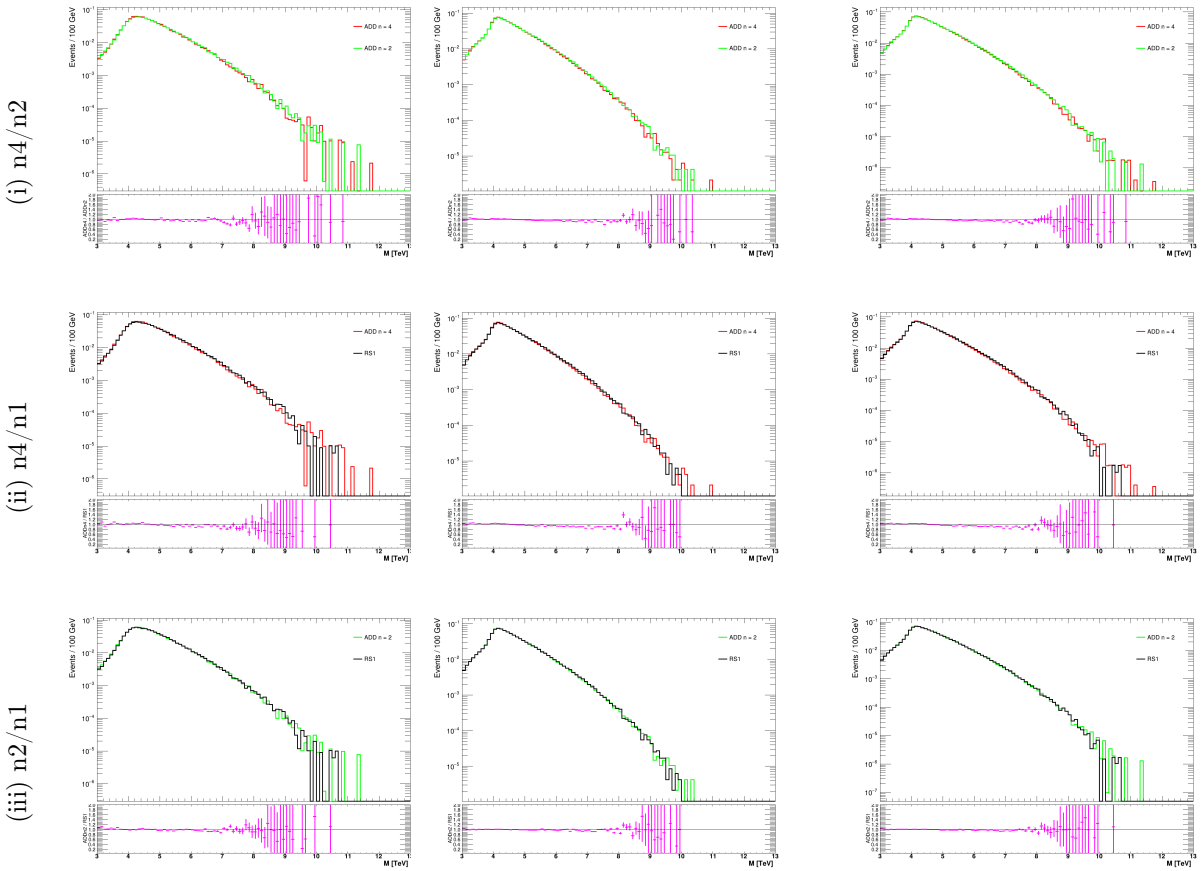

(a) Mixed **(b)** Hadronic **(c)** All

Figure H.2: Mass distribution comparison of the $M_{th} = 4$ TeV QBH sample for different models. The three columns from left to right represent the **(a)** mixed, **(b)** hadronic and **(c)** all decay modes. The three rows show the ratio of the ADDn4 model to **(i)** ADDn2 and **(ii)** RS1 models, and **(iii)** the ratio of ADDn2 model to RS1 model.

H.2 6 TeV mass threshold

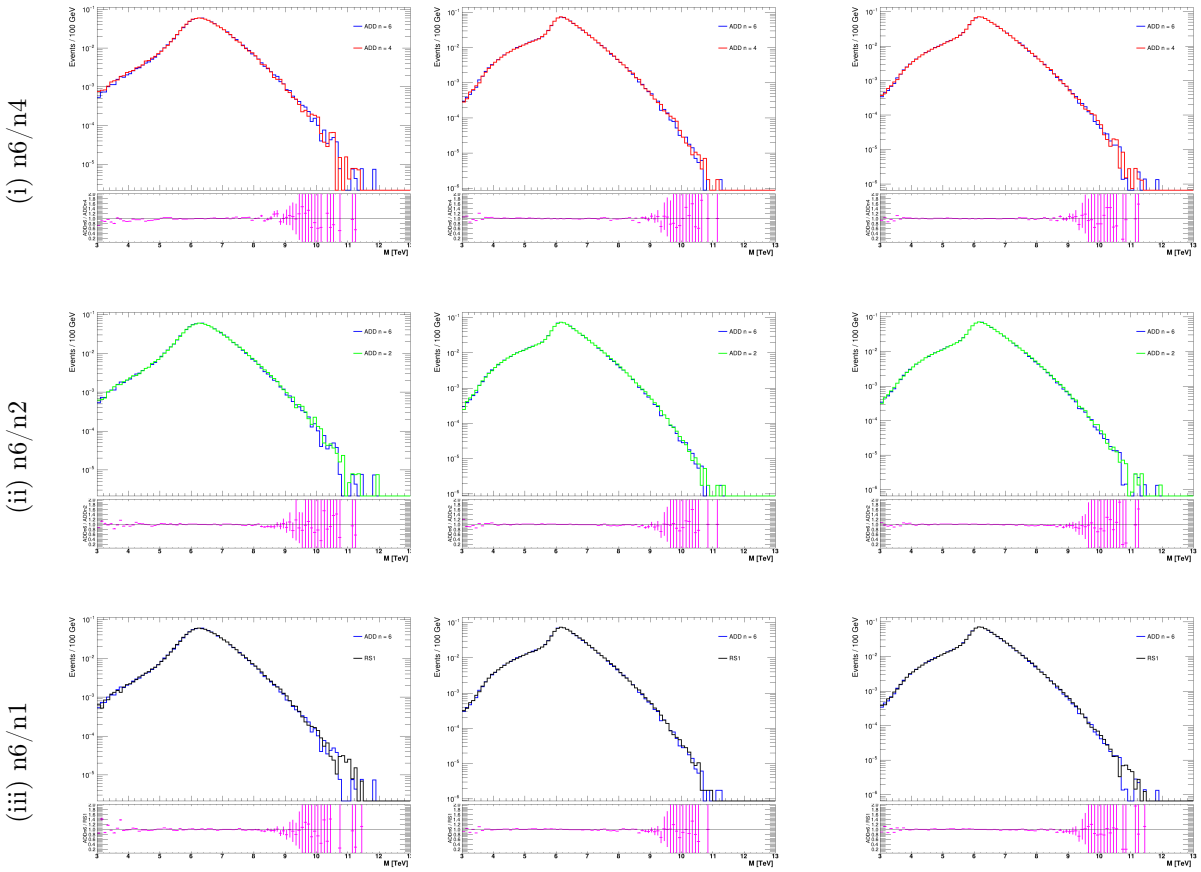

(a) Mixed **(b)** Hadronic **(c)** All

Figure H.3: Mass distribution comparison of the $M_{th} = 6$ TeV QBH sample for different models. The three columns from left to right represent the **(a)** mixed, **(b)** hadronic and **(c)** all decay modes. The three rows show the ratio of the ADDn6 model to **(i)** ADDn4, **(ii)** ADDn2 and **(iii)** RS1 models.

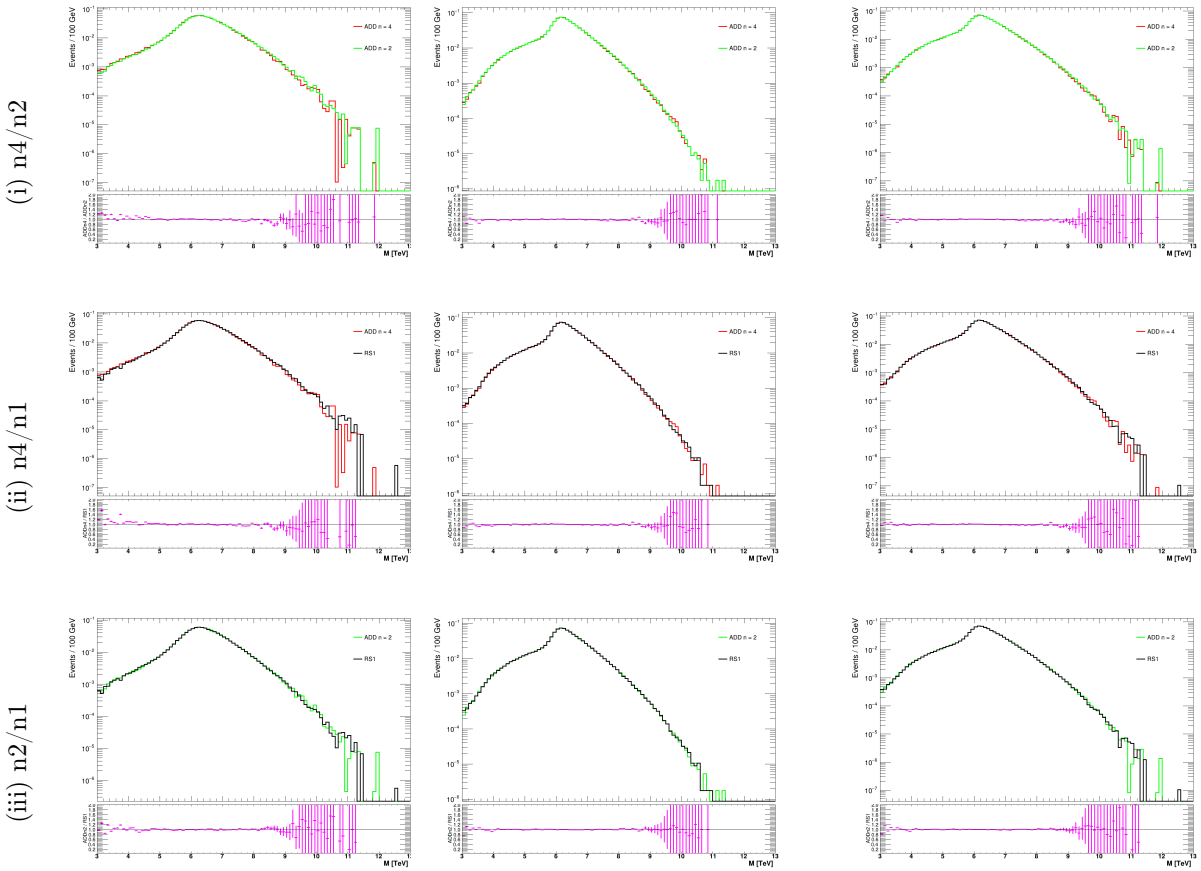

(a) Mixed **(b)** Hadronic **(c)** All

Figure H.4: Mass distribution comparison of the $M_{th} = 6$ TeV QBH sample for different models. The three columns from left to right represent the **(a)** mixed, **(b)** hadronic and **(c)** all decay modes. The three rows show the ratio of the ADDn4 model to **(i)** ADDn2 and **(ii)** RS1 models, and **(iii)** the ratio of ADDn2 model to RS1 model.

H.3 8 TeV mass threshold

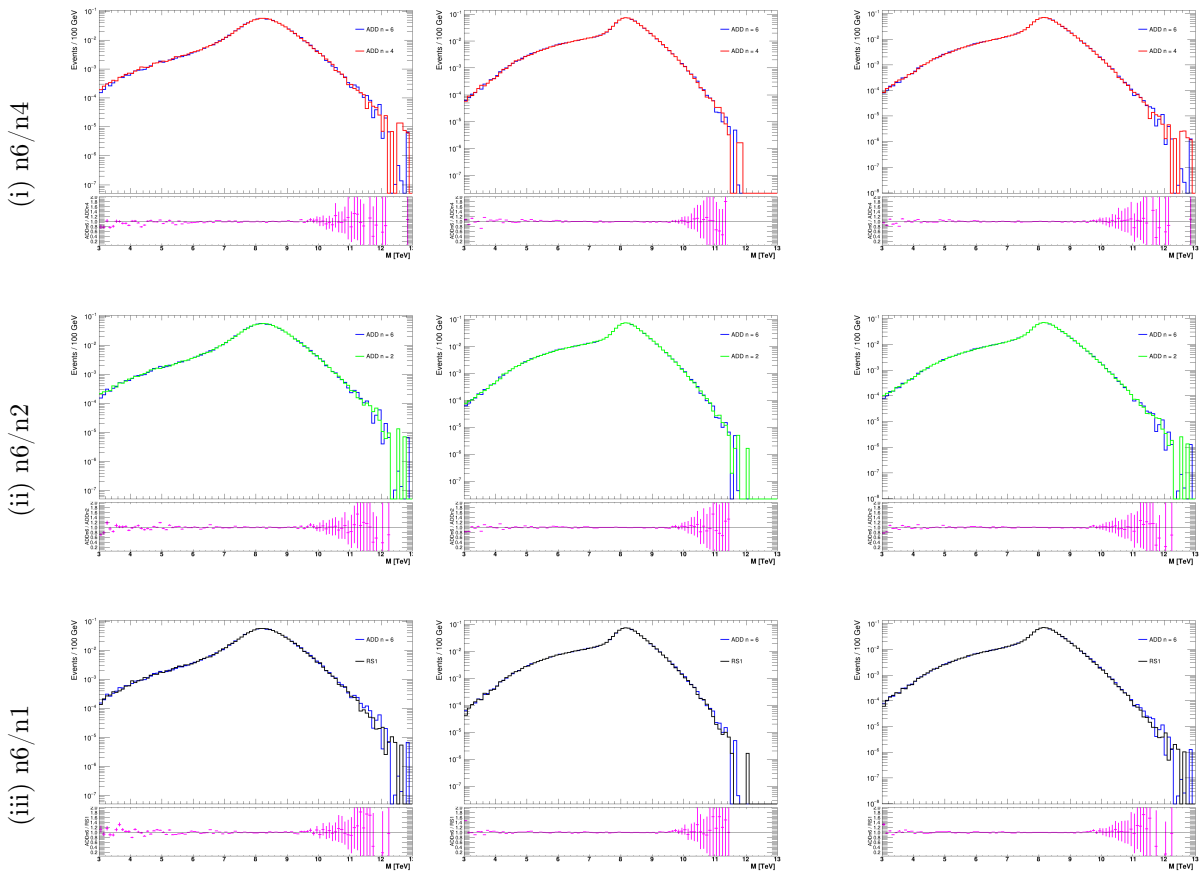

(a) Mixed **(b)** Hadronic **(c)** All

Figure H.5: Mass distribution comparison of the $M_{th} = 8$ TeV QBH sample for different models. The three columns from left to right represent the **(a)** mixed, **(b)** hadronic and **(c)** all decay modes. The three rows show the ratio of the ADDn6 model to **(i)** ADDn4, **(ii)** ADDn2 and **(iii)** RS1 models.

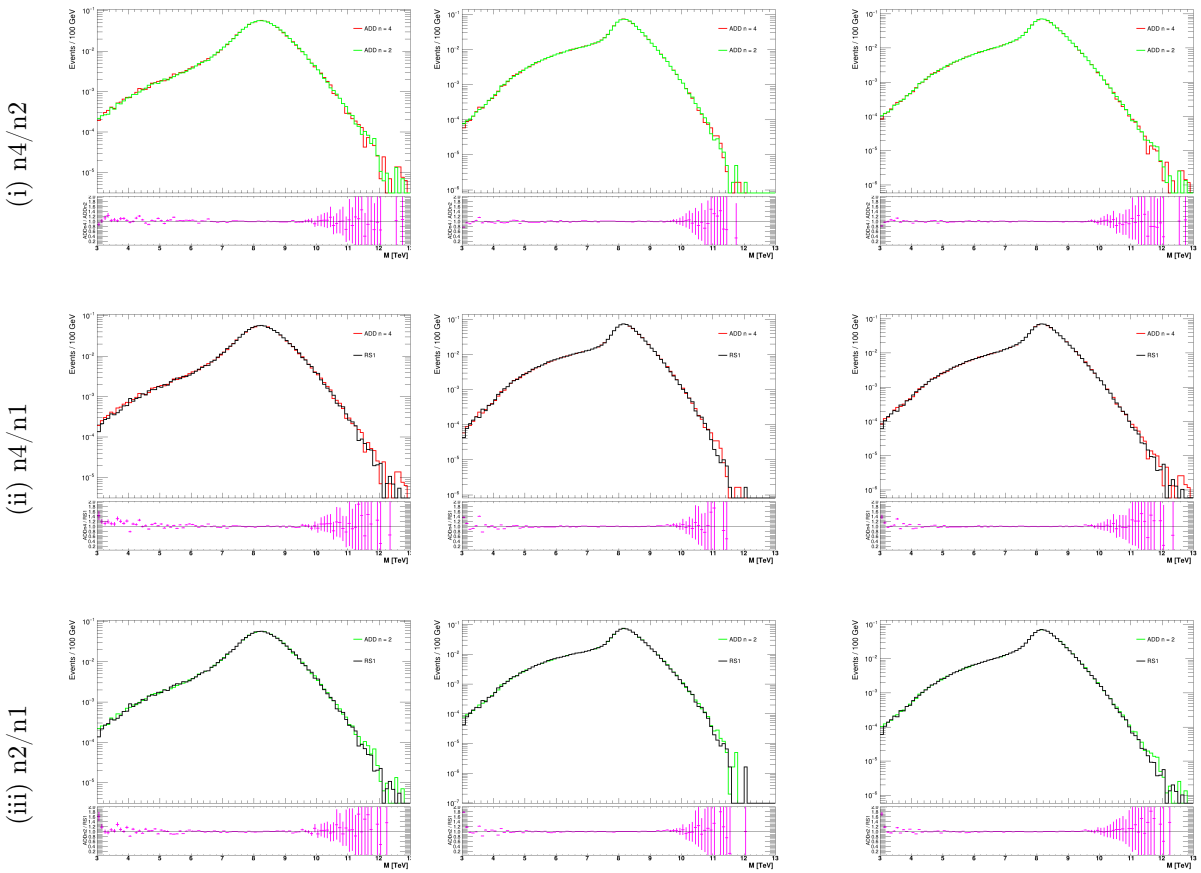

(a) Mixed **(b)** Hadronic **(c)** All

Figure H.6: Mass distribution comparison of the $M_{th} = 8$ TeV QBH sample for different models. The three columns from left to right represent the **(a)** mixed, **(b)** hadronic and **(c)** all decay modes. The three rows show the ratio of the ADDn4 model to **(i)** ADDn2 and **(ii)** RS1 models, and **(iii)** the ratio of ADDn2 model to RS1 model.

H.4 10 TeV mass threshold

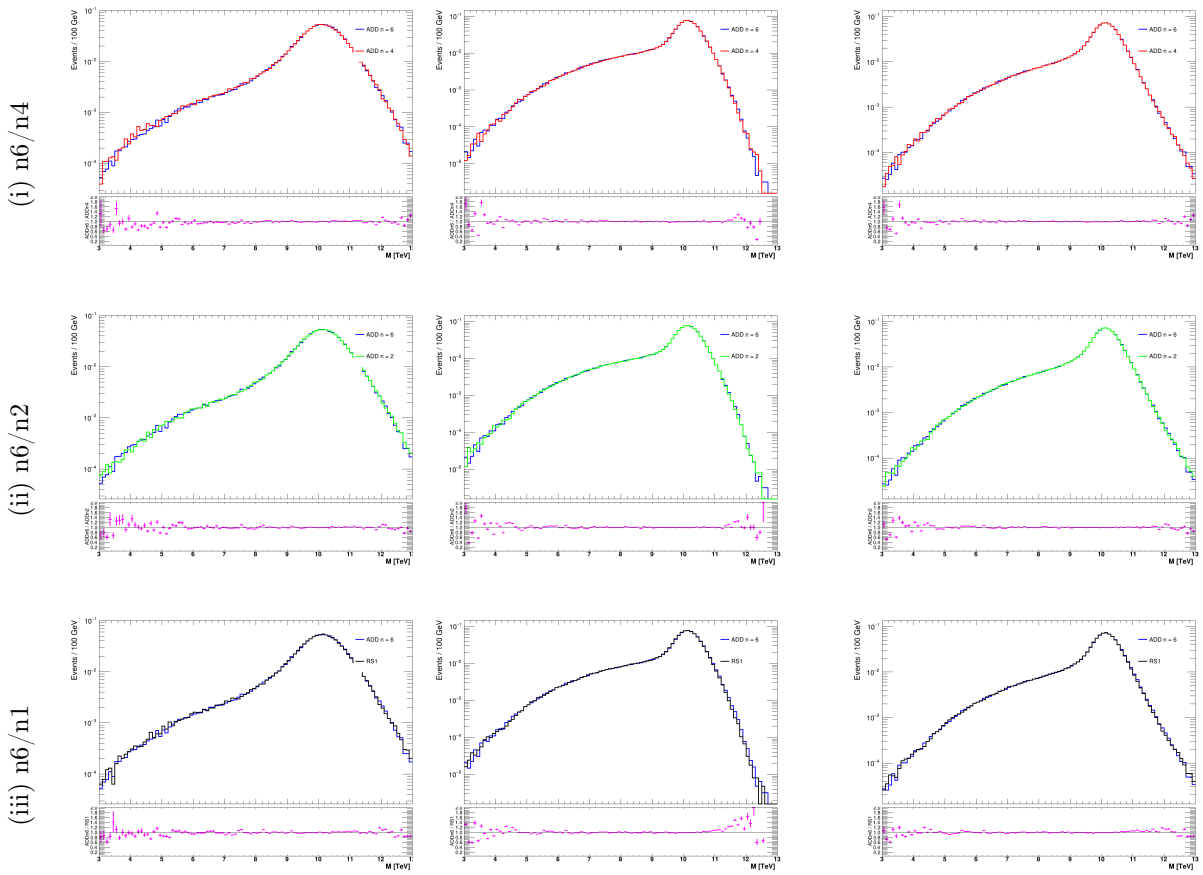

(a) Mixed **(b)** Hadronic **(c)** All

Figure H.7: Mass distribution comparison of the $M_{th} = 10$ TeV QBH sample for different models. The three columns from left to right represent the **(a)** mixed, **(b)** hadronic and **(c)** all decay modes. The three rows show the ratio of the ADDn6 model to **(i)** ADDn4, **(ii)** ADDn2 and **(iii)** RS1 models.

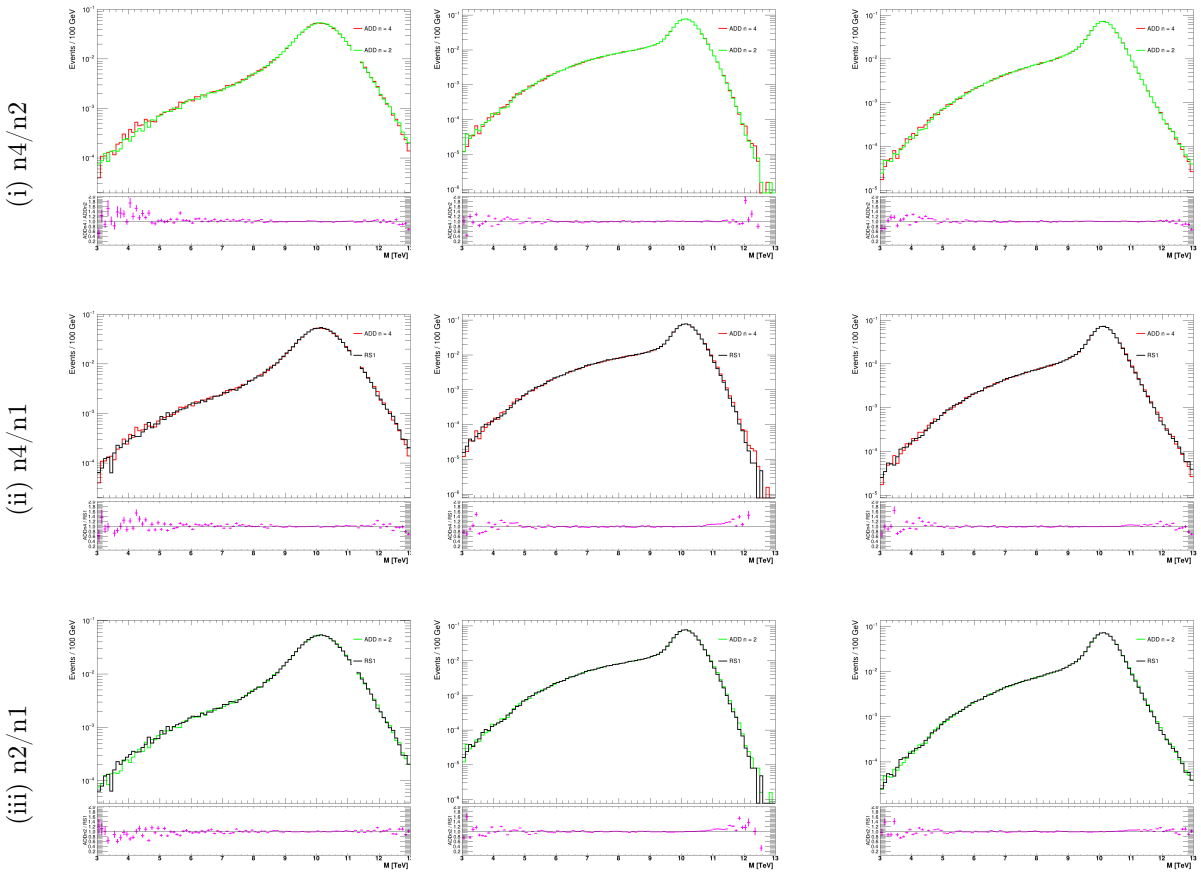

(a) Mixed **(b)** Hadronic **(c)** All

Figure H.8: Mass distribution comparison of the $M_{th} = 10$ TeV QBH sample for different models. The three columns from left to right represent the **(a)** mixed, **(b)** hadronic and **(c)** all decay modes. The three rows show the ratio of the ADDn4 model to **(i)** ADDn2 and **(ii)** RS1 models, and **(iii)** the ratio of ADDn2 model to RS1 model.

Appendix I

Distribution of the pseudo-experiments

The distribution of the number of events for the generated pseudo-experiments for each decay mode of the ADDn6 QBH signal samples and the Pythia QCD. The number of events is the integral of the distribution with $M > M_{th}$.

I.1 PYTHIA

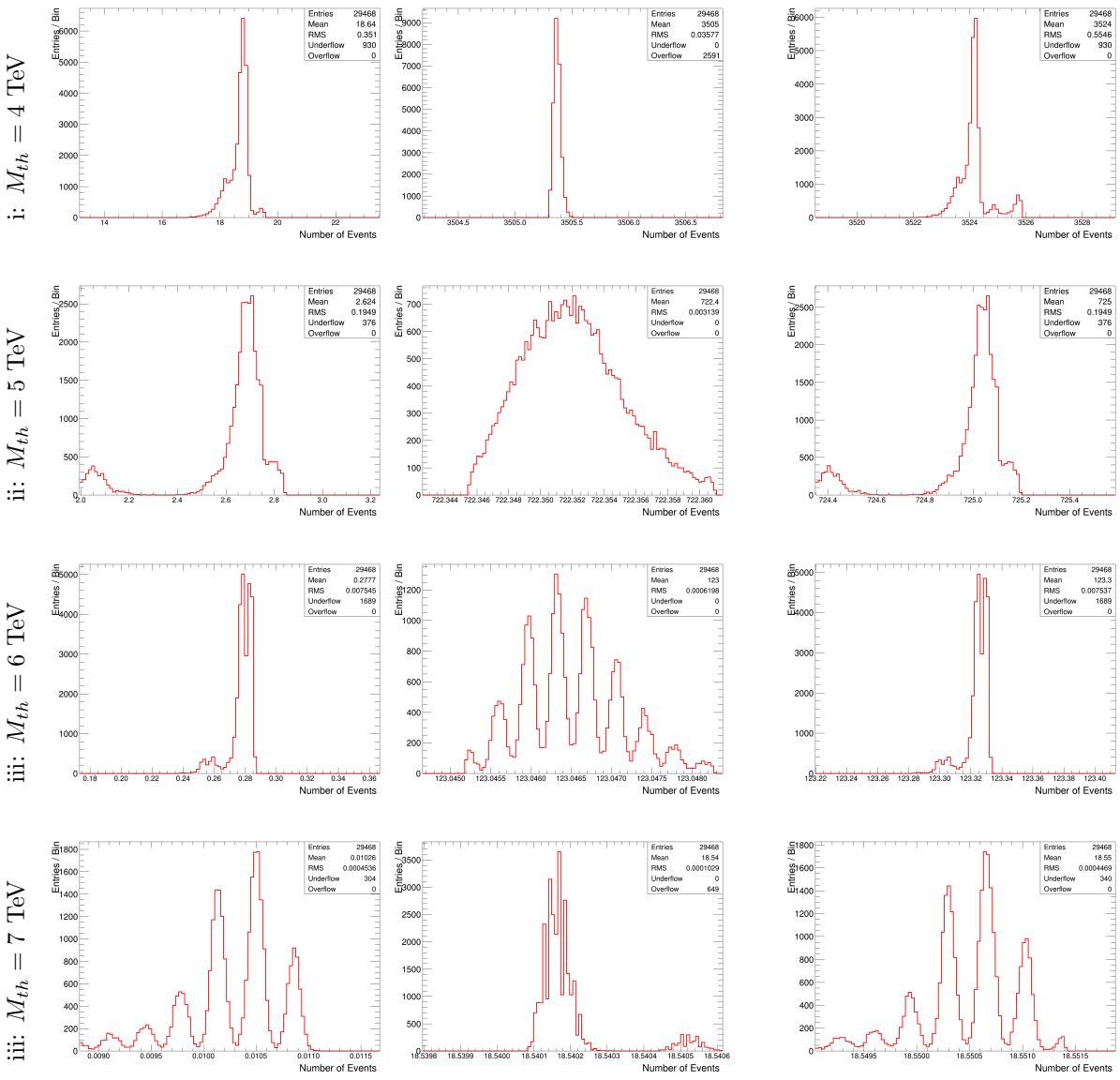

(a) Mixed **(b)** Hadronic **(c)** All

Figure I.1: The distribution of the number of events for the generated pseudo-experiments for each decay mode of the $M_{th} = 10$ TeV QBH signal sample and the PYTHIA QCD. The number of events is the integral of the distribution with $M > M_{th}$.

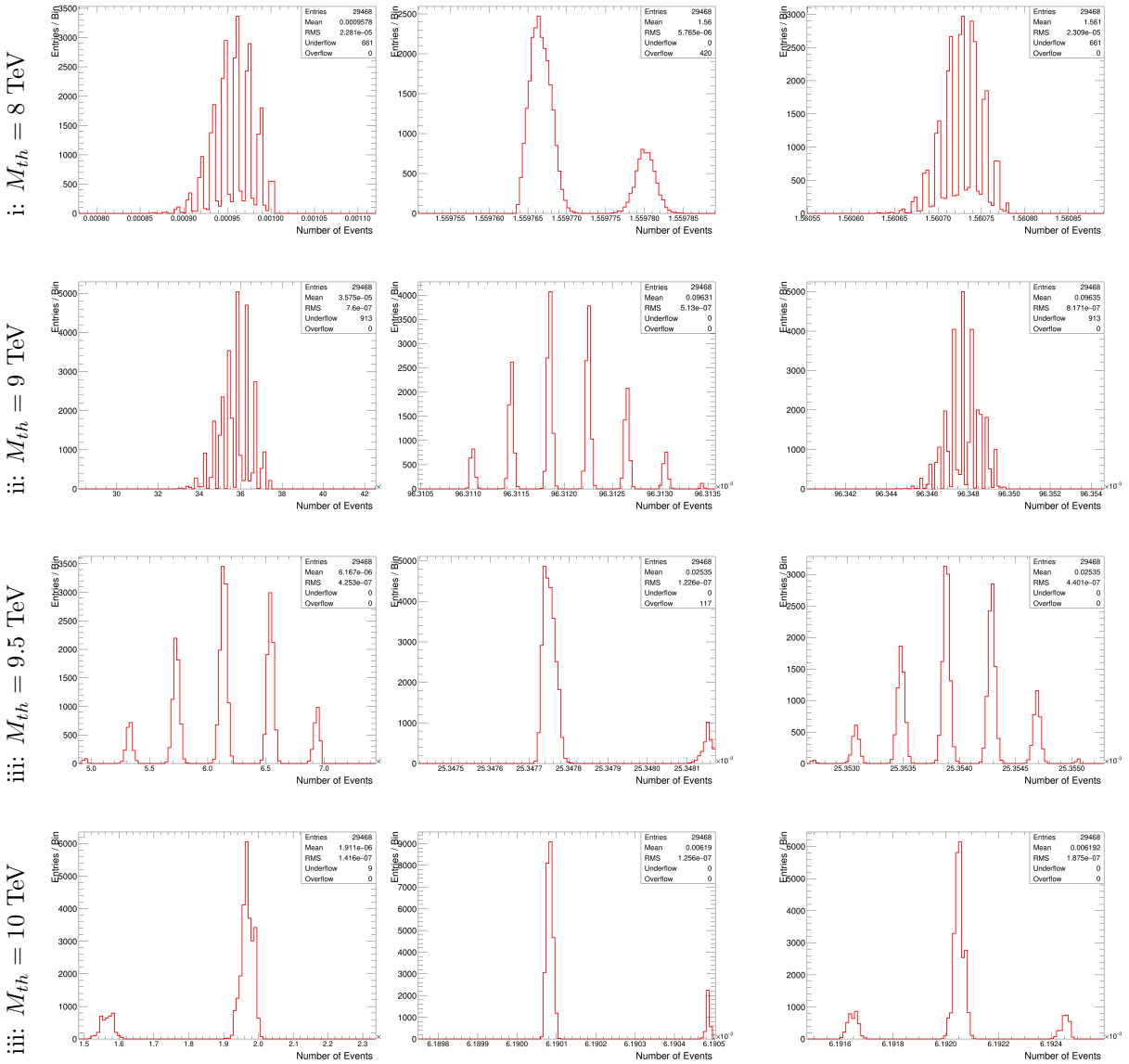

(a) Mixed **(b)** Hadronic **(c)** All

Figure I.2: The distribution of the number of events for the generated pseudo-experiments for each decay mode of the $M_{th} = 10$ TeV QBH signal sample and the PYTHIA QCD. The number of events is the integral of the distribution with $M > M_{th}$.

I.2 QBH

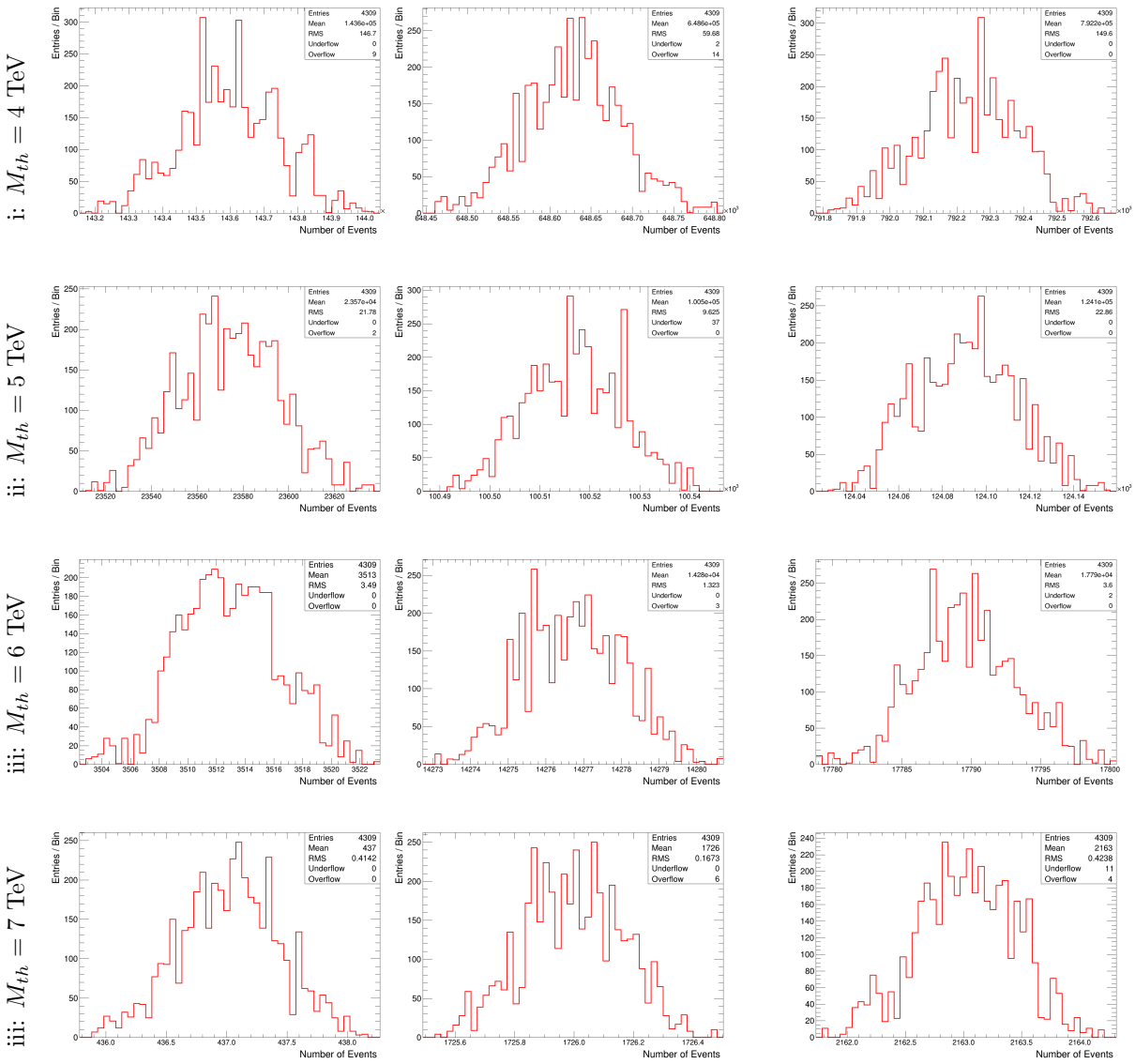

(a) Mixed **(b)** Hadronic **(c)** All

Figure I.3: The distribution of the number of events for the generated pseudo-experiments for each decay mode of the $M_{th} = 10$ TeV QBH signal sample and the Pythia QCD. The number of events is the integral of the distribution with $M > M_{th}$.

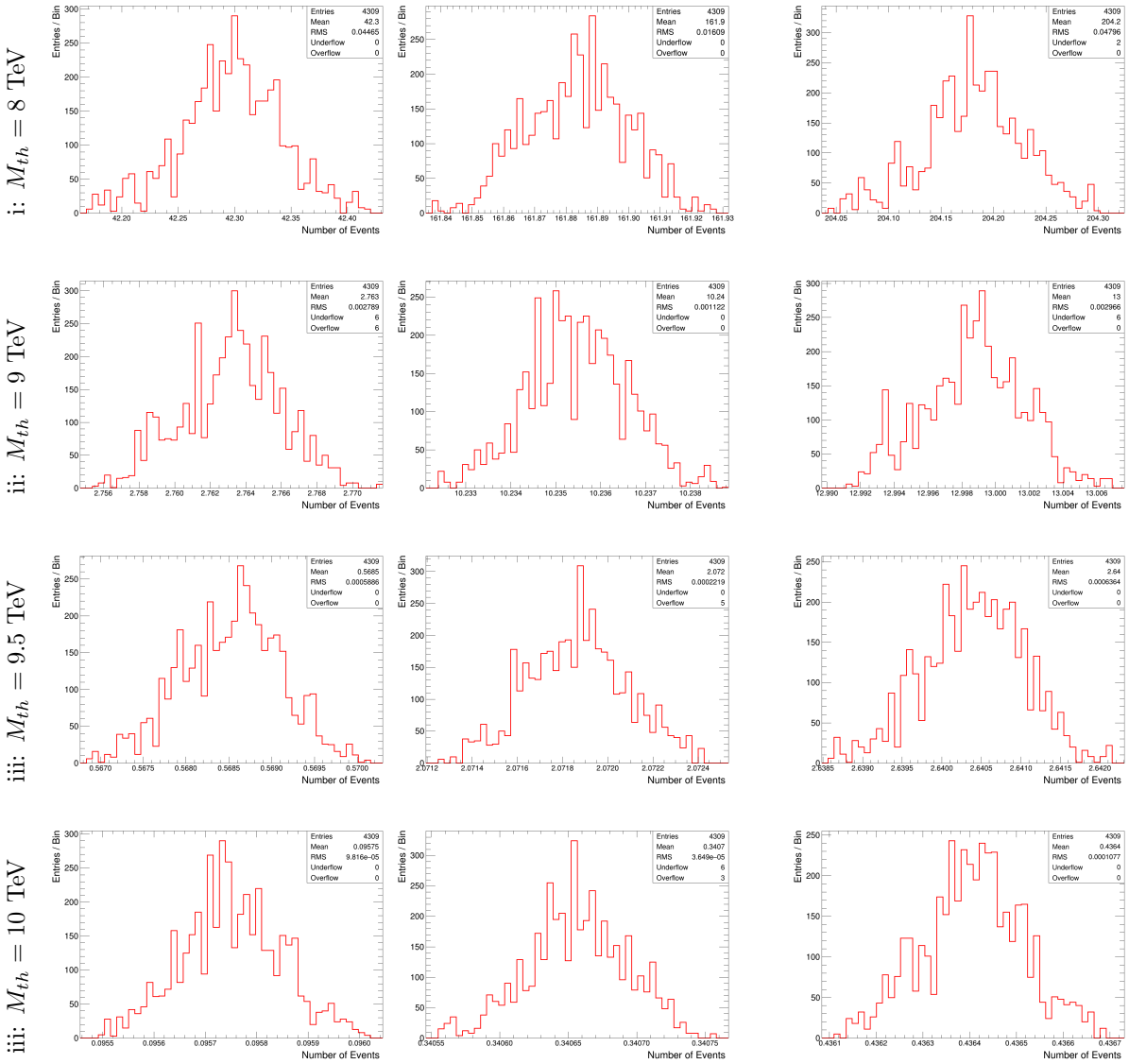

(a) Mixed **(b)** Hadronic **(c)** All

Figure I.4: The distribution of the number of events for the generated pseudo-experiments for each decay mode of the $M_{th} = 10$ TeV QBH signal sample and the Pythia QCD. The number of events is the integral of the distribution with $M > M_{th}$.

Appendix J

Mass Distribution of Signal and Background for the Different Models

The mass distribution of the QBH signal samples and the background in different topologies for the different models used in this study.

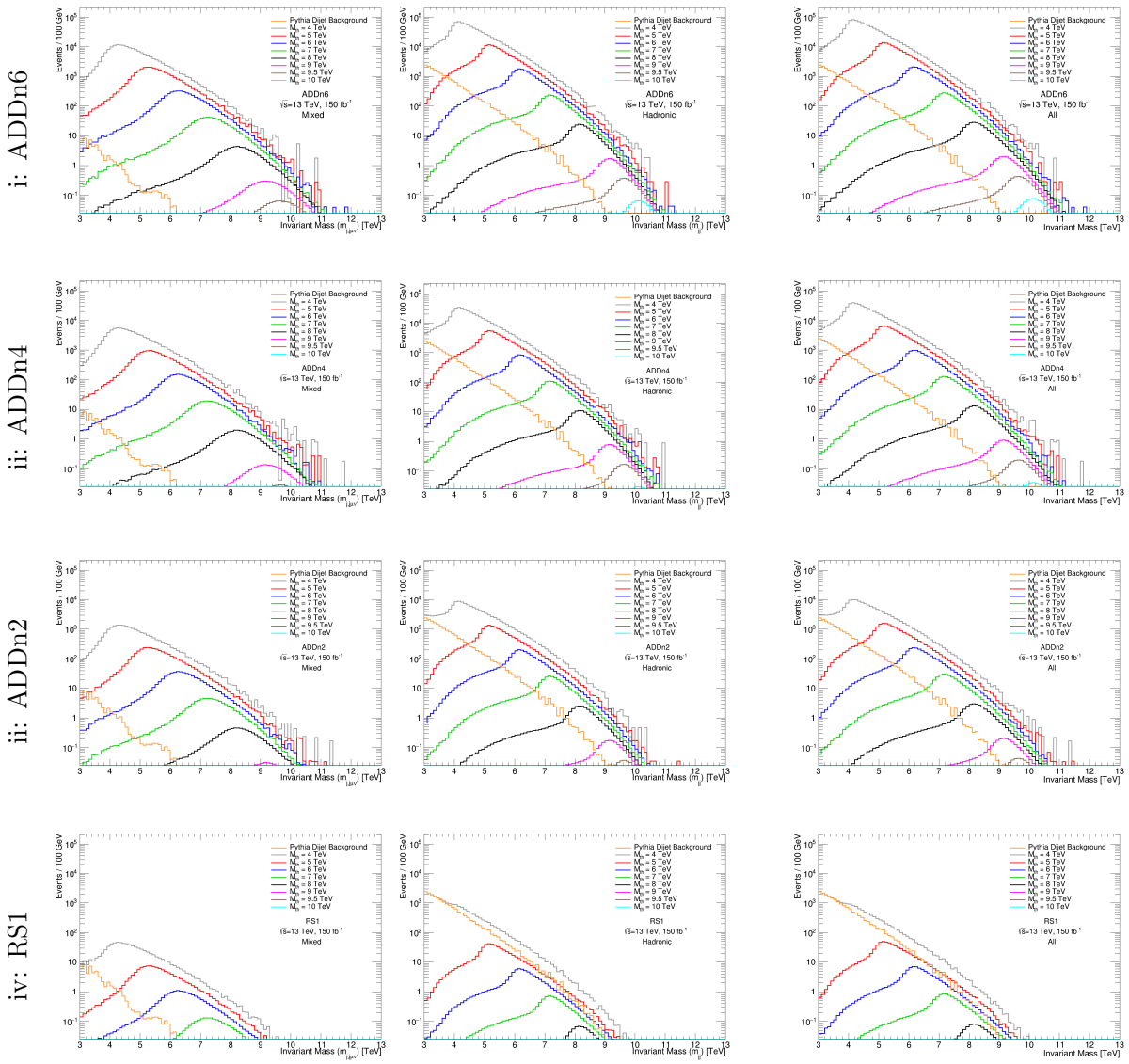

(a) Mixed **(b)** Hadronic **(c)** All

Figure J.1: Mass distribution of QBH signal samples along with the background for different models and topologies. The three columns from left to right show the **(a)** mixed, **(b)** hadronic, and **(c)** all topologies. The four rows show the **(i)** ADDn6, **(ii)** ADDn4, **(iii)** ADDn2, and **(iv)** RS1 models.

Appendix K

Likelihood Calculation

In this section we show the derivation of Equation 7.6 using the Poisson-Poisson model. The likelihood function was taken to be

$$\mathcal{L}(s,b) = \text{Pois}(n|s+b)\,\text{Pois}(m|\tau b)\,, \tag{K.1}$$

where s is the number of signal events, b is the number of background events, and n is the number of observed events which in our case comes from MC simulation. The second Poisson distribution is a control measurement to constrain b. It has a mean of τm where m is the number of events in a sample where signal is not present and τ is a scale factor which its uncertainty is often neglected. In simpler words, the second Poisson distribution encodes the background uncertainty which serves to constrain the number of background events. We used the profile likelihood ratio

$$\lambda(s) = \frac{\mathcal{L}\left(s,\hat{\hat{b}}\right)}{\mathcal{L}\left(\hat{s},\hat{b}\right)}, \tag{K.2}$$

and the test statistic

$$q_0 = -2\ln\lambda(0)\,. \tag{K.3}$$

First, we will find the conditional and unconditional ML estimators. To find $\hat{\hat{b}}$, we use

$$\frac{d}{d(b)}\ln\mathcal{L}(s,b) = 0, \tag{K.4}$$

for a given value of s, where

$$\mathcal{L}(s,b) = \frac{(s+b)^n}{n!}e^{-(s+b)}\frac{(\tau b)^m}{m!}e^{-\tau b}. \tag{K.5}$$

So

$$\ln\mathcal{L}(s,b) = n\ln(s+b) - \ln(n!) - s - b + m\ln\tau + m\ln b - \ln(m!) - \tau b. \tag{K.6}$$

Taking the derivative and simplifying the equation

$$b^2(1+\tau) + b\left[s(1+\tau) - n - m\right] - ms = 0, \tag{K.7}$$

which has the solution

$$\hat{\hat{b}}(s) = \frac{n+m-s(1+\tau)+\sqrt{(n+m-s(1+\tau))^2+4sm(1+\tau)}}{2(1+\tau)}, \tag{K.8}$$

which for the special case of the null hypothesis reduces to

$$\hat{\hat{b}}(0) = \frac{n+m}{1+\tau}. \tag{K.9}$$

For finding the the unconditional ML estimators we need to solve

$$\begin{cases} \frac{d}{d(b)} \ln \mathcal{L}(s,b) = 0, \\ \frac{d}{d(s)} \ln \mathcal{L}(s,b) = 0, \end{cases} \Rightarrow \begin{cases} \frac{n}{s+b} - 1 + \frac{m}{b} - \tau = 0, \\ \frac{n}{s+b} - 1 = 0, \end{cases} \tag{K.10}$$

which gives

$$\begin{cases} \hat{s} = n - m/\tau, \\ \hat{b} = m/\tau. \end{cases} \tag{K.11}$$

All we need to do now is to find $\ln \lambda(0)$. So

$$\ln \lambda(0) = \ln \frac{\mathcal{L}\left(s=0,\hat{\hat{b}}\right)}{\mathcal{L}\left(\hat{s},\hat{b}\right)} = \ln \mathcal{L}\left(s=0,\hat{\hat{b}}\right) - \ln \mathcal{L}\left(\hat{s},\hat{b}\right). \tag{K.12}$$

Let's first find the logarithm of each of the likelihood functions

$$\begin{cases} \ln \mathcal{L}\left(s=0,\hat{\hat{b}}\right) = n \ln\left(\frac{n+m}{1+\tau}\right) - \ln(n!) - \frac{n+m}{1+\tau} + m \ln\left(\frac{\tau(n+m)}{1+\tau}\right) - \ln(m!) - \tau\left(\frac{n+m}{1+\tau}\right), \\ \ln \mathcal{L}\left(\hat{s},\hat{b}\right) = n \ln n - \ln(n!) - n + m \ln m - \ln(m!) - m, \end{cases} \tag{K.13}$$

which reduces $\ln \lambda(0)$ to

$$\ln \lambda(0) = n \ln\left(\frac{n+m}{n(1+\tau)}\right) + m\left(\ln \frac{\tau(n+m)}{m(1+\tau)}\right) - \underbrace{\frac{n+m}{1+\tau} - \tau\frac{n+m}{1+\tau} + n + m}_{=0} \tag{K.14}$$

Before finding Z, we can take another step and get rid of τ in the favour of background uncertainty. In a Poisson distribution, the mean of the distribution is equal to its variance, so

$$V[m] = \tau b, \tag{K.15}$$

and

$$V\left[\hat{b}\right] \equiv \sigma_b^2 = V[m/\tau] = \frac{b}{\tau}. \tag{K.16}$$

Also, instead of n and m we use their expectation values, $s+b$ and τb, respectively. Since $\tau = b/\sigma_b^2$, m becomes $m = b^2/\sigma_b^2$. The test statistic becomes

$$\begin{aligned} q_0 = -2\ln\lambda(0) &= -2\left[(s+b)\ln\left(\frac{s+b+\frac{b^2}{\sigma_b^2}}{(s+b)\left(1+\frac{b}{\sigma_b^2}\right)}\right) + \frac{b^2}{\sigma_b^2}\ln\left(\frac{\frac{b}{\sigma_b^2}\left(s+b\frac{b^2}{\sigma_b^2}\right)}{\frac{b^2}{\sigma_b^2}\left(1+\frac{b}{\sigma_b^2}\right)}\right)\right] \\ &= 2\left[(s+b)\ln\left(\frac{(s+b)(b+\sigma_b^2)}{b^2+(s+b)\sigma_b^2}\right) - \frac{b^2}{\sigma_b^2}\ln\left(1+\frac{\sigma_b^2 s}{b(b+\sigma_b^2)}\right)\right], \end{aligned} \tag{K.17}$$

and significance is simply $Z = \sqrt{q_0}$.

Appendix L

Background Uncertainties

Contribution of different background uncertainties for each decay mode and threshold mass from the Pythia dijet.

M_{th} [TeV]	Decay Mode	b	Absolute (relative %) uncertainty				
			Theory Modelling	JER Uncertainty	JES Uncertainty	Statistical	Total
4.0	Mixed	6.973e+00	3.5e-01 (5.0)	1.7e+00 (24.8)	3.6e+00 (51.5)	1.6e+00 (23.0)	4.3e+00 (61.8)
	Hadronic	3.506e+03	4.1e+01 (1.2)	4.4e-01 (0.0)	2.5e+02 (7.2)	1.8e+01 (0.5)	2.5e+02 (7.3)
	All	3.524e+03	4.2e+01 (1.2)	1.8e+00 (0.1)	2.7e+02 (7.5)	1.8e+01 (0.5)	2.7e+02 (7.7)
5.0	Mixed	1.238e+00	3.2e-02 (2.6)	2.1e-01 (16.7)	7.4e-01 (59.9)	3.9e-01 (31.7)	8.6e-01 (69.9)
	Hadronic	7.224e+02	1.4e+01 (1.9)	3.1e-03 (0.0)	8.2e+01 (11.4)	7.2e+00 (1.0)	8.4e+01 (11.6)
	All	7.250e+02	1.4e+01 (1.9)	2.1e-01 (0.0)	8.4e+01 (11.6)	7.3e+00 (1.0)	8.6e+01 (11.8)
6.0	Mixed	1.449e-01	2.8e-03 (1.9)	3.2e-02 (22.2)	1.2e-01 (80.9)	2.4e-02 (16.8)	1.2e-01 (85.6)
	Hadronic	1.230e+02	2.0e+00 (1.6)	6.2e-04 (0.0)	1.6e+01 (13.1)	2.4e+00 (2.0)	1.6e+01 (13.3)
	All	1.233e+02	2.1e+00 (1.7)	3.2e-02 (0.0)	1.6e+01 (13.3)	2.4e+00 (2.0)	1.7e+01 (13.5)
7.0	Mixed	1.024e-02	7.7e-05 (0.7)	4.8e-04 (4.7)	7.0e-03 (68.2)	2.3e-03 (22.7)	7.4e-03 (72.1)
	Hadronic	1.854e+01	1.1e-01 (0.6)	1.4e-04 (0.0)	4.5e+00 (24.3)	4.9e-01 (2.6)	4.5e+00 (24.4)
	All	1.855e+01	1.2e-01 (0.6)	4.7e-04 (0.0)	4.5e+00 (24.3)	4.9e-01 (2.6)	4.5e+00 (24.4)
8.0	Mixed	9.467e-04	3.5e-05 (3.7)	5.7e-05 (6.0)	7.6e-04 (80.3)	5.9e-05 (6.2)	7.7e-04 (80.8)
	Hadronic	1.560e+00	4.7e-02 (3.0)	6.4e-06 (0.0)	4.3e-01 (27.6)	8.6e-02 (5.5)	4.4e-01 (28.3)
	All	1.561e+00	4.6e-02 (3.0)	5.7e-05 (0.0)	4.3e-01 (27.6)	9.5e-02 (6.1)	4.4e-01 (28.5)
9.0	Mixed	3.523e-05	2.6e-06 (7.5)	2.4e-06 (6.8)	3.1e-05 (88.8)	2.3e-06 (6.7)	3.2e-05 (89.6)
	Hadronic	9.631e-02	7.5e-03 (7.8)	5.2e-07 (0.0)	2.5e-02 (26.0)	5.3e-03 (5.5)	2.7e-02 (27.7)
	All	9.635e-02	7.5e-03 (7.8)	2.4e-06 (0.0)	2.5e-02 (26.0)	5.3e-03 (5.5)	2.7e-02 (27.7)
9.5	Mixed	6.163e-06	4.2e-07 (6.8)	4.3e-07 (6.9)	4.6e-06 (74.8)	1.2e-06 (19.9)	4.8e-06 (78.0)
	Hadronic	2.535e-02	3.1e-03 (12.1)	1.3e-07 (0.0)	1.1e-02 (42.5)	1.3e-03 (5.0)	1.1e-02 (44.4)
	All	2.535e-02	3.1e-03 (12.1)	4.4e-07 (0.0)	1.1e-02 (42.5)	1.3e-03 (5.0)	1.1e-02 (44.4)
10.0	Mixed	1.904e-06	2.0e-07 (10.5)	1.4e-07 (7.5)	1.8e-06 (94.8)	3.8e-08 (2.0)	1.8e-06 (95.7)
	Hadronic	6.190e-03	1.0e-03 (16.3)	1.3e-07 (0.0)	3.6e-03 (58.6)	3.8e-04 (6.1)	3.8e-03 (61.2)
	All	6.192e-03	1.0e-03 (16.4)	1.9e-07 (0.0)	3.6e-03 (58.6)	3.8e-04 (6.1)	3.8e-03 (61.2)

Table L.1: The absolute and relative uncertainty from statistical, theory modelling, and JER and JES uncertainty for the considered topologies.

Appendix M

Signal Uncertainty

The statistical and systematic uncertainty of the $M_{th} = 2, 6, 8, 10$ TeV QBH samples for the ADD model with $n = 2, 4, 6$ and RS1 model. The systematic uncertainty is due to the detector effects and the randomness associated with including them.

M_{th} [TeV]	Decay Mode	Model	s	Absolute (relative %) uncertainty		
				Statistical	JER+JES	Total
4.0	Mixed	ADDn6	1.44e+05	5.20e+02 (0.36)	3.94e+03 (2.74)	3.97e+03 (2.77)
		ADDn4	6.91e+04	2.51e+02 (0.36)	1.82e+03 (2.63)	1.83e+03 (2.66)
		ADDn2	1.78e+04	6.45e+01 (0.36)	4.54e+02 (2.55)	4.59e+02 (2.57)
		RS1	5.96e+02	2.15e+00 (0.36)	1.53e+01 (2.56)	1.54e+01 (2.59)
	Hadronic	ADDn6	6.49e+05	1.11e+03 (0.17)	3.25e+04 (5.02)	3.26e+04 (5.02)
		ADDn4	3.13e+05	5.33e+02 (0.17)	1.55e+04 (4.95)	1.55e+04 (4.95)
		ADDn2	8.11e+04	1.37e+02 (0.17)	3.91e+03 (4.82)	3.91e+03 (4.82)
		RS1	2.71e+03	4.58e+00 (0.17)	1.26e+02 (4.66)	1.26e+02 (4.66)
	All	ADDn6	7.92e+05	1.22e+03 (0.15)	3.65e+04 (4.60)	3.65e+04 (4.61)
		ADDn4	3.82e+05	5.89e+02 (0.15)	1.73e+04 (4.53)	1.73e+04 (4.53)
		ADDn2	9.89e+04	1.52e+02 (0.15)	4.36e+03 (4.41)	4.36e+03 (4.41)
		RS1	3.30e+03	5.06e+00 (0.15)	1.41e+02 (4.28)	1.41e+02 (4.28)
5.0	Mixed	ADDn6	2.36e+04	8.31e+01 (0.35)	8.39e+02 (3.56)	8.43e+02 (3.58)
		ADDn4	1.10e+04	3.92e+01 (0.36)	3.64e+02 (3.30)	3.66e+02 (3.32)
		ADDn2	2.81e+03	9.87e+00 (0.35)	9.33e+01 (3.32)	9.38e+01 (3.34)
		RS1	8.84e+01	3.10e-01 (0.35)	2.87e+00 (3.25)	2.89e+00 (3.27)
	Hadronic	ADDn6	1.01e+05	1.72e+02 (0.17)	6.61e+03 (6.58)	6.61e+03 (6.58)
		ADDn4	4.83e+04	8.21e+01 (0.17)	3.14e+03 (6.51)	3.14e+03 (6.51)
		ADDn2	1.20e+04	2.04e+01 (0.17)	7.60e+02 (6.33)	7.60e+02 (6.33)
		RS1	3.77e+02	6.41e-01 (0.17)	2.41e+01 (6.40)	2.42e+01 (6.40)
	All	ADDn6	1.24e+05	1.91e+02 (0.15)	7.45e+03 (6.00)	7.45e+03 (6.01)
		ADDn4	5.93e+04	9.09e+01 (0.15)	3.51e+03 (5.91)	3.51e+03 (5.91)
		ADDn2	1.48e+04	2.27e+01 (0.15)	8.53e+02 (5.76)	8.53e+02 (5.76)
		RS1	4.66e+02	7.12e-01 (0.15)	2.70e+01 (5.80)	2.70e+01 (5.80)

Table M.1: A table of number of signal events for each decay mode of $M_{th} = 4$ TeV and $M_{th} = 5$ TeV samples for all the considered models. The absolute and relative statistical uncertainty, the uncertainty due to JER and JES uncertainty from the emulated detector effects, and the total uncertainty are also shown.

M_{th} [TeV]	Decay Mode	Model	s	Absolute (relative %) uncertainty		
				Statistical	JER+JES	Total
6.0	Mixed	ADDn6	3.51e+03	1.23e+01 (0.35)	1.58e+02 (4.50)	1.59e+02 (4.52)
		ADDn4	1.62e+03	5.71e+00 (0.35)	7.13e+01 (4.41)	7.16e+01 (4.43)
		ADDn2	4.02e+02	1.40e+00 (0.35)	1.76e+01 (4.37)	1.76e+01 (4.39)
		RS1	1.19e+01	4.16e-02 (0.35)	5.15e-01 (4.32)	5.16e-01 (4.33)
	Hadronic	ADDn6	1.43e+04	2.47e+01 (0.17)	1.18e+03 (8.30)	1.18e+03 (8.30)
		ADDn4	6.75e+03	1.17e+01 (0.17)	5.60e+02 (8.30)	5.60e+02 (8.30)
		ADDn2	1.63e+03	2.82e+00 (0.17)	1.33e+02 (8.17)	1.33e+02 (8.17)
		RS1	4.87e+01	8.41e-02 (0.17)	3.99e+00 (8.20)	3.99e+00 (8.20)
	All	ADDn6	1.78e+04	2.76e+01 (0.16)	1.34e+03 (7.55)	1.34e+03 (7.55)
		ADDn4	8.36e+03	1.30e+01 (0.16)	6.31e+02 (7.55)	6.31e+02 (7.55)
		ADDn2	2.04e+03	3.15e+00 (0.15)	1.51e+02 (7.42)	1.51e+02 (7.42)
		RS1	6.06e+01	9.38e-02 (0.15)	4.51e+00 (7.43)	4.51e+00 (7.44)
7.0	Mixed	ADDn6	4.37e+02	1.54e+00 (0.35)	2.46e+01 (5.64)	2.47e+01 (5.65)
		ADDn4	1.99e+02	7.09e-01 (0.36)	1.10e+01 (5.53)	1.10e+01 (5.54)
		ADDn2	4.80e+01	1.69e-01 (0.35)	2.61e+00 (5.44)	2.62e+00 (5.45)
		RS1	1.35e+00	4.77e-03 (0.35)	7.32e-02 (5.41)	7.33e-02 (5.43)
	Hadronic	ADDn6	1.73e+03	3.06e+00 (0.18)	1.79e+02 (10.37)	1.79e+02 (10.37)
		ADDn4	8.05e+02	1.43e+00 (0.18)	8.44e+01 (10.48)	8.44e+01 (10.49)
		ADDn2	1.90e+02	3.37e-01 (0.18)	1.97e+01 (10.36)	1.97e+01 (10.36)
		RS1	5.34e+00	9.47e-03 (0.18)	5.56e-01 (10.42)	5.56e-01 (10.42)
	All	ADDn6	2.16e+03	3.43e+00 (0.16)	2.04e+02 (9.41)	2.04e+02 (9.41)
		ADDn4	1.00e+03	1.59e+00 (0.16)	9.53e+01 (9.50)	9.54e+01 (9.50)
		ADDn2	2.38e+02	3.77e-01 (0.16)	2.23e+01 (9.37)	2.23e+01 (9.37)
		RS1	6.69e+00	1.06e-02 (0.16)	6.29e-01 (9.41)	6.29e-01 (9.41)

Table M.2: A table of number of signal events for each decay mode of $M_{th} = 6$ TeV and $M_{th} = 7$ TeV samples for all the considered models. The absolute and relative statistical uncertainty, the uncertainty due to JER and JES uncertainty from the emulated detector effects, and the total uncertainty are also shown.

M_{th} [TeV]	Decay Mode	Model	s	Absolute (relative %) uncertainty		
				Statistical	JER+JES	Total
8.0	Mixed	ADDn6	4.23e+01	1.52e-01 (0.36)	2.82e+00 (6.68)	2.83e+00 (6.68)
		ADDn4	1.91e+01	6.89e-02 (0.36)	1.24e+00 (6.52)	1.24e+00 (6.53)
		ADDn2	4.49e+00	1.61e-02 (0.36)	2.89e-01 (6.44)	2.89e-01 (6.45)
		RS1	1.18e-01	4.24e-04 (0.36)	7.98e-03 (6.76)	7.99e-03 (6.77)
	Hadronic	ADDn6	1.62e+02	2.97e-01 (0.18)	2.14e+01 (13.24)	2.14e+01 (13.24)
		ADDn4	7.45e+01	1.36e-01 (0.18)	9.76e+00 (13.10)	9.76e+00 (13.10)
		ADDn2	1.72e+01	3.14e-02 (0.18)	2.25e+00 (13.13)	2.25e+00 (13.13)
		RS1	4.53e-01	8.31e-04 (0.18)	5.96e-02 (13.15)	5.96e-02 (13.15)
	All	ADDn6	2.04e+02	3.33e-01 (0.16)	2.43e+01 (11.88)	2.43e+01 (11.88)
		ADDn4	9.36e+01	1.53e-01 (0.16)	1.10e+01 (11.76)	1.10e+01 (11.76)
		ADDn2	2.17e+01	3.53e-02 (0.16)	2.54e+00 (11.74)	2.54e+00 (11.74)
		RS1	5.71e-01	9.33e-04 (0.16)	6.76e-02 (11.83)	6.76e-02 (11.83)
9.0	Mixed	ADDn6	2.76e+00	1.01e-02 (0.37)	2.21e-01 (8.01)	2.22e-01 (8.02)
		ADDn4	1.23e+00	4.54e-03 (0.37)	9.80e-02 (7.98)	9.81e-02 (7.99)
		ADDn2	2.80e-01	1.03e-03 (0.37)	2.25e-02 (8.02)	2.25e-02 (8.03)
		RS1	6.86e-03	2.53e-05 (0.37)	5.58e-04 (8.13)	5.59e-04 (8.14)
	Hadronic	ADDn6	1.02e+01	1.95e-02 (0.19)	1.71e+00 (16.70)	1.71e+00 (16.70)
		ADDn4	4.64e+00	8.83e-03 (0.19)	7.81e-01 (16.84)	7.81e-01 (16.84)
		ADDn2	1.04e+00	1.98e-03 (0.19)	1.73e-01 (16.63)	1.73e-01 (16.64)
		RS1	2.54e-02	4.86e-05 (0.19)	4.25e-03 (16.72)	4.25e-03 (16.72)
	All	ADDn6	1.30e+01	2.20e-02 (0.17)	1.93e+00 (14.86)	1.93e+00 (14.86)
		ADDn4	5.87e+00	9.94e-03 (0.17)	8.79e-01 (14.99)	8.79e-01 (14.99)
		ADDn2	1.32e+00	2.23e-03 (0.17)	1.95e-01 (14.81)	1.95e-01 (14.81)
		RS1	3.23e-02	5.48e-05 (0.17)	4.81e-03 (14.89)	4.81e-03 (14.89)

Table M.3: A table of number of signal events for each decay mode of $M_{th} = 8$ TeV and $M_{th} = 9$ TeV samples for all the considered models. The absolute and relative statistical uncertainty, the uncertainty due to JER and JES uncertainty from the emulated detector effects, and the total uncertainty are also shown.

M_{th} [TeV]	Decay Mode	Model	s	Absolute (relative %) uncertainty		
				Statistical	JER+JES	Total
9.5	Mixed	ADDn6	5.69e-01	2.12e-03 (0.37)	5.11e-02 (8.98)	5.11e-02 (8.99)
		ADDn4	2.50e-01	9.40e-04 (0.38)	2.11e-02 (8.43)	2.11e-02 (8.44)
		ADDn2	5.63e-02	2.10e-04 (0.37)	5.14e-03 (9.14)	5.15e-03 (9.14)
		RS1	1.32e-03	4.92e-06 (0.37)	1.21e-04 (9.13)	1.21e-04 (9.14)
	Hadronic	ADDn6	2.07e+00	4.04e-03 (0.20)	3.91e-01 (18.87)	3.91e-01 (18.87)
		ADDn4	9.34e-01	1.82e-03 (0.19)	1.77e-01 (18.95)	1.77e-01 (18.95)
		ADDn2	2.06e-01	4.01e-04 (0.20)	3.88e-02 (18.87)	3.88e-02 (18.87)
		RS1	4.77e-03	9.35e-06 (0.20)	9.12e-04 (19.13)	9.12e-04 (19.13)
	All	ADDn6	2.64e+00	4.57e-03 (0.17)	4.42e-01 (16.74)	4.42e-01 (16.74)
		ADDn4	1.18e+00	2.05e-03 (0.17)	1.98e-01 (16.73)	1.98e-01 (16.73)
		ADDn2	2.62e-01	4.53e-04 (0.17)	4.39e-02 (16.78)	4.39e-02 (16.78)
		RS1	6.09e-03	1.06e-05 (0.17)	1.03e-03 (16.96)	1.03e-03 (16.96)
10.0	Mixed	ADDn6	9.58e-02	3.62e-04 (0.38)	9.23e-03 (9.64)	9.24e-03 (9.65)
		ADDn4	4.16e-02	1.59e-04 (0.38)	4.06e-03 (9.78)	4.07e-03 (9.79)
		ADDn2	9.25e-03	3.50e-05 (0.38)	9.02e-04 (9.76)	9.03e-04 (9.77)
		RS1	2.01e-04	7.64e-07 (0.38)	1.88e-05 (9.37)	1.89e-05 (9.37)
	Hadronic	ADDn6	3.41e-01	6.83e-04 (0.20)	7.31e-02 (21.46)	7.31e-02 (21.46)
		ADDn4	1.52e-01	3.04e-04 (0.20)	3.29e-02 (21.71)	3.29e-02 (21.71)
		ADDn2	3.30e-02	6.61e-05 (0.20)	7.10e-03 (21.55)	7.10e-03 (21.56)
		RS1	7.14e-04	1.44e-06 (0.20)	1.57e-04 (21.99)	1.57e-04 (21.99)
	All	ADDn6	4.36e-01	7.73e-04 (0.18)	8.23e-02 (18.87)	8.23e-02 (18.87)
		ADDn4	1.93e-01	3.43e-04 (0.18)	3.70e-02 (19.14)	3.70e-02 (19.14)
		ADDn2	4.22e-02	7.48e-05 (0.18)	8.01e-03 (18.97)	8.01e-03 (18.97)
		RS1	9.15e-04	1.63e-06 (0.18)	1.76e-04 (19.21)	1.76e-04 (19.22)

Table M.4: A table of number of signal events for each decay mode of $M_{th} = 9.5$ TeV and $M_{th} = 10$ TeV samples for all the considered models. The absolute and relative statistical uncertainty, the uncertainty due to JER and JES uncertainty from the emulated detector effects, and the total uncertainty are also shown.

Appendix N

JER & JES Uncertainty

The effect of including the JER, JER uncertainty, and JES uncertainty on the dijet mass distribution of the QBH samples, in the ADDn6 model. The dijet events must have satisfied $p_{T_{1(2)}} > 440$ (60) and $|y^*| = |(y_1 - y_2)/2| < 0.6$.

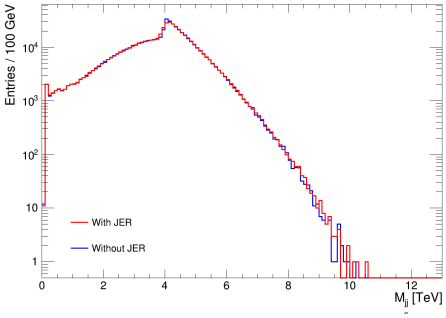

(a) $M_{th} = 4$ TeV

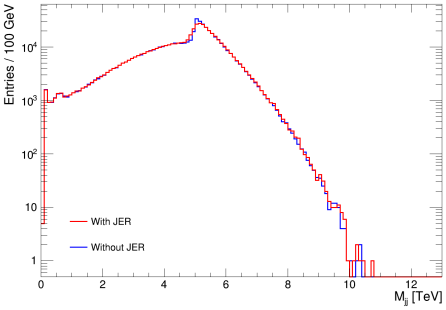

(b) $M_{th} = 5$ TeV

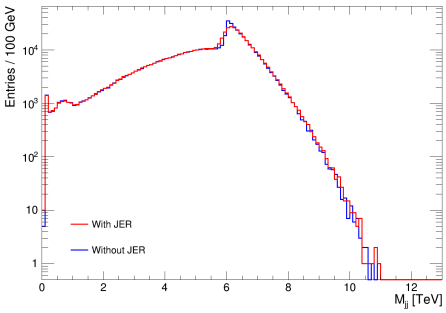

(c) $M_{th} = 6$ TeV

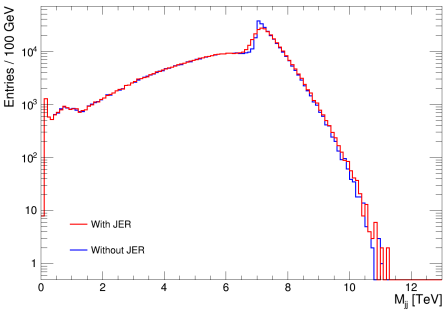

(d) $M_{th} = 7$ TeV

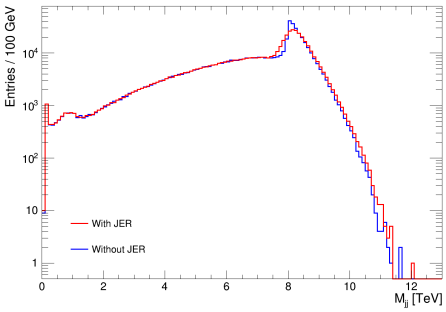

(e) $M_{th} = 8$ TeV

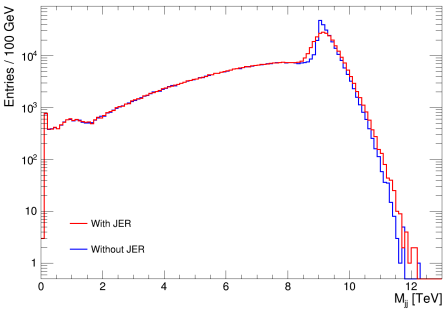

(f) $M_{th} = 9$ TeV

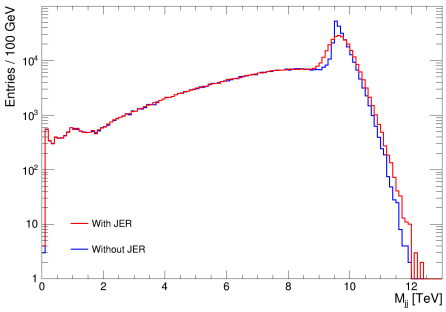

(g) $M_{th} = 9.5$ TeV

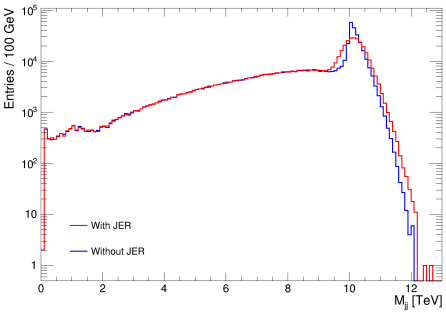

(h) $M_{th} = 10$ TeV

Figure N.1: The dijet mass distribution of QBH samples in the ADDn6 model with and without applying JER.

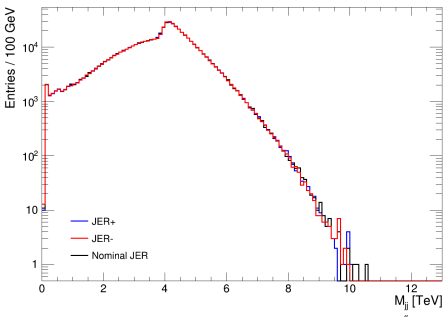

(a) $M_{th} = 4$ TeV

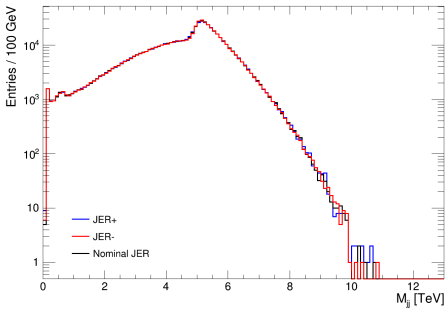

(b) $M_{th} = 5$ TeV

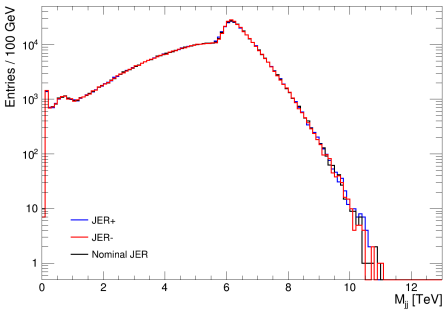

(c) $M_{th} = 6$ TeV

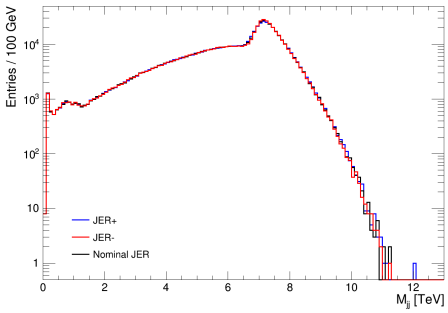

(d) $M_{th} = 7$ TeV

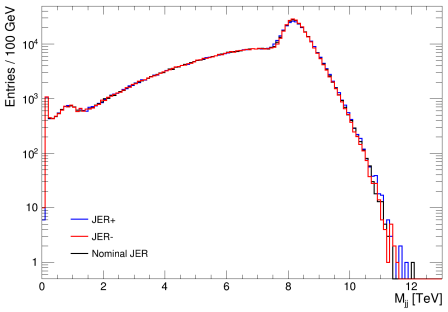

(e) $M_{th} = 8$ TeV

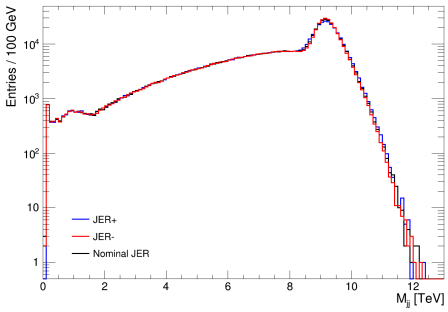

(f) $M_{th} = 9$ TeV

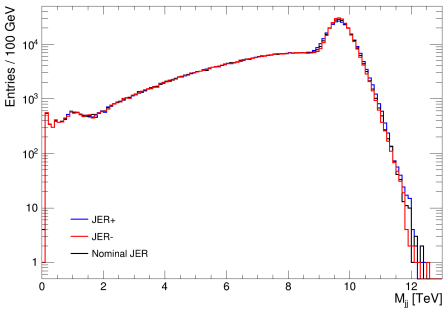

(g) $M_{th} = 9.5$ TeV

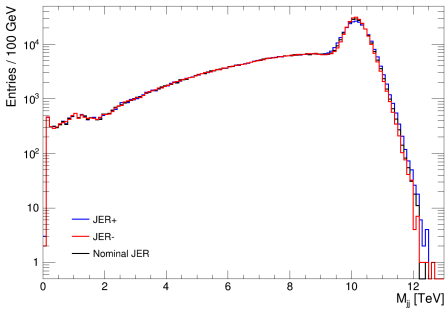

(h) $M_{th} = 10$ TeV

Figure N.2: The dijet mass distribution of QBH samples in the ADDn6 model with applying nominal JER and ± JER uncertainty.

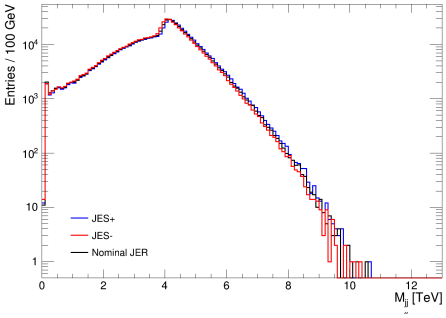

(a) $M_{th} = 4$ TeV

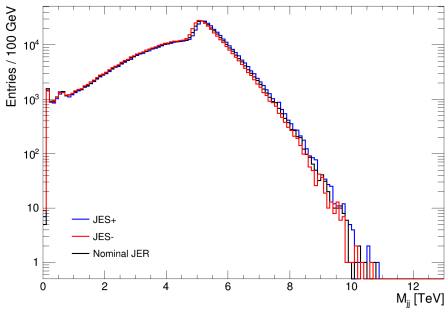

(b) $M_{th} = 5$ TeV

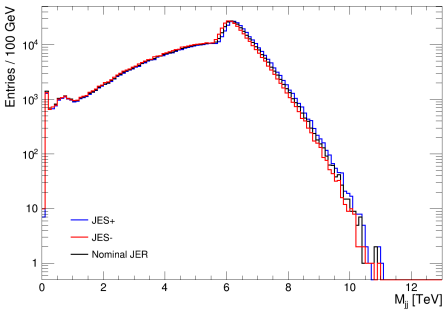

(c) $M_{th} = 6$ TeV

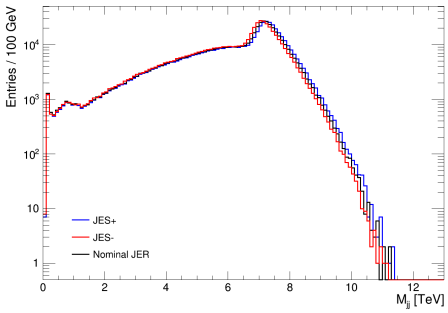

(d) $M_{th} = 7$ TeV

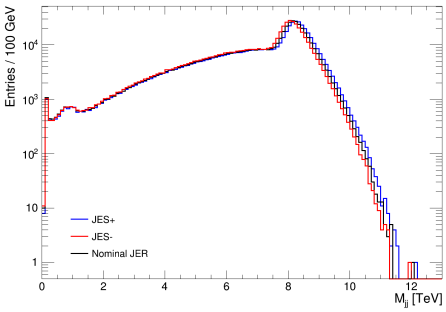

(e) $M_{th} = 8$ TeV

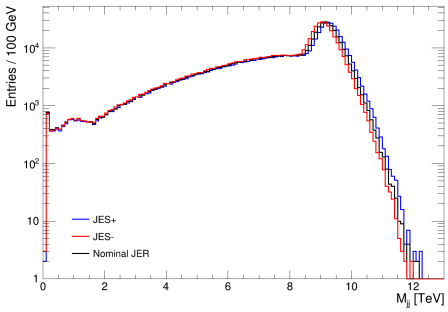

(f) $M_{th} = 9$ TeV

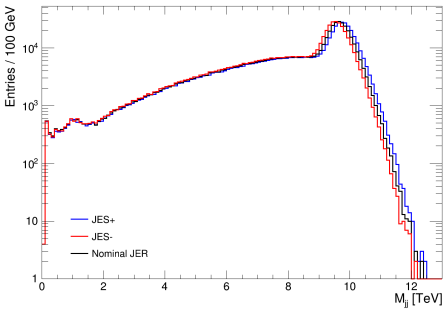

(g) $M_{th} = 9.5$ TeV

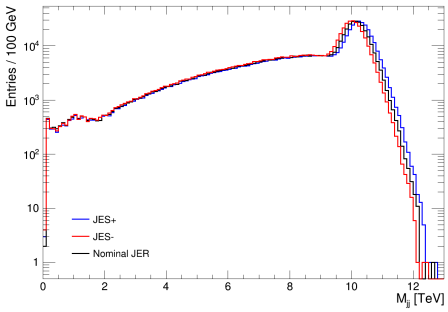

(h) $M_{th} = 10$ TeV

Figure N.3: The dijet mass distribution of QBH samples in the ADDn6 model with applying nominal JER and ± JES uncertainty.